

# **Dynamical structure formation in passive and active colloidal systems**

INAUGURAL-DISSERTATION

zur

Erlangung des Doktorgrades  
der Mathematisch-Naturwissenschaftlichen Fakultät  
der Universität zu Köln



vorgelegt von

Shibananda Das  
aus Agartala, India

Jülich 2017



Berichterstatter: Prof. Dr. Gerhard Gompper

Prof. Dr. Andreas Schadschneider

Tag der mündlichen Prüfung: 19 January 2018





I would like to dedicate this thesis to my loving parents . . .



# Acknowledgements

First of all, I would like to express my sincere acknowledgment toward Prof. Dr. Gerhard Gompper and Prof. Dr. Roland G. Winkler for providing me with the opportunity to carry out my doctoral research at the Theoretical Soft Matter and Biophysics (ICS-2 / IAS-2) institute at Forschungszentrum Jülich and also for their enthusiastic supervision and guidance throughout my PhD. Based on their broad knowledge and experience, they always provided valuable input by constructively questioning every result and offering plenty of time for discussions. In addition, I would like to express my gratitude to Prof. Dr. Andreas Schadschneider for accepting to review my thesis.

I want to thank Dr. Saskia Bucciarelli, Dr. Gerrit Vliegenthart, Prof. Dr. Peter Schurtenberger, and Prof. Dr. Anna Stradner for the good collaboration on the project of short-time diffusion of anisotropic patchy colloids. I am grateful to our collaborators in the study of magnetic dispersions, Dr. Gašper Kokot, Prof. Dr. Igor S. Aranson, and Dr. Alexey Snezhko, for sharing their knowledge about active turbulence. I would like to thank Dr. Jonas Riest, Prof. Dr. Jan K. G. Dhont, and Prof. Dr. Gerhard Nägele for their fruitful collaboration with us to explore the dynamics in clustering SALR systems.

I thank my colleagues at the Forschungszentrum Jülich for all the stimulating discussions and the precious moments we shared during and outside of work. A special thanks goes to Dr. Jin Suk Myung and Dr. Anoop Varghese for their wise advice and helpful suggestions during the initial year of my PhD.

Thanks to my friends here in Jülich, which is a long list to put in, with whom I have spent the memorable three years of my life. I deeply acknowledge my office mate Thomas Eisenstecken for the discussions related to or un-related to work and for keeping me motivated.

Lastly, I would like to thank my parents for their support and encouragement.



# Abstract

Colloidal particles are model systems for a wide range of phenomena on mesoscopic length scales from 10s of nanometers to 10s of micrometers. “Colloidal physics” therefore applies to systems as diverse as proteins in dense solutions and magnetic particles in time-dependent external fields.

In the dense and crowded environment of the cell cytoplasm, an individual protein feels the presence of and interacts with all surrounding proteins which leads to a strong coupling of their dynamics. We investigate the aggregation in protein solutions emerging from different interparticle interactions in an attempt to understand theoretical and experimental observations. Dispersions of particles with short-range attractive and long-range repulsive interactions, for example corresponding to low-salinity Lysozyme protein solutions, exhibit rich equilibrium microstructures and an intriguing phase behavior. We present simulation results in comparison with theoretical predictions for structural and, in particular, short-time diffusion properties of a colloidal model system with such interactions, both in the dispersed-fluid and equilibrium-cluster phase regions. Next, we extend our investigation to the study of colloids with anisotropic and patchy interactions. In quasi-elastic neutron scattering experiments, the short-time diffusion coefficient of the well-characterized and highly stable eye-lens protein  $\gamma_B$ -crystallin at concentrations comparable to those present in the eye lens and on length scales comparable to the nearest-neighbor distance, has been observed to slow down significantly with increasing concentration. We find, via a comparison with simulations of patchy colloids, that the presence of attractive sites on the colloid surface play an essential role in determining the local short-time dynamics. Hence, our simulations clearly demonstrates the enormous effect of weak directed attractions can have on the short-time diffusion of proteins at concentrations comparable to those in the cellular cytosol.

Further, we investigate a dispersion of magnetic spherical colloids energized by a uniaxial alternating magnetic field, which manifests dynamic self-assembly into spinners, short rod-like chains of a few particles, rotating in clockwise or counterclockwise direction. We report on active turbulence and transport in the gas of self-assembled spinners in comparison with experiments. We show that the spinners, emerging as a result of spontaneous symmetry breaking of clock/counterclockwise rotation of self-assembled particle chains, generate active vortical flows. These emergent self-induced currents promote active diffusion that can be tuned by the parameters of the external excitation field.

We apply colloidal models also to active matter systems, where we study the active Brownian particle (ABP) model for active systems to achieve insight into the stationary-state distribution of confined ABPs and to derive an expression for the bulk pressure in a sub-volume of the system. The analytical solution of the Fokker-Planck equation for an active Ornstein-Uhlenbeck particle (AOUP) in a harmonic potential is presented and a conditional distribution function is provided for the radial particle distribution at a given magnitude of the propulsion velocity. This conditional probability distribution facilitates the description of the coupling

---

of the spatial coordinate and propulsion, which yields activity-induced accumulation of particles. For the anharmonic potential, a probability distribution function is derived within the unified colored noise approximation. The comparison of the simulation results with theoretical predictions yields good agreement for large rotational diffusion coefficients, e.g., due to tumbling, even for large propulsion velocities (Péclet numbers). For the pressure in a local sub-volume, we derive corresponding expressions for ABPs confined by walls or with periodic boundaries using the virial theorem. In both cases, the local pressure comprises of an activity-induced contribution, which can be expressed in terms of a flux of particles, and a contribution by interparticle forces. We find that the local pressure of ABPs under confinement explicitly depends on the presence of the confining walls and the particle-wall interactions. Moreover, the local pressure in interacting ABP systems with periodic boundary conditions displays a nonmonotonic concentration dependence at higher activity.

# Kurzzusammenfassung

Kolloide sind ein beliebtes Modellsystem mit welchem zahlreiche Phänomene, die auf mesoskopischen Längenskalen von zehn Nanometern bis zehn Mikrometern auftreten, beschrieben werden können. “Kolloidphysik” lässt sich auf verschiedenste Systeme anwenden, von dichten Lösungen von Proteinen bis hin zu magnetischen Teilchen in einem äußeren, zeitabhängigen Feld.

In der dichten und gedrängten Umgebung des Zellplasmas kommt es durch die unmittelbare Wechselwirkung der Proteine untereinander zu einer starken Kopplung derer Dynamik. Um experimentelle Beobachtungen und theoretische Vorhersagen besser verstehen zu können, untersuchen wir mithilfe von Simulationen den Einfluss verschiedener Wechselwirkungsmodelle auf die Aggregationseigenschaften von Proteinlösungen. Lösungen von Teilchen welche einer kurzreichweitigen, anziehenden und einer langreichweitigen, abstoßenden Wechselwirkung unterliegen, wie zum Beispiel Lysozyme Proteinlösungen mit geringem Salzgehalt, weisen interessante Gleichgewichts-Mikrostrukturen und ein faszinierendes Phasenverhalten auf. Mittels Computersimulationen gewinnen wir einen Einblick in die Physik solcher komplexen Systeme und vergleichen unsere Ergebnisse mit theoretischen Vorhersagen der Clusterstruktur und der Kurzzeit-Diffusionseigenschaften. Dabei fokussieren wir uns sowohl auf die gelöste Fluid-Phase, als auch auf die Gleichgewichts-Cluster-Phase.

In einem nächsten Schritt erweitern wir unsere Untersuchungen auf Kolloide mit anisotropen “patchy”-Wechselwirkungen. In quasi-elastischen Neutronenstreuexperimenten wurde beobachtet, dass das Kurzzeit-Diffusionsverhalten von  $\gamma_B$ -Kristallin Proteinlösungen, in Konzentrationen wie sie auch in menschlichen Augenlinsen vorzufinden finden sind, mit zunehmender Konzentration erheblich abgeschwächt wird. Wir zeigen mittels Simulationen von patchy-Kolloiden, dass anisotrope, anziehende Wechselwirkungen anstelle von isotropen Wechselwirkungspotenzialen eine essenzielle Rolle im räumlich-lokalen Kurzzeitverhalten spielen. Unsere Simulationen weisen auf den enormen Einfluss von schwachen, aber räumlich gerichteten Anziehungspotentialen hin und zeigen deren Einfluss auf die Kurzzeit-Diffusion von Proteinen in Konzentrationen wie sie auch im zellulären Zytosol auftreten auf.

Des Weiteren untersuchen wir eine Lösung von magnetischen, sphärischen Kolloiden welche von außen durch ein uniaxiales und zeitlich variierendes Magnetfeld getrieben werden. Dieses System manifestiert eine dynamische Selbstorganisation hin zu sogenannten “spinners” (kurze, stabförmige Ketten bestehend aus einigen wenigen Kolloiden), welche sich im Uhrzeige-, sowie Gegenuhrzeigesinn drehen. Wir untersuchen die im System auftretende aktive Turbulenz und Transporteigenschaften im Vergleich mit experimentellen Daten. Wir zeigen, dass die spinner, resultierend durch eine spontane Symmetriebrechung von links und rechts drehender Teilchenkettens, aktive, wirbelartige Strömungen verursachen. Diese selbstinduzierten Strömungen fördern die aktive Diffusion und können durch Verändern der

---

Parameter des äußeren Magnetfeldes gesteuert werden.

Wir wenden das Modellsystem von Kolloiden auch auf Systeme aktiver Materie an. Im speziellen untersuchen wir räumlich eingespernte aktive Brownsche Teilchen (ABP) und berechnen deren Verteilungsfunktion im stationären Zustand. Zusätzlich berechnen wir den Druck eines solchen “aktiven” Gases in einem Teilvolumen des Systems. Wir geben die Lösung der Fokker-Planck Gleichung für ein Ornstein-Uhlenbeck Teilchen in einem harmonischen Potential an und eine radiale, bedingte Verteilungsfunktion für eine festgelegte Antriebsgeschwindigkeit wird abgeleitet. Diese bedingte Verteilungsfunktion gibt Einblick in die Kopplung von Position und Antriebsgeschwindigkeit der Teilchen, welche letztlich zu einer Zunahme der Teilchendichte an den einschließenden Wänden des Systems führt. Des Weiteren leiten wir eine Verteilungsfunktion für anharmonische Potenziale im Rahmen der “unified colored noise”-Näherung ab. Für große Rotationsdiffusionskoeffizienten stimmen die Simulationsdaten mit den theoretischen Vorhersagen selbst für hohe Antriebsgeschwindigkeiten sehr gut überein.

Zur Berechnung des Drucks in einem Teilvolumen des Systems, leiten wir entsprechende Ausdrücke sowohl für ABPs, welche in einem Volumen begrenzt sind, als auch für ABPs unter periodischen Randbedingungen mithilfe des Virialtheorems ab. In beiden Fällen beinhaltet der lokale Druck einen Beitrag welcher aufgrund der Aktivität der Teilchen hervorgerufen wird (kann als Teilchenfluss ausgedrückt werden) und einen Beitrag der durch die Teilchen-Teilchen Wechselwirkung verursacht wird. Wir zeigen, dass der lokale Druck von räumlich begrenzten ABPs explizit von der Präsenz der einschließenden Oberfläche, sowie den Teilchen-Wand Wechselwirkungen abhängt. Im Speziellen weist der lokale Druck eines Systems von untereinander wechselwirkenden ABPs unter periodischen Randbedingungen ein nichtmonotonisches Verhalten für hohe Aktivitäten auf.



# Contents

<b>Introduction</b>	<b>17</b>
0.1 Proteins . . . . .	17
0.2 Active matters . . . . .	22
0.3 Particles in time-dependent external fields . . . . .	24
0.4 Contents of the thesis . . . . .	26
<b>I Methods &amp; Theoretical background</b>	<b>29</b>
<b>1 Brownian motion</b>	<b>31</b>
1.1 Langevin Equation . . . . .	31
1.1.1 Overdamped motion . . . . .	31
1.2 Stochastic calculus . . . . .	32
1.2.1 Stochastic integration . . . . .	32
1.2.2 Ito's stochastic differential formula . . . . .	33
1.3 Fokker-Planck equation . . . . .	33
1.3.1 Boundary conditions . . . . .	34
1.4 Ornstein-Uhlenbeck process . . . . .	34
1.4.1 Fokker-Planck equation . . . . .	35
1.5 Brownian Dynamics . . . . .	37
1.5.1 Ermak-McCammon algorithm . . . . .	37
<b>2 Hydrodynamics</b>	<b>39</b>
2.1 Navier-Stokes equations . . . . .	39
2.1.1 Conservation laws . . . . .	39
2.1.2 Stress tensor . . . . .	41
2.1.3 Stokes equations . . . . .	41
2.1.4 Hydrodynamic interaction . . . . .	43
2.2 Turbulence . . . . .	44
2.2.1 Energy balance . . . . .	44
2.2.2 Vorticity equation . . . . .	44
2.2.3 Energy Spectrum . . . . .	45
2.2.4 Two dimensional Turbulence . . . . .	46
2.3 Multiparticle Collision Dynamics . . . . .	49
2.3.1 Algorithm . . . . .	49
2.3.2 Embedded object and boundary conditions . . . . .	51

## Contents

---

2.3.3	Thermostat . . . . .	52
2.3.4	Random MPC . . . . .	53
2.3.5	Unit and parameters . . . . .	54
2.3.6	Stress tensor . . . . .	54
2.3.7	Viscosity . . . . .	55
<b>3</b>	<b>Equilibrium microstructure and dynamics</b>	<b>57</b>
3.1	Static distribution functions . . . . .	57
3.1.1	Radial distribution function . . . . .	58
3.1.2	Static structure factor . . . . .	59
3.2	Dynamic properties . . . . .	59
3.2.1	Dynamic structure factor . . . . .	59
3.2.2	Short time dynamics . . . . .	60
<b>II</b>	<b>Protein aggregation</b>	<b>63</b>
<b>4</b>	<b>Equilibrium clusters in SALR protein solutions</b>	<b>65</b>
4.1	Lennard-Jones-Yukawa colloid system . . . . .	65
4.1.1	Colloid model . . . . .	65
4.1.2	Parameters . . . . .	67
4.2	Results: phase behavior and microstructure . . . . .	68
4.2.1	Structure factor . . . . .	68
4.2.2	Cluster formation criterion . . . . .	69
4.2.3	Cluster size distribution . . . . .	70
4.2.4	Pair correlation function . . . . .	72
4.3	Results: Dynamics . . . . .	74
4.3.1	Short time dynamics . . . . .	74
4.3.2	Cluster dynamics . . . . .	75
4.4	Summary . . . . .	78
<b>5</b>	<b>Anisotropic interaction dependent self-aggregation</b>	<b>79</b>
5.1	Attractive colloidal system . . . . .	79
5.1.1	Colloid model . . . . .	79
5.1.2	Second virial coefficient $B_2^*$ . . . . .	81
5.1.3	Phase diagram . . . . .	81
5.2	Results: short time diffusion . . . . .	82
5.3	Results: system configuration & bond lifetime . . . . .	85
5.4	Results: microstructure . . . . .	86
5.4.1	Static structure factor . . . . .	86
5.4.2	Pair correlation function . . . . .	86
5.4.3	Cluster analysis . . . . .	87
5.5	Summary . . . . .	90

### III Active Brownian Particles 91

<b>6</b>	<b>Minimal model of active particles</b>	<b>93</b>
6.1	ABP model . . . . .	93
6.1.1	Solving equations of motion . . . . .	94
6.2	Dynamics of ABPs . . . . .	95
6.2.1	Autocorrelation of orientation vector . . . . .	95
6.2.2	Diffusion . . . . .	96
6.3	Active Ornstein-Uhlenbeck Particle . . . . .	96
<b>7</b>	<b>Confined ABPs</b>	<b>99</b>
7.1	AOUP in harmonic potential . . . . .	99
7.1.1	Equations of Motion and Fokker-Planck equation . . . . .	99
7.1.2	Solution of the Equations of Motion . . . . .	100
7.1.3	Conditional probability distribution function . . . . .	103
7.2	Unified Colored Noise Approximation . . . . .	106
7.2.1	Multidimensional stationary-state positional distribution function . . . . .	106
7.2.2	Approximate multidimensional stationary-state velocity distribution function . . . . .	107
7.2.3	Radial potential . . . . .	108
7.2.4	Harmonic potential . . . . .	108
7.3	Comparison between Simulation and theoretical results . . . . .	109
7.3.1	ABP and AOUP in Harmonic Potential . . . . .	109
7.3.2	Anharmonic potential . . . . .	114
7.4	Summary . . . . .	117
<b>8</b>	<b>Local pressure in system of ABPs</b>	<b>121</b>
8.1	Virial pressure . . . . .	121
8.2	Local pressure . . . . .	123
8.2.1	Passive systems . . . . .	123
8.2.2	ABP systems . . . . .	123
8.3	Simulation results for local pressure . . . . .	127
8.3.1	Closed systems . . . . .	128
8.3.2	Periodic systems . . . . .	130
8.4	Summary . . . . .	134

### IV Self-assembled magnetic spinners 135

<b>9</b>	<b>Active turbulence</b>	<b>137</b>
9.1	Ferromagnetic dispersion particle system . . . . .	137
9.1.1	Dispersion Model . . . . .	138
9.1.2	Parameters . . . . .	139

## Contents

---

9.2	Phase diagram . . . . .	139
9.2.1	Spinners . . . . .	142
9.3	Results . . . . .	142
9.3.1	Spinner imbalance . . . . .	142
9.3.2	Spinner length . . . . .	143
9.3.3	Clustering of spinners . . . . .	144
9.3.4	Spinner lifetime . . . . .	145
9.3.5	Active transport . . . . .	145
9.3.6	Energy spectra . . . . .	150
9.4	Summary . . . . .	153
	Conclusions & outlook	155
	Bibliography	159

# Introduction

Mesoscale particles (10nm - 100 $\mu$ m) dispersed in viscous solvents are encountered in various technological processes and products, e.g., ink, adhesives, cosmetics, paints, polymer melts, foams, and food. Moreover, they are omnipresent in biological systems, e.g., proteins, DNA, bacteria, blood cells (Fig. 0.1). Understanding the dynamics of such systems, often attributed as passive or active (with intrinsic self-propulsion) soft matter systems, is of fundamental interest not only from the basic sciences point of view, such as in dynamic phase transitions, but also from the point of view of technical and biological applications. Most of these systems possess a large number of internal degrees of freedom, soft interactions between structural components on the order of thermal energy, and are sensitive to weak external forces.

The interest in the physics of soft matter systems has grown over the years, motivated by the advancement of experimental techniques, which provide insight into smaller length and time scale properties, and the wide range of applications, from nanotechnology to the life sciences. The widespread use of advanced optical microscopy and light scattering techniques has promoted understanding of the structure and dynamics of soft matter systems, and has boosted the development of theoretical and numerical methods applied in studies of emerging problems. The complexity of the studied systems has remarkably grown over the past years. Yet, the fundamental physical principles remain rather simple, so that, if not fully quantitative, at least qualitative predictions of static and dynamic properties can be achieved. In this thesis, we provide detailed numerical studies to characterize the structural and dynamical properties of a variety of systems ranging from colloidal systems, as model for globular protein solutions, and ferromagnetic particles, to simple generic models of active systems.

## 0.1 Proteins

Proteins are the fundamental building blocks of biological systems. They are large macromolecules, comprising of several long chains of amino acid residues, and perform a variety of functions within organisms, such as catalysing metabolic reactions, DNA replication, responding to stimuli, and transporting molecules. Thereby, the complex machinery of life in the interior of cells is determined by the physical properties of proteins. Proteins move in the dense and crowded environment of the cell cytoplasm, where an individual protein feels the presence and interaction potential of all the surrounding proteins [1–5]. The functionality of naturally occurring protein solutions rely on the specific protein-protein interaction, and depending on the nature of interaction, they can organize into various complex structures [6–10]. Thus, proteins can exist in various physical states, such as crystals, gels, glasses or dense liquids (Fig. 0.2). Importantly, these complex self-assembled states of proteins have

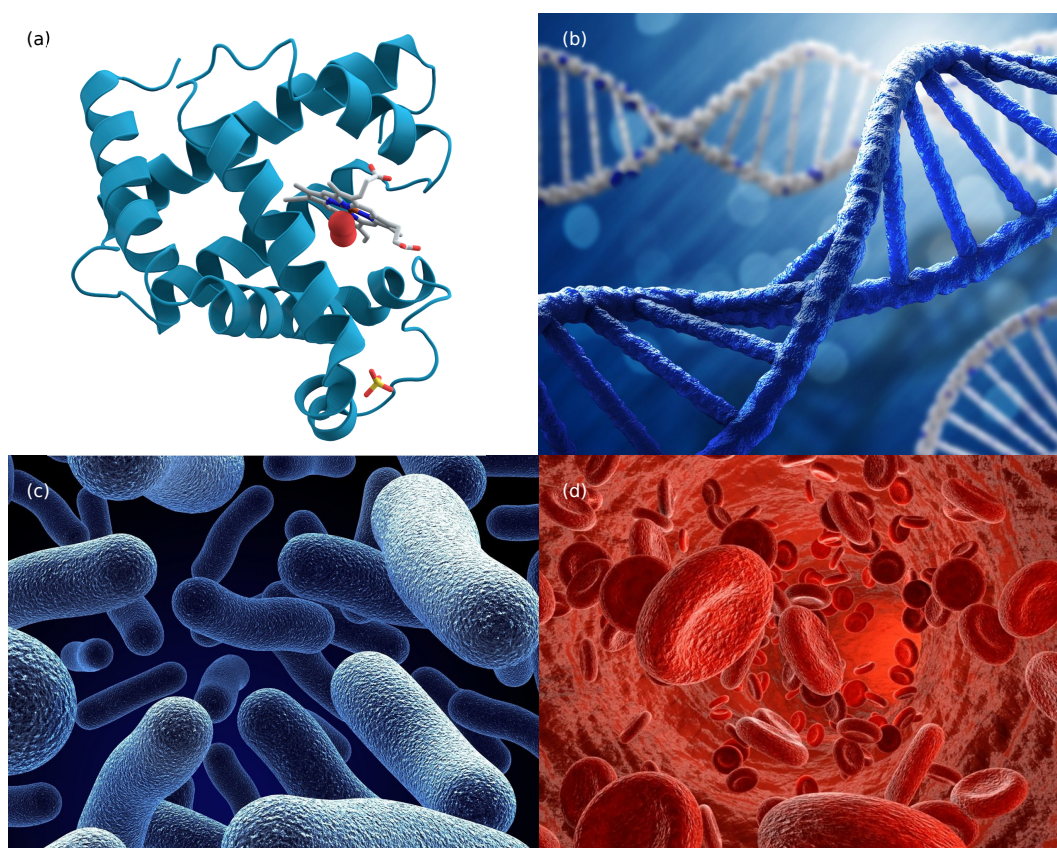


Figure 0.1: Examples of soft matter systems. (a) A 3D representation of the structure of the myoglobin protein showing turquoise  $\alpha$ -helices. It is the first protein to have its structure solved by X-ray crystallography. (source: <https://en.wikipedia.org/>) (b) The double helical structure of bio-polymer DNA, which is the hereditary material in humans and almost all other organisms. (source: <https://phys.org/>) (c) Prokaryotic microorganism bacteria as an example of biological active systems. Many motile bacteria are self-propelled by helical flagella, which protrude from their cell body and are driven by rotary motors located in the cell membrane. (source: <https://www.huffingtonpost.com/>) (d) Red blood cells (RBCs), the most common type of blood cell, carries oxygen to the body tissues of the vertebrates – via blood flow through the circulatory system. (source: <https://www.nutraingredients-usa.com/>)

very diverse physical properties. For example, glassy states in protein solutions appear as a result of dynamical molecular arrest, whereas a crystal is highly ordered equilibrium structure. Moreover, colloidal gels are the percolated system-spanning network-like structures cross-linked amongst each other and exhibit no flow in steady state. The liquid-liquid phase separation progresses from initial homogeneous solution of protein molecules via spontaneous de-mixing into a dilute and a dense liquid phase that coexist stably. A phase boundary separates the two liquid phases and allows exchange of molecules. The dense liquid phase is

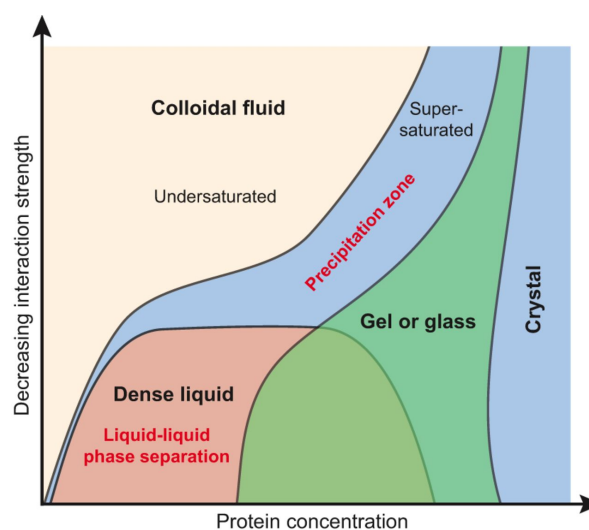


Figure 0.2: Typical phase diagram for a colloidal protein in diverse condensed phases. The explicit shape of the phase diagram varies from protein to protein. Some proteins may not be able to access all the phases pointed out here. (source: <http://jcs.biologists.org/>)

generally metastable, and leads to eventual formation of crystals or becomes trapped in a gel- or glass-like state over the course of time.

In theoretical and simulation studies, a particularly promising approach is the application of concepts from colloidal science to protein solutions in the strive to explain the experimental observations [11–15]. Such an approach involves coarse-graining of the protein structure independent of the molecular details and the proteins are modeled as colloidal particles that interact with each other via an effective interaction potential. Extensive studies have been performed to describe transitions between liquid- and solid-like states in colloidal dispersions, and experimental, theoretical, and simulation studies of systems with different interparticle interactions have been reported [6–8, 16–19]. The majority of investigations have focused on the occurrence of a hard-sphere glass transition at very high densities and the formation of colloidal gels arising due to irreversible aggregation involving strong interparticle attractions [20].

From dynamical point of view, it is expected that direct and hydrodynamic interactions strongly alter protein-diffusion already on length scales comparable to or smaller than the average distance between them, which is essential for numerous cellular processes like protein reactions, recognition and signal transduction [21–23]. The commonly conducted investigations of protein dynamics are in dilute solutions and hence, there is a need to extend in tackling the problem of measuring, understanding, and predicting the diffusion of proteins under crowded conditions, as prevailing in the cell cytosol. There have been studies mainly focused on the long-time diffusion of proteins over macroscopic distances, and clearly demonstrate the slowing down effect of a dense environment [24]. In contrast, measuring short-time diffusion over dimensions comparable to the protein size poses particular challenges for ex-

perimental analysis of protein dynamics – and only a few techniques, such as neutron spin echo (NSE) [25], are available to provide this information. There are indeed several NSE studies that report protein diffusion in crowded solutions, interpreted on the basis of colloid theories [11–15]. However, the currently available range of investigated concentrations and well-characterized proteins is still limited, and the analysis has primarily focused on understanding the effects of excluded-volume and (repulsive) screened Coulomb interactions on short-time diffusion. This is in stark contrast to the fact that numerous globular proteins exhibit a phase diagram that is very similar to that found for colloids with weak short-range attractions [6–8], which indicates the importance of attractive interactions.

Protein solutions are often characterized by short-range attractive (SA) and long-range repulsive (LR) interactions, such as low-salinity lysozyme protein solutions and suspensions of micron-sized charged colloidal particles with added small depletant [11, 26–34]. The structure and the rich phase behavior of SALR systems revealing equilibrium-cluster and percolated-cluster states has been intensely studied over the past years [11, 27, 29–31, 35, 36]. These investigations were triggered by the experimental finding of a low-wavenumber peak in the static structure factor, indicative of intermediate-range microstructural ordering (IRO), arising from the competing SA and LR [26, 28]. The competition of SA- and LR-potential contributions can lead to the occurrence of IRO, and the formation of equilibrium clusters. The existence of such clusters necessitates a delicate balance between SA, favoring aggregation, and LR suppressing macroscopic phase separation. SALR-type protein systems are particularly interesting, since the clustering of proteins can result in severe diseases such as Alzheimer and Parkinson [37, 38], and cataract formation [39].

In contrast to the broad range of studies on static properties of SALR systems [33, 40], comparably little is known about their dynamical aspects. A major challenge for simulation and theoretical studies of the dynamics of these systems is to account for solvent-mediated hydrodynamic particle interactions (HIs) which decisively influence diffusion and rheology. HIs are long-ranged, and, in general, non-pairwise additive for larger particle concentrations. Consequently, in earlier studies [11], Brownian dynamics simulations based on the generalized Lennard-Jones-Yukawa SALR model potential have been performed, where the salient HIs being completely disregarded. The theoretical description of cluster-phase states is further hampered by the occurrence of additional time and length scales associated with the distributions of particle cluster lifetimes, cluster sizes and shapes, and cluster electric charges. This renders a clear distinction between colloidal short-time and long-time regimes complicated, in contrast to homogeneous suspensions of individually diffusing monodisperse particles. An interesting experimental finding exemplifying the intriguing dynamics of SALR systems was obtained by Liu *et al.* [28]. According to these authors, the short- and long-time self-diffusion coefficients for salt-free lysozyme protein solutions, deduced from neutron spin echo (NSE) measurements, share roughly the same concentration dependence. Lysozyme solutions, however, are special SALR systems due to the non-isotropic short-range patchy attractions between the lysozyme proteins [41, 42].

In this context, colloidal particles with patterned surfaces or patchiness are an interesting model system, commonly known as patchy colloids [43–46]. Patchy models consider particles as hard or soft spheres carrying a finite and small number of attractive sites arranged



in precise geometries on the particle's surface. The interest in patchy particles is motivated by the existence of low density crystals and gel states instead of ordered structures in protein solutions, which have been related to the short-range and anisotropic interactions between proteins. They have been studied extensively due to their ability to self-assemble in rich number of clusters showing a diverse phase diagram [44, 47, 48]. In particular, one compelling aspect of the patchy colloid systems is the presence of equilibrium gel [46], a new concept arising from the study of the phase diagram in these systems. Several schemes representing the patch-patch interaction are being investigated, such as hard sphere patchy model with square well attractive sites [49, 50], or colloids with isotropic repulsion and anisotropic attraction [51, 52]. By altering the number, the interaction parameters and the local arrangement of the patches, it is possible to investigate a wide range of physical phenomena, from different self-assembly of processes of proteins, polymers to the dynamical arrest of gel-like structures. For example, limited-valence patchy colloids are a system where the liquid-gas separation can be suppressed and gels are formed without any macroscopic condensation (Fig. 0.3) [44]. Overall, patchy colloids indeed represent a valuable model system to understand the behavior of complex systems, such as amphiphilic molecules, proteins, colloidal clays, and DNA nano-assemblies [53–58].

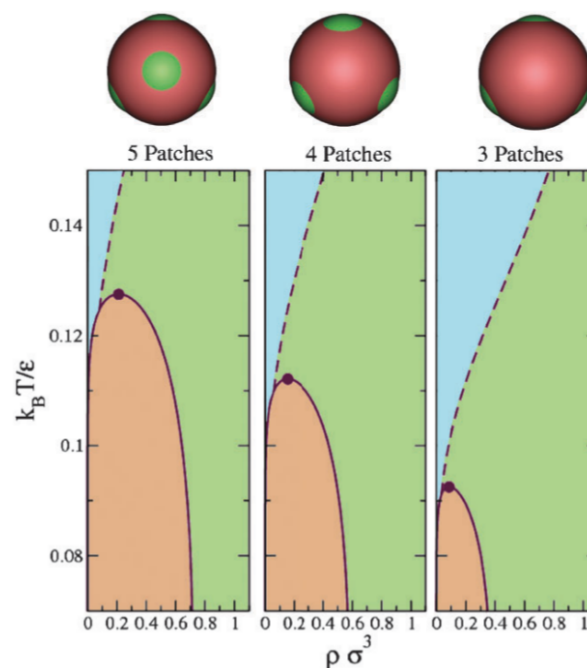


Figure 0.3: Patchy colloid phase diagrams from Ref. [44] illustrating the suppression of gas-liquid phase separation (yellow) with the decreasing number of patches on the colloid. The dotted line separates the percolation region (green) where space-spanning network appears.

### 0.2 Active matters

In recent years, active matters or self-propelled objects have attracted considerable interest from the biology and physics community. The distinct feature of these objects is their autonomous motion powered by an internal energy source or by utilizing energy from their environment [59–67]. Collection of motile macro- or microorganisms, e.g., bacteria (Fig. 0.4(a)), and molecular motors are the typical example of active matter at the microscale [60, 64, 68, 69]. Self-propulsion and transport of microorganisms in fluids is an important aspect of life, as it is fundamental for the search for food, orientation toward light, spreading of off-spring, and the formation of colonies. Swimming at the microscale occurs at low Reynolds numbers, where fluid friction and viscosity dominates over inertia [64]. At larger scales, groups of animals, e.g., flocks of birds (Fig. 0.4(b)), schools of fishes, or even human crowds can be considered as interacting self-propelled objects [70]. Active matter systems exhibit a diverse range of intriguing phenomena, such as activity-induced phase separation or large scale collective motion, which emerges from the inherent nonequilibrium aspect of their constituents [60–62, 64, 68, 71].



Figure 0.4: Example of typical active systems, (a) bacterial colonies, (b) flocks of birds.

(Figure (a) source: <http://science.sciencemag.org/content/358/6362/446/>;

Figure (b) source: <https://www.brandeis.edu/departments/physics/>)

Various synthetic microswimmers, e.g., Janus colloid, have been designed too [65, 72–75], in order to mimic the behavior of biological microorganisms or to serve as micro- and nanomachines with promising applications in technology and healthcare [65, 72]. The rational design of synthetic microswimmers for such applications greatly benefits from a thorough understanding of the relevant physical mechanisms. This comprises the propulsion mechanism of individual microswimmers, their collective behavior, and their properties in external fields and confinement [64, 65]. In order to tackle, in particular, the last two aspects, minimal models of self-propelled active particles are applied. The modeling of active systems combines tools from statistical mechanics, soft matter, and hydrodynamics. A fundamental aspect is to investigate and analyze various emergent phases, and to understand how phase transi-

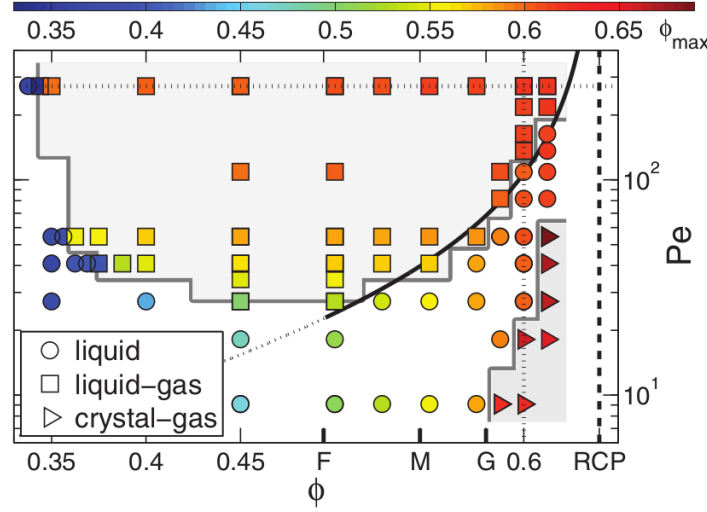


Figure 0.5: Phase diagram of active Brownian particles from Ref. [97], spanned by activity (Péclet number,  $Pe$ ) and packing fraction  $\phi$ . The different symbols denote the various phases, homogenous liquid ( $\circ$ ), the gas-liquid coexistence ( $\square$ ) and the crystal-gas coexistence ( $\triangleright$ ).

tions are governed by the microscopic interactions [68]. The alignment of active particles induced by geometry [76–80], or steric effects, e.g., in elastic collisions between elongated objects [81–83], or hydrodynamic interactions [71], lead to self-assembly and collective motion. Considerable progress in understanding nonequilibrium phenomena like swarming [84–87], turbulence [81, 86], and activity-induced clustering and phase transitions [88–97] has been achieved through the study of minimal active-particle models.

An active Brownian particle (ABP) is one such simplified and generic model of a self-propelled object. ABPs consisting of self-propelled spherical colloid particles with purely repulsive interactions are an excellent model for testing theories of active systems and is extensively applied in analytical and numerical studies. This well-established model has been used to describe active colloids, bacterial motion and cell migration. The self-propulsion direction of ABPs reorients via rotational diffusion neglecting any coupling to a momentum-conserving fluid. ABPs exhibit a rich phase behavior as they display clustering or phase separation consisting of active gases, liquids, and solids with unique mechanical properties (Fig. 0.5) [97]. They also show a universal tendency to assemble near obstacles even in the absence of attractive interactions [98, 99]. The existence of an equation of state for ABPs has been discussed intensively [66, 100–106]. An even more interesting aspect is the existence of a stationary-state distribution function of such systems. Due to their nonequilibrium character, active systems violate detailed balance [60, 66, 92, 107–109], which complicates the calculation of a stationary-state distribution function or might even render it impossible. Various theoretical approaches have been adopted to describe the nonequilibrium properties of ABPs, specifically their phase behavior [66, 92, 110–114], but also effective potentials have been determined [115–118]. In order to arrive at analytical results, approximations are typi-

cally necessary to overcome the complexity of the underlying equations. Thereby, somewhat simpler theoretical models are considered, which focus on particular aspects of the original ABP typically treated in computer simulations.

Another interesting aspect of active systems is the intrinsic swim stress developed through their motility, which influences their dynamic and collective behavior [76, 102, 103, 119]. In systems at thermal equilibrium, pressure can be defined in various ways, e.g., mechanically as force per area on a confining wall, via Clausius' virial theorem [120–122], or thermodynamically by Helmholtz free energy,  $F$ , as  $-(\partial F/\partial V)_{T,N}$  for  $N$  particles in volume  $V$  at constant temperature  $T$  [123]. However, for nonequilibrium systems, such an equivalence in pressure definition is not evident a priori due to unavailability of a free-energy functional. Yet, the mechanical pressure is still valid in out-of-equilibrium active systems, as it originates directly from the micromechanical equations of motion. Extensive studies regarding the pressure in active systems are available in the literature via the application of the ABP model [76, 100, 102–104, 119, 124, 125]. So far, pressure in active systems has been obtained mostly via direct calculations of the wall mechanical pressure and based on various virial-type expressions. The pressure in active systems, specifically the swim pressure, provides valuable insight into the phase behavior and an understanding of how statistical thermodynamic concepts can be applied [100, 102, 103].

### 0.3 Particles in time-dependent external fields

A predictive description of active fluids is challenging due to the complexity of the individual building blocks (e.g., bacteria, molecular motors, etc). In this respect, a simple physical model system, where interactions between particles are well-characterized, is highly desirable. Suspensions of colloidal particles energized by external fields provide a unique opportunity to model active systems in a well-controlled environment. Moreover, out-of-equilibrium (active) colloidal suspensions are compelling to understand dynamic aspects of self-assembling colloids [126–131], which offer a variety of properties due to their high structural controllability. External electromagnetic fields [132–135], UV radiation [136], and chemical reactions [69] have been used to supply energy for dynamic colloidal self-assembly. These assemblies are dynamic, because they exist only in the presence of an external field and the shape and flow characteristics can be controlled by direct manipulation of the driving field. Complex collective motion and hierarchical ordering in these out-of-equilibrium systems reflect the balance between various types of interactions among particles, ranging from short-range steric to long-range hydrodynamic and electromagnetic ones. This was first demonstrated at the macroscopic level in a system of magnetized disks suspended at a liquid-air interface and powered by a rotating magnetic field. Same-wise rotation of particles resulting in stable ordered phases similar to crystals [137, 138] have been observed. Similarly, computer simulations of spinning discs [139, 140] and dumbbells [141] in two dimensions yield various ordered and disordered states. Studies of ferromagnetic colloids confined at the interfaces and energized by an alternating magnetic field demonstrated a wealth of self-organized phenomena, from the formation of dynamic clusters and self-propelled entities



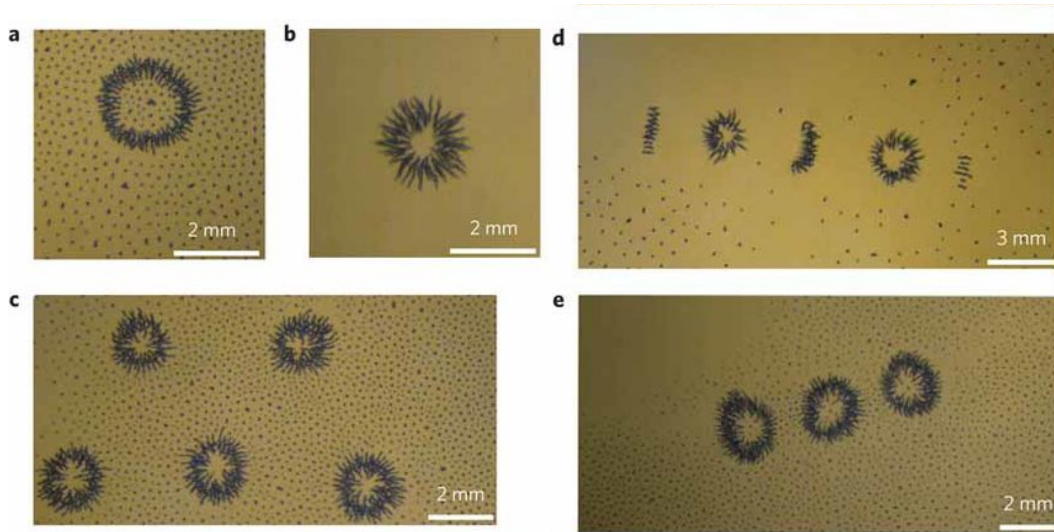


Figure 0.6: Asters formed at the liquid-liquid interface in the study of magnetic colloidal suspension energized by an alternating magnetic field in Ref. [144]. Depending on the frequency of external field the diameter of the asters varies. These asters self-assemble into more complex structures of arrays or membranes, alternating aster and linear segment hybrids, and linear trains.

(magnetic snakes, asters) (Fig. 0.6) [142–144] to rollers [145, 146].

The interest in these systems is stimulated by tunable structures suited to perform useful tasks on the microscale [147], including targeted cargo delivery [148] and stirring in microfluidic devices [149]. Emergence of turbulence in the dense fluids of living materials such as bacterial suspensions and cytoskeletal extracts is an intrinsic property [81, 128, 150–154]. A profound understanding of out-of-equilibrium dispersions is useful in creating systems that mimic bioinspired flows such as in bacterial suspension or cilia-based transport, and they can be realized as self-assembled active material that can be controlled and does not require complex fabrication techniques [155]. As an example of mimicking biological flows, there have been studies where a forest of magnetic rods, driven by magnetic fields, are created that pulsate in a similar fashion as cilia [156], diodes relying on induced electroosmosis to move nearby fluid [149, 157], and even carpets of fixed bacteria that exploit the machinery already present in biology to create complex flows [158].

As a specific example of out-of-equilibrium colloidal systems, Ref. [127] presents a study of dynamic self-assembly of magnetic particles under an alternating magnetic field at the air-water interface. The interplay between magnetic and hydrodynamic interactions lead to a diverse range of quasi-stable dynamic structures from dynamic wires, pulsating clusters to spinners and these structures are fully reversible. A phase diagram is presented which delineates these various self-assembled phases as a function of the magnetic-field frequency and amplitude of the external magnetic field (Fig. 0.7). The dynamic wires are formed through an extension of the initial cluster of particles along the axis of the applied field. Interfacial spinners emerge as a result of spontaneous symmetry breaking of clock/counterclockwise ro-

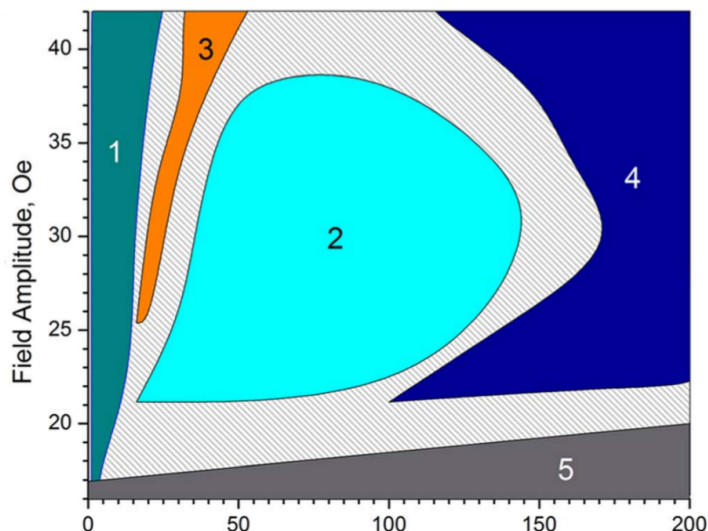


Figure 0.7: Phase diagram of dynamic self-assembled structures at the air-liquid interface in Ref. [127]. Particularly, region 1 depicts clusters exhibiting periodic shape changes in pulses, region 2 corresponds to a gas of spinners, and region 4 shows dynamic wires of one-particle thickness.

tations generated by the uniaxial alternating magnetic field. In particular, the spinner phase looks intriguing because of the hydrodynamic vortical flows induced by their rotational motion, which exhibit similar flow pattern as in bacterial suspensions.

## 0.4 Contents of the thesis

We outline the necessary theoretical and methodological framework in part I. The concepts of stochastic system are recapitulated in chapter 1, which are later applied for the system of ABPs. We also present the Ermak-McCammon numerical algorithm for solving the overdamped Langevin equation used for Brownian dynamics simulations. We outline the fundamentals of hydrodynamics in chapter 2. The hydrodynamic equations are derived from the basic conservation laws. Further, the concepts of hydrodynamic turbulence are addressed as a preface to the study involving active turbulence. An inherent aspect of mesoscopic systems is the presence of solvent-mediated hydrodynamic interactions. We introduce the multiparticle collision dynamics (MPC) method, a particle-based mesoscale hydrodynamic simulation technique, which is employed for simulating the fluid environment of our dispersion systems. Finally, in chapter 3, we present the elemental concepts of various static and dynamic properties to be analyzed for our considered systems.

In part II, we investigate colloidal solutions via multi-scale simulations to understand protein aggregation under crowded conditions, in comparison with theoretical or experimental observations. In our studies, first, we focus on the structural and dynamic effects in colloidal solutions arising from the competition of short-range attractive and long-range re-

pulsive (SALR) interaction forces, applicable to low-salinity Lysozyme-type protein solutions [11, 26–28], discussed in chapter 4. A interesting aspect of the SALR systems is the phase behavior which includes an equilibrium-cluster phase. In comparison with the large body of work on the structure and phase behavior of SALR systems, their dynamic properties are yet to be studied in detail. We investigate the dynamical aspects of SALR systems, both in the dispersed fluid-phase and the equilibrium-cluster phase, demonstrating the importance of fluid-mediated interactions, so called hydrodynamic interactions. Furthermore, the cluster dynamics in the self-aggregated equilibrium-cluster phase is analysed in addition to the microstructural properties. Chapter 5 includes the discussion of the dynamical and structural properties of the eye-lens protein  $\gamma_B$ -crystallin in crowded conditions via investigation of concentrated patchy colloid [47, 48, 159] solutions as a valuable and simple model system. In experiments, a dramatic slow down in their dynamics has been observed using a combination of dynamic light scattering and neutron spin echo measurements of the short-time diffusion [58, 160]. We try to understand the mechanism behind the slow down in dynamics via our simulation results of the short-time diffusion and a detailed analysis of microstructural aspects.

Part III of the thesis is devoted to active systems. We study active Brownian particles [97, 161] in an attempt to gain insight into active matter properties. The ABP model and its dynamic properties are described in chapter 6. In chapter 7, we analyze the distribution function of active Brownian particles under confinement by simulation and a theoretical approach. Our study focuses on the extent to which the simulation results can be reproduced by theoretical approaches, thus revealing the applicability of the applied approximation schemes. In chapter 8, at first, we present the virial pressure expression for a closed ABP system following previous studies in literature. As a main result, we provide a virial formulation of the active pressure in a local sub-volume of the system in analogy with the local pressure in passive systems. The applicability of the local pressure definition is demonstrated via a detailed characterization of various parameter dependencies of the pressure, through simulations of ABPs in comparison with the available literature.

In part IV, we investigate via a two-dimensional simulation study of an experimental system of out-of-equilibrium magnetic colloidal particles at the air-water interface. Chapter 9 includes a detailed description of the magnetic dispersion system, and the different emerging phases of self-assembled structures are presented. A complex collective behavior emerges by self-organization of magnetic particles into a spinner phase. Self-assembled spinners induce vigorous vortical flows exhibiting the properties of two-dimensional hydrodynamic turbulence. The results of active motion and active turbulence in the spinner phase are discussed, providing an insight into the novel ways to control the collective dynamics and transport in active colloidal materials.





## Part I

### Methods & Theoretical background



# Chapter 1

## Brownian motion

Objects of mesoscopic size differ considerably in length- and time-scales from embedding fluid particles. The interaction of a solute with the fluid can often be described in an effective way, where the fluid is considered as a frictional background and exerts thermal forces on the solute particle, i.e., such systems can be considered as stochastic systems. Drag and random forces are not independent, but rather linked, which is expressed by the so-called fluctuation dissipation relation [162]. In this chapter, we briefly introduce the concepts of stochastic systems, before we illustrate the computer simulation algorithm for Brownian motion.

### 1.1 Langevin Equation

The dynamics a particle embedded in a fluid at thermal equilibrium can be described as a stochastic process with Langevin equation of motion [162, 163]

$$M\ddot{\mathbf{r}} = -\gamma\dot{\mathbf{r}} + \mathbf{F} + \mathbf{I}, \quad (1.1)$$

where the frictional force  $\gamma\dot{\mathbf{r}}$  and the stochastic force  $\mathbf{I}$  characterize the effect of surrounding on the dynamics of the particle;  $\gamma$  is the friction coefficient. The stochastic force  $\mathbf{I}$  is a Gaussian and Markovian process, i.e., the correlation time is infinitely short or the autocorrelation is  $\delta$ -correlated in time, with the first two moments

$$\langle \mathbf{I} \rangle = 0, \quad (1.2)$$

$$\langle \mathbf{I}(t) \cdot \mathbf{I}(t') \rangle = 6\gamma k_B T \delta(t - t'). \quad (1.3)$$

Here,  $k_B$  is the Boltzmann constant, and  $T$  is the temperature. The strength of the second moment follows from the fluctuation-dissipation theorem [162].

#### 1.1.1 Overdamped motion

In the overdamped limit, where  $|M\ddot{\mathbf{r}}| \ll |\gamma\dot{\mathbf{r}}|$  (drag force dominates over particle inertia), the Langevin equation (1.1) can be approximated as

$$\dot{\mathbf{r}} = \frac{1}{\gamma} [\mathbf{F} + \mathbf{I}]. \quad (1.4)$$

Thus, in absence of external field, the velocity correlation reads

$$\langle \mathbf{v}(t) \mathbf{v}(t') \rangle = \frac{1}{\gamma^2} \langle \mathbf{\Gamma}(t) \mathbf{\Gamma}(t') \rangle = 6 \frac{k_B T}{\gamma} \delta(t - t'), \quad (1.5)$$

i.e., velocities are uncorrelated and they are always in thermal equilibrium for overdamped motion of a particle.

## 1.2 Stochastic calculus

A generalized form of the Langevin equation in differential form can be written as [162]

$$dx = f(x, t)dt + h(x, t)dW(t), \quad (1.6)$$

where  $x$  is the variable of interest,  $f(x, t)$  and  $h(x, t)$  are certain known functions and  $W(t)$  is a Wiener process with  $dW = W(t + dt) - W(t) = \Gamma(t)dt$  ( $\Gamma$  is the stochastic variable).

### 1.2.1 Stochastic integration

The stochastic integral for an arbitrary function  $G(t)$  in the time interval  $[0, t]$  is defined as [162]

$$S = \int_0^t dW(t')G(t') = ms - \lim_{N \rightarrow \infty} S_N(\alpha), \quad (1.7)$$

where  $ms - \lim$  stands for mean square limit.  $S_N$  converges to  $S$  in the mean square if  $\lim_{N \rightarrow \infty} \langle (S_N - S)^2 \rangle = 0$ .  $S_N(\alpha)$  is given by

$$S_N(\alpha) = \sum_{j=0}^{N-1} \tilde{G}(\tau_j) [W(t_{j+1}) - W(t_j)] \quad (1.8)$$

with  $\tilde{G}(\tau_j) = [(1 - \alpha)G(t_j) + \alpha G(t_{j+1})]$ . Here,  $t_j$ 's are the discretization of the time interval  $[0, t]$  with  $j \in 0, \dots, N$ , i.e.,  $t_j = jt/N$  and  $\alpha \in [0, 1]$ .

### Ito and Stratonovich definitions

The limit of  $S_N$  depends on the choice of the intermediate points, which is characterized by  $\alpha$ . The Ito integral is defined as the  $N \rightarrow \infty$  limit of  $S_N(\alpha)$  with  $\alpha = 0$ , whereas the Stratonovich integral is defined as the  $N \rightarrow \infty$  limit of  $S_N(\alpha)$  with  $\alpha = \frac{1}{2}$ . This implies for the Ito representation  $\tau_j = t_j$ ,  $\tilde{G}(\tau_j) = G(t_j)$  and for Stratonovich representation  $\tau_j = (t_j + t_{j+1})/2$ ,  $\tilde{G}(\tau_j) = (G(t_j) + G(t_{j+1}))/2$  [162].

### 1.2.2 Ito's stochastic differential formula

Consider a multi-variable form of the stochastic differential equation (1.6) for an  $n$ -dimensional vector  $\mathbf{x}(t) = (x_1, \dots, x_n)^T$  as

$$d\mathbf{x} = \mathbf{F}(\mathbf{x}, t)dt + \mathbf{H}(\mathbf{x}, t)d\mathbf{W}(t). \quad (1.9)$$

The  $n$ -dimensional Wiener process  $\mathbf{W}(t)$  has the properties,

$$dW_i(t)dW_j(t) = \delta_{ij}(t), \quad (1.10)$$

$$[dW_i(t)]^{N+2} = 0 \quad (N > 0), \quad (1.11)$$

$$dW_i(t)dt = 0, \quad (1.12)$$

$$dt^{1+N} = 0 \quad (N > 0), \quad (1.13)$$

which imply that  $d\mathbf{W}(t)$  is an infinitesimal of order  $\frac{1}{2}$ . Hence, any arbitrary function  $g(\mathbf{x}(t))$  of  $\mathbf{x}(t)$  follows the stochastic differential equation

$$dg(\mathbf{x}) = \left[ \sum_i F_i(\mathbf{x}, t) \partial_i g(\mathbf{x}) + \frac{1}{2} \sum_{i,j} [\mathbf{H}(\mathbf{x}, t) \mathbf{H}^T(\mathbf{x}, t)]_{ij} \partial_i \partial_j g(\mathbf{x}) \right] dt \quad (1.14)$$

$$+ \sum_{i,j} H_{ij}(\mathbf{x}, t) \partial_i g(\mathbf{x}) dW_j(t). \quad (1.15)$$

This is Ito's formula [162] and shows that a change of variables is not given by ordinary calculus unless  $g(\mathbf{x}(t))$  is linear in  $\mathbf{x}(t)$ .

## 1.3 Fokker-Planck equation

Equivalent to the Langevin approach (Eq. (1.6)), the dynamics of a particle can also be expressed in terms of a distribution function  $\Psi(\mathbf{x}, t)$ , which follows as a solution of the Fokker-Planck equation [163],

$$\frac{\partial}{\partial t} \Psi(\mathbf{x}, t) = \hat{L}_{FP} \Psi(\mathbf{x}, t), \quad (1.16)$$

with the Fokker-Planck operator

$$\hat{L}_{FP} = -\frac{\partial}{\partial x} D^{(1)}(x, t) + \frac{\partial^2}{\partial^2 x} D^{(2)}(x, t). \quad (1.17)$$

This FP equation is defined by the drift term  $D^{(1)}(x, t)$  that characterizes a ballistic motion, and by the diffusion term  $D^{(2)}(x, t)$  characterizing a diffusive motion.

### Relation between Langevin and Fokker-Planck equation

The description of fluctuations by using the Langevin equation (1.6) and the one by Fokker-Planck equation (1.16) can be related in terms of the drift and the diffusion term. This can be done by computing the moments of  $x$  and identifying them as

$$D^{(m)}(x, t) = \frac{1}{m!} \lim_{\Delta t \rightarrow 0} \frac{1}{\Delta t} \langle (x'(t + \Delta t) - x'(t))^m \rangle_{x'(t)=x}. \quad (1.18)$$

In particular, we find

$$D^{(1)}(x, t) = f(x, t) + h(x, t) \frac{\partial h(x, t)}{\partial x}, \quad (1.19)$$

$$D^{(2)}(x, t) = h(x, t)^2. \quad (1.20)$$

#### 1.3.1 Boundary conditions

The Fokker-Planck equation can be reformulated in terms of probability current  $J(x, t)$  as

$$\frac{\partial}{\partial t} \Psi(x, t) + \frac{\partial}{\partial x} J(x, t) = 0, \quad (1.21)$$

with  $J(x, t) = [D^{(1)}(x, t) - \frac{\partial}{\partial x} D^{(2)}(x, t)] \Psi(x, t)$ . Typically, the following boundary conditions are considered

- Natural boundary condition with  $J(x, t) = 0$  at  $x \rightarrow \pm\infty$ .
- Periodic boundary condition with  $\Psi(x, t) = \Psi(x + L, t)$ ,  $J(x, t) = J(x + L, t)$ .
- Reflecting boundary with  $J(x, t) = 0$  at the boundary.
- Absorbing boundary with  $\Psi(x, t) = 0$  at the boundary.

### 1.4 Ornstein-Uhlenbeck process

The Langevin equation of an Ornstein-Uhlenbeck process, for  $N$  stochastic variables  $x_i$ , in its general form is [163]

$$\dot{x}_i + \sum_{j=1}^N \gamma_{ij} x_j = \Gamma_i(t), \quad (1.22)$$

where  $\gamma_{ij}$  are time independent coefficients. The  $\Gamma_i$ 's are Gaussian stochastic forces with the moments

$$\langle \Gamma_i \rangle = 0, \quad (1.23)$$

$$\langle \Gamma_i(t) \Gamma_j(t') \rangle = b_{ij} \delta(t - t'); \quad b_{ij} = b_{ji}, \quad (1.24)$$

where  $b_{ij}$  describes the strength of the noise. Overall Eq. (1.22) describes a system of linear stochastic differential equations with constant coefficients. The general solution of Eq. (1.22) can be obtained in terms of homogeneous and inhomogeneous solutions via the method of Green's function as

$$x_i(t) = x_i^h(t) + x_i^{nh}(t), \quad (1.25)$$

where

$$x_i^h(t) = \sum_j G_{ij}(t) x_j(0), \quad (1.26)$$

$$x_i^{nh}(t) = \sum_j \int_0^t G_{ij}(t-t') \Gamma_j(t') dt'. \quad (1.27)$$

Here,  $G_{ij}$  satisfies the differential equation

$$\dot{G}_{ij} + \sum_l \gamma_{il} G_{lj} = \delta_{ij} \delta(t-t'), \quad (1.28)$$

with the solution  $G_{ij} = \exp(-\gamma_{ij}t)$ . Thus, the general solution of Eq. (1.22) is given by

$$x_i(t) = \sum_j G_{ij}(t) x_j(0) + \sum_j \int_0^t G_{ij}(t-t') \Gamma_j(t') dt'. \quad (1.29)$$

As a particular result, the first moment and the variance of the stochastic variable  $x_i$  can be expressed as

$$M_i(t) = \langle x_i(t) \rangle = \sum_j G_{ij}(t) x_j(0), \quad (1.30)$$

$$\sigma_{ij}(t) = \sigma_{ji}(t) = \langle [x_i(t) - \langle x_i \rangle][x_j(t) - \langle x_j \rangle] \rangle \quad (1.31)$$

$$= \sum_{k,l} \int_0^t \int_0^t G_{ik}(t') G_{jl}(t'') b_{kl} \delta(t' - t'') dt' dt'' \quad (1.32)$$

$$= \sum_{k,l} \int_0^t G_{ik}(t') G_{jl}(t') b_{kl} dt', \quad (1.33)$$

with the use of Eq. (1.22).

### 1.4.1 Fokker-Planck equation

For the Ornstein-Uhlenbeck process (1.22), the drift coefficients depend linearly on the coordinates and the diffusion coefficients are constant, i.e.,

$$D_i = - \sum_j \gamma_{ij} x_j; \quad D_{ij} = D_{ji} = \text{const.} \quad (1.34)$$

Hence, the Fokker-Planck equation for Eq. (1.22) can be written in a general form as

$$\frac{\partial \psi}{\partial t} = - \sum_{i,j} \gamma_{ij} \frac{\partial}{\partial x_i} (x_j \psi) + \sum_{i,j} D_{ij} \frac{\partial^2 \psi}{\partial x_i \partial x_j}, \quad (1.35)$$

where  $\psi$  has to satisfy the initial condition

$$\psi(\{x\}, t_0 | \{x^0\}, t_0) = \delta(\{x\} - \{x^0\}). \quad (1.36)$$

This is a linear differential equation which can be solved by Fourier transformation. Thus, in Fourier space the Fokker-Planck equation (1.35) reads

$$\frac{\partial \tilde{\psi}}{\partial t} = - \sum_{i,j} \gamma_{ij} q_i \frac{\partial \tilde{\psi}}{\partial q_j} + \sum_{i,j} D_{ij} q_i q_j \tilde{\psi}, \quad (1.37)$$

where  $\tilde{\psi}$  is the Fourier transform of  $\psi$  such that

$$\psi(\{x\}, t | \{x^0\}, t_0) = \frac{1}{(2\pi)^N} \int \exp(i \sum_j q_j x_j) \tilde{\psi}(\{q\}, t | \{x^0\}, t_0) d^N q. \quad (1.38)$$

Correspondingly, the initial condition Eq. (1.36) reads as

$$\psi(\{q\}, t_0 | \{x^0\}, t_0) = \exp(-i \sum_j q_j x_j^0). \quad (1.39)$$

Because of the Gaussian nature of the underlying stochastic processes, we know that  $\psi$  and its Fourier transform  $\tilde{\psi}$  must be Gaussian functions too. Hence, we use the ‘ansatz’

$$\psi(\{q\}, t | \{x^0\}, t_0) = \exp \left[ -i \sum_j q_j M_j(t - t_0) - \frac{1}{2} \sum_{i,j} q_i q_j \sigma_{ij}(t - t_0) \right]. \quad (1.40)$$

Inserting this ‘ansatz’ into Eq. (1.37) and sorting by powers of  $q$  yields the two differential equations

$$\dot{M}_i = - \sum_j \gamma_{ij} M_j, \quad (1.41)$$

$$\dot{\sigma}_{ij} = - \sum_l (\gamma_{il} \sigma_{lj} + \gamma_{jl} \sigma_{li}) + 2D_{ij}, \quad (1.42)$$

with the corresponding initial conditions

$$M_i(0) = x_i^0, \quad (1.43)$$

$$\sigma_{ij}(0) = 0. \quad (1.44)$$



The solutions can be written in terms of Green's function  $G_{ij}$  as

$$M_i(t) = \sum_j G_{ij}(t)x_j^0, \quad (1.45)$$

$$\sigma_{ij}(t) = 2 \sum_{k,l} \int_0^t G_{ik}(t')G_{jl}(t')D_{kl}dt'. \quad (1.46)$$

Now, inserting Eq. (1.40) into the Fourier equation (1.38) and performing the integration, yields the solution

$$\psi(\{x\}, t | \{x^0\}, t_0) = \frac{1}{(2\pi)^{N/2}} \frac{1}{\sqrt{|\boldsymbol{\sigma}(t - t_0)|}} \quad (1.47)$$

$$\times \exp \left( -\frac{1}{2} [x_i - G_{ik}(t - t_0)x_k^0][(\boldsymbol{\sigma}^{-1}(t - t_0))]_{ij} [x_j - G_{jl}(t - t_0)x_l^0] \right), \quad (1.48)$$

of the Fokker-Planck equation (1.35).

## 1.5 Brownian Dynamics

To study static and dynamic properties of soft matter particles, e.g., colloids and polymers, in the overdamped Langevin description, the Brownian dynamics simulation scheme is used quite often [164–166]. Several Brownian dynamics numerical algorithms are available in the literature for treating the overdamped stochastic differential equations [167–170]. Here, in particular, we discuss the Ermak-McCammon algorithm [171].

### 1.5.1 Ermak-McCammon algorithm

In a system of  $N$  Brownian particles, the dynamics of each particle  $i$  is governed by the overdamped Langevin dynamics according to Eq. (1.4). Considering discrete time steps, i.e., integrating this equation of motion over a time interval of  $\Delta t$ , we get

$$\mathbf{r}_i(t + \Delta t) = \mathbf{r}_i(t) + \frac{1}{\gamma} \int_t^{t+\Delta t} \exp[-\gamma(t - t')] (\mathbf{F}_i(t) + \mathbf{F}_i(t')) dt'. \quad (1.49)$$

If  $\Delta t \ll 1$ , we can assume  $|\dot{\mathbf{F}}_i| \approx 0$  in that time interval and the integration scheme turns into

$$\mathbf{r}_i(t + \Delta t) = \mathbf{r}_i(t) + \mathbf{F}_i(t)\Delta t + \Delta \mathbf{F}_i(t), \quad (1.50)$$

where the stochastic term  $\Delta \mathbf{F}_i$  is Gaussian with the moments

$$\langle \Delta \mathbf{F}_i(t) \rangle = 0, \quad \langle [\Delta \mathbf{F}_i(t)]^2 \rangle = 2D\Delta t; \quad (1.51)$$

$D = k_B T / \gamma$  is the diffusion coefficient. This is the Ermak-McCammon integration scheme for Brownian dynamics simulations [171].



# Chapter 2

## Hydrodynamics

In chapter 1, while describing the dynamics of many particles embedded in a stochastic environment, the correlations in the solvent have been neglected. However, the dynamics of solute particles in a fluid environment is affected by the fluid motion, which is termed as hydrodynamic interactions. We consider the fluid or gas as a continuum characterized by its mass density  $\rho(\mathbf{r}, t)$ , pressure  $p(\mathbf{r}, t)$ , and velocity  $\mathbf{v}(\mathbf{r}, t)$  at a specific position  $\mathbf{r}$  and time  $t$ . In this chapter, we discuss the hydrodynamic equations governing the time evolution of these quantities, known as the Navier-Stokes equations. A brief description of the theory and phenomenology of fluid turbulence (in two dimensions mostly) is also introduced. Furthermore, we describe the particle-based mesoscale simulation method multiparticle collision dynamics (MPC), which captures the combined effect of hydrodynamic interactions and thermal fluctuations.

### 2.1 Navier-Stokes equations

The Navier-Stokes equations are the basic governing equations of the motion for a viscous, heat conducting fluid. These balance equations are achieved by applying Newton's equation of motion, together with the assumption that the stress in the fluid is the sum of a diffusing viscous term and a pressure term.

#### 2.1.1 Conservation laws

A material volume  $V$  is a collection of fixed mass of material, i.e., it encloses the same fluid particles despite its deformation in size, position, volume or surface area over time [172]. The rate of change of a property  $g(\mathbf{r}, t)$  of such a material volume is given by

$$\frac{Dg}{Dt} = \frac{\partial g}{\partial t} + \mathbf{v} \cdot \nabla g, \quad (2.1)$$

where  $D/Dt$  is called the material derivative.

### Mass conservation

The mass inside the material volume is  $M = \int_V \rho dV$ . Since by definition material volume has fixed mass of particle, the time rate of change of mass inside the material volume is

$$\frac{dM}{dt} = \frac{d}{dt} \int_V \rho dV = 0. \quad (2.2)$$

Implementing Leibniz-Reynolds transport theorem and then applying Gauss' theorem, Eq. (2.2) can be rewritten in the form [172]

$$\frac{d}{dt} \int_V \rho dV = \int_V \left( \frac{\partial \rho}{\partial t} + \nabla \cdot (\rho \mathbf{v}) \right) dV = 0 \quad (2.3)$$

This is true for any material volume  $V$ . Hence, the integrand must be zero and we obtain the continuity equation

$$\frac{\partial \rho}{\partial t} + \nabla \cdot (\rho \mathbf{v}) = 0. \quad (2.4)$$

In an incompressible flow, the mass density within a material volume is constant, i.e., the material derivative of the mass density vanishes. In this case the continuity equation reduces to  $\nabla \cdot \mathbf{v} = 0$ . Most liquids, such as water can be treated incompressible [172].

### Momentum conservation

Momentum conservation means that the change in momentum over time must be equal to the forces acting on the fluid in the material volume. The momentum of a material volume changes due to the applied stresses on its surface and volume forces  $\mathbf{f}$ , such that

$$\frac{d}{dt}(\text{momentum}) = (\text{surface force}) + (\text{volume force}) \quad (2.5)$$

$$\Rightarrow \frac{d}{dt} \int_V \rho \mathbf{v} dV = \int_{\partial V} \boldsymbol{\sigma} \mathbf{n} dA + \int_V \mathbf{f} dV. \quad (2.6)$$

Here,  $\boldsymbol{\sigma}$  is the stress tensor, and  $\mathbf{n}$  is the surface normal vector. Applying the Leibniz-Reynolds transport theorem in combination with the continuity equation Eq. (2.4) on left hand side and Gauss' theorem on the right hand side, we find

$$\int_V \rho \frac{D\mathbf{v}}{Dt} dV = \int_V (\nabla \cdot \boldsymbol{\sigma} + \mathbf{f}) dV. \quad (2.7)$$

Again, the volume is arbitrary and by equating the integrands we obtain the Navier-Stokes equation

$$\rho \frac{D\mathbf{v}}{Dt} = \nabla \cdot \boldsymbol{\sigma} + \mathbf{f}. \quad (2.8)$$

### 2.1.2 Stress tensor

The stress  $\boldsymbol{\sigma}$  in a fluid measures the infinitesimal internal force exerted on an infinitesimal surface or fluid layer. The total stress tensor  $\boldsymbol{\sigma}$  with its components  $\sigma_{\alpha\beta}$  for a Newtonian fluid is the sum of pressure and viscous drag stresses. Thus, the symmetric stress tensor of an isotropic system can be written macroscopically as [173]

$$\begin{aligned}\sigma_{\alpha\beta} &= -P\delta_{\alpha\beta} + \sum_{\alpha'\beta'} \eta_{\alpha\beta\alpha'\beta'} \frac{\partial v_{\alpha'}}{\partial r_{\beta'}} \\ &= -P\delta_{\alpha\beta} + \eta \left( \frac{\partial v_{\alpha}}{\partial r_{\beta}} + \frac{\partial v_{\beta}}{\partial r_{\alpha}} \right) - \delta_{\alpha\beta} \left( \frac{2}{3}\eta - \eta^V \right) \nabla \cdot \mathbf{v},\end{aligned}\quad (2.9)$$

with

$$\eta_{\alpha\beta\alpha'\beta'} = \eta (\delta_{\alpha\alpha'}\delta_{\beta\beta'} + \delta_{\alpha\beta'}\delta_{\alpha'\beta}) - \left( \frac{2}{3}\eta - \eta^V \right) \delta_{\alpha\beta}\delta_{\alpha'\beta'}, \quad (2.10)$$

the local pressure  $P = P(\mathbf{r}, t)$ , the shear and bulk viscosities  $\eta$  and  $\eta^V$ , respectively, and  $\alpha, \beta, \alpha', \beta' \in \{x, y, z\}$ . With the stress tensor of Eq. (2.9), the Navier-Stokes equation turns into

$$\rho \left( \frac{\partial \mathbf{v}}{\partial t} + (\mathbf{v} \cdot \nabla) \mathbf{v} \right) = -\nabla P + \eta \Delta \mathbf{v} + \left( \frac{\eta}{3} + \eta^V \right) \nabla (\nabla \cdot \mathbf{v}) + \mathbf{f}. \quad (2.11)$$

### 2.1.3 Stokes equations

In order to analyze the relevance of the various terms in Eq. (2.11), in particular the time-dependent and non-linear inertia terms, we rescale the position, velocity, and time as [174]

$$\mathbf{v}' = \mathbf{v}/V_0, \mathbf{r}' = \mathbf{r}/L_0, t' = t/T_0, \quad (2.12)$$

where  $V_0$  is a typical velocity,  $L_0$  is a typical length, and  $T_0$  is the timescale of the problem at hand. This leads to the equation

$$Re_T \frac{\partial \mathbf{v}'}{\partial t'} + Re(\mathbf{v}' \cdot \nabla') \mathbf{v}' = -\nabla' P' + \Delta' \mathbf{v}' + \left( \frac{1}{3} + \frac{\eta^V}{\eta} \right) \nabla' (\nabla' \cdot \mathbf{v}') + \mathbf{f}', \quad (2.13)$$

where  $P' = L_0 \eta^{-1} v_0^{-1} P$ ,  $\mathbf{f}' = L_0 \eta^{-1} v_0^{-1} \mathbf{f}$  and  $\nabla' = \partial/\partial \mathbf{r}'$  are all dimensionless. Furthermore, we introduced the Reynolds numbers

$$Re = \frac{\rho v_0 L_0}{\eta}, \quad (2.14)$$

$$Re_T = \frac{\rho L_0^2}{\eta T_0}. \quad (2.15)$$

For  $Re \ll 1$  the non-linear advective term can be neglected, yielding the linearized Navier-Stokes equations. Thus, the Reynolds number is a measure of the non-linearity of the Navier-Stokes equations. In addition, considering an incompressible fluid, i.e.,  $\rho = \text{const.}$  and  $\nabla \cdot \mathbf{v} = 0$ , yields

$$\rho \frac{\partial \mathbf{v}}{\partial t} = -\nabla P + \eta \Delta \mathbf{v} + \mathbf{f}. \quad (2.16)$$

If additionally  $Re_T \ll 1$ , we can assume an instantaneous relaxation of hydrodynamics on our time-scale of interest, which leads to the Stokes equations

$$\eta \Delta \mathbf{v} - \nabla P + \mathbf{f} = 0, \quad (2.17)$$

$$\nabla \cdot \mathbf{v} = 0. \quad (2.18)$$

The Stokes equations are also known as creeping flow equations [174]. They are time-independent and linear.

### Oseen Tensor

The Stokes equations (2.17), (2.18) can be solved by Fourier transformation [175], which gives

$$\eta \mathbf{q}^2 \mathbf{v}_q - i \mathbf{q} P_q = \mathbf{f}_q, \quad (2.19)$$

$$\mathbf{q} \cdot \mathbf{v}_q = 0. \quad (2.20)$$

Solving these equations for  $\mathbf{v}_q$  and performing the inverse Fourier transformation yields

$$\mathbf{v}(\mathbf{r}) = \int \mathcal{G}(\mathbf{r} - \mathbf{r}') \mathbf{f}(\mathbf{r}') d^3 r', \quad (2.21)$$

with the Green's function

$$\mathcal{G}(\mathbf{r}) = \frac{1}{8\pi\eta r} \left( \mathbf{E} + \frac{\mathbf{r} \mathbf{r}^T}{r^2} \right), \quad (2.22)$$

known as Oseen tensor [175];  $\mathbf{E}$  is the unit matrix. The Green's function for two-dimensional hydrodynamics is given by [176]

$$\mathcal{G}(\mathbf{r}) = \frac{1}{4\pi\eta} \left( -\mathbf{E} \ln \left| \frac{\mathbf{r}}{r_0} \right| + \frac{\mathbf{r} \mathbf{r}^T}{r^2} \right), \quad (2.23)$$

where  $r_0$  is a characteristic length scale.

### 2.1.4 Hydrodynamic interaction

Due to the linearity and instantaneity of Stokes flow, the hydrodynamic force on a particle  $i$  by the surrounding fluid, due to motion of other particles, is given by

$$\mathbf{F}_i^h = - \sum_{j=1}^N \boldsymbol{\zeta}_{ij} \mathbf{v}_j \quad (2.24)$$

or, by inversion,

$$\mathbf{v}_i = - \sum_{j=1}^N \boldsymbol{\mu}_{ij} \mathbf{F}_j^h, \quad (2.25)$$

where  $\mathbf{v}_i$  is the particle velocity,  $\boldsymbol{\zeta}_{ij}$  and  $\boldsymbol{\mu}_{ij}$  are the hydrodynamic friction and mobility tensors respectively.

These generalized Stokes law points out that the velocity of a particle immersed in the fluid is influenced by the instantaneous hydrodynamic forces induced by all the particles in the system. In other words, a particle moving in a viscous fluid in presence of other  $(N - 1)$  particles will exert a force  $\mathbf{F}_i = -\mathbf{F}_i^h$  on the surrounding fluid resulting in the perturbation of fluid velocity field. This perturbation transmits through the fluid quasi-instantaneously inducing forces on the neighboring particles and also on the particle itself due to hydrodynamic back-reflections.

The flow field  $\mathbf{v}(\mathbf{r})$  created by the motion of point particles at  $\mathbf{r}_i$  can be written as

$$\mathbf{v}(\mathbf{r}) = \sum_{i=1}^N \mathcal{G}(\mathbf{r} - \mathbf{r}_i) \mathbf{F}_i. \quad (2.26)$$

In the presence of a fluid environment, the friction between a particle at  $\mathbf{r}_i$  and the viscous fluid background is described by

$$\gamma [\dot{\mathbf{r}}_i - \mathbf{v}(\mathbf{r}_i)] = \mathbf{F}_i \quad (2.27)$$

and with the Eq. (2.26), we obtain

$$\dot{\mathbf{r}}_i = \sum_{j=1}^N \left( \mathcal{G}(\mathbf{r}_i - \mathbf{r}_j) + \frac{\delta_{ij}}{\gamma} \right) \mathbf{F}_j. \quad (2.28)$$

Comparing with Eq. (2.25), we find the expression for hydrodynamic mobility tensor

$$\boldsymbol{\mu}_{ij} = \frac{\delta_{ij}}{\gamma} \mathbf{E} + (1 - \delta_{ij}) \mathcal{G}(\mathbf{r}_i - \mathbf{r}_j). \quad (2.29)$$

Thus, the hydrodynamic interactions are long-range in nature as the disturbance of the fluid velocity field induced by the forced motion of a solute particle decays with distance  $r$  as  $1/r$  [177].

## 2.2 Turbulence

The transition between laminar and turbulent flow in a fluid was demonstrated by Osborne Reynolds beyond a certain critical value of the Reynolds number  $Re$ . The Reynolds number plays a fundamental role in turbulence, since it provides a measure of the relative weight between the inertial term  $\mathbf{v} \cdot \nabla \mathbf{v}$  and the viscous term  $\nu \Delta \mathbf{v}$

$$Re \approx \frac{\mathbf{v} \cdot \nabla \mathbf{v}}{\nu \Delta \mathbf{v}}, \quad (2.30)$$

where  $\nu$  is the kinematic viscosity. In the limit of  $Re \rightarrow \infty$ , viscosity becomes irrelevant compared to inertial forces and fully developed turbulence is acquired [178]. This extremum is rephrased as zero-viscosity or inviscid limit  $\nu \rightarrow 0$ .

### 2.2.1 Energy balance

The energy balance in absence of external forcing for the Navier-Stokes equation follows from Eq. (2.11). The total kinetic energy per unit mass of the fluid is

$$E = \frac{1}{2} \int_V |\mathbf{v}|^2 d^3r, \quad (2.31)$$

and the dissipation of the energy is given by

$$\frac{dE}{dt} = \int_V \mathbf{v} \cdot \frac{\partial \mathbf{v}}{\partial t} d^3r \quad (2.32)$$

$$= \int_V \mathbf{v} \cdot \left( -(\mathbf{v} \cdot \nabla) \mathbf{v} - \frac{1}{\rho} \nabla P + \nu \Delta \mathbf{v} \right) d^3r. \quad (2.33)$$

Assuming periodic boundary conditions and using vector identities,

$$\frac{dE}{dt} = -\nu \int_V (\nabla \times \mathbf{v})^2 d^3r = -\nu \int_V |\boldsymbol{\omega}|^2 d^3r, \quad (2.34)$$

where  $\boldsymbol{\omega}$  is the vorticity of the fluid, defined as the curl of the velocity  $\boldsymbol{\omega} = \nabla \times \mathbf{v}$ . With the definition of total enstrophy  $Z = \int_V |\boldsymbol{\omega}|^2 d^3r$ , the energy balance equation reads [179]

$$\frac{dE}{dt} = -2\nu Z. \quad (2.35)$$

It states that the energy dissipation rate of a fluid flow in absence of external forces is proportional to the enstrophy and the energy is an inviscid invariant.

### 2.2.2 Vorticity equation

The vorticity equation describes the evolution of the vorticity  $\boldsymbol{\omega}$  of a fluid particle as it moves with the flow, i.e, the local rotational motion of the fluid. Taking the curl of the Navier-Stokes



equation (2.11), it yields

$$\frac{\partial \boldsymbol{\omega}}{\partial t} + (\mathbf{v} \cdot \nabla) \boldsymbol{\omega} = (\boldsymbol{\omega} \cdot \nabla) \mathbf{v} + \boldsymbol{\omega} (\nabla \cdot \mathbf{v}) - \frac{1}{\rho^2} \nabla \rho \times \nabla P + \nu \Delta \boldsymbol{\omega} + \frac{1}{\rho} (\nabla \times \mathbf{f}). \quad (2.36)$$

In case of an incompressible fluid,  $\nabla \rho = 0$ , the equation reads

$$\frac{\partial \boldsymbol{\omega}}{\partial t} + (\mathbf{v} \cdot \nabla) \boldsymbol{\omega} = (\boldsymbol{\omega} \cdot \nabla) \mathbf{v} + \nu \Delta \boldsymbol{\omega} + \frac{1}{\rho} \mathbf{f}_\omega, \quad (2.37)$$

where  $\mathbf{f}_\omega = \nabla \times \mathbf{f}$ .

In two-dimensional turbulence, the vorticity field has one non-zero component which is orthogonal to the plane of velocity and the vorticity equation reduces to

$$\frac{\partial \omega}{\partial t} + (\mathbf{v} \cdot \nabla) \omega = \nu \Delta \omega + \frac{1}{\rho} f_\omega. \quad (2.38)$$

This implies that  $\omega$  is constant in time and co-moving with the fluid when viscosity, friction and external forcing are ignored. This is a fundamental difference compared to three dimensional turbulence. This phenomenon is due to the fact that in two-dimensional turbulence the “vortex stretching term”  $(\boldsymbol{\omega} \cdot \nabla) \mathbf{v}$  vanishes, which appears as a forcing term in three dimensions resulting in unbounded growth of enstrophy in the limit  $Re \rightarrow \infty$  [179].

In two dimensions, assuming periodic boundary conditions, the enstrophy dissipation can be written as

$$\frac{dZ}{dt} = -\nu \int_V |\nabla \omega|^2 d^2r, \quad (2.39)$$

which expresses that the enstrophy,  $Z = \int |\omega|^2 d^2r$ , is also an inviscid invariant in absence of external forcing.

### 2.2.3 Energy Spectrum

Turbulence in a fluid is generally characterized by at least two-point statistical quantities. In a homogeneous isotropic turbulent flow, a useful quantity is the energy spectrum function  $E(q)$  defined such that the total turbulent kinetic energy per unit mass is given by [178]

$$E_{tot} = \frac{1}{2} \langle |\mathbf{v}|^2 \rangle \equiv \int_0^\infty E(q) dq. \quad (2.40)$$

This emphasizes the distribution of kinetic energy over different length scales.

$E(q)$  can be estimated from the two-point velocity correlation tensor,

$$R_{ij}(\mathbf{r}) = \langle v_i(\mathbf{r}) v_j(0) \rangle, \quad (2.41)$$

in Fourier space. Since the turbulent velocity field is homogeneous and isotropic, the correlation tensor is a function only of the distance between the two points. The trace of the velocity correlation tensor is  $R(\mathbf{r}) = \sum_i R_{ii}(\mathbf{r})$ , and  $R(\mathbf{r}) \rightarrow \langle |\mathbf{v}|^2 \rangle$  in the limit  $\mathbf{r} \rightarrow 0$ .

The energy spectrum tensor is the Fourier transform of the velocity correlation tensor expressed as

$$\Phi_{ij}(\mathbf{q}) = \int R_{ij}(\mathbf{r}) e^{-i\mathbf{q}\cdot\mathbf{r}} d^2r, \quad (2.42)$$

in two dimensions [179]. The spectrum  $\Phi_{ij}(\mathbf{q})$  tells how much kinetic energy is contained in eddies with wavenumber  $q$ . For an two-dimensional isotropic flow, the spectrum depends only on the magnitude of the wavenumber  $q$  and the total kinetic energy per unit mass can be expressed as

$$E_{tot} = \frac{1}{2} R_{ii}(0) = \int_0^\infty \pi \Phi_{ii}(q) q dq, \quad (2.43)$$

which in turn gives the energy spectrum relation [179]

$$E(q) = \pi \Phi_{ii}(q) q. \quad (2.44)$$

This expression for the energy spectrum  $E(q)$  can be conveyed in an alternative form as [178]

$$E(q) = \frac{1}{2} \Psi_{ii}(q), \quad (2.45)$$

with the definition  $\Psi_{ij}(q) = \int \Phi_{ij}(\mathbf{q}) dl(q)$ . Here,  $q = |\mathbf{q}|$  and the integration is over the line segments  $dl$ . It is evident that both the expressions, Eqs. (2.44) and (2.45), for energy spectrum are equivalent, as  $\int dl(q) \propto q$ .

In numerical simulations,  $E(q)$  can be estimated with the expression [180]

$$E(q) = \frac{1}{2} \sum_{q-\Delta q \ll q \ll q+\Delta q} |\hat{v}(\mathbf{q})|^2, \quad (2.46)$$

which is a discretized form of Eq. (2.45), and follows by using a similar approach to Wiener-Khinchin theorem. The sum runs over a thin shell of thickness  $2\Delta q$  around  $q$ .

### 2.2.4 Two dimensional Turbulence

Turbulent fluctuations are injected by external forcing,  $\mathbf{f}$ , at a length scale  $l_f$  and the dissipation of the energy can happen in two ways, either by friction at much larger scales  $l_\gamma \gg l_f$  or at much smaller scales  $l_\nu \ll l_f$  by viscous dissipation. Thus, defining two distinct inertial ranges  $l_f \ll l \ll l_\gamma$  and  $l_\nu \ll l_f$  over which universal statistics is predicted.

The energy and enstrophy input at intermediate scales,  $\epsilon_f$  and  $\eta_f$ , respectively, are dissipated by friction at larger scales and viscous dissipation at relatively smaller scales maintaining the energy and enstrophy balance, i.e.,  $\epsilon_f = \epsilon_\gamma + \epsilon_\nu$  and  $\eta_f = \eta_\gamma + \eta_\nu$ . With the characteristic friction and viscosity scales  $l_\gamma^2 \equiv \epsilon_\gamma/\eta_\gamma$  and  $l_\nu^2 \equiv \epsilon_\nu/\eta_\nu$  and considering the forcing scale  $l_f^2 \approx \epsilon_f/\eta_f$ , one obtains [179]

$$\frac{\epsilon_\nu}{\epsilon_\gamma} = \left(\frac{l_\nu}{l_f}\right)^2 \left(\frac{l_f}{l_\gamma}\right)^2 \frac{(l_\gamma/l_f)^2 - 1}{1 - (l_\nu/l_f)^2}, \quad (2.47)$$

$$\frac{\eta_\nu}{\eta_\gamma} = \frac{(l_\gamma/l_f)^2 - 1}{1 - (l_\nu/l_f)^2}. \quad (2.48)$$

In the range  $l_\nu \ll l_f$ ,  $\epsilon_\nu/\epsilon_\gamma \rightarrow 0$ ; i.e., all the energy flows to large scales. Additionally, if  $l_\gamma \gg l_f$ ,  $\eta_\gamma/\eta_\nu \rightarrow 0$ ; i.e., all the enstrophy goes to small scales (see Fig. 2.1).

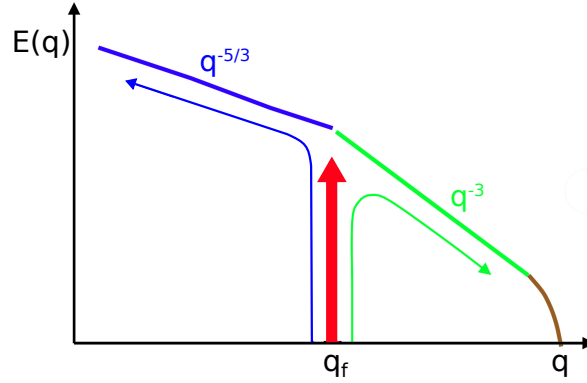


Figure 2.1: Schematic of energy spectrum in two-dimensional turbulence. It depicts the inverse energy cascade toward larger length scales and the direct enstrophy cascade toward smaller length scales. The energy injection scale at  $q_f$  is illustrated by the red arrow.

### Inverse Energy Cascade

The phenomenology of two-dimensional turbulence is usually expressed in terms of eddies. Two important properties associated with an eddy are size and energy. These two properties reveal how neighboring eddies interact, which in turn gives insight into the energy motion in the fluid system.

In 2D fluids, neighboring eddies interact via vortex cannibalization, i.e., two neighboring eddies with the same rotation merge to form a single larger eddy. Through this process, energy flow occurs from the length scale of initially smaller eddies to the length scales of a finally larger eddy. In 2D turbulence, eddies are created at smaller length scales and which continuously merge into larger eddies. These larger eddies in turn merge to form even larger ones through cannibalization and so on. That means energy gradually moves toward larger length scales after initial injection at smaller scales – this is termed inverse energy cascade.

### Kolmogorov power law

The velocity field in incompressible 3D turbulent flows is self-similar over a range of velocity scales, due to the dissipationless cascade of energy from large scales to small scales [178]. A fully developed turbulent system is characterized by the mean energy dissipation rate  $\epsilon_d$  and the kinematic viscosity  $\nu$ . Combining these two quantities the Kolmogorov or dissipational

length scale is defined as

$$l_K = \left( \frac{\nu^3}{\epsilon_d} \right)^{1/4}, \quad (2.49)$$

which characterizes the size of the smallest eddies in the fluid. Eddies smaller than this length scale disappear due to rapid dissipation of energy by viscous heating. The eddies of size  $l_K$  rotate with characteristic velocity

$$u_K = (\nu \epsilon_d)^{1/4}. \quad (2.50)$$

Kolmogorov assumed that the energy spectrum of self-similar turbulence should have the form

$$E(q, t) = u_K^2 l_K E_*(l_K q), \quad (2.51)$$

where the factor  $u_K^2 l_K = \nu^{5/4} \epsilon_d^{1/4}$  has the dimensions of the energy spectrum and  $E_*$  is a dimensionless function of  $l_K q$ . In the intermediate inertial subrange, the energy spectrum must be scale free, such that

$$E_*(l_K q) = \alpha (l_K q)^n \quad (2.52)$$

is a power law, with the proportionality constant  $\alpha$ . In addition, the energy spectrum  $E(k)$  should also be independent of viscosity  $\nu$ , as viscous forces are negligible on this scale. Considering all these relations, one obtains

$$E(q) = \alpha \nu^{(5+3n)/4} \epsilon_d^{(1-n)/4} q^n. \quad (2.53)$$

For  $E(q)$  to be independent of  $\nu$ , it is required  $n = -5/3$  and thus, we have the Kolmogorov spectrum

$$E(q) = \alpha \epsilon_d^{2/3} q^{-5/3}. \quad (2.54)$$

A similar theory for the energy spectrum in 2D, analogous to Kolmogorov theory in 3D, can be obtained by dimensional analysis with the assumption of a cascade rate being independent of spatial scale in the inverse energy cascade range [181]. Hence, we have the relation

$$E(q) \sim \epsilon_d^{2/3} q^{-5/3}, \quad (2.55)$$

which has the same dependency on  $q$  as in 3D, but with a different interpretation of the role of  $\epsilon_d$ .

### Direct enstrophy cascade

Contrary to the inverse energy cascade, the enstrophy is transferred to large wave-numbers (smaller length scales) where it is dissipated by viscosity in case of two dimensional turbulence, giving rise to the direct enstrophy cascade.

On scales smaller than the forcing correlation length  $l_f$ , the hypothesis of constant enstrophy flux  $\epsilon_\omega$  leads to a different scaling. The assumption that the squared-vorticity spectrum  $2q^2 E(q)$  depends only on  $\epsilon_\omega$  and  $q$  yields [181]

$$E(q) \sim \epsilon_\omega^{2/3} q^{-3}. \quad (2.56)$$

The enstrophy cascade to smaller length scales implies a transition to the enstrophy dissipation range  $l_D$  defined by

$$l_D = \left( \frac{\nu^3}{\epsilon_\omega} \right)^{1/6}. \quad (2.57)$$

## 2.3 Multiparticle Collision Dynamics

During the last few decades various mesoscale hydrodynamic simulation techniques, such as Lattice-Boltzmann (LB) [182–184], Dissipative Particle Dynamics (DPD) [185, 186], and multiparticle collision dynamics (MPC) [187–190], have been applied to soft matter systems, to resolve the interplay between thermal fluctuations, hydrodynamic interactions (HI), and spatiotemporally varying forces. Multiparticle collision dynamics is a particle-based hydrodynamic simulation method introduced by Malevanets and Kapral [187, 188]. The MPC algorithm exhibits unconditional numerical stability and an H-theorem has been derived [187, 188]. The discrete-time dynamics of MPC yields correct longtime hydrodynamics and also incorporates thermal fluctuations. In addition, hydrodynamic interactions can be easily switched off, rendering it useful to study the importance of such interactions [191, 192].

### 2.3.1 Algorithm

In MPC, the fluid consists of  $N$  point particles characterized by their positions  $\mathbf{r}_i$ , velocities  $\mathbf{v}_i$ , and the mass  $m$ . The algorithm consists of two subsequent steps, streaming and collision, illustrated in Fig. 2.2.

#### Streaming and Collision

In the streaming step, particles do not interact with each other, but experience a possibly present external field. In absence of such force fields, they move ballistically for the time interval  $h$ . Thereby, their positions are updated according to

$$\mathbf{r}_i(t + h) = \mathbf{r}_i(t) + h\mathbf{v}_i(t), \quad (2.58)$$

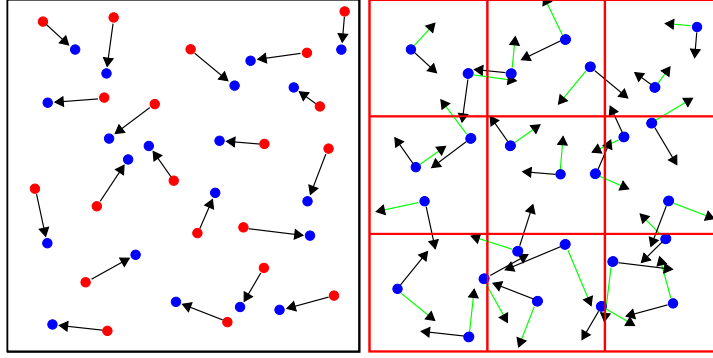


Figure 2.2: Schematic representation of Multiparticle Collision dynamics (MPC). (a) Red circles represent current particle positions, blue circles represent the new positions after streaming, and black arrows represent particle velocities. (b) The collision cells are indicated by red lines. In a collision, particle velocities (black arrow) are updated to new velocities (green arrow) w.r.t the center-of-mass frame of the particular collision cell.

where  $i = 1, \dots, N$  is the particle index. In the collision step, the system is partitioned into cubic collision cells of length  $a$ . A coarse-grained interaction is applied on the particles, through a momentum-conserving stochastic process at the collision-cell level, which replicates the hydrodynamic interaction in the system. In the stochastic rotation dynamics (SRD) version of MPC [187–189], the relative velocity of each particle, with respect to the center-of-mass velocity of the cell, is rotated by an fixed angle  $\zeta$  around an randomly orientated axis, i.e.,

$$\mathbf{v}_i(t+h) = \mathbf{v}_{cm}(t) + \mathbf{R}(\zeta)\mathbf{v}_{i,c}(t). \quad (2.59)$$

Here,  $\mathbf{v}_i(t)$  and  $\mathbf{v}_i(t+h)$  are the velocities before and after the collision,  $\mathbf{v}_{i,c} = \mathbf{v}_i - \mathbf{v}_{cm}$ ,

$$\mathbf{v}_{cm} = \frac{1}{N_c} \sum_{j \in cell}^{N_c} \mathbf{v}_j \quad (2.60)$$

is the center-of-mass velocity of the particles in the considered cell, and  $\mathbf{R}(\zeta)$  is the rotation matrix.  $\mathbf{R}(\zeta)$  can be represented as rotation by an angle  $\zeta$  around a random vector  $\mathbf{R} = (\mathcal{R}_x, \mathcal{R}_y, \mathcal{R}_z)$ ,  $|\mathbf{R}| = 1$ , i.e.,

$$\mathbf{R}(\zeta) = \begin{pmatrix} \mathcal{R}_x^2 + (1 - \mathcal{R}_x^2)c & \mathcal{R}_x\mathcal{R}_y(1 - c) - \mathcal{R}_zs & \mathcal{R}_x\mathcal{R}_z(1 - c) + \mathcal{R}_ys \\ \mathcal{R}_x\mathcal{R}_y(1 - c) + \mathcal{R}_zs & \mathcal{R}_y^2 + (1 - \mathcal{R}_y^2)c & \mathcal{R}_y\mathcal{R}_z(1 - c) - \mathcal{R}_xs \\ \mathcal{R}_x\mathcal{R}_z(1 - c) - \mathcal{R}_ys & \mathcal{R}_y\mathcal{R}_z(1 - c) + \mathcal{R}_xs & \mathcal{R}_z^2 + (1 - \mathcal{R}_z^2)c \end{pmatrix}, \quad (2.61)$$

where  $c = \cos \zeta$ ,  $s = \sin \zeta$ .  $\mathbf{R}$  is chosen randomly for every collision cell and time step. It can be defined as

$$\mathcal{R}_x = \sqrt{1 - \theta^2} \cos \varphi, \quad \mathcal{R}_y = \sqrt{1 - \theta^2} \sin \varphi, \quad \mathcal{R}_z = \theta, \quad (2.62)$$

with uncorrelated random numbers  $\varphi$  and  $\theta$  taken from uniform distributions in the intervals  $[0, 2\pi]$  and  $[-1, 1]$ , respectively.

In two dimensions, the rotation matrix reads

$$\mathbf{R}(\zeta) = \begin{pmatrix} \cos \zeta & -u \sin \zeta \\ u \sin \zeta & \cos \zeta \end{pmatrix}, \quad (2.63)$$

where  $u \in \{-1, 1\}$  is chosen with uniform probability, i.e., clockwise and counter-clockwise rotation are equally probable [189].

### Angular momentum conservation

The collision step in Eq. (2.59) violates angular momentum conservation. To conserve angular momentum locally, all particles in a cell are given an additional rigid body angular velocity and the collision rule is modified as [193, 194]

$$\mathbf{v}_i(t+h) = \mathbf{v}_{cm}(t) + \mathbf{R}(\zeta)\mathbf{v}_{i,c}(t) - \mathbf{r}_{i,c}(t+h) \times \boldsymbol{\Omega}, \quad (2.64)$$

where  $\mathbf{r}_{i,c} = \mathbf{r}_i - \mathbf{r}_{cm}$  is the particle position relative to their center-of-mass  $\mathbf{r}_{cm}$  of a cell,  $\mathbf{I}$  is the moment-of-inertia tensor of the particles in the center-of-mass reference frame, and the angular velocity  $\boldsymbol{\Omega}$  reads as,

$$\boldsymbol{\Omega} = \left[ m\mathbf{I}^{-1} \sum_{j \in cell} \{ \mathbf{r}_{j,c}(t+h) \times (\mathbf{v}_{j,c}(t) - \mathbf{R}(\zeta)\mathbf{v}_{j,c}(t)) \} \right]. \quad (2.65)$$

### Random shift

The MPC algorithm violates Galilean invariance in the original form due to partition of the system into collision cells and mostly the same particles repeatedly interacting with each other, which leads to build up of correlations. To reestablish Galilean invariance, a random shift of the collision grid is performed in every collision step [195, 196]. Before the collision, all the fluid particles are shifted by the same random vector with components uniformly distributed in the interval  $[-a/2, a/2]$ . After the collision, particles are shifted back to their original positions.

### 2.3.2 Embedded object and boundary conditions

Consider embedded particles composed of point particles, which can be colloids or polymers [197, 198] moving in the MPC fluid. Their coupling with the MPC fluid is established in the collision step. This is achieved by including these particles in the collision step, i.e., the particle velocities are updated according to Eq. (2.64) ensuring momentum exchange between embedded particles and fluid [199]. Thereby, the center-of-mass velocity of a collision cell containing the embedded particles is given by

$$\mathbf{v}_{cm}(t) = \frac{\sum_{i=1}^{N_c} m\mathbf{v}_i(t) + \sum_{k=1}^{N_c^p} M\mathbf{V}_k(t)}{mN_c + MN_c^p}, \quad (2.66)$$

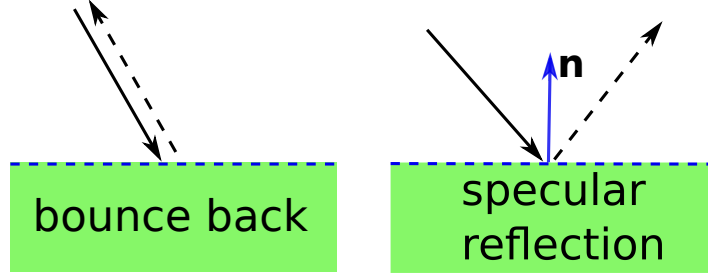


Figure 2.3: Depiction of boundary conditions during the streaming step. A fluid particle's trajectory is visualized by a solid black arrow and by a dashed arrow after the collision. The no-slip boundary condition is realized by a bounce-back, while the slip boundary condition is realized by a specular reflection.

where  $N_c^p$  is the number of embedded particles and  $N_c$  is the number of fluid particles in the particular collision cell.

The local flow field around an embedded rigid body object or bounding walls is resolved using various methods, where fluid particles are excluded from the interior of the rigid body or walls mimicking slip [200, 201] or no-slip [189, 202] boundary conditions. If the fluid particles end up inside the embedded object or the wall in the streaming step, their velocity is transformed depending on the kind of boundary condition. For no-slip boundary conditions, a fluid particle reverses its velocity from  $\mathbf{v}_i$  to  $-\mathbf{v}_i$  when it hits the surface of a rigid body or a wall. This is known as the bounce-back rule (see Fig. 2.3). For slip boundary conditions, only the velocity component in the direction of the surface normal  $\mathbf{n}$  is reversed, which corresponds to a specular reflection (see Fig. 2.3). For no-slip boundary conditions, the simple bounce-back rule fails to guarantee no-slip due to random shifts, hence ghost particles are inserted into the wall or the rigid body before the collision step (see Fig. 2.4) [189, 203]. The velocities of these ghost particles are equal to the mean rigid body or wall velocity plus a random velocity taken from a Maxwell-Boltzmann distribution with zero mean and variance  $mN_g k_B T$ , where  $N_g$  is the number of ghost particles in a particular partially filled cell. Subsequently, the ghost particles take part in the collision step just like the fluid particles.

### 2.3.3 Thermostat

The simulation of a canonical ensemble or isothermal fluid is achieved by the application of the MBS thermostat, where velocities are scaled on the level of individual MPC cells [204]. After every time step, the relative velocities  $\mathbf{v}_{i,c}$  of the MPC-particles in each cell are rescaled by  $\kappa$  to get new velocities

$$\mathbf{v}'_i = \mathbf{v}_{cm} + \kappa \mathbf{v}_{i,c}, \quad (2.67)$$

with the scaling factor

$$\kappa = \left( \frac{2E_k}{\sum_{i=1}^{N_c} m \mathbf{v}_{i,c}^2} \right)^{1/2}. \quad (2.68)$$



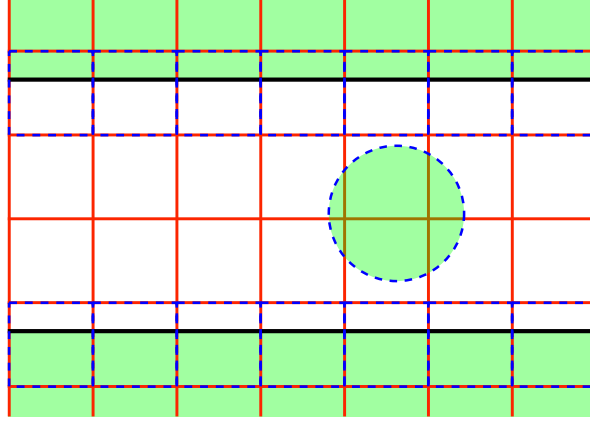


Figure 2.4: Illustration of collision grid (solid red lines) after random shift perpendicular to the walls. The solid black lines are the boundary walls and dotted blue lines mark the partially filled cells where ghost particles are added.

Here,  $E_k$  is a kinetic energy determined from the gamma distribution expected in a canonical ensemble

$$P(E_k) = \frac{1}{E_k \Gamma(f/2)} \left( \frac{E_k}{k_B T} \right)^{f/2} \exp \left( -\frac{E_k}{k_B T} \right), \quad (2.69)$$

where  $\Gamma(x)$  is the gamma function and  $f = 3(N_c - 1)$  denotes the number of degrees of freedom of a collision cell with  $N_c$  MPC particles.

### 2.3.4 Random MPC

The MPC algorithm can be easily modified to turn off hydrodynamic interactions, known as the random MPC solvent [191, 192, 205]. In random MPC, the solvent-solute interaction in the collision step of the original MPC algorithm is replaced by the interaction with a Brownian heat bath. The basic idea behind is to randomly interchange the fluid-particle velocities after each collision step, so that the local momentum conservation is destroyed and so are the hydrodynamic correlations. Each of the points of mass  $M = m\rho$  is coupled with  $\rho$  solvent particles of mass  $m$  having an effective momentum  $\mathbf{p}$  directly chosen from a Maxwell-Boltzmann distribution of variance  $Mk_B T$  and a mean given by the average momentum of the fluid field, which is zero at rest. The total center-of-mass velocity used in the collision step is then given by [192]

$$\mathbf{v}_{cm,i} = \frac{M\mathbf{v}_i + \mathbf{p}}{2M}. \quad (2.70)$$

The interaction with the fluid is performed in every collision step using the MPC collision rule,

$$\mathbf{v}_i(t+h) = \mathbf{v}_{cm,i}(t) + \mathbf{R}(\zeta)[\mathbf{v}_i(t) - \mathbf{v}_{cm,i}(t)], \quad (2.71)$$

where  $\mathbf{R}(\zeta)$  is the rotation matrix (2.61). No explicit solvent particles need to be considered, since the particle positions are irrelevant in the collision step unlike the MPC solvent and, hence, being computationally efficient.

### 2.3.5 Unit and parameters

In the MPC algorithm, lengths are measured in units of the collision cell length  $a$ , masses are measured in units of the fluid particle mass  $m$ , and time is measured in units of  $\tau = \sqrt{ma^2/k_B T}$ , i.e., we choose  $m = k_B T = a = 1$ . All other mechanical quantities can be expressed in terms of length, mass, and time. The parameters characterizing the properties of the MPC fluid, are the average number of particles per cell  $\langle N_c \rangle$ , the time step  $h$ , and the rotation angle  $\zeta$ . To obtain a fluid-like behavior, in three dimensions, the collision angle  $\zeta = 130^\circ$ , average number of MPC particles per collision cell  $\langle N_c \rangle = 10$ , and collision time  $h = 0.1\tau$  are applied [206]. These values can be tuned to modify the fluid viscosity.

### 2.3.6 Stress tensor

An expression for the stress tensor of a MPC fluid can be obtained via the virial theorem [122]. We consider a fluid volume  $V$  and define the quantity

$$G = \frac{1}{V} \sum_{i=1}^N m_i v_{i\alpha} r_{i\beta}; \quad (2.72)$$

differentiating with time yields the equality

$$\langle \dot{G} \rangle = \left\langle \frac{1}{V} \frac{d}{dt} \sum_{i=1}^N m_i v_{i\alpha} r_{i\beta} \right\rangle = \left\langle \frac{1}{V} \sum_{i=1}^N m_i v_{i\alpha} v_{i\beta} \right\rangle + \left\langle \frac{1}{V} \sum_{i=1}^N r_{i\beta} m_i \frac{dv_{i\alpha}}{dt} \right\rangle, \quad (2.73)$$

where  $\langle \dots \rangle$  can correspond to a time or an ensemble average. The average on the left hand side vanishes for a diffusive or confined system and leads to

$$\left\langle \frac{1}{V} \sum_{i=1}^N m_i v_{i\alpha} v_{i\beta} \right\rangle + \left\langle \frac{1}{V} \sum_{i=1}^N r_{i\beta} m_i \frac{dv_{i\alpha}}{dt} \right\rangle = 0, \quad (2.74)$$

which is a generalization of the virial theorem. The second term on LHS involving the change of  $v_{i\alpha}$  has an internal contribution due to all fluid particles in  $V$  and an external contribution resulting from the fluid particles outside of  $V$ , i.e.,

$$\frac{dv_{i\alpha}}{dt} = \left. \frac{dv_{i\alpha}}{dt} \right|_{int} + \left. \frac{dv_{i\alpha}}{dt} \right|_{ext}. \quad (2.75)$$

The momentum density  $\rho v_\alpha$  in a control volume changes due to inflow of fluid carrying momentum, i.e.,  $-\int dA \rho v_\alpha v_\gamma n_\gamma$ , and due to the stresses applied on the surface of  $V$ , i.e.,

$\int dA \sigma_{\alpha\gamma} n_\gamma$ . Hence, with the use of Gauss' theorem and with the assumption that gradients in  $\rho$ ,  $\mathbf{v}$ , and  $\boldsymbol{\sigma}$  are negligible inside  $V$ , we get [207]

$$\left\langle \frac{1}{V} \sum_{i=1}^N r_{i\beta} m_i \frac{dv_{i\alpha}}{dt} \Big|_{ext} \right\rangle = \sigma_{\alpha\beta} - \frac{1}{V} \left\langle \sum_{i=1}^N m_i v_{\alpha}(\mathbf{r}_i) v_{\beta}(\mathbf{r}_i) \right\rangle. \quad (2.76)$$

MPC is a discrete time random process and the stress tensor is defined at times  $t = jh$ , with  $j \in \mathbb{N}$ . The internal change of velocity  $(d\mathbf{v}/dt)|_{int}$  is due to the change of momentum in the collision step, i.e.,

$$m \frac{dv_{i\alpha}}{dt} \Big|_{int} = \frac{\delta p_{i\alpha}}{h}, \quad (2.77)$$

where  $\mathbf{p}_i = m\mathbf{v}_i$ . With this mapping, we can define the instantaneous particle-level stress tensor  $\boldsymbol{\sigma}^i$  of a MPC fluid as

$$\sigma_{\alpha\beta}^i = -\frac{1}{V} \left\langle \sum_i m_i (v_{i\alpha} - v_{\alpha}(\mathbf{r}_i)) (v_{i\beta} - v_{\beta}(\mathbf{r}_i)) \right\rangle - \frac{1}{Vh} \sum_i \Delta p_{i\alpha} r_{i\beta}. \quad (2.78)$$

### 2.3.7 Viscosity

The total viscosity  $\eta$  of a MPC fluid consists of the kinetic  $\eta_{kin}$  and the collisional  $\eta_{coll}$  part, i.e.,

$$\eta = \eta_{kin} + \eta_{coll}. \quad (2.79)$$

Analytical expressions for the viscosity parameters  $\eta_{kin}, \eta_{coll}$  can be derived using the molecular chaos approximation and can be expressed in terms of density  $\rho$ , time step  $h$ , and rotation angle  $\zeta$  as [205, 206]

$$\eta_{kin} = \frac{k_B T h}{a^d} \left( \frac{\rho/B}{\rho - 1} - \frac{1}{2} \right) \quad (2.80)$$

$$\eta_{coll} = \frac{Am(\rho - 1)}{12a^{d-2}h} \quad (2.81)$$

where  $d$  is the dimension, and the coefficients  $A$  and  $B$  are given in the Table. 2.1. For systems with small  $\rho$ , density fluctuations have pronounced effects and should be considered in the viscosity calculations. For the system of  $\langle N_c \rangle = 10$  these effects are insignificant.

$d$	$A$	$B$
2	$1 - \cos \zeta$	$1 - \cos 2\zeta$
3	$\frac{2}{3}(1 - \cos \zeta)$	$\frac{2}{5}(2 - \cos \zeta - \cos 2\zeta)$

Table 2.1: Values of  $A$  and  $B$  for two and three dimensions.

# Chapter 3

## Equilibrium microstructure and dynamics

Various methods have been developed for the estimation of static and dynamic properties to characterize a system of suspension particles. We discuss here the elementary concepts, followed by the introduction of the methods to calculate the radial distribution function  $g(r)$  and the static structure factor  $S(q)$ . Further, a discussion of the dynamic structure factor  $S(q, t)$  and the short time dynamics of colloidal particles, probed in scattering experiments, is presented.

### 3.1 Static distribution functions

Thermodynamic properties of an one-component many-body system are calculated using statistical mechanics with the three known macroscopic state variables volume of the system  $V$ , number of particles  $N$ , and total energy  $E$ . These variables can vary depending on the thermodynamic ensemble considered. We will focus in the following on the canonical ensemble, where the temperature  $T$ , particle number, and system volume are constant.

The positions of  $N$  particles can be related to macroscopic state variables by the equilibrium probability density function (PDF)  $P_N$  for  $N$  particles, with center-of-mass positions  $(\mathbf{r}_1, \mathbf{r}_2, \dots, \mathbf{r}_N) = \mathbf{r}^N$ , lying in  $V$  at  $T$ . Explicitly,  $P_N$  is given by [208]

$$P_N(\mathbf{r}^N) = \frac{e^{-\beta U(\mathbf{r}^N)}}{Z_N}, \quad (3.1)$$

where  $U(\mathbf{r}^N)$  is the  $N$ -particle potential energy and

$$Z_N = \int_{V^N} d\mathbf{r}^N \exp[-\beta U(\mathbf{r}^N)] \quad (3.2)$$

is the configurational integral, taken over all possible combinations of particle positions (partition function). To calculate the thermodynamic functions and in scattering experiment accessible properties such as  $g(r)$  and  $S(q)$ , only reduced distribution functions involving  $n \ll N$  representative particles are required. The canonical  $n$ -particle density function is

defined by [208],

$$\rho_N^{(n)} = \frac{N!}{(N-n)!} \int d\mathbf{r}^{(N-n)} P_N(\mathbf{r}^N), \quad (3.3)$$

and it is the probability density of finding  $n$  particles at positions  $\mathbf{r}_1$  to  $\mathbf{r}_n$  with no constraints on the remaining  $(N-n)$  particles. Indistinguishability of the  $N$  particles is accounted for by the factor  $N!/(N-n)!$ . For a homogeneous fluid phase state, due to the spatial uniformity and isotropic nature of the system [209]

$$\rho_N^{(n)}(\mathbf{r}_1, \mathbf{r}_2, \dots, \mathbf{r}_n) = \rho_N^{(n)}(\mathbf{r}_1 + \Delta\mathbf{r}, \mathbf{r}_2 + \Delta\mathbf{r}, \dots, \mathbf{r}_n + \Delta\mathbf{r}), \quad (3.4)$$

where  $\Delta\mathbf{r}$  is an arbitrary displacement. This implies that the one-particle density  $\rho_N^{(1)} = \rho = N/V$  is equal to the average particle number density  $\rho$ . Moreover, the two-particle density

$$\rho_N^{(2)}(\mathbf{r}, \mathbf{r}') = \rho_N^{(2)}(|\mathbf{r} - \mathbf{r}'|) \quad (3.5)$$

is then simply a function of the distance between two considered particles at position  $\mathbf{r}$  and  $\mathbf{r}'$ .

In colloidal systems away from a critical point, the correlation length  $\xi$ , defined as the distance over which two particles are correlated, is typically on the order of the range of the interaction pair-potential [209]. Thus, for  $|\mathbf{r} - \mathbf{r}'| \gg \xi$ ,

$$\rho_N^{(n)}(\mathbf{r}_1, \mathbf{r}_2, \dots, \mathbf{r}_n) \approx \prod_{i=1}^n \rho_N^{(1)}(\mathbf{r}_i) = \rho^n, \quad (3.6)$$

since these particles are then uncorrelated and the second equality holds only in a uniform system. The deviation of a fluid system from the classical ideal gas behavior is quantified by the canonical  $n$ -particle distribution function

$$g_N^{(n)}(\mathbf{r}_n) = \frac{\rho_N^{(n)}(\mathbf{r}_n)}{\prod_{i=1}^n \rho_N^{(1)}(\mathbf{r}_i)}. \quad (3.7)$$

Hence,  $g_N^{(n)}(\mathbf{r}_n)$  is a measure of the  $n$ -particle local structure in a colloidal system [208].

### 3.1.1 Radial distribution function

The two-particle distribution function of an isotropic system depends on  $r = |\mathbf{r}_i - \mathbf{r}_j|$  only, and it is referred to as the radial distribution function (RDF) [208]

$$g(r) = \lim_{N \rightarrow \infty} g_N^{(2)}(r) = \lim_{N \rightarrow \infty} \frac{N(N-1)}{\rho^2} \int d\mathbf{r}_3 \dots d\mathbf{r}_N P_N(\mathbf{r}^N), \quad (3.8)$$

where  $\lim_{N \rightarrow \infty}$  denotes the thermodynamic limit and  $g(r \gg \xi) = 1$ . The RDF in a system of large colloidal particles can be directly determined by confocal microscopy. In a simulation

study, it is obtained by counting the number of particles in a thin spherical shell, at distance  $r$  from a selected particle, of thickness  $\Delta r$  and volume  $4\pi r^2 \Delta r$ , i.e.,

$$g(r) = \frac{N(r)}{4\pi\rho r^2 \Delta r}, \quad (3.9)$$

where  $N(r)$  is the number of particles with centers inside the shell  $[r, r + \Delta r]$ . We finally note that  $g(r)$  can be expressed as [208]

$$g(r) = \lim_{N \rightarrow \infty} \frac{1}{\rho} \left\langle \frac{1}{N} \sum_{i \neq j} \delta(r - r_i) \right\rangle, \quad (3.10)$$

where  $\langle \dots \rangle$  denotes the ensemble average.

### 3.1.2 Static structure factor

The static structure factor  $S(q)$  is related to the Fourier transform of radial distribution function  $g(r)$ . This can thus be determined experimentally via widely used scattering techniques such as DLS and SANS. In a static scattering measurement, the mean intensity of scattered light,  $I(q)$ , is measured as a function of the scattered wavenumber  $q$ . The latter is related to the scattering angle  $\theta$  by  $q = (4\pi/\lambda) \sin(\theta/2)$ , where  $\lambda$  is the scattering wavelength inside the medium (see Fig. 3.1) [209]. For an ergodic system of monodisperse particles,

$$I(q) \propto \langle N \rangle P(q) S(q), \quad (3.11)$$

where  $\langle N \rangle$  is the mean number of particles in the scattering volume,  $P(q)$  is the particle form factor describing the scattering material distribution inside a particle, and the structure factor  $S(q)$  is the correlation function of the  $q$ -th component of microscopic density fluctuations characterizing the inter-particle correlations. The statistical mechanical definition of  $S(q)$  reads [209]

$$S(q) = \lim_{N \rightarrow \infty} \left\langle \frac{1}{N} \sum_{j,k} \exp(i\mathbf{q} \cdot (\mathbf{r}_j - \mathbf{r}_k)) \right\rangle = 1 + \rho \int_V d\mathbf{r} e^{i\mathbf{q} \cdot \mathbf{r}} g(r), \quad (3.12)$$

where the second relation follows from Eq. (3.8) providing the Fourier relation to RDF pointed above.

## 3.2 Dynamic properties

### 3.2.1 Dynamic structure factor

In dynamic light scattering (DLS) experiments, the scattered intensity fluctuates with time due to the Brownian motion of the center of mass, and of the orientation of particles and

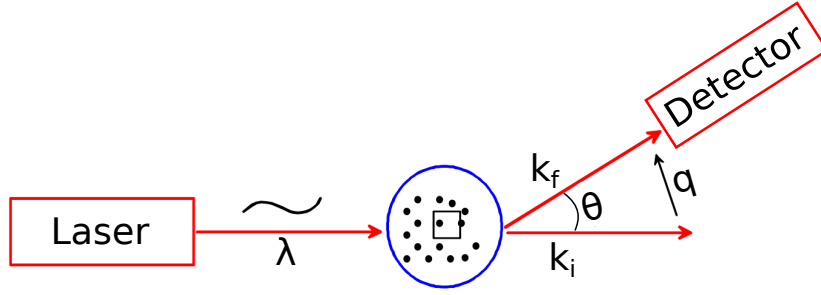


Figure 3.1: Schematic of typical scattering experiment setup.

their internal fluctuations. These fluctuations include information about the dynamics of these degrees of freedom, which are being affected by interactions between the particles. In all scattering experiments, the so-called intensity auto-correlation function (IACF)  $g_I(q, t)$  is measured and interpreted through the more simple electric field auto-correlation function (EACF)  $g_E(q, t)$  via the Siegert relation [209]

$$g_I(q, t) = \langle I(q) \rangle^2 + |g_E(q, t)|^2, \quad (3.13)$$

where  $\langle I(q) \rangle$  is the mean scattered intensity. The collective dynamic structure factor  $S(q, t)$  is proportional to the experimentally obtained EACF with the relation,

$$g_E(q, t) \propto \langle N \rangle P(q) S(q, t) \quad (3.14)$$

and is defined as

$$S(q, t) = \frac{1}{N} \sum_{i,j=1}^N \langle \exp [i\mathbf{q} \cdot (\mathbf{r}_j(t) - \mathbf{r}_i(0))] \rangle. \quad (3.15)$$

It is the time-dependent generalization of the static structure factor  $S(q) = S(q, t = 0)$  presented in Eq. (3.12), and is the time auto-correlation function of microscopic particle concentration fluctuations in Fourier space. In neutron spin echo (NSE) experiments, where quasi-elastic scattering of an initially polarized neutron beam from a sample is used,  $S(q, t)$  is directly determined from the phase shift of the scattered neutron beam.

### 3.2.2 Short time dynamics

Regarding the Brownian dynamics of colloidal particles, the short-time regime  $\tau_B \ll t \ll \tau_D$  is distinguished from the long-time regime  $t \gg \tau_D$ . Here,  $t$  denotes the correlation time,  $\tau_B$  is the characteristic relaxation time of particle velocity fluctuations, and  $\tau_D$  is a characteristic diffusion time given by  $\tau_D = \sigma^2/4D_0$  for a particle of diameter  $\sigma$ , and  $D_0 = k_B T / (3\pi\eta\sigma)$  is the single-particle translational diffusion coefficient in the solvent of viscosity  $\eta$ . For  $t \ll \tau_D$ , changes in the particles configuration are so minuscule that the direct influence of the pair interactions with neighbors on diffusion properties is not yet operative. This is different



for the solvent-mediated hydrodynamic interactions which act quasi-instantaneously even on the colloidal short-time scale. Short-time transport properties, such as the short-time self-diffusion coefficient, are thus expressible as genuine equilibrium averages, where direct interactions are only indirectly influential through their effect on the equilibrium microstructure encoded, e.g., in  $g(r)$  and  $S(q)$ . Long-time dynamic transport properties, e.g., the long-time self-diffusion coefficient and the steady-shear suspension viscosity, are influenced, in addition to HIs, by the non-hydrodynamic direct interactions in form of non-instantaneous caging (memory) effects.

### Hydrodynamic function

The short-time dynamics of Brownian particles can be probed experimentally by measuring the  $q$ -dependent dynamic structure factor,  $S(q, t)$ , using dynamic light scattering (DLS) or neutron spin echo spectroscopy (NSE) measurements, depending on the particle size, concentration, and other system properties. For short times,  $S(q, t)$  decays single exponentially, and it can be expressed in terms of the short-time diffusion function  $D(q)$  as [209, 210]

$$S(q, t \ll \tau_D) = S(q) \exp(-q^2 D(q) t). \quad (3.16)$$

Applying the generalized Smoluchowski equation describing the overdamped colloid dynamics leads to the expression [209, 210]

$$D(q) = D_0 \frac{H(q)}{S(q)}, \quad (3.17)$$

which expresses the short-time diffusion  $D(q)$  as a ratio of the so-called hydrodynamic function  $H(q)$ , and the static structure factor  $S(q)$ . The former is a dynamic quantity characterizing the effect of HIs on short-time self and collective diffusion. The microscopic expression for  $H(q)$ , obtained from generalized Smoluchowski equation, is given by

$$H(q) = \frac{1}{N\mu_0} \sum_{i,j}^N \langle \hat{\mathbf{q}} \cdot \boldsymbol{\mu}_{ij}(\mathbf{X}) \cdot \hat{\mathbf{q}} \exp[i\mathbf{q} \cdot (\mathbf{r}_i - \mathbf{r}_j)] \rangle, \quad (3.18)$$

where  $\hat{\mathbf{q}} = \mathbf{q}/|\mathbf{q}|$ , and  $\boldsymbol{\mu}_{ij}(\mathbf{X})$  is the hydrodynamic mobility matrix, for an instant many-particles configuration  $\mathbf{X}$ , relating the hydrodynamic force on a particle  $j$  to the velocity change of a particle  $i$  caused by the solvent-mediated HIs [211]. In the hypothetical case of hydrodynamically non-interacting particles, where  $k_B T \boldsymbol{\mu}_{ij} = \delta_{ij} D_0 \mathbf{E}$ , follows  $H(q) = 1$ , independent of  $q$  and volume fraction  $\phi$ .

### Self diffusion coefficient

The expression for  $H(q)$  in Eq. (3.18) can be split into self and distinct parts as

$$H(q) = \frac{1}{D_0} \langle \hat{\mathbf{q}} \cdot \mathbf{D}_{11}(\mathbf{X}) \cdot \hat{\mathbf{q}} \rangle + \frac{N-1}{D_0} \langle \hat{\mathbf{q}} \cdot \mathbf{D}_{12}(\mathbf{X}) \cdot \hat{\mathbf{q}} \exp[i\mathbf{q} \cdot \mathbf{r}_{12}] \rangle \quad (3.19)$$

$$= \frac{D_s}{D_0} + H^d(q), \quad (3.20)$$

where in place of the mobility tensor  $\boldsymbol{\mu}$ , the related diffusivity tensor  $\boldsymbol{D}$  has been used. The wavenumber-independent first part, invoking the average over the diagonal mobility matrix element  $\mu_{ii}$ , is equal to the translational short-time self-diffusion coefficient  $D_s$ , divided by  $D_0$ . Due to the increasing importance of the near-distance part of the HIs with increasing concentration,  $D_s$  becomes increasingly smaller than  $D_0$ . The wavenumber-dependent second part,  $H^d(q)$ , is a consequence of hydrodynamic cross correlations for which  $i \neq j$ , and vanishes for  $q \rightarrow \infty$ .

## Part II

# Protein aggregation



# Chapter 4

## Equilibrium clusters in SALR protein solutions

In this chapter, we present the simulation study of the short-time dynamics of SALR colloidal systems both in the monomer-dominated dispersed-fluid and the equilibrium-cluster phases. We employ the multiparticle collision dynamics (MPC) approach for the particle dynamics and asses by comparing with the predictions from the analytic BM-PA (Beenakker-Mazur-pairwise-additivity) scheme, which uses the static structure factor  $S(q)$  or likewise the associated radial distribution function  $g(r)$  as the only input [41, 212]. For analytical calculation of the radial distribution function and the associated static structure factor of the SALR system of spherical particles, the thermodynamically self-consistent Zerah-Hansen (ZH) integral equation scheme is used in the literature [213]. In addition, we explore the inter- and intra-cluster dynamics in the equilibrium-cluster phase, and determine the characteristic cluster lifetime also in comparison with analytic first-passage time calculations. If the particles forming a cluster can move individually, i.e., if the cluster is non-rigid, there is no hydrodynamic screening inside the cluster. Hence, the intra-cluster dynamics in the equilibrium-cluster phase of SALR systems is of special interest, and in particular the influence of the HIs.

### 4.1 Lennard-Jones-Yukawa colloid system

#### 4.1.1 Colloid model

We use a colloid model consisting of 60 point particles of mass  $M$  homogeneously distributed over the surface of a spherical shell of diameter  $\sigma$ , with an additional point particle at the center (see Ref. [199]). The number of points is chosen such that proper hydrodynamic behavior is achieved. The nearest neighbors, and each particle with the center, are linked via strong harmonic bonds to maintain a nearly rigid spherical shape (see Fig. 4.1). The harmonic bond potential is

$$U_{bond}(r) = \frac{K}{2}(r - r_0)^2 \quad (4.1)$$

where  $r = |\mathbf{r}|$  is the distance between the particular pair,  $r_0$  their preferred bond length, and  $\mathbf{r}$  the bond vector.

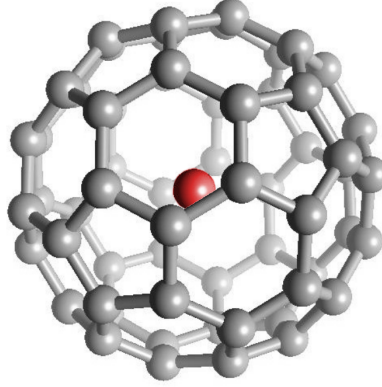


Figure 4.1: Spherical colloid composed of 60 discrete mass points. For illustration, the bonds of particle with its nearest neighbors are also displayed. The center point, which is bonded with all the other points (not shown), is depicted in red.

This discrete particle model provides a valuable alternative to a solid colloid with respect to hydrodynamic properties. In Ref. [199], it has been shown that such a discrete-point-particle model describes the hydrodynamic behavior of a solid, neutrally buoyant colloid quite well, via velocity correlation functions for translation and rotational motion, as well as the flow field during sedimentation.

### Colloidal interaction

To model the effective interaction between colloidal particles with SALR-type forces, generally the hard-core two-Yukawa and the modified Lennard-Jones Yukawa (LJY) pair potentials are considered [27, 29, 212, 214]. Dynamical simulations involving the two-Yukawa potential is rather demanding owing to its sharp hard-core excluded volume potential part. We use a Lennard-Jones-type (LJ) potential for the short-range attractive and repulsive part, consisting of a  $\mathcal{O}(x^{-100})$  steep steric repulsion combined with a short-range  $\mathcal{O}(x^{-50})$  attractive contribution. The long-range screened Coulomb repulsion part of the pair potential is accounted by a repulsive Yukawa potential. Hence, the LJY pair potential reads

$$\beta V(x) = 4\epsilon \left[ \left( \frac{1}{x} \right)^{100} - \left( \frac{1}{x} \right)^{50} \right] + \frac{A\xi}{x} \exp(-x/\xi), \quad (4.2)$$

where  $\sigma$  is the colloid diameter,  $x = r/\sigma$ , with  $r$  the colloid center-to-center distance. Here,  $\epsilon$  is the strength of short-range attraction/repulsion in units of  $k_B T$ , and  $A$  characterizes the strength of the long-range repulsion. The parameter  $A$  is related to the square of the effective electric charge of a colloidal particle [30, 215], and  $\xi$  is accordingly the Debye electrostatic screening length in units of  $\sigma$ .

The dynamics of a colloid particle is described by Newton's equation of motion, which we solve via the velocity Verlet algorithm with the forces from the potentials (4.1) and

(4.2) [216]. The colloids are embedded in a MPC fluid (see Sec. 2.3) incorporating the hydrodynamic interactions between the suspended colloids.

### 4.1.2 Parameters

The colloid diameter is chosen as  $\sigma = 6a$  and the mass  $M = 10m$  to ensure correct hydrodynamic behavior [199]. The time step for the integration of Newton's equations of motion is set to  $\Delta t_{MD} = 0.01\tau$ . A spring constant of  $K = 3000k_B T/a^2$  is chosen to maintain the spherical shape of a colloid.

The phase behavior of the LJY model system for fixed potential parameter values  $A = 2$ ,  $\xi = 1.794$ , and varying values of  $\epsilon$  has been intensely studied using MD simulations and the thermodynamic Gibbs-Duhem integration method [30]. Thereby, the selected reduced screening length  $\xi$  corresponds, for a typical colloidal diameter of  $\sigma \approx 100\text{nm}$ , to a 1:1 aqueous electrolyte solution at a concentration of about  $3\mu\text{M}$  [30]. The shape of the LJY potential for these parameters, and various attraction strength values  $\epsilon$  is shown in Fig. 4.2. The minimum of the LJY potential is located at  $x_{min} = 1.014$ , where  $\beta V(x_{min}) \approx 2 - \epsilon$  (see Fig. 4.2). The range of attraction-strength values used in this study is  $\epsilon = 2-8$ , corresponding to an effective attraction range of  $x_0 \approx 1.032$  for  $\epsilon = 3$ , and  $x_0 \approx 1.06$  for  $\epsilon = 8$ . Here,  $x_0$  is the first zero-crossing of the pair potential  $V(x)$  for  $x > 1$ .

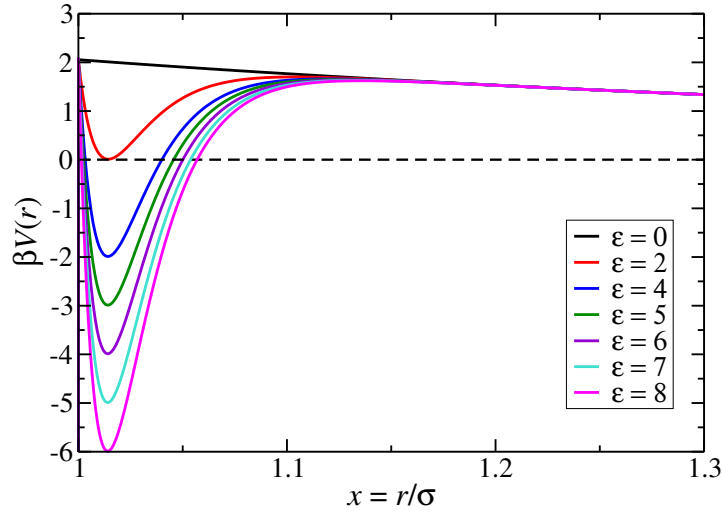


Figure 4.2: The generalized Lennard-Jones-Yukawa (LJY) potential of Eq. (4.2) for various values of the reduced attraction strength  $\epsilon$ , as indicated, and the fixed values  $A = 2$  and  $\xi = 1.794$  for the strength and range of the long-range Yukawa-repulsion part, respectively.

## 4.2 Results: phase behavior and microstructure

### 4.2.1 Structure factor

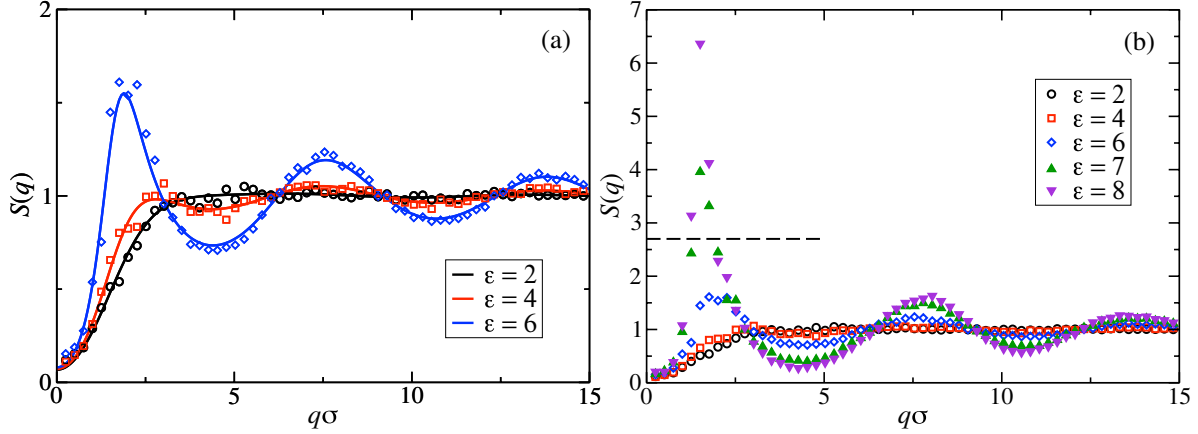


Figure 4.3: Static structure factor,  $S(q)$ , of LJY systems at reduced particle concentration  $\rho^* = \rho\sigma^3 = 0.1$ , for the indicated interaction strengths  $\epsilon$ . Simulation results are displayed by symbols and theoretical ZH integral equation predictions by solid lines. (a) MPC simulation and theoretical results of the dispersed-fluid phase for  $\epsilon = 2, 4, 6$ . (b) MPC simulation results for dispersed-fluid phase systems with  $\epsilon = 2, 4, 6$  (open symbols), and equilibrium-cluster phase systems with  $\epsilon = 7, 8$  (filled symbols). The horizontal dashed line in (b) marks the critical value  $S_{\text{crit}}(q_c) \approx 2.7$  for a first-order transition according to Godfrin *et al.* [29].

Figure 4.3 displays structure factors obtained from MPC simulations and also by the ZH calculations of LJY systems in the dispersed-fluid phase for  $\rho^* = \rho\sigma^3 = 0.1$  and various attraction parameters  $\epsilon$ . Here,  $\rho^*$  is the particle number density  $\rho = 6\phi/\pi$  in units of  $\sigma^3$ ;  $\phi$  denotes the packing fraction.

In accordance with previous findings [212,217], simulation and self-consistent ZH method results for  $S(q)$  are in excellent agreement. With increasing  $\epsilon$ , and correspondingly increasing depth of the potential well, a pronounced IRO peak of  $S(q)$  is found at a wavenumber  $q_c$  distinctly smaller than  $q_m$ , the wavenumber corresponding to the next-neighbor distance. This peak shifts to smaller  $q$  values with increasing  $\epsilon$ . In addition, Fig. 4.3(b) depicts simulation results for  $\epsilon = 7$  and 8. For these large attraction strengths, the ZH scheme does not converge any more. We emphasize that the occurrence of a low-wavenumber IRO-peak in the static structure factor  $S(q)$  at a wavenumber  $q$  smaller than the position  $q_m$  of the next-neighbor peak is a common feature of SALR systems not specific to a particular pair potential.

In Ref. [33], a relation is established between the characteristic wavenumber  $q_c$ , or likewise the average center-to-center distance of clusters defined as  $2\pi/q_c\sigma$  (in our notation), and clusters size and colloid density. Taking the mean particle number of clusters  $\bar{N}$ , and the



$\rho^*$	$\epsilon$	$2\pi/(q_c\sigma)$	$(\bar{N}/\rho^*)^{1/3}$
0.1	6	3.57	3.34
	7	4.17	4.11
	8	4.17	4.31
0.2	5	2.78	3.35
	6	3.33	4.17

Table 4.1: Characteristic lengths defined by the left- and right-hand sides of Eq. (4.3), respectively, for concentrations  $\rho^*$  and interaction strengths  $\epsilon$  as listed.

colloid particles concentration  $\rho^*$ , the equivalent relation for our systems is

$$\frac{2\pi}{q_c\sigma} = \left(\frac{\bar{N}}{\rho^*}\right)^{1/3}. \quad (4.3)$$

Table 4.1 lists values of the reduced lengths on the left and right-hand side of Eq. (4.3) for considered LJY systems. Evidently, we obtain very good agreement for the lower density, consistent with the conclusion in Ref. [33]. However, for the larger concentration  $\rho^* = 0.2$ , differences on the order of 20% – 30% are present.

### 4.2.2 Cluster formation criterion

Typical microstructural snapshots generated in the simulations are illustrated in Fig. 4.4. We identify two phases, a dispersed-fluid phase at small attraction strengths and an equilibrium-cluster phase at larger  $\epsilon$ . The emerging clusters in the latter case are clearly visible.

The IRO peak heights following from  $S(q)$  for  $\epsilon = 7$  and 8 (see Fig. 4.3(b)) clearly exceed the critical value of  $S_{\text{crit}}(q_c) \sim 2.7$  proposed in Ref. [29] as an empirical criterion signaling a first-order phase transition from the dispersed-fluid to the equilibrium-cluster phase, a transition observed in SALR systems at lower volume fractions.

It was found recently that the width of the IRO peak provides another criterion for localizing the transition from the dispersed-fluid to the equilibrium-cluster phase owing to its relation to an IRO thermal correlation length  $\xi_T$  [218]. Conceptually, for clustering systems the thermal correlation length estimates the persistence of dense structural correlation. Particle clustering emerges when  $\xi_T$  exceeds the length of interparticle repulsion  $\xi$ .  $\xi_T$  can be

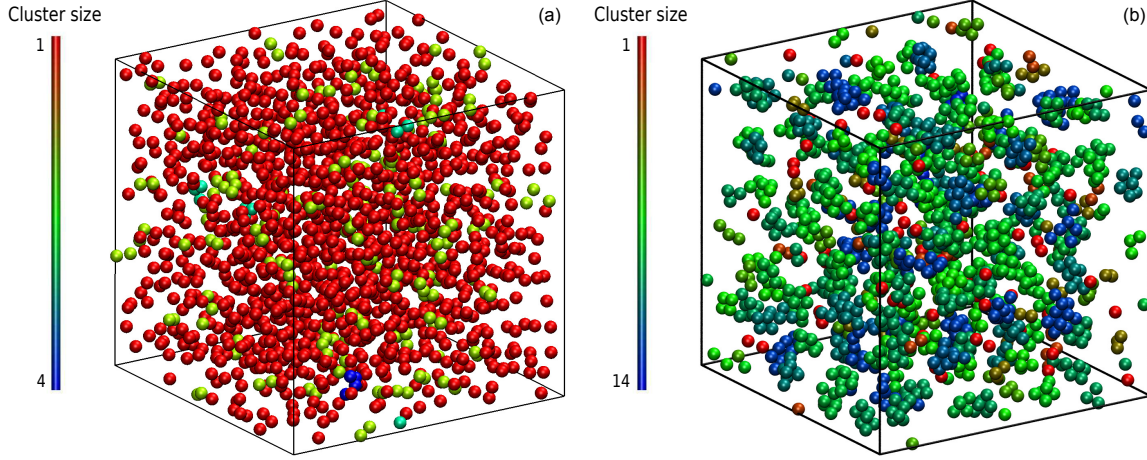


Figure 4.4: Simulation snapshots of the microstructure of a LJY system at concentration  $\rho^* = 0.1$ . (a) A dispersed-fluid phase structure is obtained for  $\epsilon = 2$ , and (b) an equilibrium-cluster phase structure for  $\epsilon = 7$ . The various colors indicate colloidal particles belonging to clusters of different sizes (see left vertical color bar).

estimated from the second-order inverse expansion of  $S(q)$  about the IRO peak  $q_c$  [218]

$$S(q) \approx \frac{S(q_c)}{1 + (q - q_c)^2 \sigma^2 \xi_T^2}. \quad (4.4)$$

In simulations,  $\xi_T$  is extracted from a quadratic Ornstein-Zernike fit of  $S(q_c)/S(q)$  of the form  $[1 + (q - q_c)^2 \sigma^2 \xi_T^2]$  about  $q_c$ . According to Ref. [33], the location of the phase transition is most robustly predicted by the combination of the two criteria for the height and width of the IRO peak.

### 4.2.3 Cluster size distribution

Further insight into the phase behavior of the system is gained from the cluster-size distribution function (CSD)  $N(s)$  defined as

$$N(s) = \left\langle \frac{s}{N_p} n(s) \right\rangle, \quad (4.5)$$

where  $N(s)$  is the average fraction of particles that are members of a cluster of size  $s$  [27]. Here,  $\langle \dots \rangle$  is the average over representative particle configurations and  $n(s)$  is the number of clusters of size  $s$  within a given configuration. Moreover,  $N_p$  denotes the total number of colloids in the simulation box, hence,  $\sum_{s=1}^{N_p} N(s) = 1$ . A cluster is defined by applying a distance criterion according to which the center-to-center distance  $|\mathbf{r}_{ij}|$  between colloids  $i$  and  $j$  obeys the condition  $|\mathbf{r}_{ij}| < r_{\text{cluster}}$ , with the cut-off distance  $r_{\text{cluster}}$ . We use  $r_{\text{cluster}} = x_{\text{max}} \sigma$ ,

where  $x_{\max} > 1$  is the location of the maximum of  $V(x)$  (see Fig. 4.2). We confirmed that a small change in the definition of the cutoff-distance, e.g., to  $r_{\text{cluster}} = x_0\sigma$  does not significantly change the shape of the CSD. Here,  $x_0$  is the first zero-crossing of  $V(x)$  for  $x > 1$ . From the shape of  $N(s)$ , four different phases have been identified in SALR systems constituting a generalized phase diagram, namely the dispersed-fluid, random-percolated, equilibrium-cluster, and percolated-cluster phases [29].

In our study, we focus on the microstructure and dynamics of the dispersed-fluid and equilibrium-cluster phases. In the dispersed-fluid phase,  $N(s)$  is monotonically decaying with increasing  $s$ , as shown in Fig. 4.5, which indicates a monomer-dominated dispersion, where only transient small clusters are formed, corresponding to a mean cluster size of  $\bar{N} = 1 - 3$ . In contrast, the distribution function in the equilibrium-cluster phase exhibits a second local maximum (peak) at a particular cluster size  $s^* > 2$ , in addition to the monomer peak at  $s = 1$ . The second local peak reflects equilibrium clusters with a preferred size around  $s^*$ , coexisting in thermodynamic equilibrium with the monomers.

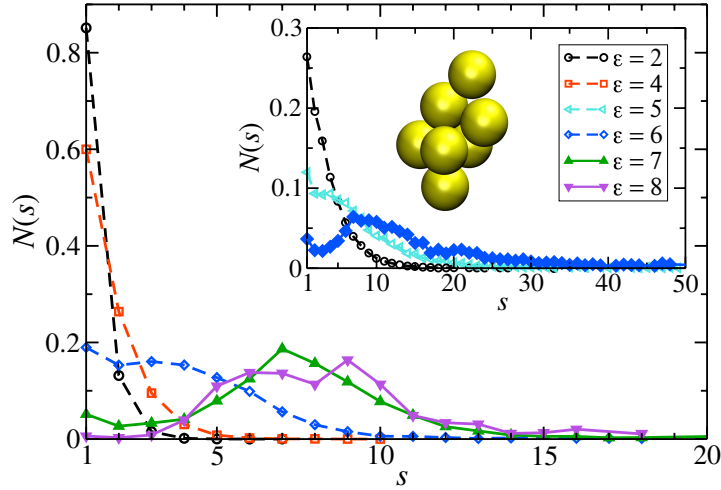


Figure 4.5: Distribution of cluster sizes,  $N(s)$ , obtained from simulation configurations as function of the cluster size  $s$ , for  $A = 2$ ,  $\xi = 1.794$ , and the indicated attraction strengths  $\epsilon$ . The concentration is  $\rho^* = 0.1$  and in the inset  $\rho^* = 0.2$ . For dispersed-fluid phase systems, open symbols connected by dashed lines are used, while equilibrium-cluster phase systems are marked by filled symbols connected by solid lines. Additionally, the inset shows a typical equilibrium cluster for  $\epsilon = 7$  and  $\rho^* = 0.1$ . Two dispersion particles are part of a cluster for distances  $r \leq r_{\text{cluster}} = x_{\max}\sigma$ , where  $x_{\max} > 1$  is the location of the first maximum of  $V(x)$  (see Fig. 4.2).

From the shapes of the CSD functions at  $\rho^* = 0.1$ , the systems with  $\epsilon = 2$  and 4 are identified as belonging to the dispersed-fluid phase, while the systems with  $\epsilon = 7$  and 8 are part of the equilibrium-cluster phase. This classification is in accordance with the  $\epsilon$ - $\rho^*$  LJY-phase diagram of Ref. [30] obtained for the same potential parameters ( $A = 2$  and  $\xi = 1.794$ ) (see Fig. 4.6), as well as the phase transition criterion  $S(q_c) \gtrsim 2.7$  [29]. Note that for  $\epsilon = 6$

and  $\rho^* = 0.1$ , a shallow peak at a  $s^* > 1$  appears, but the monomer peak at  $s = 1$  dominates. A close inspection of the simulation configurations suggest that the system for  $\epsilon = 6$  is still a member of the dispersed-fluid phase. This conclusion is supported by the schematic phase diagram of Ref. [30] (see also Fig. 4.6, where the system with  $\rho^* = 0.1$  and  $\epsilon = 6$  is inside the dispersed-fluid phase region).

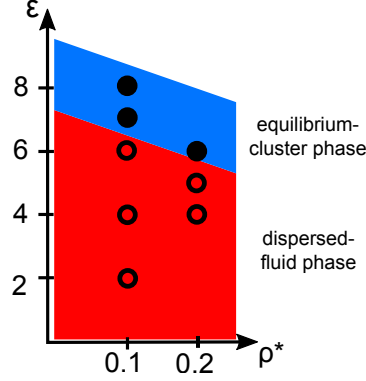


Figure 4.6: Schematic  $\rho^* - \epsilon$  phase diagram deduced from our MPC-generated cluster size distribution functions for the eight considered LJY systems. Open circles and filled circles label systems in the dispersed-fluid and equilibrium-cluster phases, respectively, according to the CSD shapes. The two uniformly colored areas mark the dispersed-fluid (red) and equilibrium-cluster (blue) phase regions of the LJY system as predicted in our simulation studies (see also Ref. [30]).

### 4.2.4 Pair correlation function

Pair correlation functions,  $g(r)$ , obtained from simulations and ZH calculations are compared in Fig. 4.7 for  $\rho^* = 0.1$ . For the dispersed-fluid phase systems, excellent agreement between analytical and simulation results is observed (see Fig. 4.7(a)). Note that the simulation results show two additional small peaks at  $x \approx 1.67$  and  $1.75$  for  $\epsilon = 6$ . This again reflects that the latter systems are close to the line separating the dispersed-fluid from the equilibrium-cluster phase. The pair correlation functions of the systems in the equilibrium-cluster phase exhibit sharp peaks at various distinct positions indicating strong local ordering (Fig. 4.7(b)). The positions of the peaks can be attributed to preferred geometric colloid configurations such as an in-line configuration of three particles (peak at  $x \approx 2$ ), an octahedral arrangement of four particles (peak at  $x \approx 1.66$ ), formation of two equilateral triangles with a common side (peak at  $x \approx 1.76$ ) [36], and cubic arrangement (peak at  $x \approx 1.43 \approx \sqrt{2}$ ).

Similarly, good agreement between ZH and MPC results for  $g(r)$  and  $S(q)$  is observed for the dispersed-fluid phase systems at the larger concentration  $\rho^* = 0.2$ , as displayed in Fig. 4.8. The system with  $\epsilon = 6$  belongs to the equilibrium-cluster phase. This follows from the respective  $N(s)$  shown in the inset of Fig. 4.5, and it is in accord with the phase diagram by Mani *et al.* [30]. The ZH results for  $S(q)$  and  $g(r)$  at  $\epsilon = 6$  are significantly different from the simulation data, in particular around the IRO peak position at  $q_c \lesssim 2.5$ . Interestingly,  $g(r)$

## 4.2 Results: phase behavior and microstructure

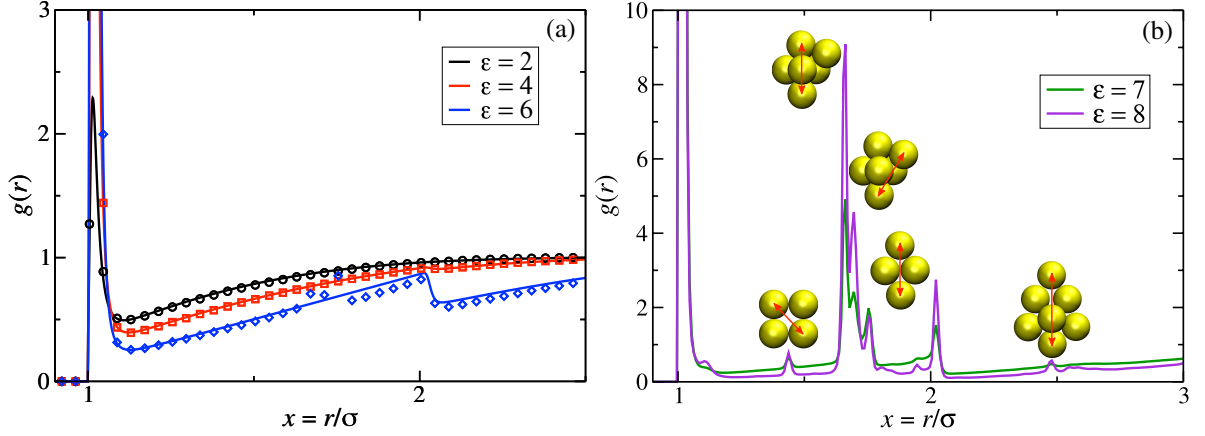


Figure 4.7: Radial distribution functions,  $g(r)$ , for the colloids of Fig. 4.3 with  $\rho^* = 0.1$  and indicated  $\epsilon$  values. (a) MPC (symbols) and ZH (solid lines) results for three systems in the dispersed-fluid phase. (b) MPC results for two systems in the equilibrium-cluster phase. The depicted cluster configurations and the arrows indicate the cluster structures associated with the respective peaks in  $g(r)$ .

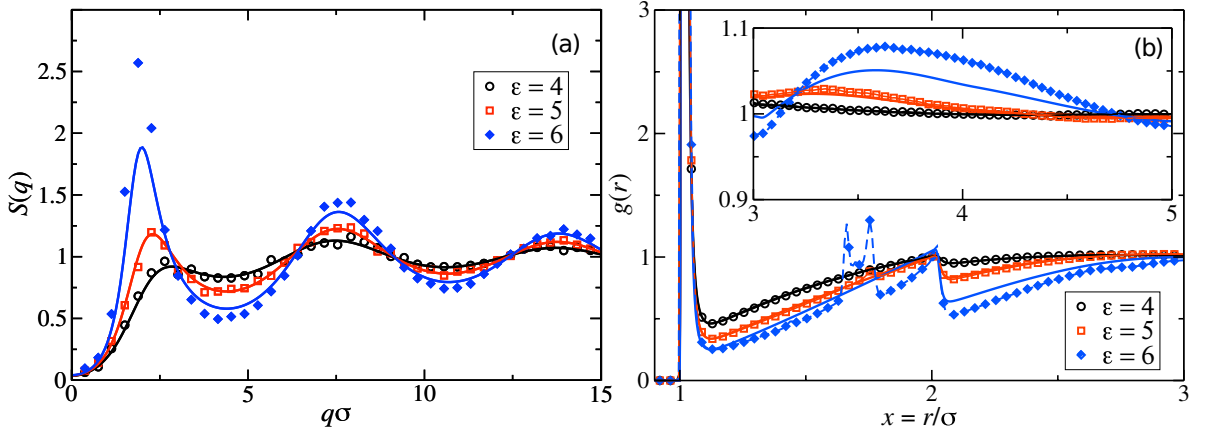


Figure 4.8: MPC simulation (symbols) and ZH (solid lines) results for (a)  $S(q)$  and (b)  $g(r)$  at  $\rho^* = 0.2$  for the indicated  $\epsilon$  values. Filled symbols: Simulation results for the equilibrium-cluster phase system ( $\epsilon = 6$ ). Open symbols: Dispersed-fluid phase systems ( $\epsilon = 4$  and  $5$ ). In (b), the blue line is a guide to the eye of the MPC distribution function. The inset shows  $g(r)$  for pair distances  $r = x\sigma$  related to the IRO structure factor peak position  $q_c\sigma$  for which  $x_c = 2\pi/q_c\sigma$ .

for the equilibrium-cluster phase system at  $\epsilon = 6$  has a broad peak for larger  $x$  that begins roughly at  $x_c = 2\pi/q_c$  and becomes more pronounced with increasing  $S(q_c)$  (see inset of Fig. 4.8b). However, as it was shown recently [34], such a broad peak in  $g(r)$  visible in the range  $3 < x_c < 5$  not necessarily implies an IRO peak in the corresponding  $S(q)$ .

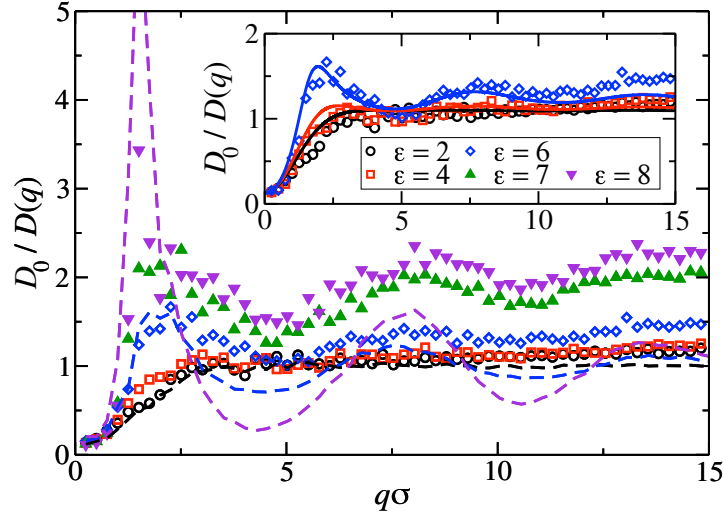


Figure 4.9: MPC results for the inverse of the short-time diffusion function,  $D(q)$ , expressed in units of the single-particle diffusion coefficient  $D_0$ , for LJY systems at  $\rho^* = 0.1$  and the indicated  $\epsilon$  values. Open (filled) symbols label systems in the dispersed-fluid (equilibrium-cluster) phase. The dashed lines are simulation results without HIs considered of  $D_0/D(q)|_{\text{no-HI}} = S(q)$ , for  $\epsilon \in \{2, 6, 8\}$ . Inset: Comparison of MPC (symbols) with BM-PA scheme results (solid lines), for systems in the dispersed-fluid phase. The BM-PA scheme uses the ZH  $S(q)$  and  $g(r)$  as input (see Figs. 4.3a and 4.7a).

## 4.3 Results: Dynamics

### 4.3.1 Short time dynamics

Figure 4.9 displays simulation results for the short-time diffusion function  $D(q)$  and includes the results from BM-PA theory too. In contrast to  $H(q)$ , which requires additional determination of  $S(q)$ ,  $D(q)$  is directly obtained experimentally in NSE or DLS measurements [41, 211]. In simulations,  $D(q)$  is obtained employing Eq. (3.16), i.e., the dynamic structure factor is determined and  $D(q)$  is extracted from the initial exponential decay of  $S(q, t)$ . Our results for  $D_0/D(q)$  reveal a well-defined IRO peak at the same wavenumber  $q_c$  as in  $S(q)$ . Moreover,  $D_0/D(q_c) = S(q_c)/H(q_c)$  increases strongly with increasing  $\epsilon$ . This reflects the similarity of  $S(q)$  and  $D_0/D(q)$  for  $q$ -values close to  $q_c$ . Analogous features are observed for the systems with  $\rho^* = 0.2$ , where the corresponding  $D(q)$ s are depicted in Fig. 4.10.

In the dispersed-fluid phase, simulation yields results for  $D(q)$  that are in excellent agreement with the corresponding BM-PA scheme results. Note that the system with  $\rho^* = 0.2$  and  $\epsilon = 6$  is in the equilibrium-cluster phase (see Figs. 4.5 and 4.8a), hence there is no quantitative agreement between simulation and BM-PA results for  $D(q)$ . The quantitative agreement with simulation results establishes the hybrid BM-PA scheme as an easy-to-apply, precise, and fast tool for assessing the short-time diffusion in SALR systems in the dispersed-

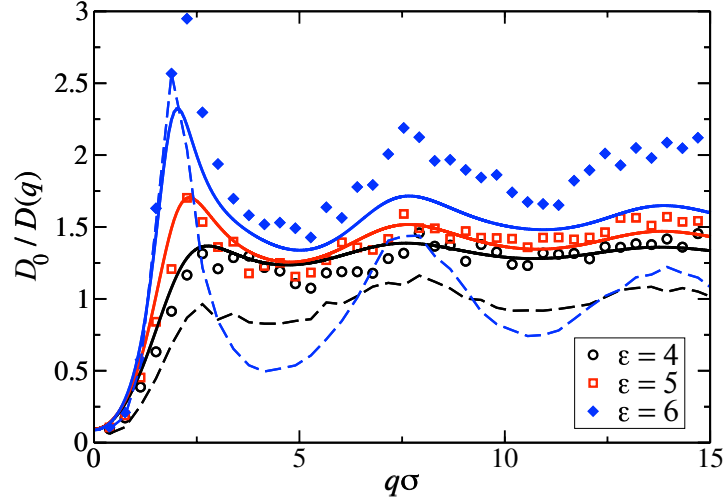


Figure 4.10: MPC simulation (symbols) and BM-PA-scheme results (solid lines) for the inverse diffusion function  $D_0/D(q)$  at  $\rho^* = 0.2$  and for three different  $\epsilon$  values. The dashed lines are the MPC generated structure factors  $S(q)$  for  $\epsilon = 4$  (black) and 6 (blue). The system with  $\epsilon = 6$  (filled diamonds) is in the equilibrium-cluster phase state.

fluid phase. This has been additionally verified recently by the comparison with NSE measurements of  $D(q)$  of lysozyme solutions [41]. The pronounced slow down of collective diffusion in SALR systems due to HIs is illustrated by the comparison of  $D_0/D(q)$  with  $D_0/D(q)|_{\text{no-HI}} = S(q)$ , the latter is obtained when HIs are ignored. According to Fig. 4.10, neglecting HIs results in a  $D_0/D(q)$  that strongly deviates from the actual one for which HIs are considered.

### 4.3.2 Cluster dynamics

An interesting dynamical quantity is the mean cluster lifetime, which, in our simulations, we determine via the cluster correlation function  $C(t)$ , defined as

$$C(t) = \frac{\langle \sum_i c_i(t) c_i(0) \rangle}{N_c(0)} \quad (4.6)$$

Here,  $c_i(t)$  is 1 if the cluster  $i$  remains intact after the lag time  $t$ , and zero otherwise. The normalizing factor  $N_c(0) = \langle \sum_i n_i(0) \rangle$  is the mean number of clusters available at time  $t = 0$  so that  $C(0) = 1$ . Therefore, the correlation function  $C(t)$  gives the fraction of clusters present at  $t = 0$  that remain intact after the lag time  $t$ . As defined earlier, a colloid belongs to a cluster as long as its distance to another colloid in the cluster is smaller than  $r_{\text{cluster}}$ . We fit the cluster correlation function by the stretched exponential function  $A \exp(-(t/\tau)^\beta)$ , with a stretching exponent  $\beta$  depending on the attraction strength  $\epsilon$ , and extract its characteristic decay time  $\tau$ . Using  $\tau$  and  $\beta$ , the average cluster lifetime  $\tau_c$  is determined as  $\tau_c = \tau/\beta\Gamma(1/\beta)$  [219].



For comparison, we estimate the cluster lifetime analytically in an approximate manner by considering only the dissociation of an isolated pair of particles. The associated dissociation or binary escape time,  $\tau_c^d$ , is the mean time required for a pair initially at the minimum distance  $x_{\min}$  to unbind by increasing its mutual distance to a value  $x_d > x_{\max}$  larger than the potential barrier position,  $x_{\max}$ . Theoretically, this characteristic time is obtained by applying the absorbing boundary condition  $f(x = x_d, t|x_{\min}) = 0$  for the conditional pair-probability density function  $f(x, t|x_{\min})$  of finding the pair at a distance  $x = r/\sigma$  at time  $t$ , given its distance was  $x_{\min}$  at time  $t = 0$ . Using the two-particle Smoluchowski equation,  $\tau_c^d$  is given by [220]

$$\tau_c^d = 4\tau_D \int_{x_{\min}}^{x_d} dx \frac{e^{\beta V(x)}}{x^2 G(x)} \int_{x_l}^x ds s^2 e^{-\beta V(s)}, \quad (4.7)$$

where  $x_l$ , with  $x_l < x_{\min}$ , is the range of the short-range, steeply repulsive part of the pair potential that prevents the particles from overlapping. Furthermore,  $G(r)$  is the longitudinal relative hydrodynamic mobility of two spherical particles at center-to-center distance  $r$ ,

$$G(r) = X_{11}(r) - X_{12}(r), \quad (4.8)$$

where  $X_{11}$  and  $X_{12}$  are the self and distinct longitudinal hydrodynamic two-sphere mobility coefficients, respectively, for stick hydrodynamic surface boundary conditions that are available for  $r > \sigma$  as power series in the inverse pair distance  $1/x$ , and as lubrication expressions for two spheres at near-contact distance [221, 222]. No noticeable differences in the results for  $\tau_c^d$  are found, if instead of the accurate two-sphere mobility series expression for  $G(r)$  by Jeffrey and Onishi [221–223], with near-contact lubrication included the simpler rational-fraction approximation for  $G(r)$  of Chan and Halle [220] is used. In calculating  $\tau_c^d$ , we use  $\sigma$  as the hydrodynamic no-slip sphere diameter.

Figure 4.11 shows the cluster lifetimes obtained from the simulations and the two-particle Smoluchowski theory. The dissociation time  $\tau_c^d$  is calculated from Eq. (4.7) using  $x_{\min}(\epsilon)$ ,  $x_b = x_{\max}(\epsilon)$ , and  $x_l = 1$  (see Fig. 4.2). We find  $\tau_c^d$  to be insensitive to the precise choice of  $x_l \leq 1$ , owing to the steep near-contact repulsion of the LJY potential in Eq. (4.2). The upper boundary value  $x_d = x_{\max}$  is consistent with the cluster cutoff  $r_{\text{cluster}}$  used in the simulation calculations of  $\tau_c$ .

The cluster lifetime  $\tau_c$  increases with increasing interaction strength  $\epsilon$  as expected. Quite interestingly, the simulation results in the dispersed-fluid regime, where  $\epsilon \leq 5$ , exhibit qualitatively the same  $\epsilon$  dependence as the binary dissociation time, quantitatively, however,  $\tau_c \approx \tau_c^d/5$  (see dashed black line). The simulation values for  $\tau_c$  increase more strongly than  $\tau_c^d$  in the equilibrium-cluster range of larger  $\epsilon$  values. Here, for a large potential barrier of height  $V_{\max} - V_{\min}$ , the simulation values for  $\tau_c$  are close to the binary escape time  $\tau_c^K$  derived from Kramer's theory for barrier crossing. The latter is given by

$$\tau_c^K = \frac{\sigma^2 (x_{\max} - x_{\min})^2}{D_0} \exp(\beta [V_{\max} - V_{\min}]). \quad (4.9)$$

The comparison of the simulation results for  $\tau_c$  with and without HIs included (with the latter not shown in the figure) reveals that HIs strongly enlarge  $\tau_c$  while the functional dependence on  $\epsilon$  is rather similar in both cases.



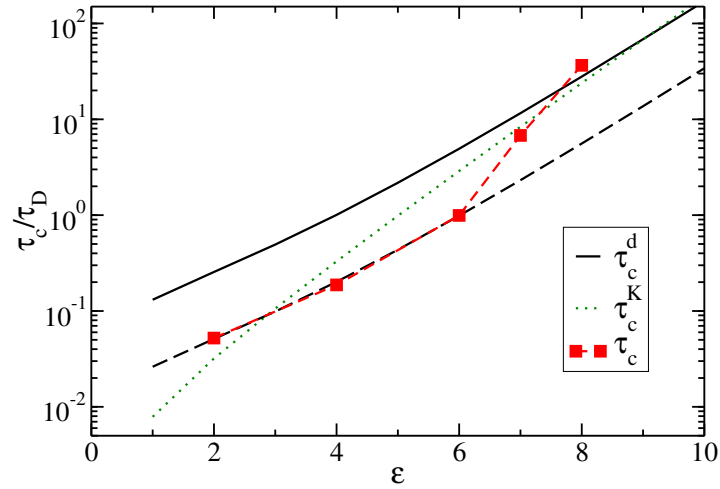


Figure 4.11: Cluster lifetime as a function of attraction strength  $\epsilon$  for dispersions with  $\rho^* = 0.1$ . The squares indicate MPC simulation results for  $\tau_c$ . The solid line is the pair dissociation time,  $\tau_c^d$ , according to Eq. (4.7). The dashed line represents  $\tau_c^d/5$ , and the dotted green line is the first passage time,  $\tau_c^K$ , according to Kramer's theory Eq. (4.9).

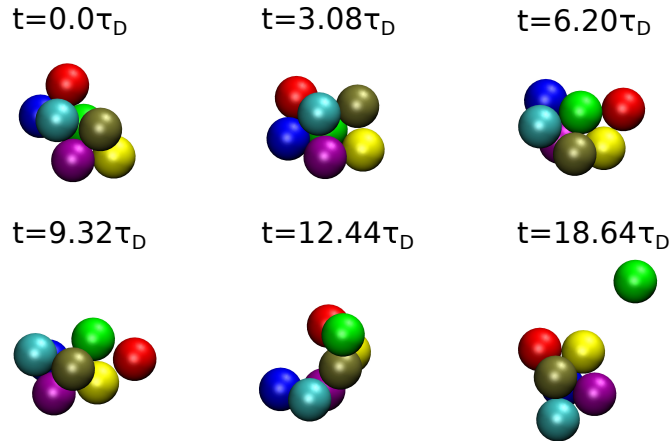


Figure 4.12: MPC generated time sequence of a cluster consisting of 7 particles for  $\epsilon = 7$  and  $\rho^* = 0.1$ , tracked until a particle (labeled in green) is dissociated.

The time evolution of a cluster of  $N_s = 7$  colloids is illustrated in Fig. 4.12. Evidently, the cluster undergoes substantial conformational changes during the considered time span of  $t \approx 19\tau_D$ . The particle labeled in green that finally detaches from the cluster is initially well bound to several of the cluster particles. As time progresses, it moves to a less stable place, where it is bound to only two particles before it dissociates from the cluster after the time  $t \approx 19\tau_D$ . The time sequence in Fig. 4.12 exemplifies the importance of HIs also for the intra-cluster dynamics, and that the dispersion dynamics as a whole cannot be adequately described by treating the dispersion as a polydisperse system of rigid Brownian-cluster objects.

## 4.4 Summary

For a representative SALR model dispersion of spherical particles interacting by the generalized Lennard-Jones-Yukawa (LJY) pair potential, static and short-time diffusion properties, and the phase behavior have been determined using multiparticle collision dynamics (MPC) simulations, where many-body HIs effects are fully accounted for, in comparison with the BM-PA scheme.

We have studied the pair structure, namely  $g(r)$  and  $S(q)$ , and the equilibrium phase behavior of LJY systems for varying values of the attraction strength (potential well depth)  $\epsilon$  and two particle concentrations  $\rho^*$ . Our phase-state mapping based on alternative criteria invoking the cluster-size distribution function and the IRO peak height and width of  $S(q)$ , is in accord with a previous study by Mani *et al.* [30] on the same model system. A phase transition from the dispersed-fluid to the equilibrium-cluster phase is observed with increasing attraction strength. In the dispersed-fluid phase, our simulation observations for  $S(q)$  and  $g(r)$  are in excellent agreement with the self-consistent ZH scheme results. Likewise for the dispersed-fluid phase we observe the good accuracy of the analytic BM-PA predictions regarding the short-time diffusion function,  $D(q)$ , by the comparison with corresponding simulation results.

Using elaborate simulations, we have studied the dynamics of LJY systems in the equilibrium-cluster phase, where for the first time the long-range HIs are fully accounted for. The simulations yield for this phase significantly smaller  $D(q)$  values as for dispersed-fluid systems. To explore the intra-cluster dynamics, we calculated the dissociation (first passage) time,  $\tau_c^d$ , for an isolated pair of LJY particles, and compared it with the simulation cluster lifetime  $\tau_c$ , for concentrated dispersions. This study was amended by the visualization of the shape changes of a cluster up to the event when a particle is leaving the cluster. The simulations revealed a highly mobile internal cluster dynamics, with pronounced conformational changes within a time span of a few  $\tau_D$  values. Thus, both, the intra-cluster dynamics and the dynamics of the dispersion as a whole are significantly influenced by many-particle HIs, which are not screened inside flexible clusters. As a consequence, the dynamics of an equilibrium-cluster dispersion cannot be described simply as a polydisperse dispersion of rigid Brownian-cluster objects.

# Chapter 5

## Anisotropic interaction dependent self-aggregation

In this chapter, we present a systematic investigation, through simulations, of the short-time diffusion coefficient of colloids with anisotropic interactions in an attempt to understand experimental observations [58], via NSE, of two small globular lens proteins known to possess either hard sphere-like repulsion ( $\alpha$ -crystallin) [224] or weak short-range attractions ( $\gamma_B$ -crystallin) [8, 160, 225]. The hard sphere-like protein  $\alpha$ -crystallin is a quite polydisperse multi-subunit protein with an average molecular weight of about  $8 \times 10^5 \text{Da}$ , an average hydrodynamic radius of about  $R_h = 9.6 \text{nm}$ , and a polydispersity of about 20% [224]. It has been shown to behave like ideal hard spheres all the way up to the glass transition occurring at a volume fraction of  $\phi = 0.58$ .  $\gamma_B$ -crystallin on the other hand is a monodisperse monomeric protein with a molecular weight of around  $2.1 \times 10^4 \text{Da}$ , and a hydrodynamic radius of  $R_h = 2.3 \text{nm}$  [160]. Its solution structure (see Fig. 5.1) and phase diagram is well reproduced by a coarse-grained potential combining a hard core repulsion and a weak short-range attraction, and assuming either a spherical or weakly elliptical shape [8, 160].

### 5.1 Attractive colloidal system

#### 5.1.1 Colloid model

We study spherical colloids as a coarse-grained model for  $\gamma_B$ -crystallin. The choice of a spherical model for  $\gamma_B$ -crystallin, despite the fact that its real shape is better described by an ellipsoid with an axial ratio of about 1.8 to 2 (see Fig. 5.1), is motivated by earlier studies in Refs. [21] and [226]. They investigated the effect of moderate geometrical anisotropy based on the known molecular shapes of globular proteins comparable to  $\gamma_B$ -crystallin, and concluded that effective sphere models together with the corresponding interaction potentials are indeed reasonable approximations for analysing diffusion in crowded solutions. We use the colloid model consisting of point particles distributed over the surface of a spherical shell (see Sec. 4.1.1).

Two separate models are considered for the colloid-colloid interactions in an attempt to achieve the proper trend in the short time dynamics. In the first model, we use a centrosym-

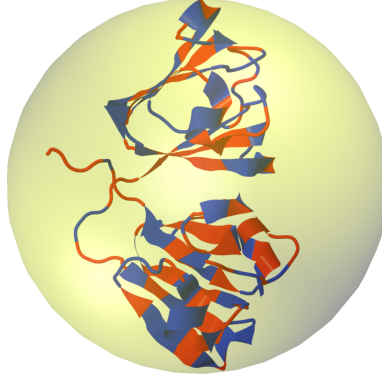


Figure 5.1:  $\gamma$ -crystallin structure with hydrophilic (blue) and hydrophobic (red) patches on the surface. The yellow sphere illustrates the coarse grained approximation of  $\gamma$ -crystallin as a spherical colloid.

metric weakly attractive short-range effective pair potential with strong repulsion,

$$U_c(r) = -\epsilon \left( \frac{\sigma}{r} \right) e^{-b\left(\frac{r}{\sigma}-1\right)} + \epsilon_r \left( \frac{\sigma}{r} \right)^{96}, \quad (5.1)$$

where  $r$  is the center-to-center distance between particles. The first term describes a short-range Yukawa attraction, where  $\epsilon$  is the interaction strength, and  $b$  is a screening parameter characterizing the interaction range, such that a larger  $b$  leads to smaller range of the attractive interaction. The second term models the hard core repulsion due to excluded volume interactions. For the temperature, we set  $k_B T / \epsilon_r = 1$ .

In the second model, we explore the effect of anisotropic interactions, and take into account directional or patchy interactions. We did not attempt to extract specific orientation-dependent interaction potentials or parameters using the known protein structure of  $\gamma_B$ -crystallins, and to develop a coarse-grained, near-atomistic protein model. In practice, we consider bi-functional patchy colloids, where two attractive patches are diametrically arranged on the colloid surface. Along with a centrosymmetric interaction,  $U_c(r)$ , between the colloids, the additional patch-patch interaction is modeled with a short-range attractive pair potential  $U_p(r)$  expressed by Eq. (5.1) and the parameters  $\epsilon_p$ ,  $\sigma_p$  and  $b_p$ . The model and the corresponding potentials are illustrated in Fig. 5.2. To capture the characteristic features of directional patch-like interactions between proteins, the attraction between two patches is much stronger than the centrosymmetric potential,  $\epsilon_p / \epsilon = 3.8$ . The diameter ratio of colloid and patch particle is set to  $\sigma / \sigma_p = 6$ . The values of the full set of parameters are then fixed again such as to guarantee that the system is in the one-phase fluid regime.

The colloids are embedded in the MPC fluid to account for hydrodynamic interactions (see Sec. 2.3). In case of patchy colloids, owing to the relatively stronger patchy attraction, hydrodynamic effects are screened and random MPC is implemented as the surrounding environment due to computational efficiency (see Sec. 2.3.4).

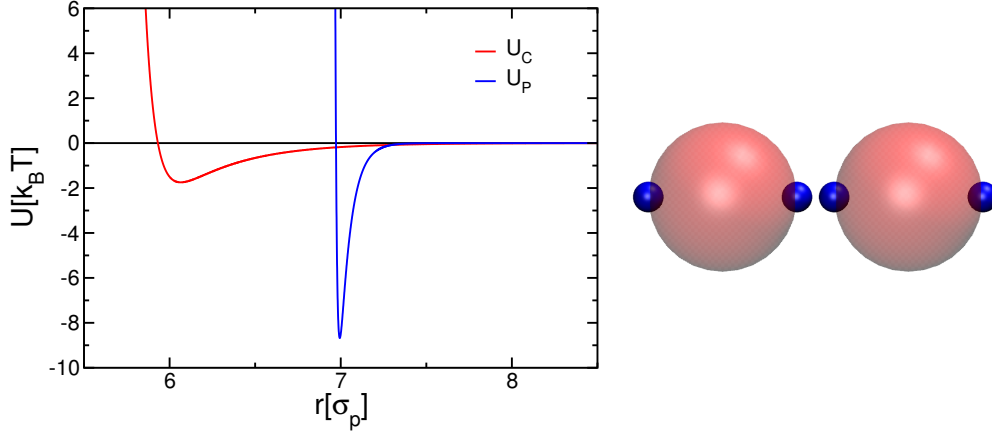


Figure 5.2: Illustration of the center-center interaction ( $U_c$ ) and the patch-patch interaction ( $U_p$ ) when two anisotropic patchy colloids, with diametrically opposite patchy interaction sites on the surface, are aligned as shown.

### 5.1.2 Second virial coefficient $B_2^*$

In order to relate the location of the simulated systems in the resulting phase diagram to the experimental conditions, we have chosen the rescaled second virial coefficient  $B_2^* = B_2/B_2^{HS}$ , where  $B_2$  is the second virial coefficient of the considered system and  $B_2^{HS}$  that of a pure hard sphere system [227]. Since patchy particles do not follow the extended law of corresponding states (ELCS), valid for centrosymmetric potentials, we compare the various systems for similar  $\Delta B_2^* = (B_2^* - B_{2,cr}^*)/|B_{2,cr}^*|$ , where  $B_{2,cr}^*$  is the value of  $B_2^*$  at the critical temperature. For a given range of  $b$  of the attractive potential,  $\epsilon$  was chosen such that  $\Delta B_2^*$  is between 0.1-0.2, comparable to the experiments. The actual values of  $B_2^*$  are listed in Table 5.1. As has been observed before in colloidal systems with patchy interactions [228], the values for  $B_{2,cr}^*$  are significantly smaller than those of isotropically interacting colloids. Our calculations of the  $B_{2,cr}^*$  values for the model with centrosymmetric and patch interactions show that the combined effect leads to a  $B_{2,cr}^*$  value, which is in-between those of pure centrosymmetric or patchy interactions (see Table 5.1). It is also important to note that experiments have shown that  $D_s(q^*)/D_0$  for  $\gamma_B$ -crystallin is almost completely independent of temperature for a range of  $298K \leq T \leq 308K$ , i.e., for a range of  $0.1 \leq \Delta B_2^* \leq 0.5$ , thus indicating that the exact choice of  $B_2^*$  is not critical as long as the sample is in the one phase region above the coexistence curve for liquid-liquid phase separation.

### 5.1.3 Phase diagram

For the centrosymmetric potentials, phase diagrams and critical temperatures were determined by Gibbs ensemble Monte Carlo (GEMC) simulations. For the patchy colloids, the Gibbs ensemble simulation results were inconclusive as to determine a full phase boundary. The relatively small patch sizes lead to a very slow relaxation of the system by reorientation of the particles. Moreover, the strong patch-patch attractions resulted in a very large scatter

$b$	$\epsilon/\epsilon_r$	$\epsilon_p/\epsilon_r$	$B_2^*$	$B_{2,cr}^*$	$\Delta B_2^* = (B_2^* - B_{2,cr}^*)/ B_{2,cr}^* $
9	2.8	0	-1.23	-1.38	0.11
15	3.45	0	-1.12	-1.29	0.13
30	3.95	0	-0.93	-1.20	0.23
15	2.5	9.5	-2.60	-2.87	0.09

Table 5.1: Values of the second virial coefficient  $B_2^*$ ,  $B_{2,cr}^*$ , and the relative distance to the critical point for the two different colloid models.

of the simulation data for various system sizes and densities (see Fig. 5.3). However, at the temperature relevant for the dynamical simulations, we have found no indication for phase separation in the GEMC simulation nor in additional NVT simulations at that temperature. In fact, the calculated isotherms were monotonously increasing with the density. Structure factors calculated for low densities ( $\phi < 0.05$ ) and extrapolated to zero wave vector nicely follow the prediction from the isothermal compressibility using the low density virial expression. These simulations yield the values for  $B_2^*$  presented in Table 5.1.

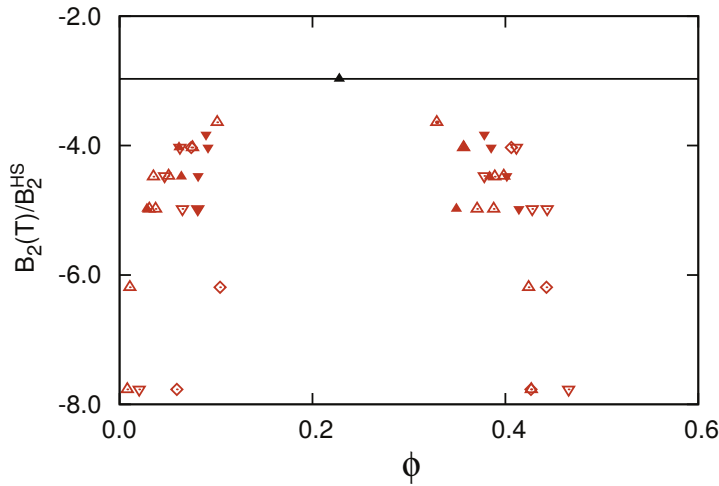


Figure 5.3: Phase diagram of colloids with anisotropic patchy interaction, where  $B_2/B_2^{HS}$  is considered as an effective temperature. The potential parameters are  $b = 15$ ,  $\epsilon/\epsilon_r = 2.5$ , and  $b_p = 15$ ,  $\epsilon_p/\epsilon_r = 9.5$  and  $\sigma/\sigma_p = 6$ . The various symbols correspond to systems of different sizes.

## 5.2 Results: short time diffusion

In experiments, quasielastic scattering (QES) techniques such as dynamic light scattering (DLS) or NSE provide a  $q$ -dependent effective diffusion coefficient  $D(q)$ , which is used to probe the dynamics of protein solutions. For dense particle systems, we expect to find dynamical regimes as sketched and described schematically in Fig. 5.4. On length scales much

larger than the nearest neighbour distance,  $d \gg \sigma$  (or  $q \ll 4\pi/\sigma$ ), QES measures collective diffusion. At distances corresponding to the nearest neighbour distance  $d \approx \sigma$ , however, QES probes relaxation of the dominant local structure determined by the nearest neighbour cage. The corresponding diffusion coefficient  $D(q_m)$ , where  $q_m \approx 2\pi/d$  is the position of the nearest neighbor peak in the static structure factor  $S(q)$ , then exhibits increasingly separated short- and long-time processes that are qualitatively described by local diffusion or “rattling” in the nearest neighbour cage, followed by cage opening and diffusion out of the cage.

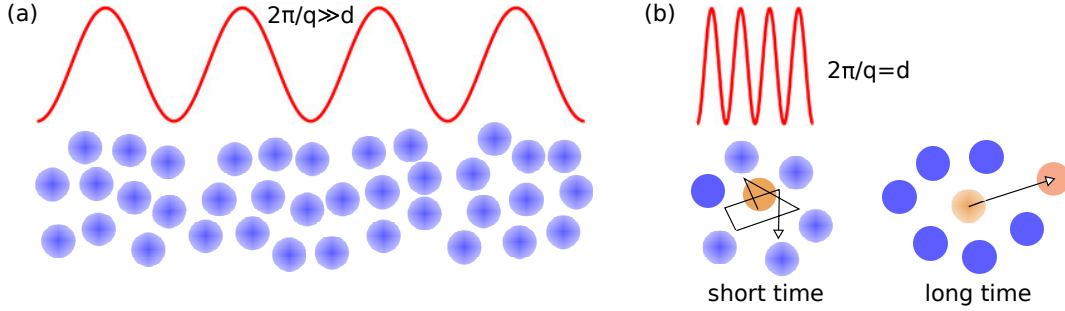


Figure 5.4: Schematic description of the link between the scattering vector  $q$  and the length scale of the density fluctuations. Shown are (a) the large-scale fluctuations probed at low  $q$  and (b) local dynamics probed at the nearest-neighbor length  $d$ , where for dense hard sphere systems, two well-separated mechanisms emerge.

In our simulations, the short time diffusion coefficient  $D(q_m)$  is obtained from the dynamic structure factor  $S(q_m, t)$ , following Eq. (3.16), for both centrosymmetric and patchy colloids (see Fig. 5.5). For the isotropic colloids, we extract short-time diffusion coefficients  $D(q_m)$  from an exponential-decay fit to the dynamic structure factors at a  $q$ -value  $q_m\sigma = 7.5$ , using only the short-time part of  $S(q_m, t)$  for the fit ( $t < 0.2\tau_D$ , where  $\tau_D = \sigma^2/4D_0$ ). In contrast, for patchy colloids, the short-time diffusion coefficient was determined by a stretched-exponential fit to the initial decay of the  $S(q_m, t)$  ( $t < 0.6\tau_D$ ). By fitting a similar stretched-exponential function to the dynamic structure factors of colloids with isotropic interactions only, we confirmed that the fit function is not altering the diffusion coefficient.

The markedly different concentration-dependent dynamical behavior on the nearest neighbor length scale of the two different colloid models, together with experimental observations for  $\alpha$ - and  $\gamma_B$ -crystallin, is reflected in the rescaled diffusion coefficient  $D(q_m)/D_0$ , as displayed in Fig. 5.6. Figure 5.6(a) demonstrates that the measured  $D(q_m)/D_0$  for  $\alpha$ -crystallin closely follows the theoretical prediction for hard spheres and indicates that colloid models quantitatively predict protein diffusion on these length scales over a broad concentration range. Knowing that the microstructure on length scales  $d \approx 2\pi/q_m$  does not change dramatically between hard sphere-like and weakly attractive particles, and following “common knowledge” that HIs should be dominant for short-time diffusion, it is then tempting to employ the hard sphere results also as a general guideline to estimate short-time diffusion on these length scales for other proteins, such as  $\gamma_B$ -crystallin [21]. Surprisingly, however, experiments suggest a drastically different dynamical behaviour. Figure 5.6a shows that

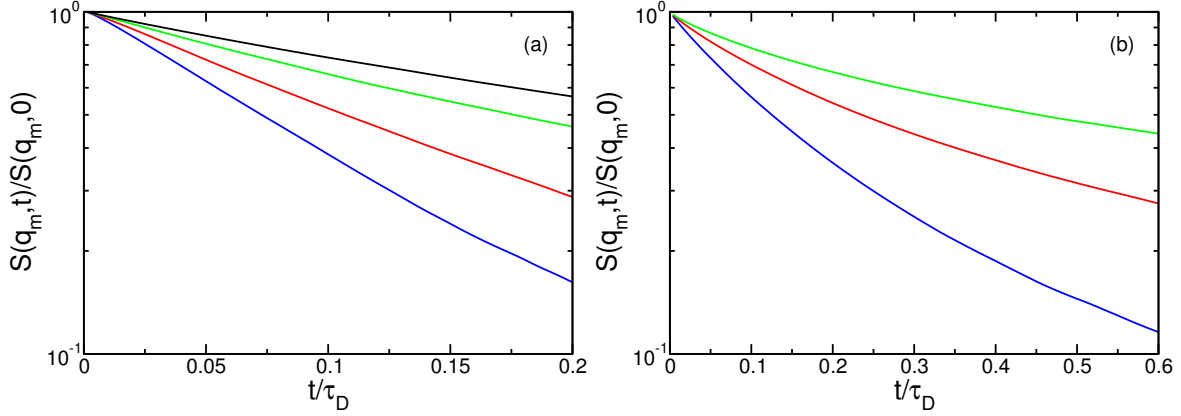


Figure 5.5: Dynamic structure factor  $S(q, t)$  as function of time  $t$  for (a) centrosymmetric colloids for the packing fraction  $\phi = 0.34, 0.26, 0.17, 0.1$  (top to bottom), and (b) patchy colloids for  $\phi = 0.3, 0.2, 0.1$  (top to bottom) with  $q = q_m$ .

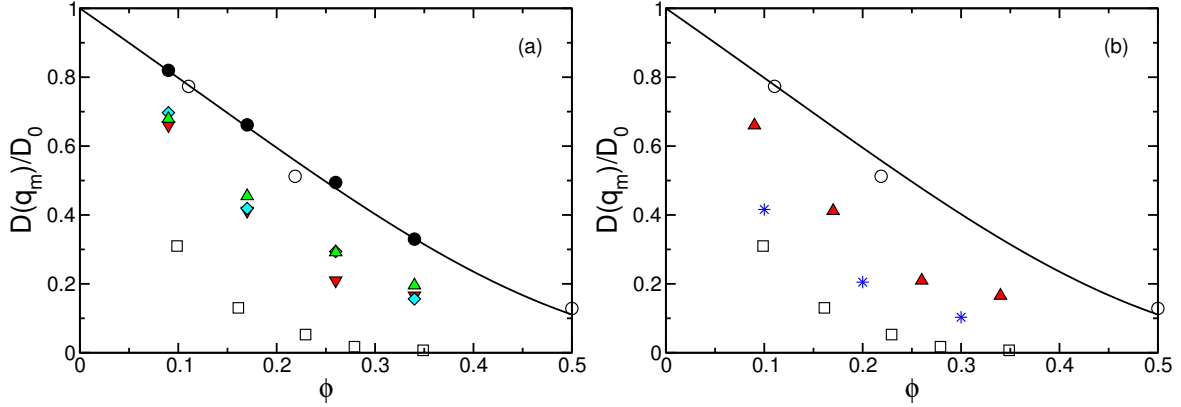


Figure 5.6: Concentration dependence of the rescaled short-time diffusion at the nearest-neighbor distance  $D(q_m)/D_0$ . Comparison between the experimentally determined values [ $\alpha$ -crystallin (open black circles) and  $\gamma_B$ -crystallin (open black squares)] and the simulation (filled black circles) and theoretical (black line) [210] results for hard spheres. Moreover, simulation results are shown in (a) for the centrosymmetric potential given by Eq. (5.1) with the parameters  $b = 30, \epsilon/\epsilon_r = 3.95$  (filled inverse red triangles),  $b = 15, \epsilon/\epsilon_r = 3.45$  (filled cyan diamonds), and  $b = 9, \epsilon/\epsilon_r = 2.8$  (filled green triangles), and in (b), the patchy particle model with  $b = 15, \epsilon/\epsilon_r = 2.5$ , and  $b_p = 15, \epsilon_p/\epsilon_r = 9.5$  and  $\sigma/\sigma_p = 6$  (blue stars). In addition, the results for the centrosymmetric potential of (a) (filled inverse red triangles) are displayed for comparison.

$D(q_m)/D_0$  for  $\gamma_B$ -crystallin dramatically slows down with increasing concentration, and decreases by almost three orders of magnitude already at a volume fraction of  $\phi = 0.35$ , which is far below close packing.

To shed light on the mechanisms responsible for the enormous slowing down of the  $\gamma_B$ -



crystallin dynamics, we perform simulations involving the two colloid models. In case of the centrosymmetric potential, we use several combinations of  $\epsilon$  and  $b$  in order to explore the effect of the range of the weak attraction on the resulting short-time diffusion coefficient. Figure 5.6a summarizes the results from these simulations for three pairs of parameters ( $b = 30$  and  $\epsilon/\epsilon_r = 3.95$ ,  $b = 15$  and  $\epsilon/\epsilon_r = 3.45$ , and  $b = 9$  and  $\epsilon/\epsilon_r = 2.8$ , respectively). In addition, results for pure hard sphere fluids are shown as a benchmark to demonstrate the quantitative agreement between simulations and available theoretical predictions [210] for such systems. Evidently, the attractive interactions result in a short-time dynamics that is significantly slower than that of hard spheres. However, the centrosymmetric attractive interactions are obviously not able to even qualitatively reproduce the experimentally observed difference between  $\alpha$ - and  $\gamma_B$ -crystallin. Moreover, a variation of the range and strength of the attraction (while maintaining a similar distance to the critical temperature, i.e., a similar  $\Delta B_2^*$ ) has only a minor effect on the resulting value of the short-time diffusion coefficient. Thus, it seems clear that a simple centrosymmetric short-range attraction consistent with the overall phase diagram is not able to account for the dramatic slowing down of the short-time diffusion observed experimentally for  $\gamma_B$ -crystallin. Here, it is worth mentioning that attempting to use a centrosymmetric potential compatible with the phase diagram of  $\gamma_B$ -crystallin indeed represents a considerable constraint on the choice of the potential, as for short-range attractive particles the critical concentration for liquid-liquid phase separation depends on the range of the attraction.

It has previously been suggested that interactions between  $\gamma_B$ -crystallins should not be described by a simple centrosymmetric pair potential, but a certain degree of patchiness should be included, similar to that found for other globular proteins [160, 229]. There are a number of structural features that can result in more directional or patchy attractions, such as a non-uniform charge distribution or hydrophobic patches on the protein surface (see Fig. 5.1). In order to elucidate the influence of such patchy interactions on the short-time diffusion of proteins, we apply the simple patchy-colloid model. Figure 5.6b shows that anisotropic patchy short-range attractions indeed lead to a much stronger slowing down of the protein short-time dynamics than in the purely centrosymmetric case. The diffusion coefficients from simulations are still larger than those extracted from experiment. Figure 5.6b nevertheless clearly demonstrates the importance of patchy attractions on short-time diffusion of proteins in crowded solutions.

### 5.3 Results: system configuration & bond lifetime

We obtain a qualitative understanding of the dramatic slowing down of the short-time diffusion in the case of attractive patches from a first qualitative inspection of the particle configurations found in the simulations. The snapshots of the colloid configurations shown in Figs. 5.7(a), 5.7(b) illustrate that both types of attraction lead to the formation of temporary protein clusters. They however strongly differ in their average size and structure. For particles with isotropic attractions, the typical density fluctuations lead to the formation of rather compact clusters, where the largest cluster comprises only a small fraction of the col-

loids. Moreover, the cluster lifetime is relatively short, which is in agreement with a simple estimate of the lifetime  $\tau_b$  of temporary bonds from the decay of the bond correlation function  $C_B(t)$  (see Fig. 5.7(c)).  $C_B(t)$  is equivalent to the cluster correlation function  $C(t)$  (see Eq. (4.6)) and is defined as [219]

$$C_B(t) = \left\langle \sum_{i<j} n_{ij}(t)n_{ij}(0) \right\rangle / N_B \quad (5.2)$$

where  $n_{ij}(t)$  takes into account if two particles are bonded and  $N_B$  is the total number of bonds at  $t = 0$ . This is comparable to an estimate of the escape time from an attractive potential well using Kramer's theory, namely  $\tau_b \approx (\Delta^2/D_0) \exp(-\epsilon/k_B T)$ , where  $\Delta$  is the width of the potential.

The addition of patchy attractions and the corresponding formation of much larger and open network-like structures, where frequently a majority of particles forms a single large cluster, yields long-lived temporary structures (see Figs. 5.7(b), 5.7(c)). The formation of large and slowly relaxing clusters due to non-specific attractive interactions in crowded protein solutions as a source of slowing down of long time diffusion has already been pointed out by Ando and Skolnick [21]. Here, we see that such interactions can also dramatically slow down local diffusion, and that this effect is strongly influenced by the existence of attractive patches.

## 5.4 Results: microstructure

A more quantitative analysis of these transient colloid structures provides additional insight on the origin of the slow-down in the dynamics of patchy colloids compared to centrosymmetric interactions.

### 5.4.1 Static structure factor

The effect of particle concentration on the structure of the colloids is evident by the behavior of the static structure factor. Figure 5.8 illustrates the structure factor for the centrosymmetric and the anisotropic patchy colloids at different volume fractions. The nearest neighbor peak at  $q\sigma \approx 7.2$  increases in height with increasing volume fraction as expected, which signifies the increasing number of neighbors at higher volume fraction. We observe that at low- $q$  regime,  $S(q)$  (at  $\phi = 0.1$ ) for the isotropic colloids tends toward a limited peak, while for colloids with patchy interactions it keeps on increasing with decreasing  $q$ , due to the presence of space spanning cluster in patchy colloid system compared to a compact cluster in isotropic ones.

### 5.4.2 Pair correlation function

Figure 5.9 displays pair correlation functions  $g(r)$  for both types of interactions at a volume fraction  $\phi = 0.1$ . The correlation function exhibits a clear nearest neighbour peak as

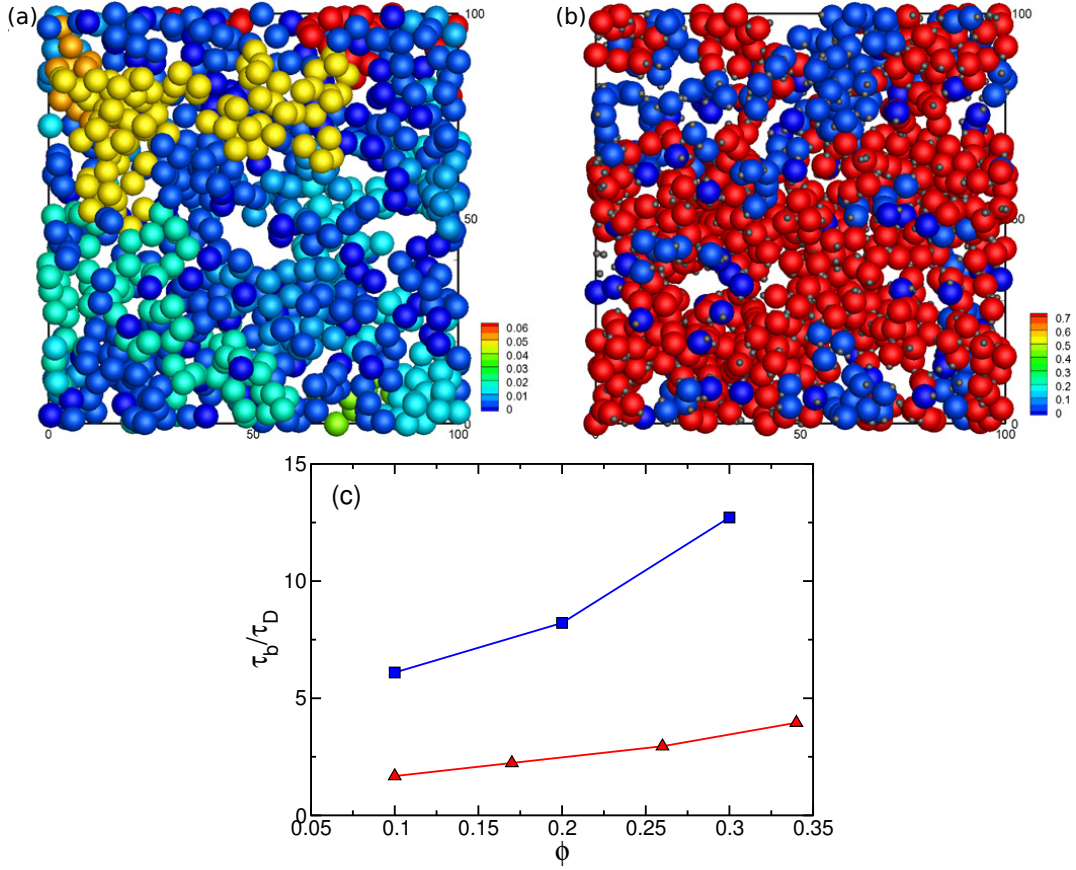


Figure 5.7: Formation of transient clusters due to weak short-range attractions. Snapshots showing the configurations of particles at  $\phi = 0.1$  for (a) centrosymmetric attraction, and (b) with two additional attractive patches. The color code corresponds to the size of the cluster,  $N_c/N$ , to which the particle belongs. Here,  $N_c$  is the number of particles in a cluster, and  $N$  is the total number of particles in the system. (c) Bond lifetime  $\tau_b$ , estimated using Eq. (5.2), as a function of volume fraction  $\phi$  for colloids with centrosymmetric attraction (red) and with additional attractive patches (blue).

well as a well-defined next nearest neighbour peak of  $g(r)$ , which indicates the formation of clusters. This peak is more pronounced for the patchy-colloid solution, and we also obtain a more pronounced depletion between the first and second neighbours in the patchy-colloid system. Both aspects point to distinct differences in the local structure, with significantly more prominent spatial correlations in the case of a patchy attraction.

### 5.4.3 Cluster analysis

The differences in the cluster structure are also reflected in the distribution of the number of nearest neighbours  $N_b$  of a particle, at least at low concentrations. The respective distribu-

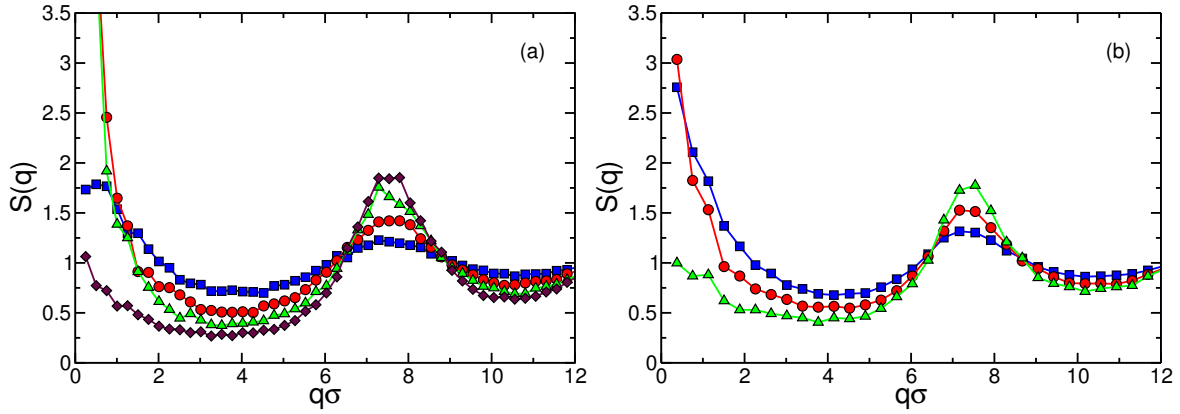


Figure 5.8: Structure factor for colloids with and without patchy interactions. (a) For colloids interacting solely by the centrosymmetric potential, at the volume fractions  $\phi = 0.1$  (blue),  $0.17$  (red),  $0.26$  (green), and  $0.34$  (brown), the potential parameters are  $b = 30$  and  $\epsilon/\epsilon_r = 3.95$ , and (b) for patchy colloids, at  $\phi = 0.1$  (blue),  $0.2$  (red), and  $0.3$  (green), the parameters are  $b = 15$ ,  $\epsilon/\epsilon_r = 2.5$ ,  $b_p = 15$ , and  $\epsilon_p/\epsilon_r = 9.5$ .

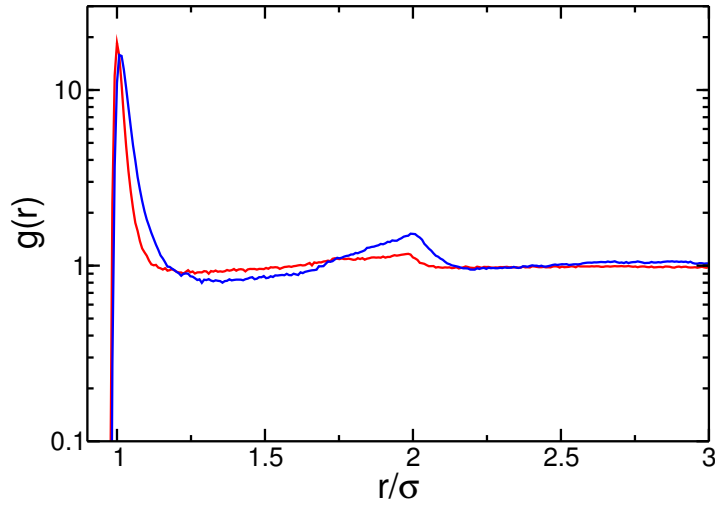


Figure 5.9: Structural correlations in colloids with and without patchy interactions; the pair correlation function of colloids with centrosymmetric (red) and additional patch interactions (blue) for  $\phi = 0.1$ . For the centrosymmetric potential, the parameters are  $b = 30$ ,  $\epsilon/\epsilon_r = 3.95$ , and for the patchy system  $b = 15$ ,  $\epsilon/\epsilon_r = 2.5$ ,  $b_p = 15$ ,  $\epsilon_p/\epsilon_r = 9.5$ , and  $\sigma/\sigma_p = 6$ .

tion functions are displayed in Figs. 5.10(a), 5.10(b). For both, the non-patchy and patchy colloids, the distribution functions at  $\phi = 0.1$  exhibit a peak at  $N_b = 2$ , i.e., aggregates of colloids with two neighbours dominate. However, the peak at  $N_b = 2$  for the patchy system is more pronounced and indicates the preferred formation of strings due to patch-patch interactions. This is further supported by the connectivity of patches (see Fig. 5.10(c)). With increasing volume fraction, the fraction of patches with one connection increases fast and

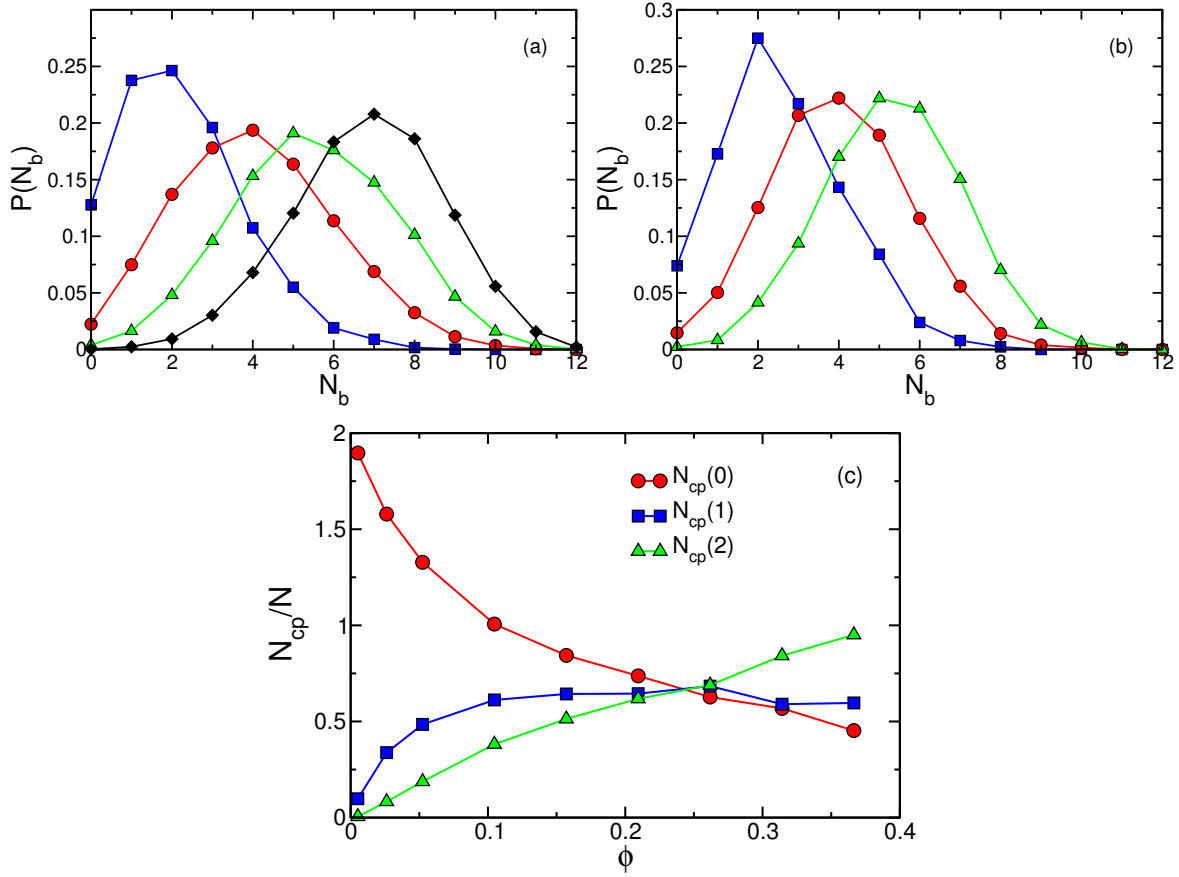


Figure 5.10: Distribution functions of the number of neighbors  $N_b$  of a colloidal particle. (a) Distribution functions for colloids interacting solely by the centrosymmetric potential at the volume fractions  $\phi = 0.1$  (blue),  $0.17$  (red),  $0.26$  (green), and  $0.34$  (black). The potential parameters are  $b = 30$  and  $\epsilon/\epsilon_r = 3.95$ . (b) Distribution functions for patchy colloids at  $\phi = 0.1$  (blue),  $0.2$  (red), and  $0.3$  (green). The potential parameters are  $b = 15$ ,  $\epsilon/\epsilon_r = 2.5$ ,  $b_p = 15$ , and  $\epsilon_p/\epsilon_r = 9.5$ . Two colloids are considered as neighbors when their separation is smaller than the radial distance at the first minimum of the pair correlation function. (c) Relative number of patches  $N_{cp}(n)$  in direct contact with each other as a function of the volume fraction, where  $n$  is the number of contacts. Zero corresponds to no patch contact, unity to one, etc. Two patches are in contact when their interaction energy is half the minimal energy of the patch-patch interaction potential.

saturates for  $\phi > 0.1$ . This corresponds to the formation of string-like structures and hence one-dimensional long-lived aggregates. In addition, the fraction of patches with two connections (three colloids) is significant and exceeds that of all other connectivities above  $\phi = 0.3$ . Such links allow for branching of string-like structures. No patch connections by more than three colloids are present, which is prevented by the packing of colloids for the chosen patch size. At higher volume fractions, the differences in the cluster structure are less pronounced.

Here, packing starts to dictate the local structure rather than specific interactions. The attraction between strings and parts of strings due to the additional isotropic potential enhances three-dimensional structure formation. Since the latter (isotropic) attraction is weaker than that for the non-patchy systems, the appearing structures are more open and network-like. These temporary system-spanning networks are the origin of the dramatic slowing down of the short-time dynamics on the length and time scales measured in the NSE experiment. They also provide a likely explanation for the unusually slow collective dynamics and the existence of an arrest line at relatively low volume fractions of  $\phi \approx 0.35$  for  $\gamma_B$ -crystallin solutions reported earlier [160].

## 5.5 Summary

Our study of colloid aggregation, applicable to protein solutions, show that the short-time diffusion of proteins over distances comparable to the average distance between nearest neighbors, crucial to many biological processes, is dramatically slowed down at concentrations comparable to those found in the cytoplasm of living cells, compared to dilute solutions. This becomes particularly pronounced when the proteins exhibit short-range attractions, a feature common to many globular proteins. Moreover, the presence of attractive patches on the protein surface can have a tremendous effect on  $D(q_m)/D_0$ , despite the fact that the overall strength of the effective pair potentials as characterized by  $B_2^*$  is comparable. Moreover, a detailed investigation of the microstructure reveals a space-spanning percolating network of the patchy colloids with a considerably higher bond-lifetime.

# Part III

## Active Brownian Particles





# Chapter 6

## Minimal model of active particles

Simplified and generic models of microswimmers assist in a thorough understanding of the relevant physical mechanisms, which comprises the propulsion mechanism of individual microswimmers, their collective behavior, and their properties in external fields and confinement [64, 65]. In this chapter, we discuss the well-known active Brownian particle (ABP) description of an active particle, namely a spherical colloid with given propulsion of fixed magnitude, which changes direction in a diffusive manner by a stochastic process [64–66, 88, 94, 97]. This model has been exploited to characterize the phase behavior of active systems [88, 92–94, 97]. We also present a somewhat simpler model with independent stochastic processes along the Cartesian coordinates of the active velocity, which corresponds to a Gaussian, but non-Markovian, colored-noise process for the activity [64, 66, 94, 230–233]. This model is referred in literature as active-Ornstein-Uhlenbeck particle (AOUP) [109]. The AOUP description has been applied in wide range of simulation and theoretical studies of confined and interacting active particles, such as motility-induced phase transitions [109, 116], alterations of the glass behavior [234], or the accumulation phenomena at walls [115], to name just a few.

### 6.1 ABP model

An ABP is a spherical colloidal particle of diameter  $\sigma$ , which is propelled with constant velocity  $v_0$  along its unit orientation vector  $e$  in  $d$  dimensions [62, 88, 93, 94, 97, 103, 231, 232]. Its translational motion is described by the Langevin equation

$$\dot{\mathbf{r}}(t) = \mathbf{v}(t) + \frac{1}{\gamma_T} (\mathbf{F}(t) + \mathbf{I}(t)), \quad (6.1)$$

with  $\mathbf{v}(t) = v_0 e(t)$ . Here,  $\mathbf{r}$  and  $\dot{\mathbf{r}}$  are the particle position and velocity, respectively,  $\mathbf{F} = -\nabla U$  is the force by the potential  $U$ , and  $\gamma_T$  is the translational friction coefficient. Thermal fluctuations are captured by the Gaussian and Markovian random force  $\mathbf{I}(t)$  with zero mean and the second moments

$$\langle I_\alpha(t) I_\beta(t') \rangle = 2\gamma_T k_B T \delta_{\alpha\beta} \delta(t - t'). \quad (6.2)$$

Strictly speaking, the stochastic process  $\mathbf{I}(t)$  does not have to be of thermal origin only, and  $k_B T$  not necessarily the thermal energy. It accounts for white-noise stochastic processes

affecting the translational motion of the ABP and may comprise active contributions. Independent of that we will refer to it as thermal motion in the following.

The orientation  $\mathbf{e}$  changes independently as

$$\dot{\mathbf{e}}(t) = \hat{\boldsymbol{\eta}}(t) \times \mathbf{e}(t), \quad (6.3)$$

where  $\hat{\boldsymbol{\eta}}$  is a Gaussian and Markovian stochastic process with zero mean and the second moment

$$\langle \hat{\boldsymbol{\eta}}(t) \cdot \hat{\boldsymbol{\eta}}(t') \rangle = 2(d-1)D_R\delta(t-t') \quad (6.4)$$

determined by the rotational diffusion coefficient  $D_R$ . Note that we assume  $\mathbf{e} \cdot \hat{\boldsymbol{\eta}} = 0$ , i.e., only the stochastic process component perpendicular to the orientation vector is contributing in its time evolution (see Eq. (6.3)). This constraint reduces the number of degrees of freedom and we have the prefactor  $(d-1)$  in Eq. (6.4) instead of  $d$ . In case of thermal noise only, the translational diffusion coefficient  $D_T = k_B T / \gamma_T$  and  $D_R$  of a colloid in dilute solution are related via  $\sigma^2 D_R / D_T = 3$  in 3d;  $\sigma$  is the diameter of the colloid [235]. In general,  $D_R$  can be larger than the thermal value due to activity-induced rotation.

### 6.1.1 Solving equations of motion

In simulations, the translational equations of motion (6.1) can be solved via the Ermak-McCammon algorithm as mentioned in Sec. 1.5.1 [171]. The equations of motion (6.3) for the orientation vector are solved as follows. By

$$\mathbf{e}'(t + \Delta t) = \mathbf{e}(t) + \mathbf{e}_\theta(t)\Delta\eta_\theta + \mathbf{e}_\phi(t)\Delta\eta_\phi \quad (6.5)$$

a unnormalized estimation of the vector  $\mathbf{e}$  is obtained, where  $\mathbf{e} = (\cos\phi \sin\theta, \sin\phi \sin\theta, \cos\theta)^T$  in spherical coordinates [103]. This follows from the random walk on a unit sphere [236]. The  $\mathbf{e}_\xi$  ( $\xi \in \{\phi, \theta\}$ ) are unit vectors, follow by differentiation  $\mathbf{e}_\xi \sim \partial\mathbf{e}/\partial\xi$  and normalization. The  $\Delta\eta_\xi$  are again Gaussian and Markovian stochastic processes with zero mean and the second moments

$$\langle \Delta\eta_\xi \Delta\eta_{\xi'} \rangle = 2D_R\delta_{\xi\xi'}\Delta t, \quad (6.6)$$

where  $\Delta t$  is the integration time step. Normalization of  $\mathbf{e}'(t + \Delta t)$  yields  $\mathbf{e}(t + \Delta t)$ , i.e.,  $\mathbf{e}(t + \Delta t) = \mathbf{e}'(t + \Delta t) / |\mathbf{e}'(t + \Delta t)|$  as the new orientation vector at time  $(t + \Delta t)$ .

We introduce the dimensionless quantities Péclet number  $Pe$  and the ratio  $\Delta$  between the translational and rotational diffusion coefficient to characterize the system, where

$$Pe = \frac{v_0\sigma}{D_T}, \quad \Delta = \frac{D_T}{\sigma^2 D_R}. \quad (6.7)$$

The Péclet number compares the importance of advective forces to thermal forces. At low  $Pe$ , thermal forces dominate and properties can be approximated by equilibrium properties.

Conversely, purely non-equilibrium phenomena become prominent at large  $Pe$ . An alternative Péclet number can be introduced via

$$\hat{P}e = Pe\Delta = \frac{v_0}{\sigma D_R}. \quad (6.8)$$

However, we prefer Eq. (6.7), since we want to resolve the effect of the two independent quantities  $v_0$  ( $\propto Pe$ ) and  $D_R$  ( $\propto \Delta^{-1}$ ) separately. Further, for simulation convenience, we rewrite the Eqs. (6.1) and (6.3) in terms of dimensionless quantities by considering  $\sigma$  and  $\sigma/v_0$  as the units of length and time, respectively.

## 6.2 Dynamics of ABPs

### 6.2.1 Autocorrelation of orientation vector

The orientation-vector equation of motion (6.3), can be rewritten for an infinitesimal time interval  $dt$  as

$$d\mathbf{e} = \mathbf{e}(t) \times d\hat{\boldsymbol{\eta}}(t) - (d-1)D_r \mathbf{e} dt \quad (6.9)$$

within the Ito calculus [103, 236].

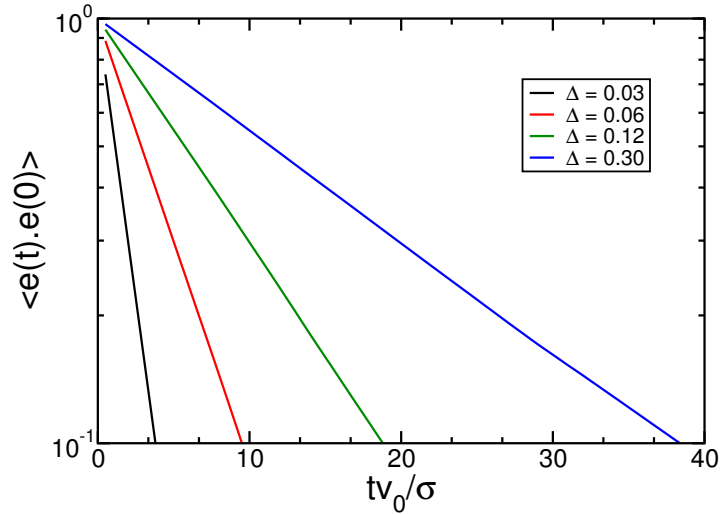


Figure 6.1: Auto-correlation functions of the orientation vector at different values of the rotational diffusion coefficient  $D_R$  (increases from top to bottom, with decreasing  $\Delta = 0.3, 0.06, 0.12, 0.3$ ;  $Pe = 100$ ).

Multiplying with  $\mathbf{e}(0)$  and averaging yields

$$\frac{d}{dt} \langle \mathbf{e}(t) \cdot \mathbf{e}(0) \rangle = -(d-1)D_r \langle \mathbf{e}(t) \cdot \mathbf{e}(0) \rangle, \quad (6.10)$$

where the average over the stochastic term vanishes as  $\mathbf{e}(t)$  is a nonanticipating function. Solving the equation gives the autocorrelation function [103, 236]

$$\langle \mathbf{e}(t) \cdot \mathbf{e}(0) \rangle = e^{-(d-1)D_R t}. \quad (6.11)$$

This implies that the orientation of self-propulsion of the ABPs relaxes due to rotational diffusion with the persistence time  $\tau_R = 1/[(d-1)D_R]$  (see Fig. 6.1).

### 6.2.2 Diffusion

The standard relation for the mean square displacement of an active Brownian particle in  $d$  dimensions can be derived employing the virial theorem [123]. For a force-free ( $\mathbf{F} = 0$ ) single particle multiplication of the equation of motion (6.1) by  $\mathbf{r}(t)$  leads to

$$\frac{1}{2} \frac{d}{dt} \langle \mathbf{r}(t)^2 \rangle = v_0 \langle \mathbf{e}(t) \cdot \mathbf{r}(t) \rangle + \frac{1}{\gamma} \langle \mathbf{\Gamma}(t) \cdot \mathbf{r}(t) \rangle, \quad (6.12)$$

where  $\langle \dots \rangle$  denotes the ensemble average. In the asymptotic limit  $t \rightarrow \infty$ , the average on the LHS represents the mean square displacement of the homogeneous and isotropic system. The averages on the RHS can be evaluated using the formal solution in the stationary state,

$$\mathbf{r}(t) = \mathbf{r}(-\infty) + \int_{-\infty}^t \left( v_0 \mathbf{e}(t') + \frac{1}{\gamma} \mathbf{\Gamma}(t') \right) dt' \quad (6.13)$$

of Eq. (6.1) and Eq. (6.11), which yields

$$\langle (\mathbf{r}(t) - \mathbf{r}(0))^2 \rangle = 2dD_T t + \frac{2v_0^2}{[(d-1)D_R]^2} [(d-1)D_R t + e^{-(d-1)D_R t}], \quad (6.14)$$

with the diffusion coefficient [103]

$$D = \frac{k_B T}{\gamma} + \frac{v_0^2}{d(d-1)D_R} \quad (6.15)$$

in the asymptotic limit  $t \rightarrow \infty$ , which increases with increasing  $v_0$  or activity (see Fig. 6.2).

## 6.3 Active Ornstein-Uhlenbeck Particle

The propulsion velocity  $v_0 \mathbf{e}$ , with the equation of motion (6.3), obeys the strict condition  $|\mathbf{e}(t)| = 1$ . For our analytical considerations, we lift this restriction and consider the frequently used equation

$$\dot{\mathbf{v}}(t) = -\gamma_R \mathbf{v}(t) + \boldsymbol{\eta}(t) \quad (6.16)$$

for the propulsion velocity [62, 64, 109, 231, 232, 237]; here, the Cartesian velocity components are independent. The damping factor  $\gamma_R$  is related to the rotational diffusion coefficient

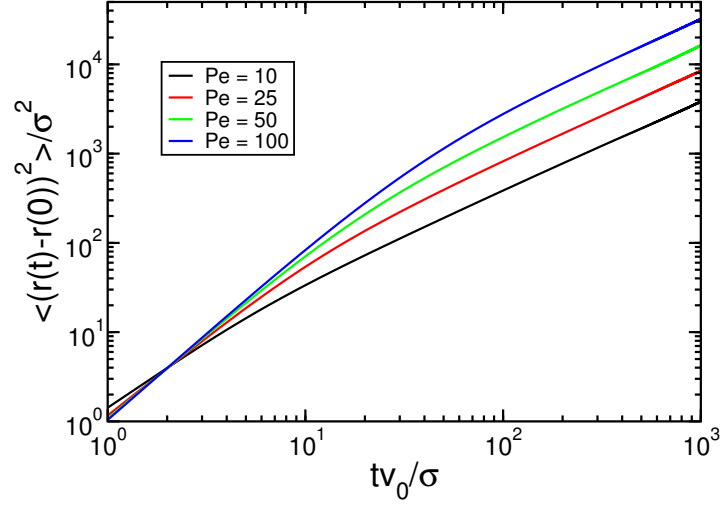


Figure 6.2: Mean square displacement (MSD) of an ABP at different activities ( $Pe = 10, 25, 50, 100$  (bottom to top);  $\Delta = 0.33$ ). As expected, the MSD shows a transition from ballistic motion to diffusion.

according to  $\gamma_R = (d - 1)D_R$ , and  $\boldsymbol{\eta}$  is a Gaussian and Markovian stochastic process with zero mean and the second moments

$$\langle \eta_\alpha(t) \eta_\beta(t') \rangle = \frac{2(d-1)}{d} v_0^2 D_R \delta_{\alpha\beta} \delta(t - t'), \quad (6.17)$$

where  $\alpha, \beta \in \{x, y, z\}$ . The Langevin equations (6.16) with noise amplitudes ( $v_0^2 D_R$ ), which are independent of the stochastic variables ( $\mathbf{v}$ ), describe a Ornstein-Uhlenbeck process (see Sec 1.4) [163]. Hence, we will refer to the active particle obeying Eqs. (6.1) and (6.16) as active-Ornstein-Uhlenbeck particle (AOUP) in the following, adopting the notation of Ref. [109].

The linear Eq. (6.16) is easily solved and yields the correlation function

$$\langle v_\alpha(t) v_\beta(t') \rangle = \frac{1}{d} \delta_{\alpha\beta} v_0^2 e^{-\gamma_R |t - t'|}. \quad (6.18)$$

Hence, for an homogenous and isotopic system, the stochastic processes, determined by Eqs. (6.4) and (6.16), yield the same correlation function for the propulsion velocity, namely  $\langle \mathbf{v}(t) \cdot \mathbf{v}(t') \rangle = v_0^2 e^{-\gamma_R |t - t'|}$  [64, 66, 88, 93, 94, 109, 231, 232].

With the Gaussian character of  $\boldsymbol{\eta}$  and the correlation function (6.18), Eq. (6.1) is the Langevin equation of a particle in the presence of white noise ( $\boldsymbol{\Gamma}$ ) and, in addition, non-Markovian colored noise. The non-Markovian character prohibits a general solution of the Langevin equation, and no closed Fokker-Planck equation can be derived in general [238]. Analytical solutions exist for a constant force and a harmonically bound particle (linear force), typically for one dimension [237–241]. For nonlinear forces approximations have to be applied.



# Chapter 7

## Confined ABPs

In this chapter, we discuss Brownian dynamics simulations and analytical calculations of active particles in three dimension, which are confined spatially by a radially symmetric potential and determine their distribution function. In the simulations, the active Brownian particle (ABP) is propelled with a prescribed velocity along a body-fixed direction, which is changing in a diffusive manner (see Sec. 6.1). For the analytical approach, we consider the active Ornstein-Uhlenbeck particle (AOUP) model, where the Cartesian components of the propulsion velocity are assumed to change independently (see Sec. 6.3).

We particularly consider ABPs and AOUPs confined in a harmonic potential [62, 79, 161, 237, 239, 240, 242, 243]. As for passive systems, harmonically bound active particles are an excellent model system to extract the generic features of confined nonequilibrium systems. Specifically, the equations of motion of AOUPs can be solved analytically, and thus provide valuable insight into the out-of-equilibrium dynamics of active systems. Correspondingly, several theoretical studies of AOUPs have been performed, predominantly in one dimension [237, 239–241]. As an extension, we provide the full solution of the dynamical equations in terms of position and velocity for arbitrary dimensions, taking into account thermal as well as self-propulsion contributions. The spatial distribution, obtained by integration of the general distribution function over velocity, of a AOUP is a Gaussian centered at the origin of the potential. However, the off-center accumulation observed for ABPs can be captured analytically by considering the spatial conditional probability distribution function of AOUPs at a given propulsion velocity. For anharmonic potentials, we apply the Unified Colored Noise Approximation (UCNA) to find an approximate stationary-state solution [238, 244]. The comparison between the simulation and analytical results reveals the quantitative suitability of the applied approximation schemes.

### 7.1 AOUP in harmonic potential

#### 7.1.1 Equations of Motion and Fokker-Planck equation

AOUPs in a radially symmetric harmonic potential

$$U_h(r) = \frac{1}{2}k\mathbf{r}^2 \quad (7.1)$$

leads to independent equations of motion for the Cartesian components of the position vector, i.e.,

$$\dot{\mathbf{r}}(t) = -\kappa \mathbf{r}(t) + \mathbf{v}(t) + \frac{1}{\gamma_T} \mathbf{F}(t), \quad (7.2)$$

with the abbreviation  $\kappa = k/\gamma_T$ . Equations (6.16) and (7.2), together with the correlation functions (6.2) and (6.17), describe an Ornstein-Uhlenbeck process and can be solved analytically [163].

Complementary, the AOUP dynamics is described by the distribution function  $\psi(\mathbf{r}, \mathbf{v}, t) = \prod_{\alpha} \psi_{\alpha}(r_{\alpha}, v_{\alpha}, t)$ , where  $\alpha \in \{x, y, z\}$  refers to the Cartesian coordinate directions, which obeys the Fokker-Planck equation (see Sec. 1.4.1) [163]

$$\frac{\partial}{\partial t} \psi = \kappa \frac{\partial}{\partial \mathbf{r}} (\mathbf{r} \psi) - \frac{\partial}{\partial \mathbf{r}} (\mathbf{v} \psi) + \gamma_R \frac{\partial}{\partial \mathbf{v}} (\mathbf{v} \psi) + \frac{k_B T}{\gamma_T} \frac{\partial^2}{\partial \mathbf{r}^2} \psi + \frac{\gamma_R v_0^2}{d} \frac{\partial^2}{\partial \mathbf{v}^2} \psi.$$

### 7.1.2 Solution of the Equations of Motion

Due to the Gaussian nature of the stochastic processes and the fact that a Gaussian is determined by its first and second moment, the full time-dependent solution of the Fokker-Planck equation can be obtained (Sec. 1.4.1) [163]. Explicitly, the conditional distribution function is given by

$$\psi_{\alpha}(r_{\alpha}, v_{\alpha}, t | r_{\alpha}^0, v_{\alpha}^0, 0) = \frac{1}{2\pi \sqrt{|\mathbf{\Lambda}(t)|}} \exp \left( -\frac{1}{2} \mathbf{x}_{\alpha}^T(t) \mathbf{\Lambda}(t)^{-1} \mathbf{x}_{\alpha}(t) \right). \quad (7.3)$$

with the abbreviation

$$\mathbf{x}_{\alpha}(t) = (r_{\alpha} - \langle r_{\alpha}(t) \rangle, v_{\alpha} - \langle v_{\alpha}(t) \rangle)^T \quad (7.4)$$

and the initial values  $\mathbf{r}^0$  and  $\mathbf{v}^0$  at the time  $t = 0$ . Note that we will use  $v_{\alpha}^0 = v_0/\sqrt{d}$  in the following. The symmetric matrix  $\mathbf{\Lambda}$  is the covariance matrix

$$\mathbf{\Lambda} = \begin{pmatrix} \Lambda_{rr} & \Lambda_{rv} \\ \Lambda_{rv} & \Lambda_{vv} \end{pmatrix} = \begin{pmatrix} \langle (r_{\alpha} - \langle r_{\alpha} \rangle)^2 \rangle & \langle (r_{\alpha} - \langle r_{\alpha} \rangle)(v_{\alpha} - \langle v_{\alpha} \rangle) \rangle \\ \langle (r_{\alpha} - \langle r_{\alpha} \rangle)(v_{\alpha} - \langle v_{\alpha} \rangle) \rangle & \langle (v_{\alpha} - \langle v_{\alpha} \rangle)^2 \rangle \end{pmatrix}, \quad (7.5)$$

$\mathbf{\Lambda}^{-1}$  its inverse, and  $|\mathbf{\Lambda}|$  the determinant. The appearing moments conveniently follow from the Langevin equations (7.2) and (6.16). From the solution of the linear equations (see



Eqs. (1.30) and (1.31)), we find

$$\langle v_\alpha(t) \rangle = \frac{v_0}{\sqrt{d}} e^{-\gamma_R t}, \quad (7.6)$$

$$\langle r_\alpha(t) \rangle = r_\alpha^0 e^{-\kappa t} + \frac{v_0}{\sqrt{d}(\gamma_R - \kappa)} (e^{-\kappa t} - e^{-\gamma_R t}), \quad (7.7)$$

$$\Lambda_{rr}(t) = \frac{k_B T}{k} (1 - e^{-2\kappa t}) + \frac{v_0^2}{d\kappa(\gamma_R + \kappa)} \quad (7.8)$$

$$+ \frac{v_0^2}{d(\kappa - \gamma_R)^2} \left( \frac{4\gamma_R}{\gamma_R + \kappa} e^{-(\kappa + \gamma_R)t} - e^{-2\gamma_R t} - \frac{\gamma_R}{\kappa} e^{-2\kappa t} \right),$$

$$\Lambda_{rv}(t) = \frac{v_0^2}{d(\gamma_R + \kappa)} (1 - e^{-(\gamma_R + \kappa)t}) - \frac{v_0^2}{d(\gamma_R - \kappa)} (e^{-(\gamma_R + \kappa)t} - e^{-2\gamma_R t}),$$

$$\Lambda_{vv}(t) = \frac{v_0^2}{d} (1 - e^{-2\gamma_R t}). \quad (7.9)$$

Since the dynamics of the velocity  $\mathbf{v}$  is independent of the position of the particle, the relaxation behavior of Eqs. (7.6) and (7.9) is naturally determined by  $\gamma_R$  only. Two independent relaxation mechanisms are present for the moments involving positions. For  $\kappa/\gamma_R \gg 1$ , the long-time behavior is dictated by the relaxation time  $1/\gamma_R$  of the propulsion velocity. In the opposite limit  $\kappa/\gamma_R \ll 1$ , the relaxation behavior of  $\Lambda_{rv}$  is still governed by  $\gamma_R$ . Only for  $\langle r_\alpha \rangle$  and  $\Lambda_{rr}$  relaxation due to confinement is important, whereby  $\Lambda_{rr}$  changes with time as

$$\Lambda_{rr}(t) = \left( \frac{k_B T}{k} + \frac{v_0^2 \gamma_T}{dk\gamma_R} \right) (1 - e^{-2\kappa t}), \quad \gamma_R t \gg 1, \quad (7.10)$$

similar to an overdamped Brownian particle [163], but with an activity-dependent amplitude. Two relaxation processes have already been found in Ref. [239] for the particle's positional autocorrelation function.

In the stationary state, the distribution function turns into

$$\psi(\mathbf{r}, \mathbf{v}) = \left( 2\pi \sqrt{|\mathbf{\Lambda}|} \right)^{-d} \exp \left( -\frac{1}{2} (\Lambda_{rr}^{-1} \mathbf{r}^2 + 2\Lambda_{rv}^{-1} \mathbf{r} \cdot \mathbf{v} + \Lambda_{vv}^{-1} \mathbf{v}^2) \right), \quad (7.11)$$

with

$$\Lambda_{rr}^{-1} = \frac{dk(\kappa + \gamma_R)^2}{dk_B T(\kappa + \gamma_R)^2 + \gamma_R \gamma_T v_0^2}, \quad (7.12)$$

$$\Lambda_{rv}^{-1} = -\frac{dk(\kappa + \gamma_R)}{dk_B T(\kappa + \gamma_R)^2 + \gamma_R \gamma_T v_0^2}, \quad (7.13)$$

$$\Lambda_{vv}^{-1} = \frac{d(\kappa + \gamma_R)(dk_B T(\kappa + \gamma_R) + \gamma_T v_0^2)}{v_0^2 [dk_B T(\kappa + \gamma_R)^2 + \gamma_R \gamma_T v_0^2]}, \quad (7.14)$$

$$|\mathbf{\Lambda}| = \frac{k_B T v_0^2}{dk} + \frac{\gamma_R v_0^4}{d^2 \kappa (\kappa + \gamma_R)^2}. \quad (7.15)$$

The distribution function (7.11) reduces to the expression derived in Refs. [239, 240] for  $d = 1$ . It is important to note that Eq. (7.11) is different from the stationary-state distribution function of a passive Brownian particle [62, 163] even in the limit  $v_0 \rightarrow 0$ , where the latter yields independent distributions for the potential and the kinetic energy (Boltzmann distribution), since the term  $\Lambda_{rv}^{-1} = k/k_B T(\gamma_R + \kappa)$  does not vanish. The result as such is not surprising, because of the differences in the underlying models. For AOUPs and ABPs, the overdamped dynamics of the particle position is considered and the velocity (orientation) is introduced as an independent degree of freedom. As a consequence, the forces on the AOUP/ABP determine its velocity. In contrast, in case of passive Brownian particles, the forces rule the acceleration.

In general, the coupling of position and velocity prevents the definition of a suitable effective temperature based on the stationary-state distribution function, aside from inconsistencies with dynamical quantities [239]. However, an effective temperature  $T_e$  can be introduced in the limit  $\gamma_R/\kappa \gg 1$  by defining  $\Lambda_{rr}^{-1} = k/k_B T_e$ , which yields

$$k_B T_e = k_B T + \frac{\gamma_T v_0^2}{\gamma_R d}, \quad (7.16)$$

as in Ref. [239]. Aside from  $k_B T$  and the dimension  $d$ ,  $T_e$  agrees with the definition in Ref. [239]. The other  $\Lambda$ s in Eq. (7.11) reduce then to  $\Lambda_{vv}^{-1} = d/v_0^2$  and  $\Lambda_{rv}^{-1} = k/\gamma_R k_B T_e$ . In the limit  $\gamma_R \rightarrow \infty$ ,  $\Lambda_{rv}^{-1}$  vanishes and independent distribution functions are obtained for  $r$  and  $v$ , identical with those of a passive Brownian particle. This is not surprising, since in this limit the stochastic process (6.18) turns into a Markovian process with a finite amplitude. Hence,  $\mathbf{v}$  can be neglected in Eqs. (6.1) and (7.2), which leads to a decoupling of the equations of motion for the position and velocity. However, as already pointed out in Ref. [239], the interesting case for active particles is the limit of strong propulsion  $\gamma_R/\kappa \ll 1$ .

We like to mention that the stationary-state second moments following from Eqs. (7.8) – (7.9) for AOUPs are identical with those of ABPs, since they involve only up to second moments of the velocity  $\mathbf{v}$  (respectively  $\mathbf{e}$ ), i.e., the correlation functions (6.11) and (6.18). However, it has to be kept in mind that the distribution function for an ABP is non-Gaussian in general. An alternative derivation of the second moment for the particle position has been presented in Ref. [241].

Integration of Eq. (7.11) over the positional coordinates yields the velocity distribution function

$$\psi(\mathbf{v}, t | \mathbf{v}^0, 0) = \left[ \frac{2\pi v_0^2}{d} (1 - e^{-2\gamma_R t}) \right]^{-d/2} \exp \left( -\frac{d(\mathbf{v} - \langle \mathbf{v} \rangle)^2}{2v_0^2(1 - e^{-2\gamma_R t})} \right), \quad (7.17)$$

which turns into

$$\psi(\mathbf{v}) = \left[ \frac{d}{2\pi v_0^2} \right]^{d/2} \exp \left( -\frac{d\mathbf{v}^2}{2v_0^2} \right) \quad (7.18)$$

in the stationary state ( $t \rightarrow \infty$ ). Equations (7.17) and (7.18) also simply follow from the Fokker-Planck equation of the Langevin equation (6.16) for the velocity.

Integration of Eq. (7.11) over the velocity coordinates yields the positional distribution function

$$\psi(\mathbf{r}, t | \mathbf{r}^0, 0) = [2\pi\Lambda_{rr}(t)]^{-d/2} \exp\left(-\frac{(\mathbf{r} - \langle \mathbf{r} \rangle)^2}{2\Lambda_{rr}(t)}\right), \quad (7.19)$$

which reduces in the stationary state to [239]

$$\psi(\mathbf{r}) = [2\pi\Lambda_{rr}]^{-d/2} \exp\left(-\frac{\mathbf{r}^2}{2\Lambda_{rr}}\right), \quad (7.20)$$

with (see Eq. (7.8))

$$\Lambda_{rr} = \frac{k_B T}{k} + \frac{v_0^2}{d\kappa(\gamma_R + \kappa)}. \quad (7.21)$$

Naturally, we obtain a simple Gaussian distribution function for  $\psi(\mathbf{r})$  of the AOUP, with a maximum at the minimum  $r = 0$  of the potential. Computer simulations of the ABP model obeying Eqs. (6.1) and (6.3) yield a different distribution with, depending on activity, an off-center maximum [79, 237].

Strictly speaking, the distribution function (7.20) should not be compared with that of an ABP. In Eq. (7.20), all velocity contributions have been integrated out, whereas for an ABP, the magnitude of the velocity is fixed. The latter corresponds to a distribution function  $\psi(\mathbf{r})$  at fixed  $v_0$ . The corresponding distribution function of an AOUP is the conditional probability distribution function  $\psi(\mathbf{r} | v_0)$ . Hence, this is the suitable distribution function of an AOUP to be compared with the spatial distribution function of an ABP.

### 7.1.3 Conditional probability distribution function

The conditional probability density  $\psi(\mathbf{r} | \mathbf{v})$  of the position  $\mathbf{r}$  for a fixed velocity  $\mathbf{v}$  is defined by the relation [163]

$$\psi(\mathbf{r}, \mathbf{v}) = \psi(\mathbf{r} | \mathbf{v})\psi(\mathbf{v}). \quad (7.22)$$

Using Eqs. (7.11) and (7.18), we find

$$\psi(\mathbf{r} | \mathbf{v}) = \left(\frac{\Lambda_{vv}}{2\pi|\mathbf{\Lambda}|}\right)^{d/2} \exp\left(-\frac{\Lambda_{vv}}{2|\mathbf{\Lambda}|} \left(\mathbf{r} - \frac{\Lambda_{rv}}{\Lambda_{vv}}\mathbf{v}\right)^2\right), \quad (7.23)$$

with  $\Lambda_{vv} = v_0^2/d$  and  $\Lambda_{rv} = v_0^2/d(\gamma_R + \kappa)$ .

The spatial distribution function for  $|\mathbf{v}| = v_0$  is obtained by integration of Eq. (7.23) over the orientation of the velocity  $\mathbf{v}$ . Evaluation of the integrals yields:

- Two dimensional (2d) system

$$\psi(r | v_0) = \frac{\Lambda_{vv}}{|\mathbf{\Lambda}|} \exp\left(-\frac{\Lambda_{vv}}{2\Lambda_{rv}|\mathbf{\Lambda}|}v_0^2\right) \exp\left(-\frac{\Lambda_{vv}}{2|\mathbf{\Lambda}|}r^2\right) I_0\left(\frac{\Lambda_{rv}}{|\mathbf{\Lambda}|}v_0 r\right), \quad (7.24)$$

where  $I_0(x)$  is the modified Bessel function of the first kind.

- Three dimensional (3d) system

$$\psi(r|v_0) = \left( \frac{\Lambda_{vv}^3}{2\pi|\Lambda|} \right)^{1/2} \frac{2}{\Lambda_{rv}v_0r} \exp\left(-\frac{\Lambda_{vr}^2}{2\Lambda_{vv}|\Lambda|}v_0^2\right) \exp\left(-\frac{\Lambda_{vv}}{2|\Lambda|}r^2\right) \sinh\left(\frac{\Lambda_{rv}v_0r}{|\Lambda|}\right). \quad (7.25)$$

We now introduce the Péclet number  $Pe$ , and the  $\Delta$  definitions of Eq. (6.7) with the strength  $\tilde{k}$  of the harmonic potential as a dimensionless quantity, where

$$\tilde{k} = \frac{k\sigma^2}{k_B T}; \quad (7.26)$$

$\sigma$  is the diameter of the particle. The factors  $\Lambda_{vv}/|\Lambda|$  and  $\Lambda_{rv}v_0/|\Lambda|$  of the distribution functions (7.24) and (7.25) then turn into

$$\frac{|\Lambda|}{\Lambda_{vv}\sigma^2} = \frac{1}{\tilde{k}} + \frac{Pe^2(d-1)\Delta}{d\tilde{k}(\tilde{k}\Delta + d-1)^2}, \quad (7.27)$$

$$\frac{|\Lambda|}{\Lambda_{rv}v_0\sigma} = \frac{\tilde{k}\Delta + d-1}{Pe\Delta} \left( \frac{1}{\tilde{k}} + \frac{Pe^2(d-1)\Delta}{d\tilde{k}(\tilde{k}\Delta + d-1)^2} \right). \quad (7.28)$$

In both expressions, the term  $1/\tilde{k}$  corresponds to the thermal (white-noise) contribution. Activity dominates when the Péclet number exceeds the critical value

$$Pe_c = \sqrt{\frac{d}{(d-1)\Delta}} (\tilde{k}\Delta + d-1). \quad (7.29)$$

The following asymptotic dependencies are obtained for Eqs. (7.24) and (7.25):

- (i)  $Pe/Pe_c \ll 1$

In this case,  $\Lambda_{vv}\sigma^2/|\Lambda| = \tilde{k}$ , and the Gaussian function in Eqs. (7.24), (7.25) turns into the Boltzmann distribution  $\exp(-kr^2/2k_B T)$  of a passive particle. The relevance of the Bessel or the hyperbolic sine function depends on the values of  $\tilde{k}$  and  $\Delta$ , respectively. However, as long as  $Pe\tilde{k}\sqrt{\Delta}/Pe_c \ll 1$ , the positional distribution is solely determined by the Boltzmann distribution of a thermal passive particle.

As noted earlier,  $\kappa/\gamma_R \gg 1$ , or  $\tilde{k}\Delta \gg 1$ , is the interesting limit for self-propulsion, which implies  $Pe_c \approx \tilde{k}\sqrt{\Delta} \gg 1$ . Interestingly,  $Pe_c$  increases then linearly with  $k$ , and can assume large values. Hence, for strongly confined AOUPs and moderate  $\Delta$ ,  $Pe/Pe_c \ll 1$  and the term  $1/\tilde{k}$  in Eqs. (7.27), (7.28) dominates even for Péclet numbers significantly larger than unity.

- (ii)  $Pe/Pe_c \gg 1$

For  $\tilde{k}$  and  $\Delta$  on the order of unity,  $Pe_c$  is also on the order of unity, hence, typically  $Pe/Pe_c \gg 1$ . Then, Eqs. (7.27) and (7.28) become  $|\Lambda|/\Lambda_{vv}\sigma^2 \approx Pe^2\Delta/\tilde{k}$  and

$|\Lambda|/\Lambda_{rv}v_0\sigma \approx Pe/\tilde{k}$ . Thus, the argument of the Bessel and hyperbolic sine function is proportional to  $1/Pe$ , i.e., is small for large  $Pe$ , and these functions will only weakly contribute to  $\psi(r|v_0)$ . Consequently, we obtain a Boltzmann distribution with the effective temperature of Eq. (7.16), where  $k_B T_e \approx k_B T Pe^2 \Delta / d(d-1)$ , because  $Pe \gg 1$ .

In limit  $Pe_c \approx \tilde{k}\sqrt{\Delta} \gg 1$ , Eqs. (7.27), (7.28) are universal functions of  $\hat{P}e$  (6.8), and  $\hat{k} = \tilde{k}\Delta = (d-1)\kappa/\gamma_R$ , i.e.,

$$\frac{|\Lambda|}{\Lambda_{vv}\sigma^2} = \frac{\hat{P}e^2(d-1)}{d\hat{k}(\hat{k}+d-1)^2}, \quad (7.30)$$

$$\frac{|\Lambda|}{\Lambda_{rv}v_0\sigma} = \frac{\hat{P}e(d-1)}{d\hat{k}(\hat{k}+d-1)}. \quad (7.31)$$

Here, the thermal process,  $\Gamma$ , does not contribute to the dynamics anymore. Note that  $Pe_c \gg 1$  follows also for  $\Delta \rightarrow 0$ , i.e.,  $\tilde{k}\Delta \lesssim 1$  and  $Pe_c \approx 1/\sqrt{\Delta}$ .

We like to emphasize that  $\Delta$  is typically smaller than unity. In case of thermal motion,  $\Delta = 1/3$  for a colloid in a fluid. Activity can cause larger rotational diffusion coefficients and, hence, smaller  $\Delta$ , which has been confirmed experimentally for *E. coli* bacteria [64, 86, 245, 246] and *Chlamydomonas reinhardtii* cells [86].

ABPs confined in a 2d harmonic potential have been considered in Ref. [161]. The analytical approximations provided in that article also follow from the distribution function Eq. (7.24). Inserting Eqs. (6.7) in Eq. (7.24), we find in the limit  $\tilde{k}\Delta = (d-1)\kappa/\gamma_R \gg 1$  and  $\tilde{k}^2\Delta/Pe^2(d-1) = k_B T \kappa^2 / \gamma_R \gamma_T v_0^2 \gg 1$

$$\psi(r|v_0) = \frac{k}{2\pi k_B T} \exp\left(-\frac{Pe^2}{4U_h(\sigma)}\right) \exp(-U_h(r)/k_B T) I_0(Pe r/\sigma). \quad (7.32)$$

This expression coincides with that derived in Ref. [161]. In the opposite limit  $\gamma_R \rightarrow \infty$ , where  $\Lambda_{rv}/|\Lambda| \rightarrow k/\gamma_R k_B T \rightarrow 0$ , Taylor expansion of the Bessel function to lowest order yields

$$\psi(r) = N_c \exp(-\beta U_h(r)) (1 + \Delta^2 Pe^2 \beta^2 U_h(\sigma) U_h(r)). \quad (7.33)$$

$N_c$  is the normalization coefficient. In terms of the dependence on the potential  $U_h(r)$  and the Péclet number, this result agrees with the expression derived in Ref. [161]. However, we find a different dependence on  $\gamma_R = D_R$  and the strength of the potential. In Ref. [161], the term  $U_h(\sigma)$  is missing and  $\Delta$  appears only linearly. This might be related to the alternative approach of Ref. [161]. The advantage of our result is that we not only obtain limiting expressions, but can also describe the crossover from small to large  $\gamma_R$ .

Finally, the conditional probability density  $\psi(\mathbf{v}|\mathbf{r})$  is given by

$$\psi(\mathbf{v}|\mathbf{r}) = \left(\frac{\Lambda_{rr}}{2\pi|\Lambda|}\right)^{d/2} \exp\left(-\frac{\Lambda_{rr}}{2|\Lambda|}\left(\mathbf{v} - \frac{\Lambda_{rv}}{\Lambda_{rr}}\mathbf{r}\right)^2\right). \quad (7.34)$$

## 7.2 Unified Colored Noise Approximation

An analytical solution of Eqs. (6.1) and (6.16) is the exception rather than the rule. Naturally, a Fokker-Planck equation can be derived for the coupled Langevin equations due to their Gaussian and Markovian character [163]. The stochastic process for  $\mathbf{r}$  only, however, is no longer Markovian, which is reflected by the colored noise correlation function Eq. (6.18). This implies the lack of a Fokker-Planck-type equation for the (reduced) probability density function  $\psi(\mathbf{r}, t)$  [238]. At the moment, at best an approximate Fokker-Planck-type equation can be derived [238, 247, 248]. One of the approximation schemes is denoted as *Unified Colored Noise Approximation* (UCNA) [238]. This approximation has been applied to ABPs in Refs. [106, 115, 117, 243, 244]. Here, our goal is to elucidate the applicability and validity of the UCNA for the ABP model of Sec. 6.1 confined in an anharmonic potential.

### 7.2.1 Multidimensional stationary-state positional distribution function

A derivation of the multidimensional stationary-state probability distribution function within the UCNA is presented in Refs. [238, 244]). In brief, the Langevin equation for  $\mathbf{r}$  within the UCNA is obtained by calculating the time derivative of Eq. (6.1) and insertion of Eq. (6.16) [238, 244]. Thereby, we neglect the random force  $\mathbf{F}$ . This yields

$$\ddot{\mathbf{r}} = \left( -\gamma_R + \frac{1}{\gamma_T} (\nabla \mathbf{F})^T \right) \dot{\mathbf{r}} + \frac{\gamma_R}{\gamma_T} \mathbf{F} + \boldsymbol{\eta}. \quad (7.35)$$

By considering the overdamped limit, i.e.,  $\gamma_R \rightarrow \infty$ , the Langevin equation is obtained [238, 244]

$$\dot{\mathbf{r}} = \frac{\gamma_R}{\gamma_T} \mathbf{M}^{-1} \mathbf{F} + \mathbf{M}^{-1} \boldsymbol{\eta}, \quad (7.36)$$

with the abbreviation

$$\mathbf{M} = \gamma_R \mathbf{E} - \frac{1}{\gamma_T} (\nabla \mathbf{F})^T \quad (7.37)$$

and the unit matrix  $\mathbf{E}$ . Equation (7.36) represents a Markovian approximation of the colored noise random process.

The Fokker-Planck equation corresponding to Eq. (7.36) within the Stratonovich definition is [163, 244]

$$\frac{\partial \psi(\mathbf{r}, t)}{\partial t} = -\frac{\gamma_R}{\gamma_T} \nabla \cdot (\mathbf{M}^{-1} \mathbf{F} \psi) + \frac{\gamma_R v_0^2}{d} \nabla \cdot [\mathbf{M}^{-1} \nabla \cdot (\mathbf{M}^{-1} \psi)].$$

In case of a vanishing probability current, the stationary-state solution follows from

$$\mathbf{M}^{-1} \mathbf{F} \psi - \frac{\gamma_T v_0^2}{d} \mathbf{M}^{-1} \nabla \cdot (\mathbf{M}^{-1} \psi) = 0. \quad (7.38)$$

By multiplying twice with  $\mathbf{M}$  and using the derivative of the determinant  $|\mathbf{M}|$  of  $\mathbf{M}$ , this equation becomes

$$\nabla\psi = \left( \frac{d}{\gamma_T v_0^2} \mathbf{M} \mathbf{F} + \frac{1}{|\mathbf{M}|} \nabla \mathbf{M} \right) \psi \quad (7.39)$$

by applying the relation

$$\frac{\partial M_{\beta\gamma}}{\partial r_\alpha} = \frac{1}{\gamma_T} \frac{\partial^3 U}{\partial r_\alpha \partial r_\beta \partial r_\gamma} = \frac{\partial M_{\alpha\gamma}}{\partial r_\beta} = \frac{\partial M_{\alpha\beta}}{\partial r_\gamma}. \quad (7.40)$$

The solution of Eq. (7.39) is

$$\psi(\mathbf{r}) = \frac{|\mathbf{M}|}{Z} \exp \left( -\frac{d\gamma_R}{\gamma_T v_0^2} U - \frac{d}{2\gamma_T^2 v_0^2} \nabla U \cdot \nabla U \right), \quad (7.41)$$

where  $Z$  insures the normalization of the distribution function [243].

### 7.2.2 Approximate multidimensional stationary-state velocity distribution function

A Fokker-Planck equation corresponding to Eq. (7.35) can be derived as follows [109, 243]. With  $\dot{\mathbf{r}} = \mathbf{u}$ , Eq. (7.35) is equivalent to

$$\dot{\mathbf{r}} = \mathbf{u}, \quad (7.42)$$

$$\dot{\mathbf{u}} = -\mathbf{M}\mathbf{u} + \frac{\gamma_R}{\gamma_T} \mathbf{F} + \boldsymbol{\eta}. \quad (7.43)$$

The respective Fokker-Planck equation for the distribution function  $\psi(\mathbf{r}, \mathbf{u})$  is

$$\frac{\partial}{\partial t} \psi(\mathbf{r}, \mathbf{u}, t) = -\mathbf{u} \cdot \frac{\partial \psi}{\partial \mathbf{r}} + \frac{\partial}{\partial \mathbf{u}} \cdot (\mathbf{M}\mathbf{u}\psi) - \frac{\gamma_R}{\gamma_T} \mathbf{F} \cdot \frac{\partial \psi}{\partial \mathbf{u}} + \frac{\gamma_R v_0^2}{d} \frac{\partial^2 \psi}{\partial \mathbf{u}^2}, \quad (7.44)$$

No general solution of this equation has been derived so far. In Refs. [109, 243], approximate stationary-state distribution functions are provided, either by a perturbation expansion [109] or by the ansatz  $\psi(\mathbf{r}, \mathbf{u}) = \psi(\mathbf{u}|\mathbf{r})\psi(\mathbf{r})$ , with the conditional distribution function  $\psi(\mathbf{u}|\mathbf{r})$ , which yields a zero current  $\int \mathbf{u}\psi(\mathbf{r}, \mathbf{u})d^d u$  [243]. For our system, the conditional velocity distribution function is

$$\psi(\mathbf{u}|\mathbf{r}) = \sqrt{|\mathbf{M}|} \left( \frac{d}{2\pi v_0^2 \gamma_R} \right)^{d/2} \exp \left( -\frac{d}{2v_0^2 \gamma_R} \mathbf{u}^T \mathbf{M} \mathbf{u} \right) \quad (7.45)$$

and  $\psi(\mathbf{r})$  is identical with Eq. (7.41). The approximation yields a Gaussian distribution for the velocity  $\mathbf{u}$ , with a position dependent variance [243]. By the substitution  $\mathbf{u} = \mathbf{v} + \mathbf{F}/\gamma_T = \mathbf{v} - \frac{\partial U}{\partial \mathbf{r}}/\gamma_T$ , we obtain the conditional distribution function for the velocity  $\mathbf{v}$ .

An interesting quantity is the mean square velocity  $\langle \dot{\mathbf{r}}^2 \rangle_u = \langle \mathbf{u}^2 \rangle_u$ , where the subscript indicates averaging over the velocity at a given position. Via the distribution function (7.45), we obtain

$$\langle \mathbf{u}^2 \rangle_u = \frac{v_0^2 \gamma_R}{3} \text{Tr}(\mathbf{M}^{-1}), \quad (7.46)$$

where  $\text{Tr}(\mathbf{M}^{-1})$  denotes the trace of the matrix  $\mathbf{M}^{-1}$  [243].

### 7.2.3 Radial potential

In case of a radially symmetric potential  $U(r) = U(|\mathbf{r}|)$ , Eq. (7.41) becomes

$$\psi(r) = \frac{1}{Z} \left( 1 + \frac{1}{\gamma_R \gamma_T} \frac{\partial^2 U}{\partial r^2} \right) \exp \left( -\frac{d\gamma_R}{\gamma_T v_0^2} U - \frac{d}{2\gamma_T^2 v_0^2} \left( \frac{\partial U}{\partial r} \right)^2 \right). \quad (7.47)$$

This distribution function agrees with that presented in Ref. [244] except of the factor in front of the exponential function—Eq. (6) of Ref [244] contains an additional term with a first derivative of the potential. Note that the normalization factor  $Z$  is

$$Z = \int \exp \left( -\frac{d\gamma_R}{\gamma_T v_0^2} U - \frac{d}{2\gamma_T^2 v_0^2} \left( \frac{\partial U}{\partial r} \right)^2 \right) \left( 1 + \frac{1}{\gamma_R \gamma_T} \frac{\partial^2 U}{\partial r^2} \right) r^{d-1} dr. \quad (7.48)$$

In the limit  $\gamma_R \rightarrow \infty$ , which corresponds to the limit of an overdamped dynamics (see Eq. (7.36)), the potential term in the exponent of Eqs. (7.47) and (7.41) dominates and the distribution function reduces to

$$\psi(\mathbf{r}) = \frac{1}{Z_0} \exp \left( -\frac{d\gamma_R}{\gamma_T v_0^2} U(\mathbf{r}) \right), \quad (7.49)$$

with the respective normalization factor  $Z_0$ . Hence, a Boltzmann distribution with the potential  $U$  and the effective temperature (7.16) is obtained. Note that the white-noise process  $\Gamma$  has been neglected in UCNA. This result is consistent with the general expectation for the Langevin equation (6.1) in the limit  $\gamma_R \rightarrow \infty$  discussed in Sec. 7.1.2 following Eq. (7.16).

The conditional distribution function  $\psi(\mathbf{u}|\mathbf{r})$  for the velocity (7.45) is

$$\begin{aligned} \psi(\mathbf{u}|\mathbf{r}) &= \left( \frac{d(\gamma_T \gamma_R r + \partial U / \partial r)}{2\pi v_0^2 \gamma_T \gamma_R r} \right)^{d/2} \exp \left( -\frac{d}{2v_0^2} \left[ 1 + \frac{1}{\gamma_T \gamma_R r} \frac{\partial U}{\partial r} \right] u^2 \right) \\ &\times \exp \left( -\frac{d}{2v_0^2 \gamma_T \gamma_R} \left[ \frac{\partial^2 U}{\partial r^2} - \frac{1}{r} \frac{\partial U}{\partial r} \right] u_r^2 \right), \end{aligned} \quad (7.50)$$

where  $u_r = \mathbf{u} \cdot \mathbf{e}_r$  is the radial velocity and  $\mathbf{e}_r$  the radial unit vector.

In addition, the mean square velocity (7.46) is given by

$$\langle \mathbf{u}^2 \rangle_u = \frac{v_0^2 \gamma_R}{3} \left( \gamma_R + \frac{1}{\gamma_T r} \frac{\partial U}{\partial r} \right)^{-1} \left[ 3 + \left( \frac{1}{r} \frac{\partial U}{\partial r} - \frac{\partial^2 U}{\partial r^2} \right) \left( \gamma_R \gamma_T + \frac{\partial^2 U}{\partial r^2} \right)^{-1} \right]. \quad (7.51)$$

### 7.2.4 Harmonic potential

For the harmonic potential  $U_h$  of Eq. (7.1), the distribution function (7.47) is equal to  $\psi(r)$  of Eq. (7.20), i.e., the distribution function within UCNA agrees exactly with the full solution for a harmonic potential. Similarly, with the substitution  $\mathbf{u} = \mathbf{v} - \kappa \mathbf{r}$ , Eq. (7.50) becomes equal to the exact solution Eq. (7.34) for a radial harmonic potential.

This is not surprising, since the distribution function  $\psi(\mathbf{r}, \mathbf{u}) = \psi(\mathbf{u}|\mathbf{r})\psi(\mathbf{r})$  with Eqs. (7.41) and (7.45) satisfies the stationary-state Fokker-Planck equation (7.44) for a constant matrix  $\mathbf{M}$ . Hence, the approach of Ref. [243] provides an exact solution for Eq. (6.1)—without thermal noise—and Eq. (6.16) for linear and harmonic potentials.



## 7.3 Comparison between Simulation and theoretical results

### 7.3.1 ABP and AOUP in Harmonic Potential

Here, we will compare the theoretical results derived in Sec. 7.1.2 and 7.1.3 for an AOUP in a harmonic potential with respective simulation results for an ABP.

#### One-dimensional system

Typically one dimensional harmonically confined AOUPs are considered [237, 239–241]. In contrast, our approach presented so far, with the definitions (6.4) and (6.17), is only meaningful for  $d > 1$ . However, Eqs. (6.16) and (6.17) can simply be adapted to a pure 1d motion by setting

$$\dot{v}(t) = -\gamma_R v(t) + \eta(t), \quad (7.52)$$

$$\langle \eta(t)\eta(t') \rangle = 2v_0^2 \gamma_R \delta(t - t'). \quad (7.53)$$

The general solution presented in Sec. 7.1 still applies, we just have to set  $d = 1$  and replace  $(d - 1)D_R$  by a nonzero  $\gamma_R$ .

Integration of the (1d) conditional probability (7.23) over the two possible (plus/minus) directions of motion yields the conditional probability distribution function

$$\psi(x|v_0) = \left( \frac{\Lambda_{vv}}{2\pi|\Lambda|} \right)^{1/2} \left[ \exp \left( -\frac{\Lambda_{vv}}{2|\Lambda|} \left( x - \frac{\Lambda_{rv}}{\Lambda_{vv}} v_0 \right)^2 \right) + \exp \left( -\frac{\Lambda_{vv}}{2|\Lambda|} \left( x + \frac{\Lambda_{rv}}{\Lambda_{vv}} v_0 \right)^2 \right) \right]. \quad (7.54)$$

It is a superposition of two Gaussian functions with maxima at the positions

$$\frac{x_m}{\sigma} = \pm \frac{\Lambda_{rv} v_0}{\sigma \Lambda_{vv}} = \pm \frac{Pe \Delta_1}{\tilde{k} \Delta_1 + 1}, \quad (7.55)$$

with  $\Delta_1 = D_T/\sigma^2 \gamma_R$ . An estimation of  $x_m$ , respectively  $r_m$  of higher dimensional systems, follows from the (general) condition of vanishing (average) velocity  $\dot{r} = 0$  (Eq. (6.1)), i.e., the balance of the active and confining force, which yields

$$\gamma_T |\mathbf{v}| = |\mathbf{F}|, \quad (7.56)$$

and, hence,

$$x_m = \frac{v_0}{\kappa} = \frac{Pe}{\tilde{k}}. \quad (7.57)$$

This is identical with the expression following from Eq. (7.55) for strong confinement  $\tilde{k} \Delta_1 \gg 1$ .

Activity-induced off-center-peaked distribution functions for harmonically confined ABPs in 1d have been obtained in Ref. [237] by computer simulations. Moreover, the distribution function of run-and-tumble particles (RTPs) [249] confined in a harmonic potential is discussed in Refs. [79, 237], and a power-law distribution function is derived, with an exponent depending on the tumbling rate. This power-law distribution exhibits a singularity at the position  $x_m$  for strong confinement. In contrast, the Gaussian function is typically finite at its maximum, and  $|x|$  values larger than  $|x_m|$  are accessible. Thus, the distribution functions for ABPs and RTPs are qualitatively different. However, common to both results is the presence of off-center peaks of the probability distribution function at the same location for strong confinement.

### Three-dimensional system

Figure 7.1 displays the radial conditional probability distribution function,  $\psi(r|v_0)$ , of AOUPs and simulation results of ABPs for various force constants and Péclet numbers. The distribution functions of the ABPs exhibit the expected activity-induced off-center accumulation with a maximum shifting to larger radial distances with increasing Péclet number [237]. A qualitatively similar behavior is obtained for AOUPs, most pronounced for  $\tilde{k}\Delta \approx \kappa/\gamma_R \gg 1$  (Fig. 7.1(c)). The critical Péclet numbers (7.29) for  $\tilde{k} = 1, 10^1$ , and  $10^2$  are  $Pe_c = 5.1, 11.2$ , and  $71.6$ . As discussed in Sec. 7.1.3 (i), for  $Pe \ll Pe_c$  and  $Pe\tilde{k}\sqrt{\Delta}/Pe_c \ll 1$ , the distribution function of an AOUP naturally agrees well with the ABP result, since activity is of minor importance, and the Boltzmann distribution of a passive particle is obtained. However, for  $\tilde{k} = 100$  good agreement between  $\psi(r|v_0)$  for AOUPs and ABP simulation results is even obtained for Péclet numbers as large as  $Pe \approx 40$  (see Fig. 7.1(c) and discussion in Sec. 7.1.3 (i)). For the respective parameters  $\tilde{k}\Delta \gg 1$ ,  $Pe_c \approx 70$ , i.e.,  $Pe/Pe_c < 1$ , and the Gaussian distribution of Eq. (7.25) is still close to a Boltzmann distribution. Yet, the argument of the hyperbolic sine function is not necessarily small anymore ( $\tilde{k}\sqrt{\Delta} \gg 1$ ), which leads to a pronounced off-center maximum.

In the opposite limit,  $Pe \gg Pe_c$ , the AOUP results qualitatively describe the behavior of ABPs. The quantitative agreement depends on the stiffness of the harmonic potential. For  $\tilde{k} = 1$ , reasonable agreement is obtained for all considered Péclet numbers  $Pe \leq 10^2$  (Fig. 7.1(a)). This is not surprising, since this corresponds to the limit  $\gamma_R/\kappa > 1$ , and a Boltzmann distribution is obtained for  $\psi(r/v_0)$ , with the effective temperature of Eq. (7.16), as discussed in Sec. 7.1.3 (ii). For stronger confinement, significant deviations appear between the AOUP and ABP results, specifically for  $\tilde{k} = 10$ , the more the larger  $Pe$ . In contrast, the differences are smaller again for  $\tilde{k} = 100$ , where  $Pe_c$  is larger.

Estimations of the radial positions with vanishing velocity according to Eq. (7.57)—we obtain the same (radial) value in any dimension—for the various Péclet numbers are indicated by vertical short, black bars in Fig. 7.1, and the respective maxima of the distribution functions from simulations by colored bars. For small Péclet numbers, the exact position of the maximum of the simulation data is difficult to identify due to statistical inaccuracies. As soon as a clear maximum appears, its position agrees well with the theoretical prediction (7.57) at large potential stiffness ( $\tilde{k} = 100$ ). Here, the difference between the position of the maximum

### 7.3 Comparison between Simulation and theoretical results

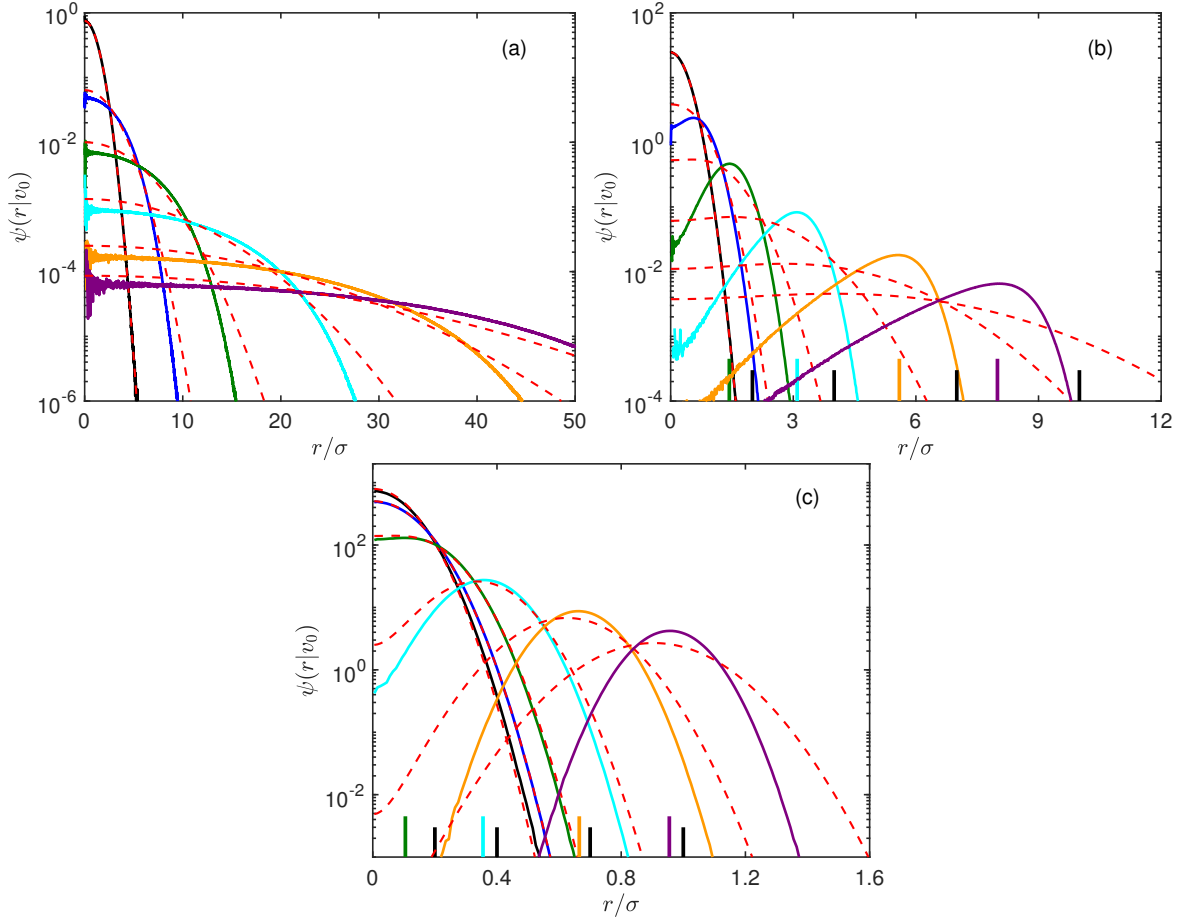


Figure 7.1: Radial conditional probability distribution functions of ABPs (solid lines) and AOUPs (dashed lines) confined in a three-dimensional radially harmonic potential for the Péclet numbers  $Pe = 1, 10, 20, 40, 70$ , and  $100$  (left to right). The stiffness of the harmonic potential is (a)  $\tilde{k} = 1$ , (b)  $\tilde{k} = 10$  and (c)  $\tilde{k} = 100$ . In all three cases the ratio of diffusion coefficients is  $\Delta = 0.3$  (see Eq. (6.7)). The dashed lines are calculated according to the expressions (7.25). The colored (long) vertical bars at the  $x$ -axis indicate the positions of the maximum of distribution functions, and the black (short) lines mark the distances  $r_m$  of zero radial velocity according to Eq. (7.57).

and  $r_m$  decreases from approximately 10% to 5% with increasing  $Pe \geq 40$ . The deviations for  $\tilde{k} = 10$  are in the range of 35% – 20% for  $Pe \geq 20$ . Hence, Eq. (7.57) provides an upper estimate of the maximum of the distribution function, whose accuracy improves with increasing potential stiffness and Péclet number. The maxima of the analytical approach are shifted toward smaller radial distances, as is evident from Fig. 7.1, but the linear dependence on  $Pe$  is maintained.

Figure 7.2 illustrates the dependence of the radial conditional distribution function of AOUPs on  $\Delta$  at a fixed  $Pe$ . Thereby, the inset of Fig. 7.2(a) shows that the maximum of

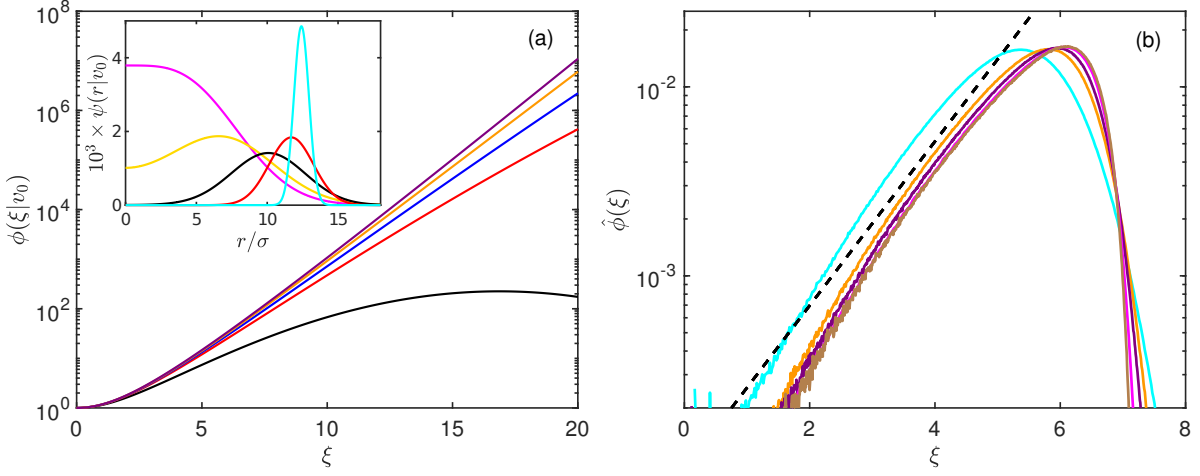


Figure 7.2: (a) Probability distribution function  $\phi$  (Eq. (7.58)) of an AOUP as function of the variable  $\xi = r\Lambda_{vv}/|\Lambda|$  for  $Pe = 500$ ,  $\tilde{k} = 40$ , and  $\Delta = 0.3, 1, 2, 5, 50$  (bottom to top). The inset shows the distribution function  $\psi(r|v_0)$  as function of  $r$  for  $\Delta = 0.05, 0.1, 0.3, 1$ , and  $10$  (left to right). Curves of the same  $\Delta$  are displayed in the same color. (b) Probability distribution function  $\hat{\phi}$  (Eq. (7.61)) of an ABP as function  $\xi$  for  $\tilde{k} = 10$ ,  $\Delta = 0.3$ , and  $Pe = 40, 70, 100, 200, 1000$  (left to right). The color code is the same as in Fig. 7.1(b). The dashed line indicates the exponential  $e^\xi$ .

$\psi(r|v_0)$  shifts to large radial distances with increasing  $\Delta$ , or decreasing  $\gamma_R = 2D_R$ . The hyperbolic sine term in Eq. (7.25) suggests that  $\psi(r|v_0)$  increases exponentially for appropriate  $r$  as long as the Gaussian function is changing only slowly. Such an exponential dependence has been presented in Ref. [237]. To highlight this asymptotic behavior, we present the distribution function

$$\phi(\xi|v_0) = \frac{1}{\xi} \sinh(\xi) \exp\left(-\frac{\xi^2}{2\xi_0^2}\right) \quad (7.58)$$

for the scaled radial distance  $\xi = r\Lambda_{vv}/|\Lambda|$  in Fig. 7.2. It is related to  $\psi(\xi|v_0)$  via

$$\psi(\xi|v_0) = \sqrt{\frac{2\xi_0^3}{\pi}} \exp\left(-\frac{1}{2\xi_0^2}\right) \phi(\xi|v_0), \quad (7.59)$$

where  $\xi_0$  is given by

$$\xi_0^{-2} = \frac{d-1}{d\Delta\tilde{k}} \left(1 + \frac{Pe_c^2}{Pe^2}\right). \quad (7.60)$$

The latter reduces to  $\xi_0^2 = d\Delta\tilde{k}/(d-1)$  in the limit  $Pe \gg Pe_c = \tilde{k}\sqrt{\Delta} \gg 1$ . Evidently,  $\phi(\xi|v_0)$  increases exponentially for  $\xi \gtrsim 5$  and  $\Delta \gtrsim 10$ .

Interestingly,  $\psi(\xi|v_0)$  is independent of the Péclet number for  $Pe \gg Pe_c$ . Note that this is always the case when the thermal contribution by  $\Gamma$  is neglected. Thus, we obtain a unique

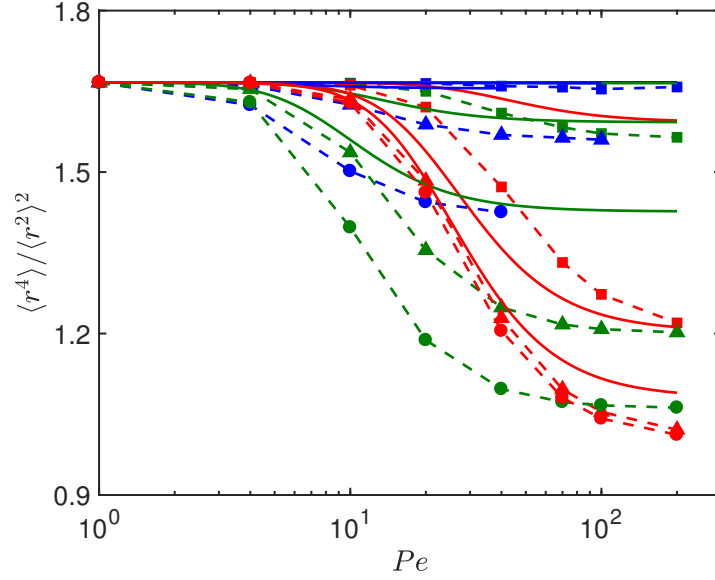


Figure 7.3: Kurtoses as function of the Péclet number for  $\tilde{k} = 1$  (blue), 10 (green), and 100 (red) and  $\Delta = 0.01$  (squares), 0.1 (triangles), and 1 (bullets). The solid lines are AOUP results according to Eq. (7.62) and the symbols are ABP results. The dashed lines are guides for the eye.

distribution independent of  $Pe$  for a given  $\Delta$ . The dependence on the Péclet number is adsorbed in the variable  $\xi$ .

Similarly, the radial probability distribution function

$$\hat{\phi}(\xi) = \left( \frac{|\Lambda|}{\Lambda_{vv}} \right)^3 \psi(r) \quad (7.61)$$

of an ABP, with  $\psi(r)$  the probability distribution function from Fig. 7.1(b), is displayed in Fig. 7.2(b). Again, we obtain close agreement of the various curves for large Péclet numbers, with the same scaling variable  $\xi$  as for AOUPs. The range of exponential growth is rather short, but would increase for  $\Delta \gg 1$ .

However,  $\Delta < 1$  is more relevant for self-propelled particles, as pointed out before. Here, the range of radial distances over which the distribution functions increase exponentially is rather shorter than longer. The presence of an exponential regime depends on  $\tilde{k}\Delta$ . For  $\Delta \rightarrow 0$ ,  $\zeta_0^2 \rightarrow 0$  and the Gaussian function in Eq. (7.58) decays fast with increasing  $\xi$ , suppressing an exponential regime. In contrast, for very strong potentials with  $\tilde{k}\Delta \gg 1$ , we observe a pronounced,  $Pe$ -independent exponential regime.

The differences between the ABP and AOUP results of Fig. 7.1 reflect the variance in the equations of motion (6.3) and (6.16). Since the second moment of both models is identical, we characterize their differences by the kurtosis  $K$ . Note that both,  $\psi(r|v_0)$  of an AOUP and the distribution function of an ABP are non-Gaussian in general. With the conditional

distribution function (7.25) for a AOUP, we obtain in 3d

$$K = \frac{\langle \mathbf{r}^4 \rangle_{v_0}}{\langle \mathbf{r}^2 \rangle_{v_0}^2} = \frac{5}{3} - \frac{2}{27} \frac{\Lambda_{rv}^4 v_0^4}{\Lambda_{vv}^4 \Lambda_{rr}^2}. \quad (7.62)$$

Figure 7.3 shows kurtoses for the parameters of Fig. 7.1.  $K$  decreases with increasing Péclet number, corresponding to a platykurtic kurtosis; this means that the distribution functions are flatter than a Gaussian and decay faster at the tails. Thereby, the kurtoses of the ABPs are smaller than those of the equivalent AOUPs. As discussed before, at small  $\tilde{k}$ , the distribution functions are essentially Gaussian with  $K$  close to  $5/3$ .

### 7.3.2 Anharmonic potential

We consider the potential

$$\tilde{U} = \frac{1}{k_B T} U = \left( \frac{1}{\tilde{r} - 5} \right)^{12}, \quad (7.63)$$

where  $\tilde{r} = r/\sigma$ , as an example for an anharmonic potential. Here, we scale the potential energy with the thermal energy  $k_B T$ , which provides a consistent definition of dimensionless parameters with the previous sections.

The radial distribution function (7.47) now reads

$$\psi(\tilde{r}) = \frac{1}{Z} \left( 1 + \frac{\Delta}{(d-1)} \frac{\partial^2 \tilde{U}}{\partial \tilde{r}^2} \right) \exp \left( -\frac{d(d-1)}{Pe^2 \Delta} \tilde{U} - \frac{d}{2Pe^2} \left( \frac{\partial \tilde{U}}{\partial \tilde{r}} \right)^2 \right) \quad (7.64)$$

in terms of the Péclet number and  $\Delta$ . Hence,  $\psi(r)$  is determined by the two independent parameters,  $Pe$  and  $\Delta$ .

In the following, we elucidate the extent to which the UCNA provides a solution of the dynamics of AOUPs and ABPs, respectively.

### Comparison of AOUP simulations with UCNA

Figure 7.4 displays probability distribution functions of an AOUP without thermal noise for various Péclet numbers. For  $\Delta = 0.1$  (Fig. 7.4(a)), the simulation data agree very well with the UCNA for  $Pe \lesssim 10$ , and they are still qualitatively reproduced for  $Pe = 100$ . For  $Pe \lesssim 1$ , the distribution function monotonously decreases with increasing radial distance  $r$ , whereas a peak appears at larger  $Pe$ . The peak for  $Pe = 10$  is caused by the factor with the second derivative in front of the exponential function of Eq. (7.64). This term increases strongly when  $\tilde{r}$  approaches the singularity at  $\tilde{r} = 5$ . For  $Pe \lesssim 10$ , the exponential factor decays fast with increasing  $\tilde{r}$ , before the term  $[\Delta/(d-1)] \partial^2 \tilde{U} / \partial \tilde{r}^2$  becomes relevant. Here, the distribution function can well be described by Eq. (7.49). With increasing  $Pe$ , the exponential factor decays at larger radii and the pre-factor gains importance, resulting in the peak.

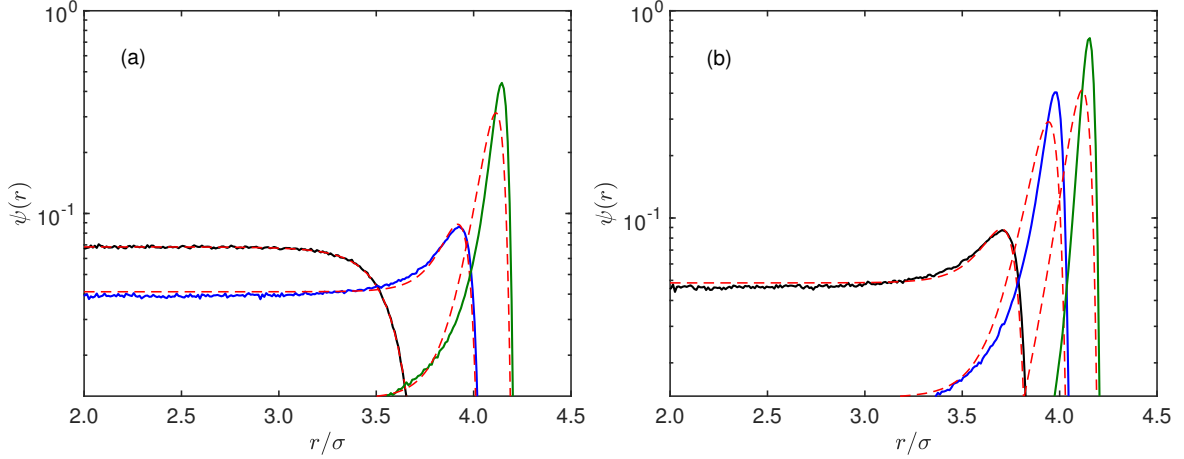


Figure 7.4: Radial stationary-state distribution functions of an AOUP confined in the anharmonic potential (7.63) for the Péclet numbers  $Pe = 1, 10, 100$  (left to right) and (a)  $\Delta = 0.1$ , (b)  $\Delta = 1$ . The solid lines are simulation results of Eq. (6.1), without thermal noise, and Eq. (6.16). The dashed lines are analytical results within UCNA (Eq. (7.64)).

Deviations between simulations and theory appear for  $Pe > 10$ . These differences are even more pronounced for  $\Delta > 0.1$ . At  $\Delta = 1$  (Fig. 7.4(b)), good agreement is still obtained for  $Pe \lesssim 1$ , but larger  $Pe$  lead to marked discrepancies between theory and simulation curves, with peak heights of the simulation data exceeding those of the theoretical prediction substantially. Here, theory predicts the behavior only rather qualitatively. Considering smaller  $\Delta$ , we find good agreement for even larger Péclet numbers.

In the limit  $\Delta \gg 1$ , Eq. (7.64) reduces to

$$\psi(\tilde{r}) = \frac{1}{Z_\infty} \frac{\partial^2 \tilde{U}}{\partial \tilde{r}^2} \exp \left( -\frac{d}{2Pe^2} \left( \frac{\partial \tilde{U}}{\partial \tilde{r}} \right)^2 \right). \quad (7.65)$$

Interestingly, this function is independent of  $\Delta$  for any  $Pe$ . A comparison shows that Eq. (7.65) indeed describes the simulation data very well for  $Pe \gg 1$ . Good agreement is already obtained for  $Pe \approx 1$  in the vicinity of the peak of the distribution function. Only for small  $\tilde{r}$  deviations are found due to the fast decay of  $\partial^2 \tilde{U} / \partial \tilde{r}^2$  with decreasing  $\tilde{r}$ .

#### Comparison of ABP simulations and UCNA

Figure 7.5 shows simulation results for the radial positional probability distribution function of ABPs. Qualitatively, the shape of the curves is very similar to the AOUP results. However, the appearing peaks for ABPs are sharper and higher. Quantitatively, we obtain close agreement with the theoretical prediction over a range of Péclet numbers, where the range depends on  $\Delta$ . For  $\Delta = 0.01$  (Fig. 7.5(a)), we observe deviations for  $Pe \gtrsim 100$ . At

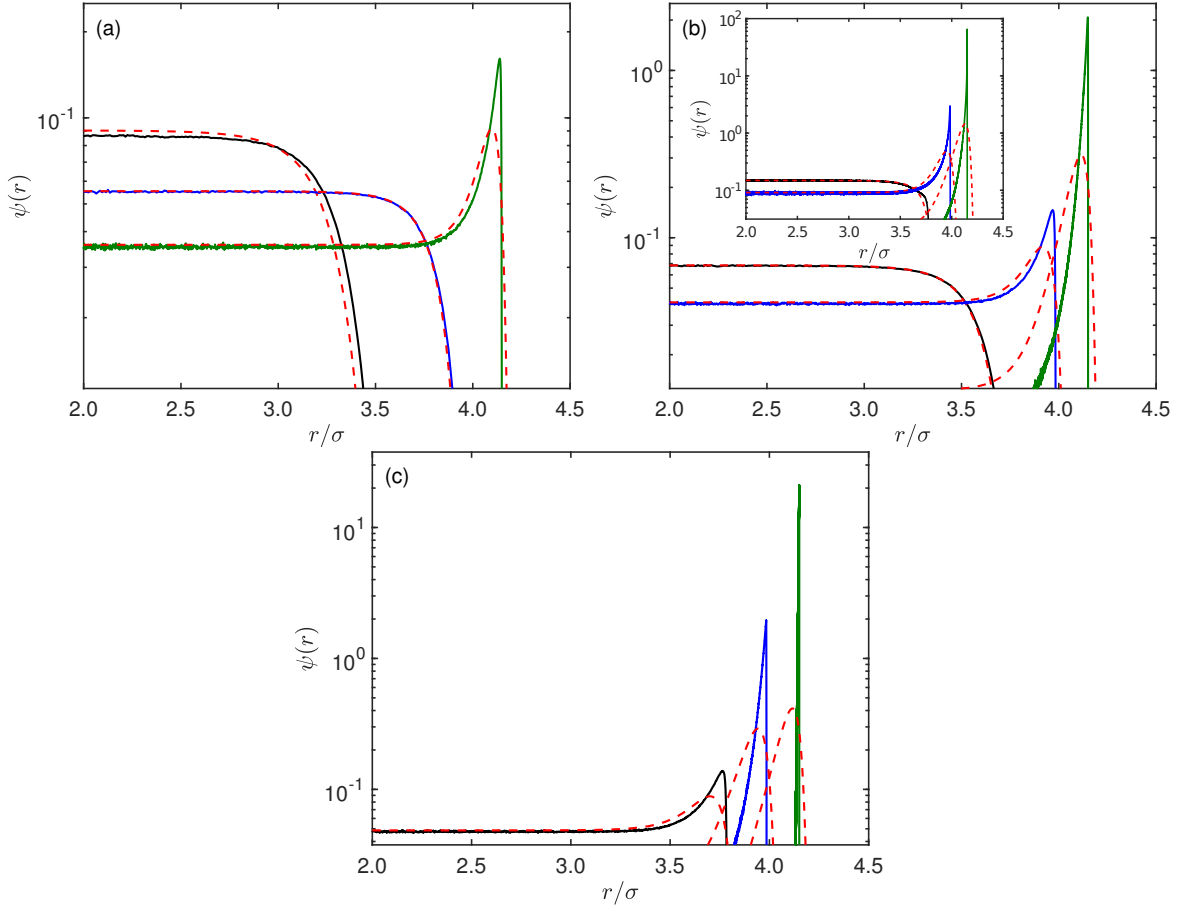


Figure 7.5: Radial stationary-state distribution functions of an ABP confined in the anharmonic potential (7.63) for (a)  $\Delta = 0.01$ , (b)  $\Delta = 0.1$  and (c)  $\Delta = 1$ , and the Péclet numbers  $Pe = 1, 10$ , and  $100$  (left to right). The solid lines are simulation results of Eq. (6.1), without thermal noise, and Eq. (6.3). The dashed lines are analytical results within the UCNA (Eq. (7.64)). The inset in (b) shows results for a 2d system for the same parameters.

$\Delta = 0.1$  (Fig. 7.5(b)), the curves for  $Pe = 10$  already digress from each other, and for  $\Delta = 1$  (Fig. 7.5(c)), deviations are present for  $Pe \gtrsim 1$ .

The inset of Fig. 7.5(b) displays results for a 2d system. The qualitative behavior is the same as in 3d. However, the peaks are somewhat higher and narrower. The agreement with the theoretical approach is equally good.

Hence, the simulation and theoretical results are consistent with the assumption of UCNA, and an adequate theoretical representation is obtained for  $\gamma_R \rightarrow \infty$ , or  $\Delta \rightarrow 0$ . Alternatively, the UCNA applies for  $Pe \gg 1$  in the limit  $\Delta \rightarrow \infty$ . However, the latter limit is of little practical importance, since typically  $\Delta < 1$  for biological and synthetic microswimmers. The limitations of the UCNA for microswimmers are evident for  $\Delta \approx 0.3$ , where thermal fluctuations determine the rotational diffusion. Here, we already see deviations be-



tween simulation results and the theoretical prediction for  $Pe \lesssim 1$  (see Fig. 7.5(c)). We neglect thermal fluctuations in the current study. For Péclet numbers on the order of unity, thermal fluctuations may matter and determine the properties of the active system. Hence, the distribution function of the radial position would be given by the Maxwell-Boltzmann distribution  $\psi(\tilde{r}) \sim \exp(-\beta\tilde{U})$  rather than the UCNA.

Considering the condition (7.56) for the balance of active and confining forces, we find very good agreement of this prediction with the peak positions from simulations as well as theoretical predictions for all Péclet numbers.

### Mean square velocity

The radial mean square velocity  $\langle \mathbf{u}^2 \rangle_u = \langle \dot{\mathbf{r}}^2 \rangle_u$  (7.51) for the potential (7.63) reads

$$\frac{\langle \mathbf{u}^2 \rangle_u}{v_0^2} = \frac{1}{3} \left( 1 + \frac{\Delta}{(d-1)\tilde{r}} \frac{\partial \tilde{U}}{\partial \tilde{r}} \right)^{-1} \left[ 3 + \left( \frac{1}{\tilde{r}} \frac{\partial \tilde{U}}{\partial \tilde{r}} - \frac{\partial^2 \tilde{U}}{\partial \tilde{r}^2} \right) \left( \frac{d-1}{\Delta} + \frac{\partial^2 \tilde{U}}{\partial \tilde{r}^2} \right)^{-1} \right] \quad (7.66)$$

in terms of  $\Delta$ . Evidently, this expression is independent of the Péclet number. Figure 7.6 shows simulation and theoretical results for the radial dependence of  $\langle \mathbf{u}^2 \rangle_u / v_0^2$ . Evidently, the mean square ABP velocity is constant over most of the potential range. Only at large radial distances,  $\langle \mathbf{u}^2 \rangle_u$  drops rapidly. Consistent with the radial probability distribution  $\psi(r)$ , the simulation data drop to zero at  $\tilde{r}_m = r_m/\sigma$  determined by the condition (7.56) for the various Péclet numbers. Interestingly, the simulation results are independent of  $\Delta$ . In contrast, the analytical expression (7.66) is independent of  $Pe$ , but depends on  $\Delta$ . Hence, the approximate conditional velocity distribution function (7.50) (see also Eq. (7.45)), qualitatively reproduces the simulation result, but misses important dependencies on  $Pe$  and  $\Delta$ .

## 7.4 Summary

We have investigated the properties of active Brownian particles confined in a radially symmetric potential. Two potentials have been considered, a harmonic and an anharmonic potential with a singularity at a finite radius. In the analytical approach, the AOUP model has been adopted, and the general time-dependent nonequilibrium distribution function for the harmonic potential has been determined. In case of the anharmonic potential, the stationary-state multidimensional distribution function within the Unified Colored Noise Approximation (UCNA) has been considered [244]. In computer simulations, stationary-state distribution functions have been determined for ABPs in three dimensions.

A primary goal of our study is to clarify the extent to which the simulation results can be reproduced by the theoretical approaches. The study of ABPs and AOUPs confined in a harmonic potential clearly reveals the strong effect of the condition  $|\mathbf{v}| = v_0 = \text{const.}$  on the stationary-state properties. Thereby, it is essential to compare appropriate distribution functions, which is the conditional probability distribution function  $\psi(r, |v_0)$  for AOUPs. We find good agreement between AOUP and ABP results for weak potentials  $k \lesssim 1$  up to rather large

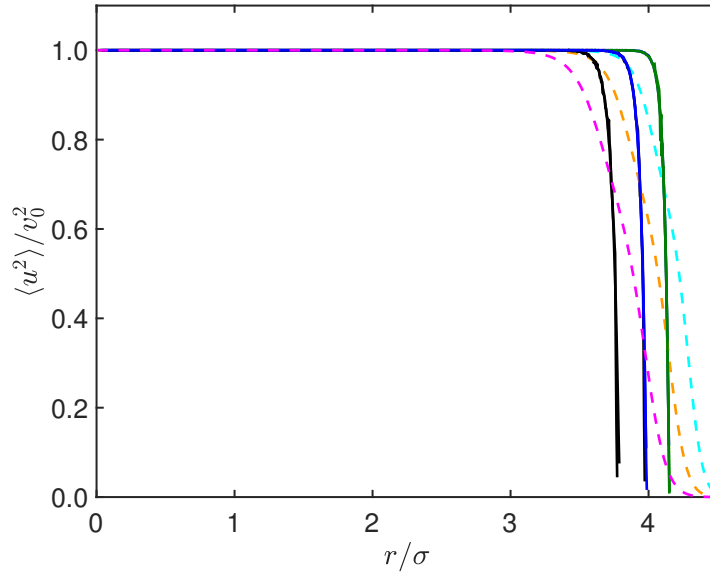


Figure 7.6: Mean square radial velocity  $\langle \mathbf{u}^2 \rangle_u$  of an ABP confined in the three-dimensional potential (7.63) as function of the radial distance  $\tilde{r} = r/\sigma$  for various  $Pe$  and  $\Delta$ . The solid lines are simulation results, where  $Pe = 1, 10$ , and  $100$  (left to right). Here,  $\langle \mathbf{u}^2 \rangle_u$  is independent of  $\Delta$ , and the curves for the various  $\Delta$  at a given  $Pe$  superimpose. The dashed lines are calculated according to Eq. (7.66), where  $\Delta = 1, 0.1$ , and  $0.01$  (left to right). Here, the theoretical expression is independent of the Péclet number.

Péclet numbers. For larger stiffness ( $\tilde{k} \gtrsim 10$ ), strong deviations appear when  $Pe$  exceeds the critical value  $Pe_c$  of Eq. (7.29), where activity dominates over thermal fluctuations. Thereby, agreement is better for larger stiffness of the potential, which is partially related to the increasing critical Péclet number,  $Pe_c$ , with increasing  $\tilde{k}$ . In particular, for AOUPs, we find a distribution function  $\psi(\xi|v_0)$ , where  $\xi \sim Pe^2 r$ , which is independent of the Péclet number in the limit  $Pe \gg Pe_c$ . The dependence on the propulsion velocity is absorbed in the variable  $\xi$ . Only a dependence on  $\tilde{k}\Delta$  remains, i.e., the potential strength and the rotational diffusion coefficient. Interestingly, a similar scaling is obtained for the radial distribution function of ABPs.

Our studies of an anharmonic system within the UCNA yield good agreement with simulations for an AOUP. The probability distribution functions agree well for  $\Delta \lesssim 0.1$  and  $Pe \lesssim 100$ . Thereby, the agreement improves with decreasing  $\Delta$ , i.e., increasing rotational diffusion coefficient. The distribution functions obtained from simulations of ABPs exhibit larger differences to the UCNA results; visible disparities appear already for  $Pe = 10$  at  $\Delta = 0.1$ , which increase with increasing  $Pe$  and  $\Delta$ .

In general, the colored-noise correlation function applied for the UCNA is

$$\langle \mathbf{v}(t) \cdot \mathbf{v}(0) \rangle = 3\hat{D}\gamma_R e^{-\gamma_R t}, \quad (7.67)$$

with independent parameters  $\gamma_R$  and the (translational) diffusion coefficient  $\hat{D}$  [238, 244].

The relation to our studies is established by setting  $v_0^2 = 3\hat{D}\gamma_R$  (cf. Eq. (6.18)) with the independent parameters  $\gamma_R$  and  $v_0$ . The two different approaches lead to distinctly different regimes of applicability of the UCNA. As discussed in Ref. [238], the UCNA is suitable, i.e., the second derivative in Eq. (7.35) can be neglected, in the limits  $\gamma_R \rightarrow \infty$  and  $\gamma_R \rightarrow 0$ . In contrast, for our independent parameters, only the limit  $\gamma_R \rightarrow \infty$  applies. For smaller  $\gamma_R$ , or larger  $\Delta$ , the propulsion velocity  $v_0$ , or the Péclet number, has to be small (see Eq. (5.37) of Ref. [238]). This is consistent with our presented results.



# Chapter 8

## Local pressure in system of ABPs

The pressure in active systems comprises three contributions, the ideal gas pressure, swim pressure, and a contribution due to interparticle and wall interactions. The swim pressure is the first moment of the self-propulsive force [76, 102, 103], given by the virial

$$P_s = \frac{1}{dV} \sum_{i=1}^N \langle \mathbf{F}_i^{ac} \cdot \mathbf{r}_i \rangle, \quad (8.1)$$

where  $\mathbf{F}_i^{ac}$  is the propulsion force of particle  $i$ . Swim pressure is a purely entropic quantity arising from self-propulsion [113], which has been proposed as an intrinsic feature to understand self-assembly and the phase behavior of active systems. For ABP systems, the swim pressure dependence on the confining wall and the particle-wall interaction has been reported along with a pressure definition in case of periodic open systems [103].

In this chapter, we present an expression for the local pressure in active systems arising due to particle flux within a local region of the whole ABP system. We present a characterization of the local pressure, starting from ideal gas ABPs to ABPs with excluded-volume interactions, for various parameters. Such local pressure in ABP systems, defined in terms of local observables, is a non-zero quantity, in contrast to the results presented in Ref. [104], and is consistent with the available literature about pressure in active systems. In particular, it is applicable to systems with periodic boundaries. We find the “active flux” component of the local pressure to be equivalent to the swim pressure of active particles. The pressure in confined systems has a prolonged boundary effect on the bulk value of the system and leads to a value smaller than that of an open system, which is related to the smaller flux due to decreasing local density by surface accumulation. Further, the local pressure definition can very well be applied to systems of ABPs with phase separation, and exhibits a van-der-Waals-type pressure-volume curve typical for gas-liquid coexistence, as has been observed earlier [102, 103].

### 8.1 Virial pressure

The virial theorem is frequently used to estimate the average pressure over the entire volume of a confined system. Such a virial expression can be attained for a system of ABPs confined by impenetrable walls [103, 104]. Multiplication of Eq. (6.1) by  $\mathbf{r}_i$  and then taking ensemble

average yields

$$\gamma_T v_0 \langle \mathbf{e}_i \cdot \mathbf{r}_i \rangle + \langle \mathbf{F}_i \cdot \mathbf{r}_i \rangle + \langle \mathbf{F}_i^s \cdot \mathbf{r}_i \rangle = 0, \quad (8.2)$$

since  $\langle \dot{\mathbf{r}}_i \cdot \mathbf{r}_i \rangle = (1/2) \frac{d}{dt} \langle \mathbf{r}_i^2 \rangle$ , the time derivative of mean square displacement, vanishes in the stationary state for a confined diffusive system. The force term in Eq. (8.2) can be written in terms of contributions from internal forces and the wall forces as

$$\sum_{i=1}^N \langle \mathbf{F}_i \cdot \mathbf{r}_i \rangle = \frac{1}{2} \sum_{i=1}^N \sum_{j=1}^N \langle \mathbf{F}_{ij} \cdot (\mathbf{r}_i - \mathbf{r}_j) \rangle + \sum_{i=1}^N \langle \mathbf{F}_i^s \cdot \mathbf{r}_i \rangle, \quad (8.3)$$

where the latter is related to the mechanical wall pressure of the system. As shown in Ref. [103], for special geometries such as cuboidal and spherical volumes the average wall pressure is given by

$$P = -\frac{1}{dV} \sum_{i=1}^N \langle \mathbf{F}_i^s \cdot \mathbf{r}_i \rangle. \quad (8.4)$$

Therefore, following the virial expression (8.2), sum over all the particles yields the expression for the pressure relating it to the bulk properties

$$P = \frac{1}{dV} \left[ 3Nk_B T + \gamma_T v_0 \sum_{i=1}^N \langle \mathbf{e}_i \cdot \mathbf{r}_i \rangle + \frac{1}{2} \sum_{i=1}^N \sum_{j=1}^N \langle \mathbf{F}_{ij} \cdot (\mathbf{r}_i - \mathbf{r}_j) \rangle \right]. \quad (8.5)$$

The first term on the right-hand side is the ideal-gas contribution to the pressure originating from the stochastic random forces  $\mathbf{F}_i$ . The other two terms are the virial contribution due to active and interparticle forces. The second term on the right-hand side is the swim pressure of ABPs, as mentioned earlier in Eq. (8.1). For a dilute system of active particles, i.e., in case of zero interparticle forces, the virial pressure has the form

$$P = \frac{Nk_B T}{V} \left( 1 + \frac{v_0^2}{d(d-1)D_R D_T} \right) + \frac{1}{dV} \frac{v_0}{(d-1)D_R} \sum_{i=1}^N \langle \mathbf{F}_i^s \cdot \mathbf{e}_i \rangle. \quad (8.6)$$

The first term corresponds to the ideal bulk pressure

$$P_{id} = \frac{Nk_B T}{V} \left( 1 + \frac{v_0^2}{d(d-1)D_R D_T} \right) \quad (8.7)$$

in a system of active particles [100, 102, 250]. The second term accounts for the interactions with the walls, and is responsible for various phenomena such as wall accumulation. It disappears in the limit of  $V \rightarrow \infty$ .

## 8.2 Local pressure

### 8.2.1 Passive systems

In Ref. [251], the pressure within a local volume  $V$  is computed following Schweitz virial relation for open systems. The Schweitz virial relation states that [251, 252]

$$\left\langle \sum_{i=1}^N \frac{\mathbf{p}_i^2}{M_i} \Lambda_i(\mathbf{r}) \right\rangle + \left\langle \sum_{i=1}^N (\mathbf{r}_i \cdot \mathbf{F}_i) \Lambda_i(\mathbf{r}) \right\rangle + \left\langle \sum_{i=1}^N (\mathbf{r}_i \cdot \mathbf{p}_i) \dot{\Lambda}_i \right\rangle = 0, \quad (8.8)$$

where  $\mathbf{p}_i$  and  $M_i$  are the momentum and mass of particle  $i$ , and  $\Lambda_i$  determines whether or not particle  $i$  is within the region of interest (volume  $V$ ) at time  $t$ .  $\Lambda_i$  is unity if the particle is within the region and zero otherwise. For open systems, this relation can be derived by setting the time derivative of the function  $\left\langle \sum_{i=1}^N (\mathbf{r}_i \cdot \mathbf{p}_i) \Lambda_i(\mathbf{r}) \right\rangle$  to zero in the stationary state.

The expression for the local pressure within the volume  $V$ ,  $P_{local}$ , can be derived from the Schweitz virial relation.  $P_{local}$  has two components, the kinetic component  $P_{kin}$ , which expresses the particle momentum flux across the boundaries of the region of interest and the interaction component  $P_{int}$ , appearing due to interparticle interaction forces. Thus, the local pressure can be expressed as  $P_{local} = P_{kin} + P_{int}$ , with [251]

$$P_{kin} = \frac{1}{dV} \left\langle \sum_{i=1}^N (\mathbf{r}_i \cdot \mathbf{p}_i) \dot{\Lambda}_i \right\rangle, \quad (8.9)$$

$$P_{int} = \frac{1}{dV} \left[ \left\langle \sum_{\text{in out}} (\mathbf{r}_i - l_{ij} \mathbf{r}_{ij}) \cdot \mathbf{F}_{ij} - \sum_{\text{out out}} l_{ij} \mathbf{r}_{ij} \cdot \mathbf{F}_{ij} \right\rangle \right]. \quad (8.10)$$

Here,  $l_{ij}$  is the fraction of the line joining particles  $i$  and  $j$  that lies inside  $V$ ,  $\sum_{\text{in out}}$  contains contributions when particle  $i$  is inside the volume and particle  $j$  is outside, and  $\sum_{\text{out out}}$  is when both particle  $i, j$  are outside.

### 8.2.2 ABP systems

To derive a local pressure expression for an ABP system, we consider a local volume of the whole system, i.e., a sub-volume in a periodic system or in the bulk of a confined system. We start with deriving a virial expression, analogous to the Schweitz virial (8.8) in passive systems, for ABP particles in the local volume.

The overdamped equations of motion (6.1), (6.3) of particle  $i$  can be rewritten in the stochastic differential form as

$$d\mathbf{r}_i = \left( v_0 \mathbf{e}_i + \frac{1}{\gamma_T} \mathbf{F}_i \right) dt + \frac{1}{\gamma_T} d\mathbf{\Gamma}_i, \quad (8.11)$$

$$d\mathbf{e}_i = \mathbf{e}_i \times d\hat{\boldsymbol{\eta}}_i - \gamma_R \mathbf{e}_i dt, \quad (8.12)$$

within Ito calculus [103, 236]. The time evolution of the average of any observable quantity  $\hat{O}$  from any stochastic process can be written as

$$\frac{d}{dt} \langle \hat{O} \rangle = \left\langle \frac{d}{dt} \hat{O} \right\rangle = \langle \mathcal{L} \hat{O} \rangle, \quad (8.13)$$

where the backhand operator  $\mathcal{L}$  follows from Ito's formula for change of variables (see Sec. 1.2.2) [162]. For the equations (8.11), (8.12), the operator  $\mathcal{L}$  is given by

$$\mathcal{L} = \left( v_0 \mathbf{e} + \frac{1}{\gamma_T} \mathbf{F} \right) \cdot \nabla_r + D_T \nabla_r^2 - \gamma_R \mathbf{e} \cdot \nabla_e + \frac{2}{3} \gamma_R \nabla_e^2. \quad (8.14)$$

In the following analytical approach we neglect the random force  $\mathbf{F}$ . Thus, considering the observables  $\hat{O} = (\mathbf{r}_i \cdot \mathbf{v}_i) \Lambda_i$  and  $\hat{O} = \mathbf{r}_i^2 \Lambda_i$  in Eq. (8.13), which involve the particle position  $\mathbf{r}_i$  and the self-propulsion velocity  $\mathbf{v}_i = v_0 \mathbf{e}_i$ , we obtain the following relations

$$\langle (\dot{\mathbf{r}}_i \cdot \mathbf{v}_i) \Lambda_i \rangle + \left\langle (\mathbf{r}_i \cdot \mathbf{v}_i) \dot{\Lambda}_i \right\rangle - \gamma_R v_0 \langle (\mathbf{e}_i \cdot \mathbf{r}_i) \Lambda_i \rangle = 0, \quad (8.15)$$

$$v_0 \langle (\mathbf{e}_i \cdot \mathbf{r}_i) \Lambda_i \rangle + \frac{1}{\gamma_T} \langle (\mathbf{F}_i \cdot \mathbf{r}_i) \Lambda_i \rangle = 0. \quad (8.16)$$

Here, all the time derivatives corresponding to LHS of Eq. (8.13) vanishes in the stationarity state.  $\Lambda_i$  has the same meaning as for the passive systems measuring if particle  $i$  is within the sub-volume, and  $\dot{\Lambda}_i$  follows the relation

$$\dot{\Lambda}_i = \dot{\mathbf{r}} \cdot \frac{\partial \Lambda}{\partial \mathbf{r}}. \quad (8.17)$$

For a cuboid, the explicit mathematical form of  $\Lambda(\mathbf{r})$  can be written as  $\Lambda = \Lambda_x \Lambda_y \Lambda_z$ , with  $\Lambda_\alpha$  ( $\alpha \in \{x, y, z\}$ ) expressed in terms of the Heaviside step function  $\Theta(r_\alpha)$  in the following manner

$$\Lambda_\alpha = \Theta(r_\alpha - L_\alpha^1) - \Theta(r_\alpha - L_\alpha^2), \quad (8.18)$$

where  $L_\alpha^1$  and  $L_\alpha^2$  are the positions of the boundaries of the local region. Therefore, the time derivative of each  $\Lambda_\alpha$  yields

$$\dot{\Lambda}_\alpha = \frac{\dot{r}_\alpha}{|\dot{r}_\alpha|} \left[ \delta(t - t') \Big|_{r_\alpha=L_\alpha^1} - \delta(t - t') \Big|_{r_\alpha=L_\alpha^2} \right], \quad (8.19)$$

with the help of delta function property  $\delta(x) = (1/|\dot{x}|)\delta(t)$ , and is consistent with Eq. (8.17). Following these expressions, it is clear that  $\dot{\Lambda}$  produces a positive  $\delta$ -function peak at the moment when a particle enters and negative peak when it leaves the region of interest.

The combination of the expressions (8.15) and (8.16) yields the local virial relation,

$$\frac{\gamma_T}{\gamma_R} \left\langle \sum_{i=1}^N (\dot{\mathbf{r}}_i \cdot \mathbf{v}_i) \Lambda_i \right\rangle + \frac{\gamma_T}{\gamma_R} \left\langle \sum_{i=1}^N (\mathbf{r}_i \cdot \mathbf{v}_i) \dot{\Lambda}_i \right\rangle + \left\langle \sum_{i=1}^N (\mathbf{F}_i \cdot \mathbf{r}_i) \Lambda_i \right\rangle = 0, \quad (8.20)$$



for the system of ABPs. This expression is similar to the Schweitz virial (8.8) involving volume terms (sum over particles within the local volume) and boundary terms (sum over particles crossing the boundary). In particular, the volume term  $(\gamma_T/\gamma_R) \left\langle \sum_{i=1}^N (\dot{\mathbf{r}}_i \cdot \mathbf{v}_i) \Lambda_i \right\rangle$  is analogous to the average kinetic energy term in Eq. (8.8), and  $\left\langle \sum_{i=1}^N (\mathbf{F}_i \cdot \mathbf{r}_i) \Lambda_i \right\rangle$  is equivalent to the interaction term, signifying the total force on particle  $i$  due to interaction with all the other particles in the absence of any external force. Similar to the momentum-flux term for passive systems, Eq. (8.20) includes the “active flux”  $(\gamma_T/\gamma_R) \left\langle \sum_{i=1}^N (\mathbf{r}_i \cdot \mathbf{v}_i) \dot{\Lambda}_i \right\rangle$  as a boundary term, due to self-propulsion and accounts for the exchange of particles between the volume  $V$  and its surroundings; it disappears in closed systems.

Now, the virial relation (8.20) can be used to determine a boundary expression for the local pressure in active systems. Pressure is defined as momentum flux across an arbitrary surface in a system [253]. The “active flux” term

$$\Phi_{ac} = \frac{\gamma_T}{\gamma_R} \left\langle \sum_{i=1}^N (\mathbf{r}_i \cdot \mathbf{v}_i) \dot{\Lambda}_i \right\rangle \quad (8.21)$$

of the local virial (8.20) can be accounted for the self-propulsion contribution to the pressure. To realize this, we separate the particle self-propulsion velocity  $\mathbf{v}_i$  into its components normal and tangential to the boundary as,  $\mathbf{v}_i = (\mathbf{v}_i \cdot \mathbf{n}_b) \mathbf{n}_b + (\mathbf{v}_i \cdot \mathbf{t}_b) \mathbf{t}_b$ , where  $\mathbf{n}_b$  is the normal pointing outwards to the volume and  $\mathbf{t}_b$  is the tangent to the local volume boundary. Then, the “active flux” turns into

$$\Phi_{ac} = \frac{\gamma_T}{\gamma_R} \left\langle \sum_{i=1}^N (\mathbf{v}_i \cdot \mathbf{n}_b) (\mathbf{r}_i \cdot \mathbf{n}_b) \dot{\Lambda}_i \right\rangle. \quad (8.22)$$

Due to the stochastic nature of the orientation vector, i.e.,  $\langle \mathbf{e}_i \rangle = 0$ , the term involving the tangential component of the velocity vanishes. Since  $\dot{\Lambda}_i$  is nonzero only at the boundary,  $(\mathbf{r}_i \cdot \mathbf{n}_b)$  is equal to the boundary position and can be taken out of the average. Thus, considering one particular direction, we have  $\Phi_{ac} = (\gamma_T/\gamma_R) \left\langle \sum_{i=1}^N (\mathbf{v}_i \cdot \mathbf{n}_b) \dot{\Lambda}_i \right\rangle (L_2 - L_1)$ , where  $L_2$  and  $L_1$  are the boundary positions (see Fig. 8.1), i.e.,  $\Phi_{ac}$  is the total outward “active flux” across the boundaries. At a certain instance of time, particles entering the region will contribute  $(\mathbf{r}_i \cdot \mathbf{v}_i)$  and particles leaving contribute  $-(\mathbf{r}_i \cdot \mathbf{v}_i)$ . But, the overall contribution is non-zero, as the velocity vector  $\mathbf{v}_i$  for particles leaving and entering are opposite in sign.

Further, from the virial equation (8.20), we obtain

$$\Phi_{ac} = -\frac{\gamma_T}{\gamma_R} \left\langle \sum_{i=1}^N (\dot{\mathbf{r}}_i \cdot \mathbf{v}_i) \Lambda_i \right\rangle - \left\langle \sum_{i=1}^N (\mathbf{F}_i \cdot \mathbf{r}_i) \Lambda_i \right\rangle. \quad (8.23)$$

For ideal ABP systems ( $\mathbf{F}_i = 0$ ),  $\left\langle \sum_{i=1}^N (\dot{\mathbf{r}}_i \cdot \mathbf{v}_i) \Lambda_i \right\rangle = v_0^2 \left\langle \sum_{i=1}^N \mathbf{e}_i^2 \Lambda_i \right\rangle = \langle N_r \rangle v_0^2$  and yields

$$\Phi_{ac} = -\frac{\gamma_T}{\gamma_R} \langle N_r \rangle v_0^2, \quad (8.24)$$

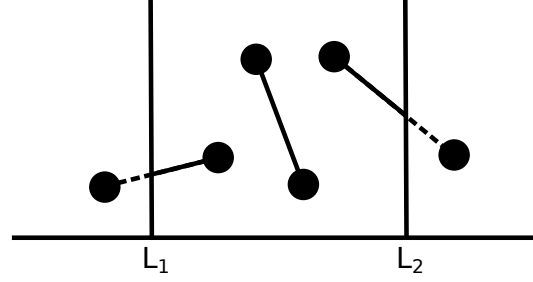


Figure 8.1: Schematic of the local region with boundaries at  $L_1$  and  $L_2$ . The fraction  $l_{ij}$  of the line joining particle  $i$  and  $j$  which lies inside the local region is denoted as a solid line.

with the total number  $N_r$  of ABPs in the local volume. This expression relates  $\Phi_{ac}$  to the ideal bulk pressure as

$$\Phi_{ac} = -dV P_{bulk}, \quad (8.25)$$

where  $P_{bulk} = \bar{\rho}_r k_B T (v_0^2 / d(d-1) D_R D_T)$  is the bulk pressure of an active system with average local bulk density  $\bar{\rho}_r$  of the considered region. It should be noted that  $\bar{\rho}_r$  is always smaller for confined systems compared to periodic systems, because of wall accumulation for the earlier case. Consequently, the local pressure in the bulk of a confined ABP system has an extended wall effect owing to the wall accumulation. In general, the self-propulsion or “active flux” contribution to the pressure can thus be written as

$$P_{ac} = -\frac{1}{dV} \Phi_{ac}. \quad (8.26)$$

In this context, it is important to point out that the virial relation (8.20) can even be extended for whole confined volume, i.e.,  $\Lambda$  takes into account the whole system ( $\Lambda = 1$ ). But there is no exchange of particles through the boundaries due to hard walls, leading to “active flux” being zero. In such a scenario, we have  $\gamma_R v_0 \left\langle \sum_{i=1}^N (\mathbf{e}_i \cdot \mathbf{r}_i) \Lambda_i \right\rangle$  with a non-zero value equal to  $\langle (\dot{\mathbf{r}}_i \cdot \mathbf{v}_i) \Lambda_i \rangle$  and we get back the virial (8.2) (neglecting  $\mathbf{I}$ ).

In presence of interparticle interactions, pressure will have additional contribution from the interparticle forces across surface. The interaction term,  $\left\langle \sum_{i=1}^N (\mathbf{F}_i \cdot \mathbf{r}_i) \Lambda_i \right\rangle$ , in Eq. (8.20) can be split into contributions due to interactions with particles inside and outside the region of interest following the approach in Ref. [251]. The latter case can be related to interaction component of the pressure as

$$P_{int} = -\frac{1}{dV} \left\langle \sum_{\text{in out}} (\mathbf{r}_i - l_{ij} \mathbf{r}_{ij}) \cdot \mathbf{F}_{ij} - \sum_{\text{out out}} l_{ij} \mathbf{r}_{ij} \cdot \mathbf{F}_{ij} \right\rangle. \quad (8.27)$$

Thus, we obtain the local pressure  $P_{local}^B$  as a combination of Eqs. (8.25), (8.27) as

$$P_{local}^B = -\frac{1}{dV} \left[ \frac{\gamma_T}{\gamma_R} \left\langle \sum_{i=1}^N (\mathbf{v}_i \cdot \mathbf{n}_b)(\mathbf{r}_i \cdot \mathbf{n}_b) \dot{\Lambda}_i \right\rangle + \left\langle \sum_{\text{in out}} (\mathbf{r}_i - l_{ij} \mathbf{r}_{ij}) \cdot \mathbf{F}_{ij} - \sum_{\text{out out}} l_{ij} \mathbf{r}_{ij} \cdot \mathbf{F}_{ij} \right\rangle \right]. \quad (8.28)$$

This is a boundary expression for the pressure on a sub-volume  $V$  of the total system of ABPs, which accounts for the swim pressure in terms of “active flux” through the surface together with the cross-boundary interparticle interactions. We get the volume expression for pressure by inserting Eq. (8.28) in the local virial (8.20), which yields

$$P_{local}^V = \frac{1}{dV} \left[ \frac{\gamma_T}{\gamma_R} \left\langle \sum_{i=1}^N (\dot{\mathbf{r}}_i \cdot \mathbf{v}_i) \Lambda_i \right\rangle + \left\langle \sum_i \sum_{j>i} l_{ij} \mathbf{r}_{ij} \cdot \mathbf{F}_{ij} \right\rangle \right]. \quad (8.29)$$

This is an expression for the bulk pressure within a sub-volume embedded in the whole volume of the system, with the active contribution

$$P_{ac}^V = \frac{1}{dV} \frac{\gamma_T}{\gamma_R} \left\langle \sum_{i=1}^N (\dot{\mathbf{r}}_i \cdot \mathbf{v}_i) \Lambda_i \right\rangle, \quad (8.30)$$

and the interaction contribution

$$P_{int}^V = \frac{1}{dV} \left\langle \sum_i \sum_{j>i} l_{ij} \mathbf{r}_{ij} \cdot \mathbf{F}_{ij} \right\rangle. \quad (8.31)$$

### 8.3 Simulation results for local pressure

We validate the local pressure expression via simulations of ABPs confined between walls and exposed to periodic boundaries, where we consider ABPs with and without excluded-volume interactions. Several parameter dependencies of the local pressure are characterized. The local pressure, along the  $z$ -axis, is calculated in a sub-volume  $V$  of the whole three-dimensional system. As indicated in Fig. 8.2, the dashed lines can correspond to walls or periodic boundaries depending on the considered system, but the other two directions always apply periodic boundaries. All the simulations of confined systems are carried out such that the box dimension normal to the walls is larger than the persistence length  $l_p = v_0/2D_R$  of an ABP, in particular, we consider wall separation  $L_z \geq 5l_p$ . The interparticle repulsive excluded-volume interactions between ABPs are captured by the truncated and shifted Lennard-Jones potential [167]

$$U_{LJ} = \begin{cases} \epsilon \left[ \left( \frac{\sigma}{r} \right)^{12} - \left( \frac{\sigma}{r} \right)^6 \right] - C, & r < r_c \\ 0, & r > r_c \end{cases}, \quad (8.32)$$

where  $r_c = \sqrt[6]{2}\sigma$  is the cut-off distance,  $C = \epsilon[(\sigma/r_c)^{12} - (\sigma/r_c)^6]$ , and the interaction strength  $\epsilon/k_B T = Pe$ .

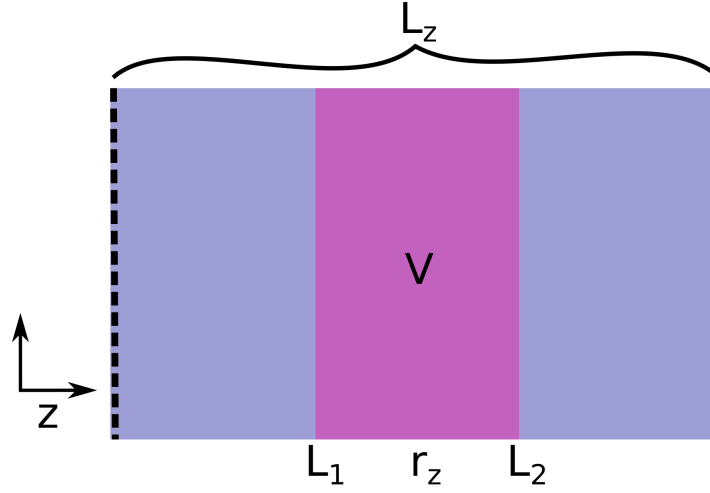


Figure 8.2: Schematic of the sub-volume  $V$  (magenta) of the whole three-dimensional system (blue) considered for local pressure calculation along  $z$ -axis. Depending on the considered system, the dashed lines can correspond to walls or periodic boundaries, while periodic boundaries are applied in the other two directions.  $L_z$  corresponds to wall separation, and  $r_z$  is the center position of the sub-volume in  $z$ -axis.

### 8.3.1 Closed systems

At first, we determine the local pressure in a system of ABPs confined by walls and without any explicit interparticle interactions (ideal active gas). Figure 8.3 shows the local pressure calculated in a volume  $V$  with its center located at different positions along the wall separation of the confined system, where the center position of a local volume in the direction normal to the wall is  $r_z$  and the volume dimension in that direction is  $0.1L_z$  (see Fig. 8.2). The local pressures calculated via the expressions (8.28) and (8.29) are identical, even the individual active and interaction components are equal. The mechanical pressure of the system, determined from the force per area of the confining walls, and the virial pressure from Eq. (8.6) are also presented. The local pressure remains constant through out the bulk of the system within an error of less than 2% and acquires the value of mechanical/virial pressure of the system. This indicates that by using Eq. (8.28), the local pressure can be computed anywhere in the bulk of the system.

Pressure in the non-interacting ABP system as a function of the activity or the Péclet number is displayed in Fig. 8.4(a), for a wall separation of  $L_z = 100\sigma$  and density  $\rho\sigma^3 = 0.3$ . The local pressure calculated with the expression (8.29) coincides with the mechanical/virial pressure of the system. The pressure (in reduced units of Sec. 6.1) increases monotonically with increasing Péclet number, but deviates from the linear dependence of an active ideal gas for large  $Pe$ . The local pressure for an ideal ABP system, from expression (8.24), in the reduced units of  $\gamma v_0/\sigma^2$ , is proportional to  $\bar{\rho}_r Pe$ . We observe that the bulk density  $\bar{\rho}_r$  decreases with increasing Péclet number (inset Fig. 8.4(a)) due to boundary effects and shows a

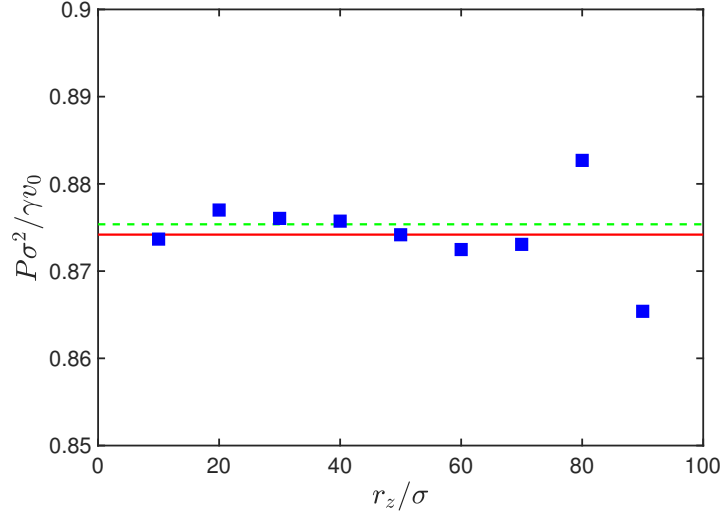


Figure 8.3: Local pressure, in a system of non-interacting ABPs, along the wall separation by considering local volumes (blue squares); the center position of the volumes normal to the walls is denoted by  $r_z$ . The red line shows the mechanical pressure determined from the confining walls with Eq. (8.4) and the green line shows virial pressure of the system computed using Eq. (8.5).

$\bar{\rho}_r = \rho(1 - cPe)$  dependency on the Péclet number, with  $c \approx 0.0017$  for  $L_z = 100\sigma$ . Hence, overall the pressure increases, but with a non-linear dependence of  $P \sim Pe(1 - cPe)$  on  $Pe$ , with increasing activity of the ABPs.

Figure 8.4(b) illustrates the pressure in an ideal ABP system as a function of system size  $L_z$  (wall separation) at a fixed density  $\rho\sigma^3 = 0.3$  and fixed Péclet number  $Pe = 120$ . The boundary effect on the pressure enters through the second term in the virial pressure expression (8.6). With the increase in the system size, the boundary effect decreases and the pressure approaches the ideal bulk pressure value. The pressure curve can be fitted by the wall separation dependence

$$P = P_{id}(1 - c/L_z), \quad (8.33)$$

with  $c \approx l_p$ , as indicated in Fig. 8.4(b). The boundary effect on the local pressure can be interpreted in terms of the bulk density  $\bar{\rho}_r$  as pointed out earlier. The inset of Fig. 8.4(b) shows that the local density  $\bar{\rho}_r$  in the bulk of the system increases with increasing wall separation as  $\bar{\rho}_r = \rho(1 - l_p/L_z)$ . Hence, the local density acquires the ideal bulk value as  $L_z \rightarrow \infty$  and so does the pressure, i.e., the boundary effect reduces with increasing system size and we observe an increase in the local pressure.

Extending the local pressure calculation to a system of ABPs with interparticle excluded-volume interactions, we observe that the local pressure in the bulk assumes the virial-pressure value of the whole system or, identically, the mechanical pressure value on the boundary walls, for various Péclet numbers, as depicted in Fig. 8.5 for a system with  $L_z = 100\sigma$  and  $\rho\sigma^3 = 0.2$ . The non-linear Péclet number dependence  $P \sim Pe(1 - 0.0015Pe)$  is observed

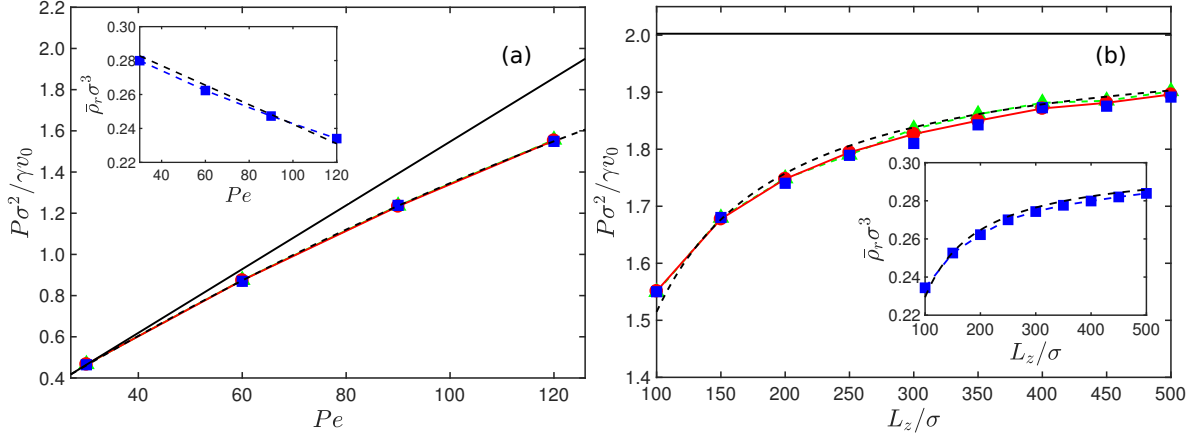


Figure 8.4: (a) Pressure in a system of non-interacting ABPs for the Péclet numbers  $Pe = 30, 60, 90, 120$ . The solid black line shows linear dependence on  $Pe$ . The inset shows the Péclet number dependence of the local density (blue) and the fit curve  $\bar{\rho}_r = \rho(1 - 0.0017Pe)$  (black). (b) Pressure as a function of system size at a fixed Péclet number  $Pe = 120$ . The inset shows local bulk density dependence on the wall separation (blue) with the fitted curve  $\bar{\rho}_r = \rho(1 - l_p/L_z)$  (black). The solid black line indicates the ideal bulk pressure  $P_{id}$  (8.7). The local pressure (8.29) is indicated in blue, the mechanical pressure (8.4) in red, and the virial pressure (8.5) in green, in both (a) and (b).

and the quadratic contribution is smaller than the non-interacting case. For interacting ABPs, there is comparatively less wall accumulation resulting in a higher bulk density compared to ideal ABPs and the pressure exhibits a very small increase. In particular, the inset of Fig. 8.5 shows the contribution of the swim pressure and interaction term separately for the virial pressure (8.5) in combination with the active contribution  $P_{ac}^V$  (8.30) and interaction contribution  $P_{int}^V$  (8.31) to the local pressure (8.29). We observe that the active component is equivalent to the swim pressure as has been pointed out earlier for ideal ABP systems in Eq. (8.24).

### 8.3.2 Periodic systems

We extend our definition of local pressure to the systems with periodic boundaries. In Ref. [103], the pressure has been defined in terms of the diffusion coefficient and also in terms of a virial expression for the periodic boundary system as

$$P = \rho k_B T \left( \frac{D}{D_T} - \frac{1}{6} \sum_{i=1}^N \sum_{j=1}^N \sum_n \langle \mathbf{F}_{ij}^n \cdot \mathbf{R}_n \rangle \right), \quad (8.34)$$

$$P = \rho k_B T \left( 1 + \gamma_T v_0 \sum_{i=1}^N \langle \mathbf{e}_i \cdot \mathbf{r}_i \rangle + \frac{1}{6} \sum_{i=1}^N \sum_{j=1}^N \sum_n \langle \mathbf{F}_{ij}^n \cdot (\mathbf{r}_i - \mathbf{r}_j - \mathbf{R}_n) \rangle \right), \quad (8.35)$$

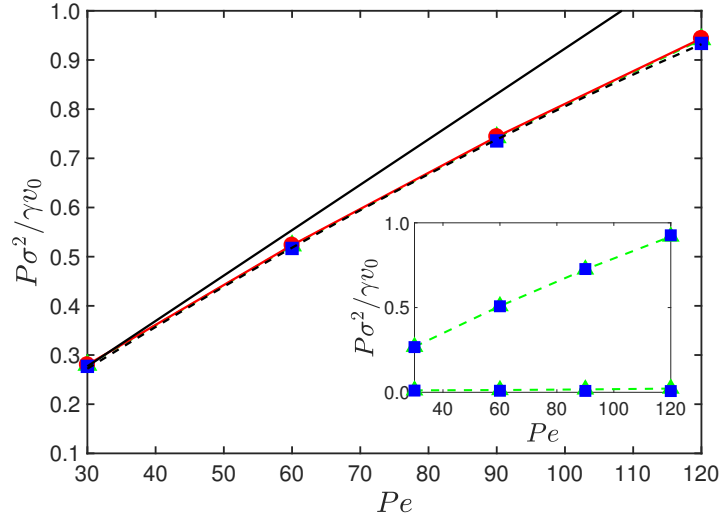


Figure 8.5: Pressure computed in a system of ABPs with excluded-volume interactions, which are confined between walls for various Péclet numbers. The local pressure (8.29) is indicated in blue, the mechanical pressure (8.4) in red and the virial pressure (8.5) in green. The solid black line shows linear dependence on  $Pe$  and the dashed black line is the fit curve  $P \sim Pe(1 - 0.0015Pe)$ . The inset shows the individual contributions to the virial pressure (green) and the local pressure (blue).

where  $\mathbf{R}_n = \mathbf{n}V^{1/3}$ , the winding vector  $\mathbf{n}$  counts the number of periodic boxes a particle has traversed, and  $\mathbf{F}_{ij}(\mathbf{r}_i - \mathbf{r}_j - \mathbf{R}_n) = \mathbf{F}_{ij}^n$ . In an ideal ABP system with periodic boundaries, pressure is proportional to the Péclet number (in our reduced units) and particle density with the explicit expression  $P = \rho k_B T Pe \Delta / (d - 1)d$  as evident from the above equations. We computed the local pressure in a periodic system of non-interacting ABPs and compared it with the virial pressure (8.35) (see Fig. 8.6). We observe agreement of the two definitions when pressure is plotted as a function of the Péclet number  $Pe$  and the density  $\rho$ .

Similarly, the local pressure definition is applied to the system of ABPs with excluded-volume interactions. Figure 8.7 illustrates the density dependence of the pressure for the considered Péclet numbers. The pressure has been normalized by the ideal active-pressure value  $P_{id}$  (8.7) and multiplied by the volume fraction  $\phi = \pi \rho \sigma^3 / 6$  to retain the linear dependence on density. The local pressure yields the same value as the virial pressure calculated by the virial expression (8.35). We observe a clear Péclet number dependence of the pressure. For small Péclet numbers ( $Pe \approx 30$ ), the pressure increases with increasing  $\phi$ . However, the pressure shows a non-monotonic behavior for higher Péclet numbers [76, 100, 102, 103]. From the phase diagram of Refs. [97, 103], we find that  $Pe = 90$  is close to phase separation and Péclet numbers above that ( $Pe > 90$ ) fall in the phase separating region. From Fig. 8.7, we observe that for ABPs in the phase separating region ( $Pe > 90$ ), the local pressure shows a jump at the critical volume fraction as has been observed in previous studies [103]. We also observe the similar density dependence of the local pressure at the lower volume fractions

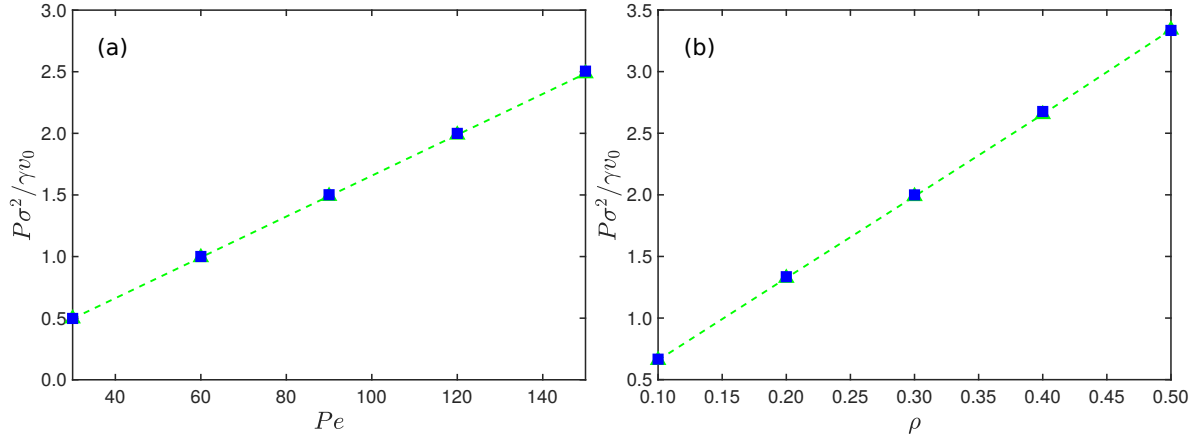


Figure 8.6: Pressure as a function of (a) Péclet number (fixed  $\rho = 0.3$ ) and (b) density (fixed  $Pe = 120$ ) in the systems of non-interacting ABPs with periodic boundaries. The local pressure (8.29) is indicated in blue and the virial pressure (8.35) in green.

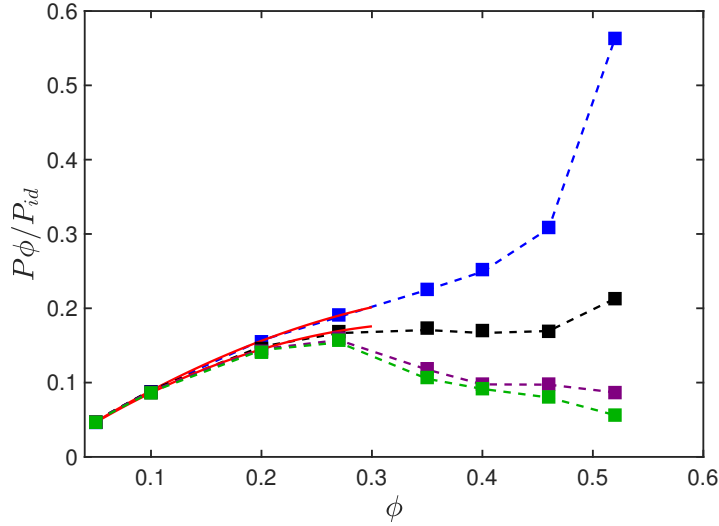


Figure 8.7: Pressure in systems of ABPs with excluded-volume interactions for the Péclet numbers  $Pe = 30$  (blue),  $90$  (black),  $300$  (magenta),  $825$  (green). The local pressure (8.29) is indicated by the squares and the virial pressure (8.35) by the dashed lines. The values are normalized by the  $P_{id}$  (8.7) of ideal ABPs at the same Péclet numbers. The red lines indicate the dependence  $P\phi/P_{id} = \phi(1 - c\phi)$ .

( $\phi < \phi_c$ ), which can be fitted by

$$\frac{P\phi}{P_{id}} = \phi(1 - c\phi), \quad (8.36)$$

with  $c \approx 1.38$ , as indicated in Fig. 8.7. Such behavior of the pressure has been observed in Refs. [102, 103]. The nonlinear concentration dependence of the pressure with a positive  $c$  yields a negative second virial coefficient  $B_2$ , which follows from the virial expansion of



pressure

$$\frac{P}{P_{id}} = 1 + B_2\rho + \dots \quad (8.37)$$

This yields, for Eq. (8.36), the second virial coefficient  $B_2 = -\pi\sigma^3c/6$ . In classical thermodynamics, a negative  $B_2$  value suggests the possibility of a gas-liquid phase transition as observed in ABP systems.

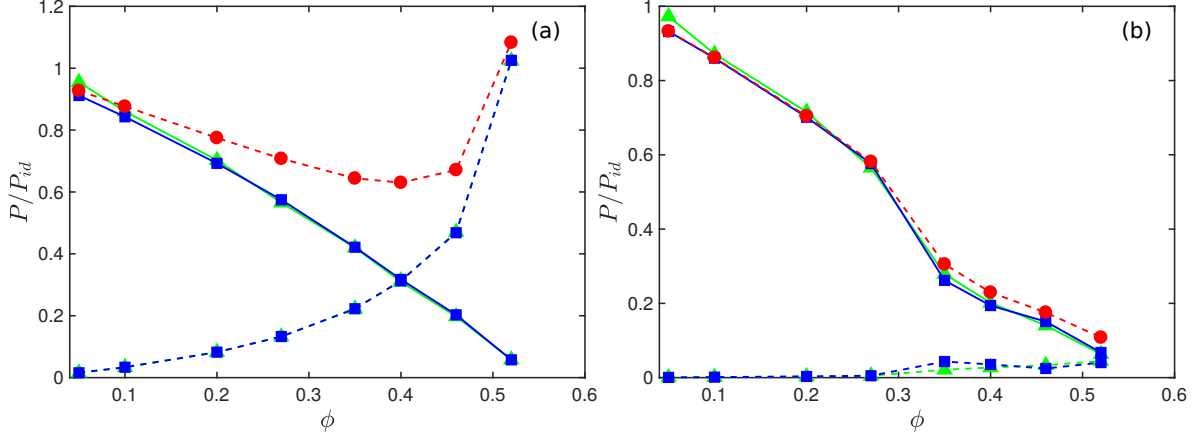


Figure 8.8: The local pressure of ABPs and its individual contributions for the Péclet numbers (a)  $Pe = 30$  and (b)  $Pe = 825$ , in comparison with individual contributions of the virial pressure (8.35). The values are normalized by the  $P_{id}$  (8.7) of ideal ABPs at the same Péclet numbers. The red symbols indicate the total local pressure (8.29). The blue symbols correspond to the local pressure components  $P_{ac}^V$  (solid line) and  $P_{int}^V$  (dashed line). The green symbols indicate swim pressure (solid line) and interaction (dashed line) contribution to the virial pressure (8.35).

Figure 8.8 displays the individual terms contributing to the local pressure, in comparison with the swim pressure and interaction term of Eq. (8.35), for the Péclet number  $Pe = 30$  and  $Pe = 825$ . The active-pressure component  $P_{ac}^V$  decrease monotonically with increasing volume fraction at small  $Pe = 30$  (Fig. 8.8(a)). With increasing density, particles are more obstructed by other ABPs and the interaction component increases gradually. This results in a decrease of “active flux” and the swim pressure contribution shows an decrease, while the interaction contribution increases monotonically. Overall, the total pressure decreases initially due to a reduced particle flux, but the  $P_{int}^V$  contribution dominate at large  $\phi$  and the respective pressure also increases with concentration.

The relevance of the individual contributions changes with increasing Péclet number. For  $Pe = 825$  (phase separating region), the activity-induced contribution to the pressure still decrease monotonically with increasing  $\phi$ . However, there is a very small contribution from the interparticle interactions and the local pressure is essentially identical with the active pressure  $P_{ac}^V$ . The jump in  $P_{ac}^V$  value reflects the phase transition at the critical density  $\phi_c$  [97]. The significantly small interaction contribution can be attributed to the fact that  $P_{int}^V$  depends roughly linearly on  $Pe$ , while  $P_{ac}^V \sim Pe^2$  and outweighs the growth of  $P_{int}^V$ .

### 8.4 Summary

We have presented theoretical and simulation results for the local pressure in systems of active Brownian particles. An expression for the pressure via a local virial equation is derived for a sub-volume in the bulk of the systems with confinement or with periodic boundary conditions. In particular, we have shown that the local pressure has a contribution associated with an “active flux” across the boundaries equivalent to momentum flux in passive systems. As an extension to this, the local pressure can be defined in terms of a boundary and a volume expression. We demonstrated, via characterization of the local pressure, that the activity-induced terms in both boundary and volume definitions are equivalent to the swim pressure of the active particles. Our simulations of non-interacting ABPs in systems under confinement showed that the local pressure in the bulk is the same as the mechanical pressure at the walls and has a value less than the ideal-bulk value due to surface accumulation and correspondingly a reduced bulk density. Even for interacting ABPs (excluded-volume) under confinement, the local pressure reproduces the mechanical pressure value on the bounding walls with an additional contribution due to interparticle interactions. Further, the local pressure calculation has been applied to periodic systems of ABPs with excluded-volume interactions, where the pressure increases with concentration and then decreases at higher concentrations for Péclet numbers exceeding a certain value. Quantitatively, the pressure dependence can be described by the relation  $P \sim \phi(1 - c\phi)$ , in agreement with previous studies [102, 103]. Considering the various contributions to the pressure individually, we also find that the contribution from activity dominates over the interparticle contribution for  $Pe > Pe_c$  in the phase separated region.

## Part IV

### Self-assembled magnetic spinners



# Chapter 9

## Active turbulence

Turbulent fluid motion can be found across multiple length- and time-scales. It has fascinated scientists for centuries and still poses a major challenge for theoretical physics [179,254]. The well-known high Reynolds number hydrodynamic turbulence in three dimensions is triggered by energy injection at the macroscale and cascading of energy to smaller scales. As an extension, the notion of active turbulence was recently introduced in the context of active fluids exemplified by suspensions of swimming bacteria, mixtures of microtubules and molecular motors, cell tissues, and other non-equilibrium systems [81, 128, 150–154, 255]. In contrast to hydrodynamic turbulence, the complex spatio-temporal behavior is caused by energy injection at the microscopic scale (e.g., of bacteria by rotation of their flagella) and subsequent cascading of energy toward larger scales. Active turbulence formally occurs at exceedingly small Reynolds numbers, rendering the fluid inertia negligible. Not surprisingly, statistical properties of active turbulence appear to be very different from its classical counterpart. Active turbulence does not exhibit a wide inertial range [81, 256] and a non-universal power-law behavior at large scales was recently reported [257].

In this chapter, we report on a simulation study of active turbulence and transport in a system of self-assembled ferromagnetic spinners in an external magnetic field in comparison with experimental observations. We find that the spinners and added inert particles exhibit active diffusion (diffusive motion is promoted by the activity of the system) while the diffusion arising from thermal noise is negligible in our system. Erratic motion of spinners results in a turbulent-like two-dimensional velocity field. This field exhibits the inverse energy-scaling  $q^{-5/3}$  with wave-number  $q$ , consistent with high-Reynolds number ( $Re$ ) two-dimensional turbulence [179], while  $Re \approx 30$  for the flow generating spinners in our system. Overall, our findings expand our understanding of synthetic tunable active systems with activity originating from rotations rather than self-propulsion.

### 9.1 Ferromagnetic dispersion particle system

We consider a two-dimensional simulation system with circular dispersion particles embedded in an explicit solvent described by MPC. Although in experiments, ferromagnetic microparticles are dispersed at the air-water interface (quasi-2D), the restriction to a two-dimensional system facilitates studies of larger system with more particles, which is necessary to characterize the chaotic turbulent properties of the flow field.

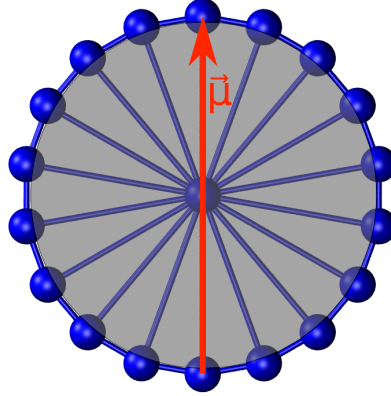


Figure 9.1: Two-dimensional disc-like dispersion particle composed of mass points connected with their neighbors. The arrow indicates the magnetic moment  $\boldsymbol{\mu} = \mu \mathbf{u} / \sigma$ .

### 9.1.1 Dispersion Model

A two-dimensional disc-like particle is modeled in analogy with the three-dimensional spherical colloid described in Sec. 4.1.1 [199]. Here, we distribute 18 point particles of mass  $M$  uniformly over the circumference of a circle of diameter  $\sigma$ , with an additional point particle at the center (see Fig. 9.1). The shape is maintained by strong harmonic bonds between both, the nearest neighbors and each particle with the center. The bond potential is

$$U_{bond}(R) = \frac{K}{2}(R - R_0)^2 \quad (9.1)$$

where  $R = |\mathbf{R}|$  is the distance between the particular pair,  $R_0$  their preferred bond length, and  $\mathbf{R}$  the bond vector.

Each particle carries a magnetic dipole. Aside from the bond potential, the applied force field accounts for magnetic dipole-dipole interactions, interactions with an external magnetic field, and excluded volume-interactions between different dispersion particles. The dipole-dipole interaction between a pair of particles is given by

$$U_{dipole}(R, \theta) = -\frac{\mu_0^2}{4\pi\epsilon_0 R^3} \left[ 3(\boldsymbol{\mu}_1 \cdot \hat{\mathbf{R}})(\boldsymbol{\mu}_2 \cdot \hat{\mathbf{R}}) - \boldsymbol{\mu}_1 \cdot \boldsymbol{\mu}_2 \right] \quad (9.2)$$

where  $\mu_0$  is the vacuum permeability,  $\boldsymbol{\mu}_1$  and  $\boldsymbol{\mu}_2$  are the magnetic moments of the colloids,  $\theta$  is the angle between  $\boldsymbol{\mu}_1$  and  $\boldsymbol{\mu}_2$ , and  $\hat{\mathbf{R}} = \mathbf{R}/|\mathbf{R}|$  is the unit vector along the center-to-center distance between the particle pair. The interaction potential with the external magnetic field  $\mathbf{B}$  is

$$U_{ext}(t) = -\boldsymbol{\mu} \cdot \mathbf{B}(t), \quad (9.3)$$

with the magnetic moment  $\boldsymbol{\mu} = \mu \mathbf{u} / \sigma$ . Here,  $\mathbf{u}$  is the vector between two beads diametrically opposite on the circle (see Fig. 9.1). In addition, excluded-volume interactions between

dispersed particles are captured by the truncated and shifted Lennard-Jones potential [167]

$$U_{LJ} = \begin{cases} \epsilon \left[ \left( \frac{\sigma}{R} \right)^{12} - \left( \frac{\sigma}{R} \right)^6 \right] - C, & R < R_c \\ 0, & R > R_c \end{cases}, \quad (9.4)$$

where  $\epsilon$  is the strength of the interaction,  $R_c = \sqrt[6]{2}\sigma$  is the cut-off distance, and  $C = \epsilon[(\sigma/R_c)^{12} - (\sigma/R_c)^6]$ .

The dynamics of the colloids is treated by standard molecular dynamics simulations. The dynamics of the colloidal mass points is described by Newton's equations of motion, which are solved by the velocity Verlet algorithm [167]. Hydrodynamic interactions are incorporated by the embedding multiparticle collision dynamics (MPC) fluid. Here, we use the angular-momentum conserving two dimensional variant of the algorithm (see Sec. 2.3) [193, 258].

### 9.1.2 Parameters

The particle diameter is  $\sigma = 6a$  and the mass of an constituent point particle is  $M = 10m$ . A spring constant of  $K = 5000k_B T/a^2$  is applied such that the circular shape of the colloids is maintained. Moreover the Lennard-Jones interaction strength is chosen as  $\epsilon/k_B T = 1$ . The time step  $\Delta t_{MD} = 0.01\tau$  is used for the molecular dynamics simulations of the dispersion particle dynamics.

In the 2D MPC approach, the collision angle  $\zeta = 130^\circ$ , average number of MPC particles per collision cell  $\langle N_c \rangle = 10$ , and collision time  $h = 0.1\tau$  are applied. This yields the kinematic viscosity  $\nu \approx 0.37a^2/\tau$ . The corresponding translation and rotational diffusion coefficients are  $D_0 = 4.4 \times 10^{-2}a^2/\tau$  and  $D_R = 2 \times 10^{-3}/\tau$  for a dispersion in dilute solution.

The magnetic moment of the dispersion particles is set to  $\mu = 480\sqrt{k_B T a^3/\mu_0}$  and the strength of the alternating magnetic field to  $B_0 = 0.8\sqrt{k_B T \mu_0/a^3}$ . This alternating external magnetic field leads to self-assembled spinners of average length  $L_s \approx 3.51\sigma$  at the frequency  $\omega = 2\pi f_B = 0.05\tau^{-1}$  (see fig. 9.6). We can define the Reynolds number with respect to spinners and the rotational flows they generate. The typical rotational velocity of the fluid at the end point of spinner is  $v \approx L_s \omega/2$ . This yields the Reynolds number  $Re \approx L_s^2 \omega/2\nu \approx 30$  for this specific set of parameters.

## 9.2 Phase diagram

Dispersion particles under the influence of an uniaxial alternating field undergo rotation as a consequence of their non-negligible inertia, and the fluid their motion entrains. Following Ref. [127] the equation of motion for an individual particle orientation can be written as

$$I_r \frac{d^2 \phi}{dt^2} + \alpha_r \frac{d\phi}{dt} = \mu H_0 \sin(\omega t) \sin(\phi), \quad (9.5)$$

where  $I_r$ ,  $\alpha_r$ ,  $\mu$  are the moment of inertia, the rotational drag, and the magnetic moment. This equation describes the balance between viscous and magnetic torques on the particle and the particle's inertia. The magnetic contribution on the right hand side can be decomposed in clockwise and counter-clockwise oscillations

$$H_0 \sin(\omega t) \sin(\phi) = \frac{H_0}{2} (\cos(\phi - \omega t) - \cos(\phi + \omega t)). \quad (9.6)$$

This implies clockwise and counterclockwise rotations are equally probable. If we consider one of the oscillations, the equation corresponds to rotation of the particle with frequency  $\omega$  and the threshold for this rotation to happen is  $\frac{\mu H_0}{2} > \alpha_r \omega$ .

The torque exerted on the dispersion particles dissipates locally in the liquid and results in hydrodynamic flows around the particles. Thereby, the particles interact mainly via two specific type of forces, magnetic dipole-dipole interaction and hydrodynamic forces. As a consequence of the interplay between these two forces the system exhibits a diverse range of quasi-stable dynamic structures. These various phases, as a function of the field frequency and field amplitude, are illustrated in the phase diagram Fig. 9.2. This is in accordance with the experimental observations in Ref. [127].

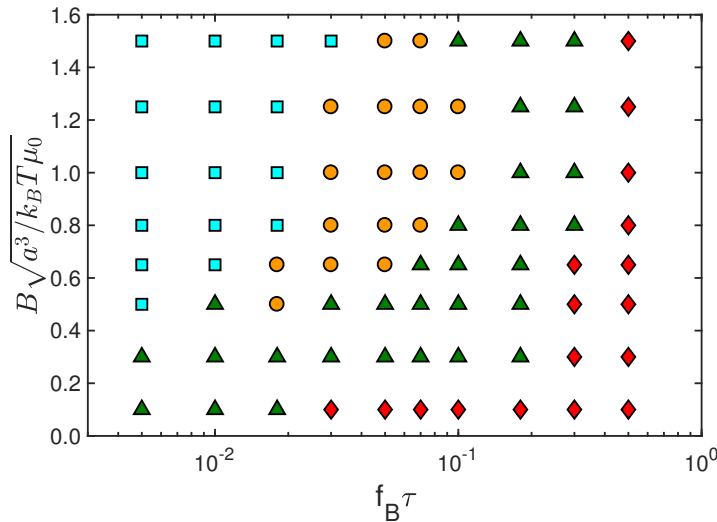


Figure 9.2: Phase diagram illustrating the various dynamic states versus the magnitude and frequency of the alternating magnetic field as obtained from the simulations. Red diamonds depict dynamic wires. Orange circles correspond to the spinner phase. Cyan squares outlines the pulsating clusters. Green triangles correspond to the state where a mixture of different dynamic structures is observed.

At relatively low frequencies, loose extended clusters are formed and they show periodic shape changes in pulses with the magnetic frequency (Fig. 9.3(a)). With increasing frequency the dynamic spinner phase appears at an intermediate range (Fig. 9.3(c)). In this phase particles self-assemble into short chains and rotate at the frequency of the applied field. At higher frequencies dynamic wires are formed through merging and extension of initial cluster of particles along the axis of applied field (Fig. 9.3(d)). The elongation of the clusters into a wire



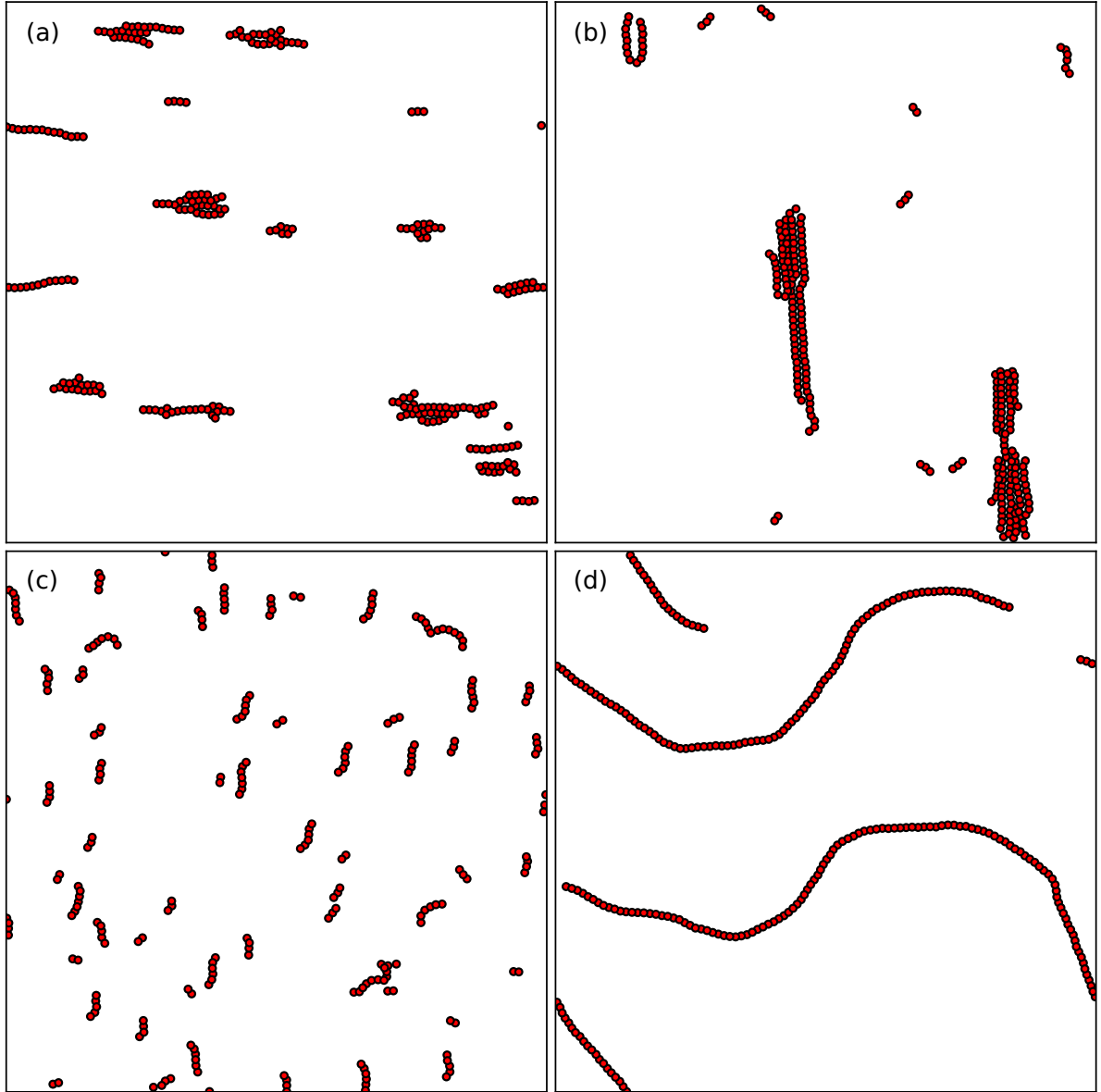


Figure 9.3: Snapshot of different phase appearances depending on the applied field parameters. (a) Pulsating clusters observed at  $\omega = 2\pi f_B = 0.005\tau^{-1}$  and  $B_0 = 0.8\sqrt{k_B T \mu_0 / a^3}$ , (b) mixture of different dynamic structures at  $\omega = 2\pi f_B = 0.1\tau^{-1}$  and  $B_0 = 0.8\sqrt{k_B T \mu_0 / a^3}$ , (c) spinner phase formed at  $\omega = 2\pi f_B = 0.05\tau^{-1}$  and  $B_0 = 0.8\sqrt{k_B T \mu_0 / a^3}$ , and (d) dynamic wires formed at  $\omega = 2\pi f_B = 0.5\tau^{-1}$  and  $B_0 = 0.8\sqrt{k_B T \mu_0 / a^3}$ .

continues until it becomes one particle thick. At some particular intermediate frequencies, mixture of different dynamic structures coexist (Fig. 9.3(b)).

### 9.2.1 Spinners

Magnetic spinners are short chains of self-assembled dispersion particles with the resulting magnetic moment oriented along the chains. They have some distribution of lengths due to prevailing magnetic dipole-dipole interaction and the average length of the spinners is defined by the frequency of the external driving field (see Sec. 9.3.2). The spinner phase appears in a certain parameter range of the applied field because the uniaxial symmetry of the field breaks down spontaneously. The applied magnetic field drives the chain to align along the field orientation and results in periodic reversal of the direction of rotation. The chain will preferably start rotating in clockwise (CW) or counterclockwise (CCW) direction with the same frequency as the applied uniaxial magnetic field, if its rotational inertia is large compared to the viscous drag by the fluid. Since both kind of rotations are equally probable, initial direction of spinner rotation is decided by its interaction with neighboring particles and flows. These spinners vigorously move around the system and exhibit complex dynamic behavior due to the collision with each other, they disintegrate and re-assemble. The collective motion of all the spinners creates an overall gas-like appearance of the system (Fig. 9.4(a)). The rotating spinners inject energy by exerting torques on the liquid which induces strong large-scale vortical flows in the system [259]. The energy injection rate and the corresponding injection scale can be tuned by the frequency and amplitude of the applied magnetic field.

## 9.3 Results

In our simulations, there are three subsystems of particles available in the spinner phase, e.g., active self-assembled spinners, individual particles and non-magnetic (inactive) tracers (Fig. 9.4a). While the spinners are not self-propelling entities (activity comes from rotation only), they get advected by the flows generated by the neighboring spinners. Hence, the spinners are the dominant active component in the system that induces a diffusive motion of the non-magnetic tracers. Short-lived active-spinner trajectories (thin colored lines) and a long-lived tracer trajectory (thick black line) are illustrated in Fig. 9.4(b).

### 9.3.1 Spinner imbalance

Spinner are strongly hydrodynamically and magnetically coupled, which leads to phases with dominant direction of rotation. This can be quantified as spinner imbalance  $I_s = (N_+ - N_-)/(N_+ + N_-)$ , where  $N_+$  and  $N_-$  are the number of CW and CCW spinners, respectively. The phases with complete global synchronization, i.e., all spinners rotating in the same direction, corresponds to  $I_s = \pm 1$ , while spinners with completely random rotational motion will have  $I_s = 0$ . Figure 9.5 shows the spinner imbalance from our simulation study within a certain time window. The spinner imbalance exhibits significant fluctuations around  $I_s = 0$ , i.e., CW and CCW rotations are equally probable and no global synchronization can be identified over a longer time frame.

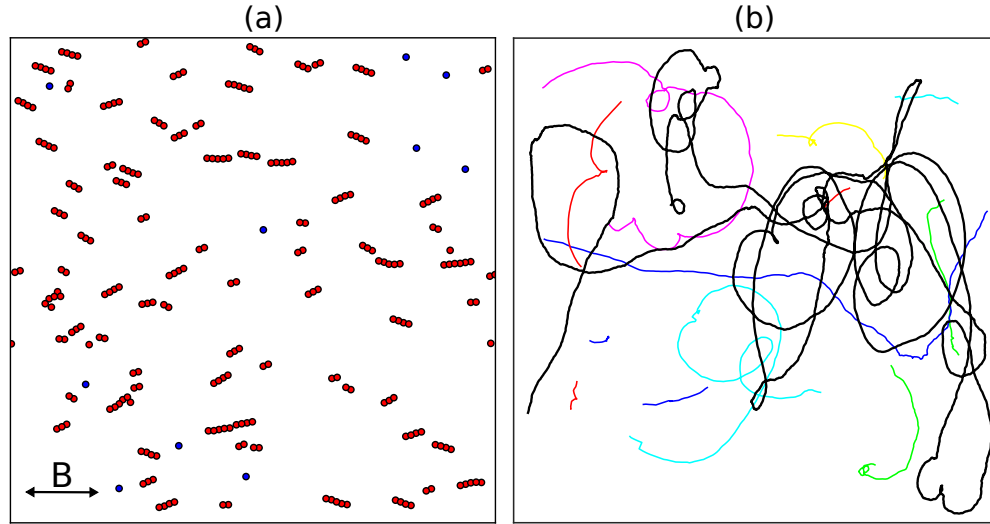


Figure 9.4: (a) A snapshot of self-assembled magnetic spinners (red) with passive tracers (blue). A uniaxial in-plane alternating magnetic field  $B$  creates a swarm of spinners. (b) Typical tracer (thick black line) and spinners trajectories (colored). The frequency of the magnetic field is  $f_B = 0.008\tau^{-1}$ , the dispersion particle packing fraction  $\phi = 0.028$ , and the particle and the tracer diameter  $\sigma = \sigma_T = 6a$ .

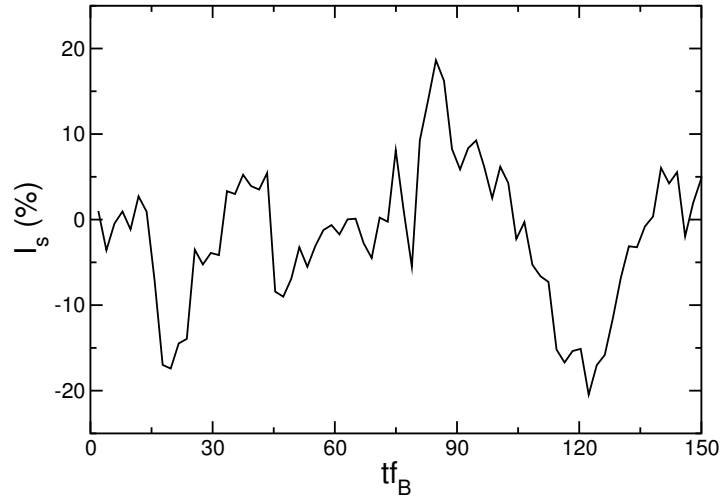


Figure 9.5: Imbalance in number of spinners with different sense of rotation as function of time. The spinner phase is dynamically self-assembled at the frequency of the magnetic field  $f_B = 0.05/2\pi\tau^{-1}$ .

### 9.3.2 Spinner length

The dynamic spinner phase can be characterized by a well defined average spinner length that depends on the driving frequency of the external magnetic field. The dependence of the spinner length on the frequency  $f_B$  of the external magnetic field is displayed in Fig. 9.6.

The length is determined by the balance between the viscous torque  $\gamma_H \omega$  of the fluid and the magnetic torque. For two-dimensional systems, the hydrodynamic friction coefficient  $\gamma_H$  exhibits the spinner length dependence

$$\gamma_H \sim L_s^2 / \ln(\tilde{L}/L_s). \quad (9.7)$$

Here,  $\tilde{L}$  is a characteristic length scale. The magnetic torque is proportional to the length of the spinner. Hence, we find

$$\frac{L_s}{\ln \tilde{L} - \ln L_s} \sim \frac{1}{f_B}. \quad (9.8)$$

As shown in Fig. 9.6,  $L_s$  decreases nearly linearly with increasing frequency and can well be fitted by Eq. (9.8) with  $\tilde{L} \approx 4.7\sigma$ .

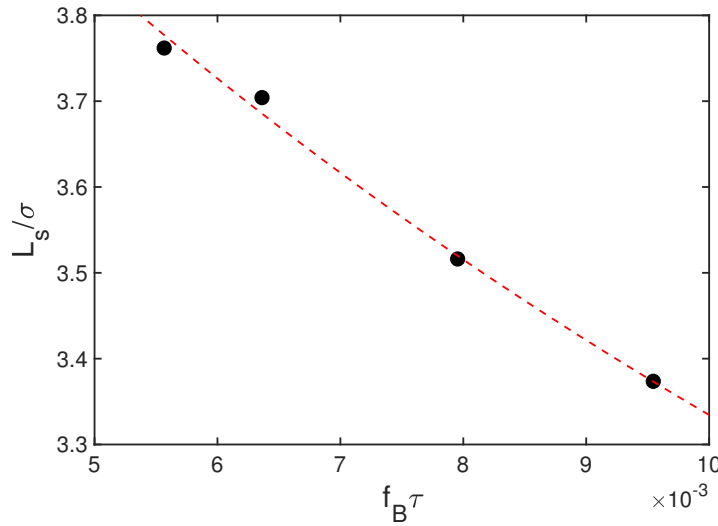


Figure 9.6: Average spinner length  $L_s$  as a function of the frequency  $f_B$  of the external magnetic field. The dashed red line is a fit to Eq. (9.8) following from the torque balance.

### 9.3.3 Clustering of spinners

Analysis of the spinners via the correlation of spinner-spinner rotation orientation revealed the presence of a short-range dynamic order (Fig. 9.7(a)) in the spatial spinner arrangement. There is a strong correlation of the spinners with co-rotating orientation at short distances, which decays with a power law of  $-1.32$  (inset Fig. 9.7(a)). This spatial spinner arrangement can be further confirmed by a closer inspection of the radial distribution function  $g(r)$ . In Fig. 9.7(b),  $g(r)$  indicates more pronounced peaks for spinners with the same sense of rotation (black curve) compared to neighboring spinners rotating in opposite direction (red curve). This apparent clustering is similar to that observed in simulations of higher-density

microrotors [260,261], where a macroscopic phase separation has been numerically observed. However, our system inhabits significantly more complex phenomena, because the spinner number is not fixed and fluctuates around a well-defined average prescribed by the parameters of the driving field, as they are perpetually created and annihilated.

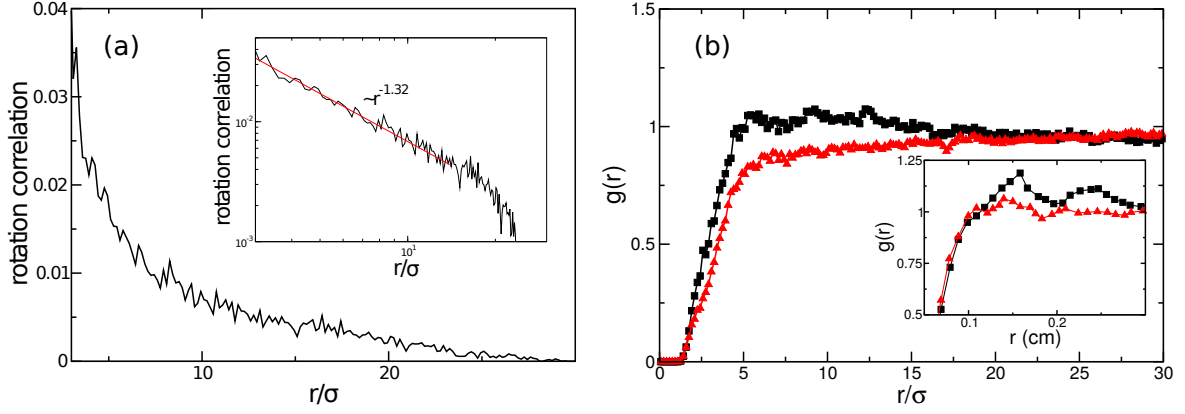


Figure 9.7: (a) Correlation of the rotation orientation for neighboring spinners. The inset shows the correlation in log scale, which decays with a power law of  $-1.32$  with increasing distance. (b) Normalized radial pair-distribution function  $g(r)$  for co-rotating (black) and counter-rotating spinners (red). A clustering peak can be observed from the co-rotating  $g(r)$ . The inset shows  $g(r)$  observed in experiments.

### 9.3.4 Spinner lifetime

Due to collisions spinners are perpetually annihilated and created with a lifetime that could be controlled by the frequency of the alternating magnetic field. To estimate a characteristic spinner lifetime  $\tau_s$ , we calculate the cluster correlation function  $C(t)$  of spinners, which determines the fraction of spinners still intact after a time  $t$  (inset Fig. 9.8). By fitting a stretched exponential function, we obtain the average spinner lifetime  $\tau_s$  (see Sec. 4.6). Figure 9.8 displays lifetimes as a function of the frequency of the external magnetic field and shows that the lifetime increases nearly linearly with frequency. A similar behavior of the spinner lifetime has been observed in experiments.

### 9.3.5 Active transport

#### Mean square displacement

Figure 9.9 shows a typical center-of-mass mean square displacement (MSD) of spinners and tracers as a function of time. The MSD of tracers is somewhat larger than that of spinners, consistent with experimental observations. Two clear distinct regimes can be identified for the spinner dynamics, ballistic motion at short times and diffusive motion for long times.

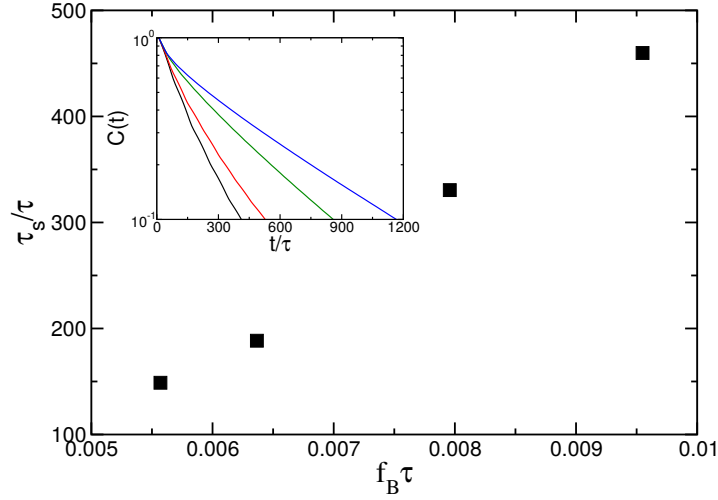


Figure 9.8: Average spinner life time as a function of the frequency  $f_B$  of the external magnetic field. The inset shows the cluster correlation functions  $C(t)$  for the four considered frequencies.

Initially, the MSD increases quadratically with increasing time, but turns in a linear regime for  $t f_B \gtrsim 10$ . The time scale for the cross-over between the ballistic and the diffusive regime is set by the spinner mean-free time, i.e., the time between a collision with another spinner or a free particle. The diffusive regime is not fully developed for spinners due to their finite life time as a consequence of the hindered spinner motion and their strong magnetic and hydrodynamic interactions with their neighbors.

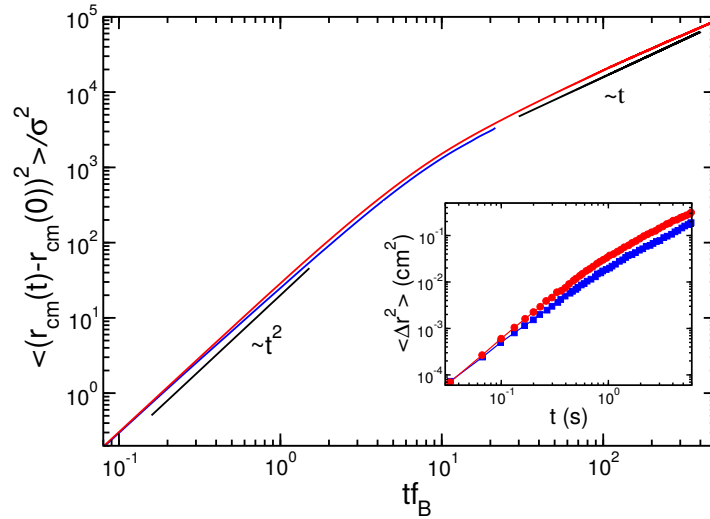


Figure 9.9: Center-of-mass mean square displacement (MSD) for spinners (blue curve) and tracers (red curve). The black lines indicate ballistic motion ( $\propto t^2$ ) at short times and active diffusion, with the same scaling as normal diffusion ( $\propto t$ ), at long times. The inset presents MSD curves from experiments.

### Characteristic ballistic spinner velocity

The ballistic motion is characterized by a velocity  $v$ , which we can extract from the initial part of the mean square displacement by the relation

$$\langle (\mathbf{r}_{cm}(t) - \mathbf{r}_{cm}(0))^2 \rangle = v^2 t^2, \quad (9.9)$$

where  $\mathbf{r}_{cm}$  is the center-of-mass position of the spinner or the inert particle. As displayed in Fig. 9.10(a), the characteristic velocity  $v$  for inert particles exhibits a weak dependence on the applied frequency of the external magnetic field in the frequency range of the spinner phase. In experiments, similarly the root mean square (rms) velocity  $v_{rms}$  can be calculated, as the ensemble average over the spinners, which characterizes the ballistic motion. It is evident that simulations yield qualitatively a similar behavior as observed in experiments. The simulation results for active transport are scaled with  $\sigma$  and  $\sigma/v$  (for the system with external frequency  $f_B = 0.008\tau^{-1}$ ), as relevant length and time scales.

The rotational motion of the spinners creates a radially decaying flow field. A characteristic velocity scale can be estimated from the Stokes flow around a rotating spherical (disk-like) particle of diameter  $L_s$  (spinner length), which is

$$v(\bar{r}) = \frac{\omega L_s}{2} \left( \frac{L_s}{2\bar{r}} \right)^{d-1} \quad (9.10)$$

in  $d$ -dimensions with the rotation frequency  $\omega$ . The typical distance  $\bar{r}$  of tracers and spinners is determined by the spinner concentration, i.e.,  $\bar{r} \sim 1/\sqrt{\rho_A}$ , where  $\rho_A$  is the particle number density. In experiments, the distance  $\bar{r} \approx 0.15\text{cm}$  is obtained from the radial pair distribution function (Fig. 9.7(b) inset) and the frequency is  $f_B = 60\text{Hz}$ . Thus, we find  $v(\bar{r}) \approx 0.13\text{ cm/s}$  for the spinner length  $L_s = 0.04\text{ cm}$  in three dimensions ( $d = 3$ ), in reasonable agreement with the value observed in experiments (Fig. 9.10(a)). It should be noted that the flow field decays less rapidly in the strict two dimensional situation of simulations compared to the quasi-two-dimensional experimental condition with three-dimensional hydrodynamics, which implies larger characteristic velocities in simulations.

### Diffusion

In simulations, the lifetime of the spinners just exceeds the crossover time between ballistic and diffusive motion such that no pronounced diffusive regime is obtained and no spinner diffusion coefficient can be extracted. In contrast, a clear diffusive regime is obtained for tracers. We extract the diffusion coefficient  $D$  of the tracer particles from the linear regime of the MSD to characterize activity-induced transport in the system, as

$$\langle (\mathbf{r}(t) - \mathbf{r}(0))^2 \rangle = 4Dt, \quad (9.11)$$

where  $\mathbf{r}$  is the displacement at time  $t$ .

Diffusion coefficients for the inert particles are displayed in Fig. 9.10(b) as a function of the frequency  $f_B$ , which includes diffusion coefficients from experiments too. The simulation results are in qualitative agreement with the experimental values. The frequency independence

of the diffusion coefficient is a result of the competition between a faster rotation leading to faster fluid motion and the decreasing spinner length with increasing frequency  $f_B$  of the field.

To get insight into the dependence of diffusion on activity in the system, we analyzed the inert-particle diffusion coefficient at different active-particle number densities  $\rho_A$ . Obtained results are shown in Fig. 9.10(c) including experimental observations. The inert-particle diffusion coefficient exhibits a monotonic increase with the number density until the system becomes too dense to sustain the spinner phase (immobile clusters of magnetic particles are formed for high number densities [127]). The observed nearly linear dependence qualitatively resembles previously observed enhanced tracer diffusion in suspensions of swimming organisms [263–267]. However, the Reynolds numbers in suspensions of swimming organisms are typically much smaller than unity, whereas in our spinner system  $Re \approx 30$ . Furthermore, swimmers exhibit typically a characteristic dipole flow field, while spinners create a rotational flow field. This points to significant differences in the origin of the emerging flow field.

We further explored the dependence of the diffusion coefficient on the inert-particle size to gain additional information on activity-induced transport in the spinner system. For inert particles larger than spinners (particle diameter  $\sigma_T >$  major spinner axis), the particle diffusion coefficient shows a  $D \propto 1/\sigma_T$  dependence as expected from Stokes-Einstein relation (Fig. 9.10d). Hence, the stirred fluid, containing the spinners, appears as a random, white-noise environment. Remarkably, for smaller particles, the trend is in reverse, i.e., the diffusion coefficient decreases with particle size. The non-monotonic dependence indicates a change in the statistical properties of the ambient fluid. A diffusion coefficient independence on particle size has been obtained, for example, for passive particles embedded in an active fluid with temporal exponentially correlated noise [268]. In contrast, for larger tracers the fluid acts as a thermal bath. Similarly, a non-monotonic size dependence of particle diffusion was recently observed in bacterial suspensions [266]. The monotonic dependence breaks down once a particle size becomes comparable with a characteristic fluid flow scale. In the case of our system, this scale approximately corresponds to the size of a spinner, while in a bacterial suspensions [266] it is determined by a typical size of self-organized bacterial flows. Moreover, our results imply that there is an optimal inert particle size for fastest mixing for a given active system, indicated by the maximum diffusion coefficient. These findings clearly demonstrates that active transport can be tuned.

Overall, simulation results for the activity-induced transport are in good qualitative agreement with the experimental observations. It is important to note, however that the flow fields in two (simulations) and three dimensions (experiment) associate different velocity scales (as mentioned earlier), therefore a quantitative match is not expected. Despite that, simulations yield the same dependencies of diffusion coefficients on the frequency, active particle density, and tracer size (Fig. 9.10(b)-(d)) as observed in experiments.



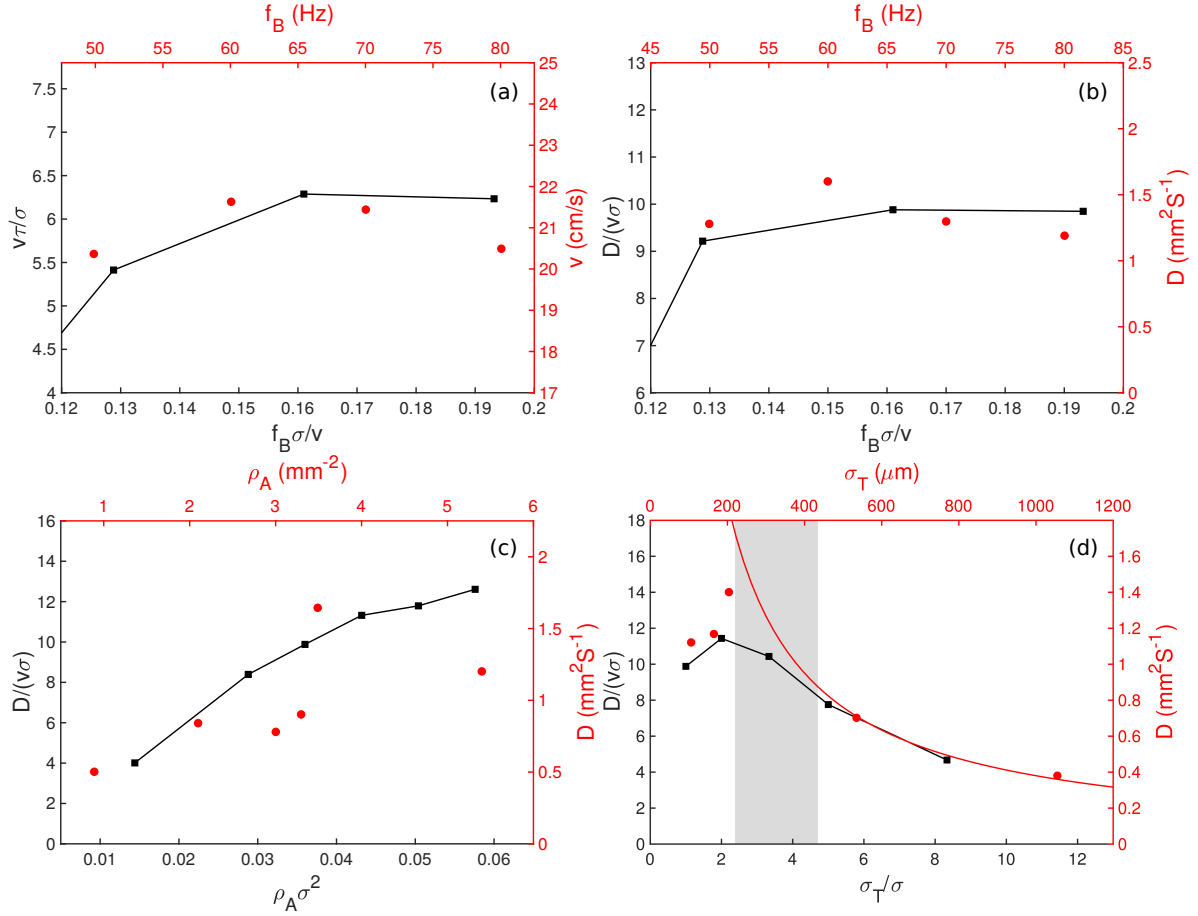


Figure 9.10: Active transport and diffusion. (a) The dependence of characteristic ballistic velocity  $v$  on the frequency  $f_B$  for inert particles in simulations (black);  $\rho_A\sigma^2 = 0.036$  and  $\sigma_T/\sigma = 1$ . Results from experiments (red) are shown for comparison. (b) Dependence of the active diffusion coefficient on  $f_B$  for inert particles as obtained from the simulations (black,  $\rho_A\sigma^2 = 0.036$  and  $\sigma_T/\sigma = 1$ ) and experiments (red). Outside the measured frequency window, the active particles' self-organization does not result in a pure spinner phase [127]. (c) Active diffusion coefficient as a function of the active particle number density  $\rho_A$  for inert particles as obtained from simulations (black,  $f_B\sigma/v = 0.161$  and  $\sigma_T/\sigma = 1$ ) and experiments (red). For the higher number densities, the system shows the onset of a high-density phase where the spinners are absent [262]. (d) The active diffusion coefficient is a non-monotonic function of the inert particle size for simulations (black,  $f_B\sigma/v = 0.161$  and  $\rho_A\sigma^2 = 0.036$ ), in accordance with experiments (red). The red line indicates the dependence  $\propto 1/\sigma_T$  as expected from the Stokes-Einstein relation. The gray area corresponds to the range of spinner sizes in simulation.

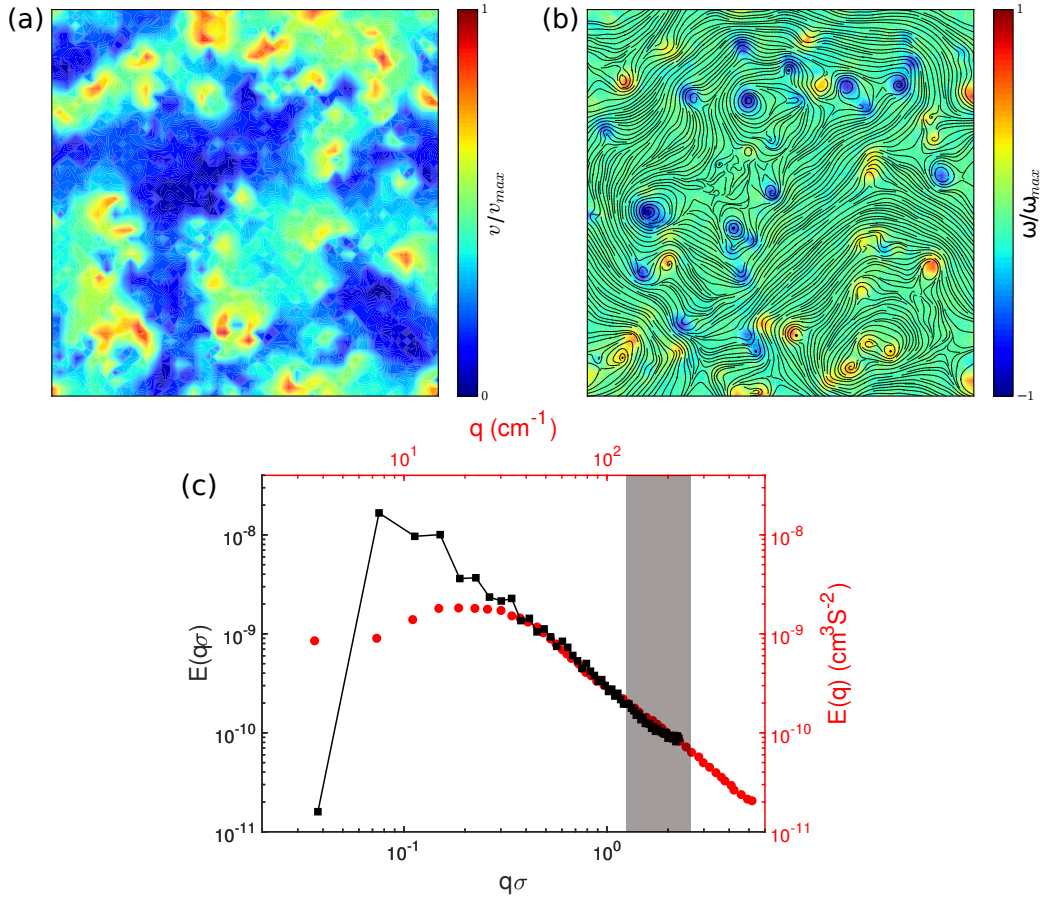


Figure 9.11: Two-dimensional turbulence. (a) The normalized velocity magnitude  $v/v_{max}$  of the hydrodynamic flow velocity generated by spinners. (b) The normalized vorticity  $\omega/\omega_{max}$  fields of the spinner system, which enables a distinction between CW (blue) and CCW (red) rotating spinners. Streamlines are superimposed to give a sense of flow. (c) Energy spectrum  $E(q)$  of the hydrodynamic flows as obtained from simulations (black) and experiment (red). Two-dimensional turbulent flow reverse energy cascade toward small wave numbers  $q$  (large scales) with  $q^{-5/3}$  scaling. The energy injection region is broad due to a heterogeneity of spinner sizes (gray area). The simulation parameters are  $f_B\sigma/v = 0.161$  and  $\rho_A\sigma^2 = 0.036$ .

### 9.3.6 Energy spectra

The magnitude of the hydrodynamic velocity field, induced by the rotating spinners, illustrates the regions of stronger motion concentrated around the spinners (Fig. 9.11(a)). In addition, Fig. 9.11(b) shows the vorticity field generated by the spinners, in combination with streamlines. This depicts a clear distinction between CW (blue) and CCW (red) rotating spinners and we observe the accumulation of co-rotating vortices. To further investigate the

self-induced vortical flows in the spinner phase, we calculate energy spectrum according to Eq. (2.46) of turbulent fluctuations in our system. A typical energy spectrum  $E(q)$  of the flows as extracted from simulations is shown in Fig. 9.11(c) together with the experimental results.  $E(q)$  strongly resembles the spectrum of an inverse energy cascade in two-dimensional turbulence [179]. The energy-injection scale is shown as gray area in Fig. 9.11(c); the broad range arises from the heterogeneity in spinner size. Although the values of the accessible wave-numbers  $q$  are constrained by the limiting size of our simulation system, we observe a clear characteristic power-law behavior of  $q^{-5/3}$  over more than an order of magnitude in length scale in accordance with experimental spinner systems.

The self-organized spinner system is intrinsically heterogeneous consisting of individual particles and spinners. The spinners encompass various sources of randomness, such as spinner size and life time, depending on the frequency of the external driving field. Hence, the system is quite dynamic by nature and particles frequently change their states; individual particles join spinners or spinners disintegrate into individual particles. To shed light on the relevance of the effects of dynamic heterogeneities on the turbulence, we considered an additional set of systems with spinners of fixed lengths, i.e., the spinner-size heterogeneity is removed.

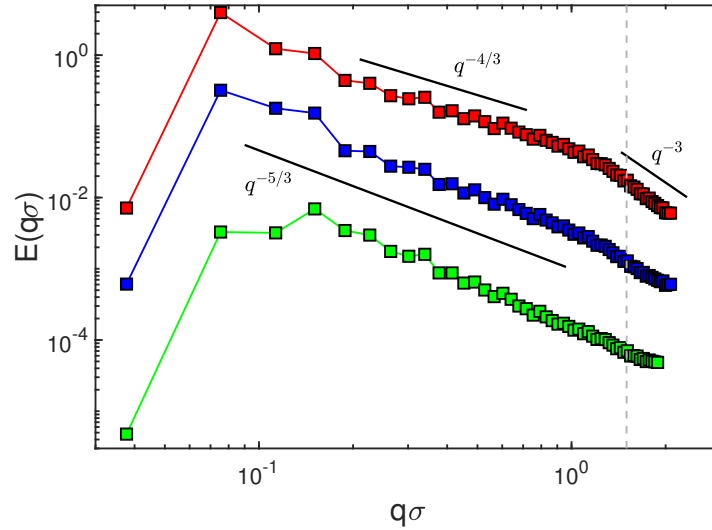


Figure 9.12: Energy spectra from simulations at three different packing fractions  $\phi_s = 0.226$ ,  $0.113$ , and  $0.056$  (top to bottom). The forcing length scale is indicated by the gray vertical line. The  $q$  dependency is expressed by the black lines. The spinner length is fixed at  $L_s = 4\sigma$ , and the field frequency is  $f_B\sigma/v = 0.161$  ( $Re \approx 38$ ). The curves are multiplied by constants to accommodate clearer inspection of the  $q$  exponent.

Figure 9.12 shows energy spectra from simulations of fixed-length spinner systems for various densities. The energy spectrum  $E(q)$  approaches the hydrodynamic turbulence exponent,  $q^{-5/3}$ , at low packing fractions  $\phi$ , within the boundaries of the rotating spinner phase. At elevated packing fractions, the exponent starts to deviate from the hydrodynamic turbu-

lence value (see Fig. 9.12), since other interactions, e.g., steric and magnetic, become more relevant, and the system undergoes a transition to another dynamic phase comprised of non-rotating aggregates. Remarkably, the energy spectra yield very similar exponents for the various concentrations, as well as a crossover to a larger exponent of approximately  $-3$  at large wave-numbers and high concentrations.

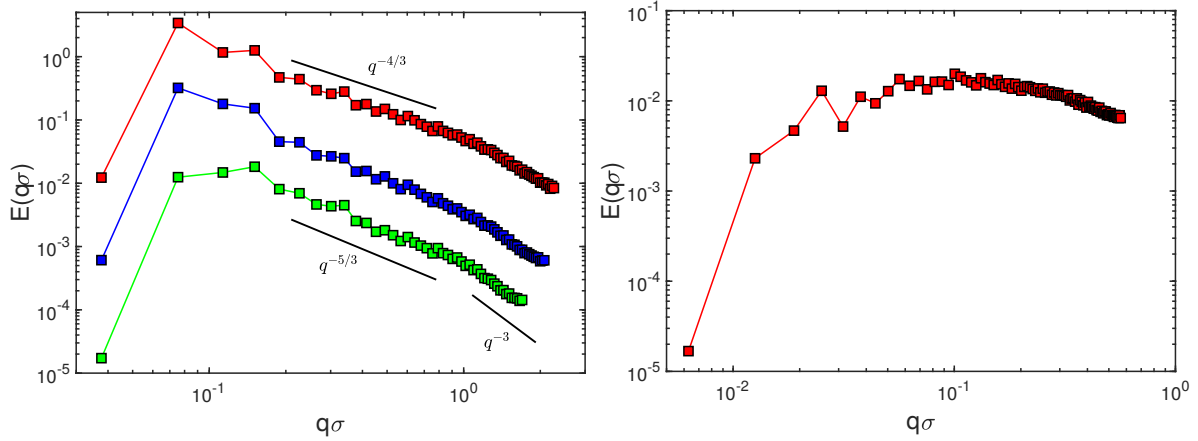


Figure 9.13: Energy spectra for mono-disperse spinners from simulations. (a) Spectra for spinners of lengths  $L_s/\sigma = 3, 4$ , and  $6$  (top to bottom) at the spinner packing fraction  $\phi_s = 0.113$  ( $Re \approx 38$ ). The top and bottom curves are shifted vertically by a constant factor with respect to the middle curve for better distinction. (b) Spectrum for spinners of length  $L_s/\sigma = 2$  at the spinner packing fraction  $\phi_s = 0.113$  with  $Re \approx 10$ .

Further, we find that the energy spectra and corresponding exponents for the mono-disperse systems with average spinner lengths  $L_s = 3\sigma$  and  $4\sigma$ , shown in Fig. 9.13(a), are similar to the exponent observed in the experiments and simulations (Fig. 9.11(c)) for the polydisperse system, with average spinner length  $\langle L_s \rangle \approx 3.5\sigma$ . Hence, polydispersity is of minor importance for active turbulence in our system. Moreover, simulations of a polydisperse system with fixed length of spinners and length distribution of the self-organized system yield very similar energy spectra. A further increase in the spinner length in simulations ( $L_s/\sigma = 4 - 6$ ) leads to a slight increase of the magnitude of the energy exponent. Simulations also reveal that energy spectra for very short spinners ( $L_s/\sigma < 3$ ,  $Re < 10$ ) (Fig. 9.13(b)) are almost constant over all length scale, i.e., these spinners behave like white-noise sources. Thus, a minimal spinner length and Reynolds number is necessary to generate turbulence. Finally, Fig. 9.13(a) exhibits also the crossover to a power-law exponent  $-3$  at length scales smaller than the energy-injection scale, the value characteristic for enstrophy flux of hydrodynamic turbulence, both in 2D and 3D (see Sec. 2.2.4) [179].

### Mesoscale turbulence - relation to other systems

Similar turbulent behavior has been observed for low-to-moderate Reynolds numbers in forced turbulence in 2D conducting fluid layers [179], surfactant films [269] and bubbly

flows [270, 271]. There the turbulence was forced either by a fixed grid or by a fixed array of magnets (ordered or randomly positioned) beneath the films with a typical  $Re$  number in the range between  $10^2 - 10^4$ . There the existence and robustness of the inverse energy cascade and  $(-5/3)$  scaling were well established [179]. Turbulent features have been also observed in viscoelastic polymer solutions (elastic turbulence) at  $Re$  numbers as low as  $10^{-3}$  [272]. The turbulence there is driven by a slow nonlinear response of the polymer solution to external shear due to long relaxation times of the polymers. The corresponding exponent there is believed to be close to  $(-1)$  [272]. Turbulent behavior has been also observed in active systems, in particular, dense bacterial suspensions [81, 151]. In bacterial turbulence, an apparent turbulent motion is associated with the onset of collective behavior and the reported experimental exponent seem to be close to  $(-8/3)$ . However, this scaling was observed only in a very narrow range of the wavenumbers and for conditions not applicable to our system. This scaling behavior was attributed to an apparent visco-elastic response of highly concentrated bacterial suspension. In a follow-up study [273], active turbulence in a model of rigid self-propelled colloidal rods in the overdamped regime was explored by simulations, and power-law spectra with a classical exponent  $-5/3$  consistent with hydrodynamic 2D turbulence in the inertial regime were observed. Our system is relatively dilute ( $1\% - 5\%$  area fraction) and no collective motion has been observed. A novel feature of our system is that it actively injects vorticity at the length scale of the spinners without self-propulsion. The injection process is spatially and temporally random due to perpetual self-assembly, advection, and collisions of spinners. It suggests that two-dimensional turbulence might be fully developed over a much wider range of Reynolds numbers than in three dimensions, provided that the driving is spatially and temporarily random.

## 9.4 Summary

We studied in detail the transport properties of active spinner suspensions comprised of self-assembled spinners with both clockwise and counter-clockwise types of rotational motion through two-dimensional simulations, to obtain an in-depth understanding of active turbulence in quasi-2D experimental system. The spinner suspension induces vigorous vortical flows at the interface that exhibit properties of well developed two-dimensional hydrodynamic turbulence despite the orders of magnitude lower Reynolds number in our studies ( $Re \approx 30$ ). The energy spectrum of the generated flows shows the characteristic  $q^{-5/3}$  decay. We observe that the active-diffusion coefficient increases nearly linear with the spinner density and is approximately independent of the frequency of the driving magnetic field. Moreover, we find a non-monotonic dependence of the active diffusion coefficient on the inert particle size, where Stokes-Einstein relation holds for large inert particles (larger than a spinner) and diffusion is suppressed for small particles. We uncover dynamic segregation and clustering of spinners with the same sense of rotation. Thus, our observations provide predictive tools for active-particle manipulation at the microscale.



# Conclusions & outlook

A numerical approach has been applied to study the dynamical structures, both in equilibrium systems of colloidal protein suspensions and in out-of-equilibrium systems, specifically, active Brownian particles and ferromagnetic particles in an external magnetic field. We have applied the already available concepts of colloidal physics to these systems to get a thorough insight into their structural and dynamical properties.

We have investigated the aggregation in protein solutions emerging from different interparticle interactions. Dispersed particles interacting by a generalized Lennard-Jones-Yukawa (LJY) pair potential as a representative for particles with short-range attractive and long-range repulsive interactions were considered. The equilibrium microstructural and short-time diffusion properties, and the phase behavior are studied with hydrodynamic simulations. The theoretical predictions for the dispersed-fluid phase are in excellent agreement with simulation results. For particle attraction strengths exceeding a critical value, simulations yield an equilibrium cluster phase. Calculations of the cluster mean lifetime and the comparison with the dissociation time of an isolated particle pair reveal quantitative differences, pointing to the importance of many-particle hydrodynamic interactions for the cluster dynamics. The cluster lifetime in the cluster-fluid phase increases far more strongly with increasing attraction strength than in the dispersed-fluid phase. Significant changes in the cluster shapes are also observed in the course of time. These observations about the influence of HIs on cluster conformational changes and lifetimes are applicable, on a qualitative level, to general Brownian particle systems, where thermodynamic clusters are formed. Further, our study of colloidal aggregation corresponding to eye-lens protein  $\gamma_B$ -crystallin reveals the strong influence of particle surface patchiness on short-time diffusion properties of proteins over distances comparable to the distances between nearest neighbors. The presence of attractive patches dramatically slows down the short-time dynamics even though the effective pair potential strength is comparable to colloids with isotropic interactions. Thereby, in order to understand and predict the dynamics of crowded protein solutions, it is thus not sufficient to perform in vitro experiments under dilute conditions and use estimates of the overall strength of interparticle interactions together with standard colloid models. There is a clear need for an extension of the often-used simple colloid models and to incorporate more molecular features into such coarse-grained models when attempting to describe local short-time diffusion in crowded solutions. Moreover, colloids with patchy attractions are intriguing to study not just because of their rich phase diagram, but from dynamical viewpoint too.

We have also presented a study of the active Brownian particle (ABP) spherical colloidal model for systems of self-propelled objects. The stationary-state distribution function of active Brownian particles confined in a radially symmetric harmonic and anharmonic potential has been investigated with a combination of theory and simulation. In the simulations, the

ABP is propelled with a prescribed velocity along a body-fixed direction, which is changing in a diffusive manner. For the analytical approach, the Cartesian components of the propulsion velocity are assumed to change independently (active Ornstein-Uhlenbeck particle, AOUP). This results in very different velocity distribution functions. ABPs and AOUPs confined in a harmonic potential exhibits the impact of the condition of fixed velocity of ABPs on the stationary-state properties, as it yields the activity-induced accumulation of particles. This reveals the importance of comparing appropriate distribution functions, which is the conditional probability distribution function for AOUPs. For the anharmonic potential, the Unified Colored Noise Approximation (UCNA) is applied to derive a probability distribution function. The UCNA results are in good agreement with simulation results for an AOUP, and the agreement increases with increasing rotational diffusion coefficient. However, the distribution functions from simulation of ABPs exhibit visible disparities which increases with increasing activity and decreasing rotational diffusion, thereby, revealing the applicability of the approximation scheme for ABPs. Moreover, we derived an expression for the pressure in a local sub-volume of a system of ABPs confined by walls or with periodic boundaries using the virial theorem, which includes an active and an interparticle-interaction contribution. The local pressure of ABPs under confinement is dependent on the wall interaction, which results in surface accumulation. Furthermore, the local pressure in interacting ABP systems with periodic boundary conditions increases initially with concentration and then decreases again at higher concentration for Péclet numbers exceeding a certain value, similar to a van der Waals-like pressure-concentration curve. We find that the local pressure is dominated by the contribution from activity for Péclet number less than the critical value at a relatively smaller volume fraction and at larger volume fractions, the interaction component has significant contribution. This contribution decreases with increasing Péclet number, since the active component increases quadratically with Péclet number compared to the linear increase of interparticle interaction contribution. Overall, the evaluation of the local pressure can provide valuable insight into the phase behavior of active systems.

Our study of colloidal particles subjected to an external alternating forcing exhibit complex collective behavior and self-assembled patterns. A dispersion of magnetic microparticles energized by a uniform uniaxial alternating magnetic field exhibits dynamic arrays of self-assembled spinners rotating in either direction. We observe that the spinners, developing as a consequence of spontaneous symmetry breaking of clock/counterclockwise rotation of aggregated particle chains, induce vigorous vortical flows that exhibit properties of a two-dimensional hydrodynamic turbulence even at the orders of magnitude lower Reynolds number in our studies. The same-chirality spinners (clockwise or counterclockwise) show a tendency to aggregate and form dynamic clusters. Furthermore, the emergent self-induced currents promote active diffusion that could be tuned by the parameters of the external excitation field. Our simulation study exhibited a similar qualitative behavior as experimental observations. It provides insight into fundamental aspects of collective transport in active spinner materials and yields new rules for particle manipulation at the microscale. The embedded inert particles exhibit an unusual diffusion behavior, a finding which illustrates that the active transport can be tuned by external parameters.



We close this section by discussing some possible future extensions of these systems and phenomena.

Our results of colloidal system with Lennard-Jones-Yukawa (LJY) pair potential contribute to an improved understanding of the Brownian particle dynamics in SALR systems. As a future technological application, the transport properties can be used as salient input to the previously developed membrane ultrafiltration model [274], in its application to protein solutions under SALR conditions. Furthermore, the intra-cluster structure and dynamics can be studied in more detail using the hydrodynamic MPC simulations.

Regarding the dramatic influence of weak attractive patches on local short-time diffusion, it is not only of considerable importance for the general case of crowding phenomena in cells and other dense protein environments, but may also have direct implications for the specific system used in this study. Eye-lens protein solutions have not only been investigated due to their role in cataract formation, but their dynamics has recently also been investigated due to speculations that the occurrence of presbyopia (an age-related inability of the eye to focus on close objects) – a result of a gradual hardening of the eye lens – may be linked to an arrest or glass transition of the concentrated protein solutions that make up the interior of the fiber cells in the lens. While the molecular origins of such an age-related arrest transition are unknown, our study demonstrates that the additional presence of one or several attractive patches on the protein surface, for example due to a local site mutation that creates an additional charged patch, may dramatically alter the local and macroscopic dynamic properties and drive the solution into an arrested state. It will thus be interesting to look in more detail into the molecular properties of the various crystallins found in lenses with and without presbyopia, including more sophisticated colloidal model with shape anisotropy or molecular details.

Our study of active Brownian particles in harmonic potential can be extended in the analytical description of the non-equilibrium dynamics of many interacting active particles, such as ABPs connected by harmonic bonds. The UCNA scheme for anharmonic radially symmetric potential, has shed light onto its applicability for ABPs. The good agreement with simulations for higher rotational diffusion suggest that UCNA can very well be applied to describe the properties of ABPs with a large rotational diffusion coefficient, corresponding typical to run-and-tumble motion rather than thermal rotational diffusion. With the help of the stationary-state distribution function of the ABPs, other properties can be calculated, such as an effective free energy [115]. By the latter, the thermodynamic framework of passive systems can be applied and equations of states be derived [106]. Furthermore, the evaluation of the local pressure can be employed to get valuable insight into the phase behavior of active systems. In particular, it can be used to calculate pressure differences in the dense fluid phase and the dilute gas phase of the motility induced phase separated states of active systems.

The spinner system, as a result of dynamic self-assembly in an external alternating magnetic field, presents a new member of active systems displaying active turbulence behavior and constitutes a novel class of materials with tunable properties. The uniqueness of this particular system comes from the fact that activity originates from rotations only and is not associated with self-propulsion. A trivial extension of this study would be self-assembly of magnetic particles suspended in the bulk of a three-dimensional fluid. Further, the suspension

## Conclusions & outlook

---

of magnetic particles can be exposed to rotating field instead of an alternating field, or put under certain geometric confinement, which can induce a different sort of collective phenomena. It would be interesting to observe the hydrodynamic flows, in particular turbulence, with larger magnetic dispersions as the Reynolds number increases. Moreover, how the active turbulence changes, or disappears, with decreasing particle size, as slowly thermal diffusion kicks in and becomes prominent, would be engaging to look into.

# Bibliography

- [1] R. J. Ellis, Macromolecular crowding: an important but neglected aspect of the intracellular environment, *Current opinion in structural biology* 11 (1) (2001) 114–119.
- [2] D. Hall, A. P. Minton, Macromolecular crowding: qualitative and semiquantitative successes, quantitative challenges, *Biochimica et Biophysica Acta (BBA)-Proteins and Proteomics* 1649 (2) (2003) 127–139.
- [3] G. Ralston, Effects of "crowding" in protein solutions, *J. Chem. Educ* 67 (10) (1990) 857.
- [4] H.-X. Zhou, G. Rivas, A. P. Minton, Macromolecular crowding and confinement: biochemical, biophysical, and potential physiological consequences, *Annu. Rev. Biophys.* 37 (2008) 375–397.
- [5] S. B. Zimmerman, A. P. Minton, Macromolecular crowding: biochemical, biophysical, and physiological consequences, *Annual review of biophysics and biomolecular structure* 22 (1) (1993) 27–65.
- [6] A. Lawlor, G. D. McCullagh, E. Zaccarelli, G. Foffi, K. A. Dawson, Interactions in systems with short-range attractions and applications to protein crystallisation, in: *Trends in Colloid and Interface Science XVI*, Springer, 2004, pp. 104–109.
- [7] W. Poon, Crystallization of globular proteins, *Physical Review E* 55 (3) (1997) 3762.
- [8] A. Stradner, G. M. Thurston, P. Schurtenberger, Tuning short-range attractions in protein solutions: from attractive glasses to equilibrium clusters, *Journal of Physics: Condensed Matter* 17 (31) (2005) S2805.
- [9] Y. Liu, E. Fratini, P. Baglioni, W.-R. Chen, S.-H. Chen, Effective long-range attraction between protein molecules in solutions studied by small angle neutron scattering, *Physical review letters* 95 (11) (2005) 118102.
- [10] P. D. Godfrin, I. E. Zarraga, J. Zarzar, L. Porcar, P. Falus, N. J. Wagner, Y. Liu, Effect of Hierarchical Cluster Formation on the Viscosity of Concentrated Monoclonal Antibody Formulations Studied by Neutron Scattering, *The Journal of Physical Chemistry B* 120 (2) (2016) 278–291.
- [11] F. Cardinaux, E. Zaccarelli, A. Stradner, S. Bucciarelli, B. Farago, S. U. Egelhaaf, F. Sciortino, P. Schurtenberger, Cluster-Driven Dynamical Arrest in Concentrated

## Bibliography

---

- Lysozyme Solutions, *The Journal of Physical Chemistry B* 115 (22) (2011) 7227–7237.
- [12] M. Grimaldo, F. Roosen-Runge, F. Zhang, T. Seydel, F. Schreiber, Diffusion and dynamics of  $\gamma$ -globulin in crowded aqueous solutions, *The Journal of Physical Chemistry B* 118 (25) (2014) 7203–7209.
- [13] W. Häussler, Neutron spin echo studies on ferritin: free-particle diffusion and interacting solutions, *European Biophysics Journal* 37 (5) (2008) 563–571.
- [14] C. Le Coeur, S. Longeville, Microscopic protein diffusion at high concentration by neutron spin-echo spectroscopy, *Chemical Physics* 345 (2) (2008) 298–304.
- [15] F. Roosen-Runge, M. Hennig, T. Seydel, F. Zhang, M. W. Skoda, S. Zorn, R. M. Jacobs, M. Maccarini, P. Fouquet, F. Schreiber, Protein diffusion in crowded electrolyte solutions, *Biochimica et Biophysica Acta (BBA)-Proteins and Proteomics* 1804 (1) (2010) 68–75.
- [16] P. N. Pusey, W. Van Megen, Phase behaviour of concentrated suspensions of nearly hard colloidal spheres, *Nature* 320 (6060) (1986) 340–342.
- [17] K. N. Pham, A. M. Puertas, J. Bergenholtz, S. U. Egelhaaf, A. Moussard, P. N. Pusey, A. B. Schofield, M. E. Cates, M. Fuchs, W. C. Poon, Multiple glassy states in a simple model system, *Science* 296 (5565) (2002) 104–106.
- [18] E. Zaccarelli, W. C. Poon, Colloidal glasses and gels: The interplay of bonding and caging, *Proceedings of the National Academy of Sciences* 106 (36) (2009) 15203–15208.
- [19] F. Sciortino, P. Tartaglia, E. Zaccarelli, Evidence of a higher-order singularity in dense short-ranged attractive colloids, *Physical review letters* 91 (26) (2003) 268301.
- [20] V. Trappe, P. Sandkühler, Colloidal gels—low-density disordered solid-like states, *Current opinion in colloid & interface science* 8 (6) (2004) 494–500.
- [21] T. Ando, J. Skolnick, Crowding and hydrodynamic interactions likely dominate in vivo macromolecular motion, *Proceedings of the National Academy of Sciences* 107 (43) (2010) 18457–18462.
- [22] S. R. McGuffee, A. H. Elcock, Diffusion, crowding & protein stability in a dynamic molecular model of the bacterial cytoplasm, *PLoS computational biology* 6 (3) (2010) e1000694.
- [23] A. Miermont, F. Waharte, S. Hu, M. N. McClean, S. Bottani, S. Léon, P. Hersen, Severe osmotic compression triggers a slowdown of intracellular signaling, which can be explained by molecular crowding, *Proceedings of the National Academy of Sciences* 110 (14) (2013) 5725–5730.

- 
- [24] M. Weiss, Crowding, diffusion, and biochemical reactions, *New Models of the Cell Nucleus: Crowding, Entropic Forces, Phase Separation, and Fractals* 307 (2013) 383.
- [25] F. Mezei, Neutron spin echo: A new concept in polarized thermal neutron techniques, *Zeitschrift für Physik A Hadrons and nuclei* 255 (2) (1972) 146–160.
- [26] A. Stradner, H. Sedgwick, F. Cardinaux, W. C. K. Poon, S. U. Egelhaaf, P. Schurtenberger, Equilibrium cluster formation in concentrated protein solutions and colloids, *Nature* 432 (7016) (2004) 492–495.
- [27] P. D. Godfrin, R. Castañeda-Priego, Y. Liu, N. J. Wagner, Intermediate range order and structure in colloidal dispersions with competing interactions, *The Journal of Chemical Physics* 139 (15) (2013) 154904.
- [28] Y. Liu, L. Porcar, J. Chen, W. R. Chen, P. Falus, A. Faraone, E. Fratini, K. Hong, P. Baglioni, Lysozyme protein solution with an intermediate range order structure, *Journal of Physical Chemistry B* 115 (22) (2011) 7238–7247.
- [29] P. D. Godfrin, N. E. Valadez-Pérez, R. Castaneda-Priego, N. J. Wagner, Y. Liu, Generalized phase behavior of cluster formation in colloidal dispersions with competing interactions, *Soft Matter* 10 (28) (2014) 5061–5071.
- [30] E. Mani, W. Lechner, W. K. Kegel, P. G. Bolhuis, Equilibrium and non-equilibrium cluster phases in colloids with competing interactions, *Soft Matter* 10 (25) (2014) 4479–4486.
- [31] F. Cardinaux, A. Stradner, P. Schurtenberger, F. Sciortino, E. Zaccarelli, Modeling equilibrium clusters in lysozyme solutions, *Europhysics Letters (EPL)* 77 (4) (2007) 48004.
- [32] A. J. Chinchalikar, V. K. Aswal, J. Kohlbrecher, A. G. Wagh, Small-angle neutron scattering study of structure and interaction during salt-induced liquid-liquid phase transition in protein solutions, *Physical Review E* 87 (6) (2013) 062708.
- [33] J. A. Bollinger, T. M. Truskett, Fluids with competing interactions. i. decoding the structure factor to detect and characterize self-limited clustering, *The Journal of Chemical Physics* 145 (6) (2016) 064902.
- [34] J. Riest, *Dynamics in Colloid and Protein Systems: Hydrodynamically Structured Particles, and Dispersions with Competing Attractive and Repulsive Interactions*, Forschungszentrum Jülich GmbH Zentralbibliothek, Jülich, 2016.
- [35] A. Archer, N. Wilding, Phase behavior of a fluid with competing attractive and repulsive interactions, *Physical Review E* 76 (3) (2007) 031501.
- [36] N. E. Valadez-Pérez, R. Castañeda-Priego, Y. Liu, Percolation in colloidal systems with competing interactions: the role of long-range repulsion, *RSC Advances* 3 (47) (2013) 25110–25119.

## Bibliography

---

- [37] R. Piazza, M. Pierno, S. Iacopini, P. Mangione, G. Esposito, V. Bellotti, Microheterogeneity and aggregation in  $\beta$ 2-microglobulin solutions: Effects of temperature, pH, and conformational variant addition, *European Biophysics Journal* 35 (5) (2006) 439–445.
- [38] N. Kovalchuk, V. Starov, P. Langston, N. Hilal, Formation of stable clusters in colloidal suspensions, *Advances in Colloid and Interface Science* 147-148 (2009) 144–154.
- [39] S. Yannopoulos, V. Petta, Understanding the dynamics of biological colloids to elucidate cataract formation and develop a methodology for its early diagnosis, *Philosophical Magazine* 88 (33-35) (2008) 4161–4168. [arXiv:0812.3898](#).
- [40] J. A. Bollinger, T. M. Truskett, Fluids with competing interactions. II. Validating a free energy model for equilibrium cluster size, *The Journal of Chemical Physics* 145 (6) (2016) 064903. [arXiv:1605.04815](#).
- [41] J. Riest, Y. Liu, G. Nägele, D. Godfrin, Short-time dynamics of Lysozyme solutions with competing short-range attraction and long-range repulsion: Experiment and theory, to be submitted.
- [42] M. Roos, M. Ott, M. Hofmann, S. Link, E. Rössler, J. Balbach, A. Krushelnitsky, K. Saalwächter, Coupling and Decoupling of Rotational and Translational Diffusion of Proteins under Crowding Conditions, *Journal of the American Chemical Society* 138 (32) (2016) 10365–10372.
- [43] Z. Zhang, S. C. Glotzer, Self-assembly of patchy particles, *Nano Letters* 4 (8) (2004) 1407–1413.
- [44] E. Bianchi, R. Blaak, C. N. Likos, Patchy colloids: state of the art and perspectives., *Physical chemistry chemical physics : PCCP* 13 (14) (2011) 6397–410.
- [45] A. B. Pawar, I. Kretzschmar, Fabrication, assembly, and application of patchy particles, *Macromolecular rapid communications* 31 (2) (2010) 150–168.
- [46] F. Sciortino, E. Zaccarelli, Reversible gels of patchy particles, *Current Opinion in Solid State and Materials Science* 15 (6) (2011) 246–253.
- [47] E. Bianchi, J. Largo, P. Tartaglia, E. Zaccarelli, F. Sciortino, Phase Diagram of Patchy Colloids: Towards Empty Liquids, *Physical Review Letters* 97 (16) (2006) 168301.
- [48] F. Sciortino, Gel-forming patchy colloids and network glass formers: thermodynamic and dynamic analogies, *The European Physical Journal B-Condensed Matter and Complex Systems* 64 (3) (2008) 505–509.
- [49] N. Kern, D. Frenkel, Fluid-fluid coexistence in colloidal systems with short-ranged strongly directional attraction, *The Journal of Chemical Physics* 118 (21) (2003) 9882.

- 
- [50] A. Shiryayev, X. Li, J. D. Gunton, Simple model of sickle hemoglobin, *The Journal of chemical physics* 125 (2) (2006) 024902.
- [51] J. Chang, A. M. Lenhoff, S. I. Sandler, Determination of fluid–solid transitions in model protein solutions using the histogram reweighting method and expanded ensemble simulations, *The Journal of chemical physics* 120 (6) (2004) 3003–3014.
- [52] A. W. Wilber, J. P. Doye, A. A. Louis, E. G. Noya, M. A. Miller, P. Wong, Reversible self-assembly of patchy particles into monodisperse icosahedral clusters, *The Journal of chemical physics* 127 (8) (2007) 08B618.
- [53] K. Van Workum, J. F. Douglas, Symmetry, equivalence, and molecular self-assembly, *Physical Review E* 73 (3) (2006) 031502.
- [54] C. N. Likos, H. Löwen, M. Watzlawek, B. Abbas, O. Jucknischke, J. Allgaier, D. Richter, Star Polymers Viewed as Ultrasoft Colloidal Particles, *Physical Review Letters* 80 (20) (1998) 4450–4453.
- [55] G. Rosenthal, S. H. Klapp, Ordering of amphiphilic janus particles at planar walls: A density functional study, *The Journal of chemical physics* 134 (15) (2011) 154707.
- [56] B. Ruzicka, E. Zaccarelli, L. Zulian, R. Angelini, M. Sztucki, A. Moussaïd, T. Narayanan, F. Sciortino, Observation of empty liquids and equilibrium gels in a colloidal clay, *Nature materials* 10 (1) (2011) 56–60.
- [57] S. C. Glotzer, J. A. Anderson, Nanoparticle assembly: Made to order, *Nature materials* 9 (11) (2010) 885–887.
- [58] S. Bucciarelli, J. S. Myung, B. Farago, S. Das, G. A. Vliegenthart, O. Holderer, R. G. Winkler, P. Schurtenberger, G. Gompper, A. Stradner, Dramatic influence of patchy attractions on short-time protein diffusion under crowded conditions, *Science Advances* 2 (12) (2016) e1601432–e1601432.
- [59] E. Lauga, T. R. Powers, The hydrodynamics of swimming microorganisms, *Rep. Prog. Phys.* 72 (2009) 096601.
- [60] S. Ramaswamy, The mechanics and statistics of active matter, *Annu. Rev. Cond. Mat. Phys.* 1 (2010) 323.
- [61] T. Vicsek, A. Zafeiris, Collective motion, *Phys. Rep.* 517 (2012) 71.
- [62] P. Romanczuk, M. Bär, W. Ebeling, B. Lindner, L. Schimansky-Geier, Active Brownian particles, *Eur. Phys. J. Spec. Top.* 202 (2012) 1.
- [63] M. C. Marchetti, J. F. Joanny, S. Ramaswamy, T. B. Liverpool, J. Prost, M. Rao, R. A. Simha, Hydrodynamics of soft active matter, *Rev. Mod. Phys.* 85 (2013) 1143.

## Bibliography

---

- [64] J. Elgeti, R. G. Winkler, G. Gompper, Physics of microswimmers—single particle motion and collective behavior: a review, *Rep. Prog. Phys.* 78 (2015) 056601.
- [65] C. Bechinger, R. Di Leonardo, H. Löwen, C. Reichhardt, G. Volpe, G. Volpe, Active particles in complex and crowded environments, *Rev. Mod. Phys.* 88 (2016) 045006.
- [66] M. C. Marchetti, Y. Fily, S. Henkes, A. Patch, D. Yllanes, Minimal model of active colloids highlights the role of mechanical interactions in controlling the emergent behavior of active matter, *Curr. Opin. Colloid Interface Sci.* 21 (2016) 34.
- [67] A. Zöttl, H. Stark, Emergent behavior in active colloids, *J. Phys.: Condens. Matter* 28 (2016) 253001.
- [68] M. Marchetti, J. Joanny, S. Ramaswamy, T. Liverpool, J. Prost, M. Rao, R. A. Simha, Hydrodynamics of soft active matter, *Reviews of Modern Physics* 85 (3) (2013) 1143.
- [69] F. Ndlec, T. Surrey, A. C. Maggs, S. Leibler, Self-organization of microtubules and motors, *Nature* 389 (6648) (1997) 305–308.
- [70] A. Cavagna, I. Giardina, Bird flocks as condensed matter, *Annu. Rev. Condens. Matter Phys.* 5 (1) (2014) 183–207.
- [71] E. Lauga, T. R. Powers, The hydrodynamics of swimming microorganisms, *Reports on Progress in Physics* 72 (9) (2009) 096601.
- [72] G. A. Ozin, I. Manners, S. Fournier-Bidoz, A. Arsenault, Dream nanomachines, *Adv. Mater.* 17 (2005) 3011.
- [73] R. Dreyfus, J. Baudry, M. L. Roper, M. Fermigier, H. A. Stone, J. Bibette, Microscopic artificial swimmers, *Nature* 437 (2005) 862.
- [74] J. Palacci, S. Sacanna, A. P. Steinberg, D. J. Pine, P. M. Chaikin, Living crystals of light-activated colloidal surfers, *Science* 339 (2013) 936.
- [75] G. Volpe, I. Buttinoni, D. Vogt, H. J. Kümmerer, C. Bechinger, Microswimmers in patterned environments, *Soft Matter* 7 (2011) 8810.
- [76] X. Yang, M. L. Manning, M. C. Marchetti, Aggregation and segregation of confined active particles, *Soft Matter* 10 (2014) 6477.
- [77] E. Lauga, W. R. DiLuzio, G. M. Whitesides, H. A. Stone, Swimming in circles: Motion of bacteria near solid boundaries, *Biophys. J.* 90 (2006) 400.
- [78] A. P. Berke, L. Turner, H. C. Berg, E. Lauga, Hydrodynamic attraction of swimming microorganisms by surfaces, *Phys. Rev. Lett.* 101 (2008) 038102.
- [79] J. Tailleur, M. E. Cates, Sedimentation, trapping, and rectification of dilute bacteria, *EPL* 86 (2009) 60002.



- 
- [80] J. Elgeti, G. Gompper, Wall accumulation of self-propelled spheres, *EPL* 101 (2013) 48003.
- [81] H. H. Wensink, J. Dunkel, S. Heidenreich, K. Drescher, R. E. Goldstein, H. Löwen, J. M. Yeomans, Meso-scale turbulence in living fluids, *Proceedings of the National Academy of Sciences* 109 (36) (2012) 14308–14313.
- [82] F. Peruani, A. Deutsch, M. Bär, Nonequilibrium clustering of self-propelled rods, *Phys. Rev. E* 74 (2006) 030904.
- [83] Y. Yang, V. Marceau, G. Gompper, Swarm behavior of self-propelled rods and swimming flagella, *Phys. Rev. E* 82 (2010) 031904.
- [84] M. F. Copeland, D. B. Weibel, Bacterial swarming: a model system for studying dynamic self-assembly, *Soft Matter* 5 (2009) 1174.
- [85] N. C. Darnton, L. Turner, S. Rojevsky, H. C. Berg, Dynamics of bacterial swarming, *Biophys. J.* 98 (2010) 2082.
- [86] K. Drescher, J. Dunkel, L. H. Cisneros, S. Ganguly, R. E. Goldstein, Fluid dynamics and noise in bacterial cell-cell and cell-surface scattering, *Proc. Natl. Acad. Sci. USA* 109 (2011) 108.
- [87] J. D. Partridge, R. M. Harshey, Swarming: flexible roaming plans, *J. Bacteriol.* 195 (2013) 909.
- [88] J. Bialké, T. Speck, H. Löwen, Crystallization in a dense suspension of self-propelled particles, *Phys. Rev. Lett.* 108 (2012) 168301.
- [89] I. Buttinoni, J. Bialké, F. Kümmel, H. Löwen, C. Bechinger, T. Speck, Dynamical clustering and phase separation in suspensions of self-propelled colloidal particles, *Phys. Rev. Lett.* 110 (2013) 238301.
- [90] B. M. Mognetti, A. Šarić, S. Angioletti-Uberti, A. Cacciuto, C. Valeriani, D. Frenkel, Living clusters and crystals from low-density suspensions of active colloids, *Phys. Rev. Lett.* 111 (2013) 245702.
- [91] Y. Fily, S. Henkes, M. C. Marchetti, Freezing and phase separation of self-propelled disks, *Soft Matter* 10 (2014) 2132.
- [92] J. Stenhammar, D. Marenduzzo, R. J. Allen, M. E. Cates, Phase behaviour of active Brownian particles: the role of dimensionality, *Soft Matter* 10 (2014) 1489.
- [93] G. S. Redner, M. F. Hagan, A. Baskaran, Structure and dynamics of a phase-separating active colloidal fluid, *Phys. Rev. Lett.* 110 (2013) 055701.
- [94] Y. Fily, M. C. Marchetti, Athermal phase separation of self-propelled particles with no alignment, *Phys. Rev. Lett.* 108 (2012) 235702.

## Bibliography

---

- [95] V. Lobaskin, M. Romenskyy, Collective dynamics in systems of active brownian particles with dissipative interactions, *Phys. Rev. E* 87 (2013) 052135.
- [96] A. Zöttl, H. Stark, Hydrodynamics determines collective motion and phase behavior of active colloids in quasi-two-dimensional confinement, *Phys. Rev. Lett.* 112 (2014) 118101.
- [97] A. Wysocki, R. G. Winkler, G. Gompper, Cooperative motion of active Brownian spheres in three-dimensional dense suspensions, *EPL* 105 (2014) 48004.
- [98] R. Ni, M. A. Cohen Stuart, P. G. Bolhuis, Tunable long range forces mediated by self-propelled colloidal hard spheres, *Phys. Rev. Lett.* 114 (2015) 018302.
- [99] Y. Fily, A. Baskaran, M. F. Hagan, Dynamics of self-propelled particles under strong confinement, *Soft Matter* 10 (2014) 5609.
- [100] A. P. Solon, J. Stenhammar, R. Wittkowski, M. Kardar, Y. Kafri, M. E. Cates, J. Tailleur, Pressure and phase equilibria in interacting active Brownian spheres, *Phys. Rev. Lett.* 114 (2015) 198301.
- [101] A. P. Solon, Y. Fily, A. Baskaran, M. E. Cates, Y. Kafri, M. Kardar, J. Tailleur, Pressure is not a state function for generic active fluids, *Nat. Phys.* 11 (2015) 673.
- [102] S. C. Takatori, W. Yan, J. F. Brady, Swim pressure: Stress generation in active matter, *Phys. Rev. Lett.* 113 (2014) 028103.
- [103] R. G. Winkler, A. Wysocki, G. Gompper, Virial pressure in systems of spherical active Brownian particles, *Soft Matter* 11 (2015) 6680.
- [104] T. Speck, R. L. Jack, Ideal bulk pressure of active Brownian particles, *Phys. Rev. E* 93 (2016) 062605.
- [105] G. Falasco, F. Baldovin, K. Kroy, M. Baiesi, Mesoscopic virial equation for nonequilibrium statistical mechanics, *New J. Phys.* 18 (2016) 093043.
- [106] U. Marini Bettolo Marconi, C. Maggi, S. Melchionna, Pressure and surface tension of an active simple liquid: a comparison between kinetic, mechanical and free-energy based approaches, *Soft Matter* 12 (2016) 5727.
- [107] M. E. Cates, Diffusive transport without detailed balance in motile bacteria: does microbiology need statistical physics?, *Rep. Prog. Phys.* 75 (2012) 042601.
- [108] C. Battle, C. P. Broedersz, N. Fakhri, V. F. Geyer, J. Howard, C. F. Schmidt, F. C. MacKintosh, Broken detailed balance at mesoscopic scales in active biological systems, *Science* 352 (2016) 604.
- [109] É. Fodor, C. Nardini, M. E. Cates, J. Tailleur, P. Visco, F. van Wijland, How far from equilibrium is active matter?, *Phys. Rev. Lett.* 117 (2016) 038103.

- 
- [110] J. Bialké, H. Löwen, T. Speck, Microscopic theory for the phase separation of self-propelled repulsive disks, *EPL* 103 (2013) 30008.
- [111] R. Wittkowski, A. Tiribocchi, J. Stenhammar, R. J. Allen, D. Marenduzzo, M. E. Cates, Scalar  $\phi^4$  field theory for active-particle phase separation field theory for active-particle phase separation, *Nat. Commun.* 5 (2014) 4351.
- [112] T. Speck, A. M. Menzel, J. Bialké, H. Löwen, Dynamical mean-field theory and weakly non-linear analysis for the phase separation of active Brownian particles, *J. Chem. Phys.* 142 (2015) 224109.
- [113] S. C. Takatori, J. F. Brady, Towards a thermodynamics of active matter, *Phys. Rev. E* 91 (2015) 032117.
- [114] T. Speck, Stochastic thermodynamics for active matter, *EPL* 114 (2016) 30006.
- [115] U. Marini Bettolo Marconi, C. Maggi, Towards a statistical mechanical theory of active fluids, *Soft Matter* 11 (2015) 8768.
- [116] T. F. F. Farage, P. Krinninger, J. M. Brader, Effective interactions in active Brownian suspensions, *Phys. Rev. E* 91 (2015) 042310.
- [117] U. M. B. Marconi, M. Paoluzzi, C. Maggi, Effective potential method for active particles, *Mol. Phys.* 114 (2016) 2400.
- [118] M. Rein, T. Speck, Applicability of effective pair potentials for active brownian particles, *Eur. Phys. J. E* 39 (2016) 84.
- [119] F. Ginot, I. Theurkauff, D. Levis, C. Ybert, L. Bocquet, L. Berthier, C. Cottin-Bizonne, Nonequilibrium equation of state in suspensions of active colloids, *Phys. Rev. X* 5 (2015) 011004.
- [120] R. G. Winkler, H. Morawitz, D. Y. Yoon, Novel molecular dynamics simulations at constant pressure, *Molec. Phys.* 75 (1992) 669.
- [121] R. G. Winkler, R. Hentschke, Liquid benzene confined between graphite surfaces. a constant pressure molecular dynamics study, *J. Chem. Phys.* 99 (1993) 5405.
- [122] R. G. Winkler, C.-C. Huang, Stress tensors of multiparticle collision dynamics fluids, *J. Chem. Phys.* 130 (2009) 074907.
- [123] R. Becker, *Theory of Heat*, Springer Verlag, Berlin, 1967.
- [124] E. Bertin, An equation of state for active matter, *Physics* 8 (2015) 44.
- [125] S. C. Takatori, J. F. Brady, Forces, stresses and the (thermo?) dynamics of active matter, *Curr. Opin. Colloid Interface Sci.*

## Bibliography

---

- [126] S. Mann, Self-assembly and transformation of hybrid nano-objects and nanostructures under equilibrium and non-equilibrium conditions, *Nature materials* 8 (10) (2009) 781–792.
- [127] G. Kokot, D. Piet, G. M. Whitesides, I. S. Aranson, A. Snezhko, Emergence of re-configurable wires and spinners via dynamic self-assembly, *Scientific reports* 5 (2015) 9528.
- [128] A. Snezhko, Non-equilibrium magnetic colloidal dispersions at liquid–air interfaces: dynamic patterns, magnetic order and self-assembled swimmers, *Journal of Physics: Condensed Matter* 23 (15) (2011) 153101.
- [129] J. Yan, M. Bloom, S. C. Bae, E. Luijten, S. Granick, Linking synchronization to self-assembly using magnetic janus colloids, *Nature* 491 (7425) (2012) 578–581.
- [130] A. Demortiere, A. Snezhko, M. V. Sapozhnikov, N. Becker, T. Proslie, I. S. Aranson, Self-assembled tunable networks of sticky colloidal particles, *Nature communications* 5 (2014) 3117.
- [131] N. Osterman, I. Poberaj, J. Dobnikar, D. Frenkel, P. Ziherl, D. Babić, Field-induced self-assembly of suspended colloidal membranes, *Physical review letters* 103 (22) (2009) 228301.
- [132] B. A. Grzybowski, H. A. Stone, G. M. Whitesides, Dynamics of self assembly of magnetized disks rotating at the liquid–air interface, *Proceedings of the National Academy of Sciences* 99 (7) (2002) 4147–4151.
- [133] J. E. Martin, A. Snezhko, Driving self-assembly and emergent dynamics in colloidal suspensions by time-dependent magnetic fields, *Reports on Progress in Physics* 76 (12) (2013) 126601.
- [134] H. Löwen, Colloidal dispersions in external fields: recent developments, *Journal of Physics: Condensed Matter* 20 (40) (2008) 404201.
- [135] J. Dobnikar, A. Snezhko, A. Yethiraj, Emergent colloidal dynamics in electromagnetic fields, *Soft Matter* 9 (14) (2013) 3693–3704.
- [136] J. Palacci, S. Sacanna, A. P. Steinberg, D. J. Pine, P. M. Chaikin, Living crystals of light-activated colloidal surfers, *Science* 339 (6122) (2013) 936–940.
- [137] B. A. Grzybowski, H. A. Stone, G. M. Whitesides, Dynamic self-assembly of magnetized, millimetre-sized objects rotating at a liquid–air interface, *Nature* 405 (6790) (2000) 1033–1036.
- [138] E. Climent, K. Yeo, M. R. Maxey, G. E. Karniadakis, Dynamic self-assembly of spinning particles, *J. Fluids Eng.* 129 (2007) 379.

- 
- [139] Y. Goto, H. Tanaka, Purely hydrodynamic ordering of rotating disks at a finite reynolds number, *Nat. Commun.* 6 (5994).
- [140] I. O. Götze, G. Gompper, Mesoscale simulations of hydrodynamic squirmer interactions, *Phys. Rev. E* 82 (2010) 041921.
- [141] B. C. van Zuiden, J. Paulose, W. T. M. Irvine, D. Bartolo, V. Vitelli, Spatiotemporal order and emergent edge currents in active spinner materials, *Proc. Natl. Acad. Sci. USA* 113 (2016) 12919.
- [142] A. Snezhko, M. Belkin, I. Aranson, W.-K. Kwok, Self-assembled magnetic surface swimmers, *Physical review letters* 102 (11) (2009) 118103.
- [143] M. Belkin, A. Glatz, A. Snezhko, I. Aranson, Model for dynamic self-assembled magnetic surface structures, *Physical Review E* 82 (1) (2010) 015301.
- [144] A. Snezhko, I. S. Aranson, Magnetic manipulation of self-assembled colloidal asters, *Nature materials* 10 (9) (2011) 698.
- [145] M. Driscoll, B. Delmotte, M. Youssef, S. Sacanna, A. Donev, P. Chaikin, Unstable fronts and motile structures formed by microrollers, *Nature Physics*.
- [146] A. Kaiser, A. Snezhko, I. S. Aranson, Flocking ferromagnetic colloids, *Science Advances* 3 (2) (2017) e1601469.
- [147] B. A. Grzybowski, M. Radkowski, C. J. Campbell, J. N. Lee, G. M. Whitesides, Self-assembling fluidic machines, *Applied physics letters* 84 (10) (2004) 1798–1800.
- [148] J. Edd, *Proceedings of the ieee/rsj international conference on intelligent robots and systems*.
- [149] S. T. Chang, V. N. Paunov, D. N. Petsev, O. D. Velev, Remotely powered self-propelling particles and micropumps based on miniature diodes, *Nature materials* 6 (3) (2007) 235–240.
- [150] C. Dombrowski, L. Cisneros, S. Chatkaew, R. E. Goldstein, J. O. Kessler, Self-concentration and large-scale coherence in bacterial dynamics, *Physical Review Letters* 93 (9) (2004) 098103.
- [151] A. Sokolov, I. S. Aranson, Physical properties of collective motion in suspensions of bacteria, *Physical review letters* 109 (24) (2012) 248109.
- [152] T. Sanchez, D. T. Chen, S. J. DeCamp, M. Heymann, Z. Dogic, Spontaneous motion in hierarchically assembled active matter, *Nature* 491 (7424) (2012) 431–434.
- [153] T. E. Angelini, E. Hannezo, X. Trepas, M. Marquez, J. J. Fredberg, D. A. Weitz, Glass-like dynamics of collective cell migration, *Proceedings of the National Academy of Sciences* 108 (12) (2011) 4714–4719.

## Bibliography

---

- [154] K. J. Solis, J. E. Martin, Complex magnetic fields breathe life into fluids, *Soft matter* 10 (45) (2014) 9136–9142.
- [155] C. E. Sing, L. Schmid, M. F. Schneider, T. Franke, A. Alexander-Katz, Controlled surface-induced flows from the motion of self-assembled colloidal walkers, *Proceedings of the National Academy of Sciences* 107 (2) (2010) 535–540.
- [156] B. Evans, A. Shields, R. L. Carroll, S. Washburn, M. Falvo, R. Superfine, Magnetically actuated nanorod arrays as biomimetic cilia, *Nano letters* 7 (5) (2007) 1428–1434.
- [157] M. Z. Bazant, T. M. Squires, Induced-charge electrokinetic phenomena: theory and microfluidic applications, *Physical Review Letters* 92 (6) (2004) 066101.
- [158] N. Darnton, L. Turner, K. Breuer, H. C. Berg, Moving fluid with bacterial carpets, *Biophysical journal* 86 (3) (2004) 1863–1870.
- [159] C. De Michele, S. Gabrielli, P. Tartaglia, F. Sciortino, Dynamics in the presence of attractive patchy interactions, *The Journal of Physical Chemistry B* 110 (15) (2006) 8064–8079.
- [160] S. Bucciarelli, L. Casal-Dujat, C. De Michele, F. Sciortino, J. Dhont, J. Bergenholtz, B. Farago, P. Schurtenberger, A. Stradner, Unusual dynamics of concentration fluctuations in solutions of weakly attractive globular proteins, *The journal of physical chemistry letters* 6 (22) (2015) 4470–4474.
- [161] A. Pototsky, H. Stark, Active Brownian particles in two-dimensional traps, *EPL* 98 (2012) 50004.
- [162] C. Gardiner, *Handbook of stochastic methods*. 1985, Springer Series in Synergetics.
- [163] H. Risken, *The Fokker-Planck Equation*, Springer, Berlin, 1989.
- [164] H. Löwen, J.-P. Hansen, J.-N. Roux, Brownian dynamics and kinetic glass transition in colloidal suspensions, *Physical Review A* 44 (2) (1991) 1169.
- [165] D. Heyes, J. Melrose, Brownian dynamics simulations of model hard-sphere suspensions, *Journal of non-newtonian fluid mechanics* 46 (1) (1993) 1–28.
- [166] P. Tian, G. D. Smith, Translocation of a polymer chain across a nanopore: A brownian dynamics simulation study, *The Journal of chemical physics* 119 (21) (2003) 11475–11483.
- [167] M. P. Allen, D. J. Tildesley, *Computer Simulation of Liquids*, Clarendon Press, Oxford, 1987.
- [168] E. Platen, An introduction to numerical methods for stochastic differential equations, *Acta numerica* 8 (1999) 197–246.

- 
- [169] A. Scala, Brownian dynamics simulation of polydisperse hard spheres, *The European Physical Journal Special Topics* 216 (1) (2013) 21–29.
- [170] A. Scala, T. Voigtmann, C. De Michele, Event-driven brownian dynamics for hard spheres, *The Journal of chemical physics* 126 (13) (2007) 134109.
- [171] D. L. Ermak, J. McCammon, Brownian dynamics with hydrodynamic interactions, *J. Chem. Phys.* 69 (1978) 1352.
- [172] P. K. Kundu, I. Cohen, D. Dowling, *Fluid mechanics*. 1990.
- [173] L. Landau, E. L. F. Mechanics, Pergamon, New York.
- [174] J. K. Dhont, *An introduction to dynamics of colloids*, Vol. 2, Elsevier, 1996.
- [175] M. Lisicki, Four approaches to hydrodynamic green's functions—the oseen tensors, *arXiv preprint arXiv:1312.6231*.
- [176] R. Di Leonardo, S. Keen, F. Ianni, J. Leach, M. Padgett, G. Ruocco, Hydrodynamic interactions in two dimensions, *Physical Review E* 78 (3) (2008) 031406.
- [177] M. Lisicki, G. Nägele, Colloidal hydrodynamics and interfacial effects, in: *Soft Matter at Aqueous Interfaces*, Springer, 2016, pp. 313–386.
- [178] G. K. Batchelor, *The theory of homogeneous turbulence*, Cambridge university press, 1953.
- [179] G. Boffetta, R. E. Ecke, Two-dimensional turbulence, *Annual Review of Fluid Mechanics* 44 (2012) 427–451.
- [180] S. P. Singh, S. Mittal, Energy spectra of flow past a circular cylinder, *International Journal of Computational Fluid Dynamics* 18 (8) (2004) 671–679.
- [181] R. H. Kraichnan, Inertial ranges in two-dimensional turbulence, *The Physics of Fluids* 10 (7) (1967) 1417–1423.
- [182] G. R. McNamara, G. Zanetti, Use of the boltzmann equation to simulate lattice-gas automata, *Physical review letters* 61 (20) (1988) 2332.
- [183] X. Shan, H. Chen, Lattice boltzmann model for simulating flows with multiple phases and components, *Physical Review E* 47 (3) (1993) 1815.
- [184] C. Holm, K. Kremer, *Advanced computer simulation approaches for soft matter sciences III*, Vol. 221, Springer, 2008.
- [185] P. Hoogerbrugge, J. Koelman, Simulating microscopic hydrodynamic phenomena with dissipative particle dynamics, *EPL (Europhysics Letters)* 19 (3) (1992) 155.

## Bibliography

---

- [186] P. Espanol, P. Warren, Statistical mechanics of dissipative particle dynamics, *EPL (Europhysics Letters)* 30 (4) (1995) 191.
- [187] A. Malevanets, R. Kapral, Mesoscopic model for solvent dynamics, *J. Chem. Phys.* 110 (1999) 8605.
- [188] R. Kapral, Multiparticle collision dynamics: Simulations of complex systems on mesoscale, *Adv. Chem. Phys.* 140 (2008) 89.
- [189] G. Gompper, T. Ihle, D. M. Kroll, R. G. Winkler, Multi-particle collision dynamics: A particle-based mesoscale simulation approach to the hydrodynamics of complex fluids, *Adv. Polym. Sci.* 221 (2009) 1.
- [190] A. Malevanets, J. M. Yeomans, Dynamics of short polymer chains in solution, *Europhys. Lett.* 52 (2000) 231–237.
- [191] N. Kikuchi, A. Gent, J. M. Yeomans, Polymer collapse in the presence of hydrodynamic interactions, *Eur. Phys. J. E* 9 (2002) 63.
- [192] M. Ripoll, R. G. Winkler, G. Gompper, Hydrodynamic screening of star polymers in shear flow, *Eur. Phys. J. E* 23 (2007) 349.
- [193] H. Noguchi, G. Gompper, Transport coefficients of off-lattice mesoscale-hydrodynamics simulation techniques, *Phys. Rev. E* 78 (2008) 016706.
- [194] M. Theers, R. G. Winkler, Bulk viscosity of multiparticle collision dynamics fluids, *Phys. Rev. E* 91 (2015) 033309.
- [195] T. Ihle, D. M. Kroll, Stochastic rotation dynamics: A Galilean-invariant mesoscopic model for fluid flow, *Phys. Rev. E* 63 (2001) 020201(R).
- [196] T. Ihle, D. M. Kroll, Stochastic rotation dynamics I: Formalism, Galilean invariance, Green-Kubo relations, *Phys. Rev. E* 67 (2003) 066705.
- [197] C.-C. Huang, R. G. Winkler, G. Sutmann, G. Gompper, Semidilute polymer solutions at equilibrium and under shear flow, *Macromolecules* 43 (2010) 10107.
- [198] K. Mussawisade, M. Ripoll, R. G. Winkler, G. Gompper, Dynamics of polymers in a particle based mesoscopic solvent, *J. Chem. Phys.* 123 (2005) 144905.
- [199] S. Poblete, A. Wysocki, G. Gompper, R. G. Winkler, Hydrodynamics of discrete-particle models of spherical colloids: A multiparticle collision dynamics simulation study, *Phys. Rev. E* 90 (2014) 033314.
- [200] A. Malevanets, R. Kapral, Solute molecular dynamics in a mesoscopic solvent, *J. Chem. Phys.* 112 (2000) 7260.



- 
- [201] S. H. Lee, R. Kapral, Friction and diffusion of a brownian particle in a mesoscopic solvent, *J. Chem. Phys.* 121 (2004) 11163.
- [202] Y. Inoue, Y. Chen, H. Ohashi, Development of a simulation model for solid objects suspended in a fluctuating fluid, *J. Stat. Phys.* 107 (2002) 85.
- [203] A. Lamura, G. Gompper, T. Ihle, D. M. Kroll, Multiparticle collision dynamics: Flow around a circular and a square cylinder, *Europhys. Lett.* 56 (2001) 319–325.
- [204] C.-C. Huang, A. Chatterji, G. Sutmann, G. Gompper, R. G. Winkler, Cell-level canonical sampling by velocity scaling for multiparticle collision dynamics simulations, *J. Comput. Phys.* 229 (2010) 168.
- [205] N. Kikuchi, C. M. Pooley, J. F. Ryder, J. M. Yeomans, Transport coefficients of a mesoscopic fluid dynamics model, *J. Chem. Phys.* 119 (2003) 6388–6395.
- [206] M. Ripoll, K. Mussawisade, R. G. Winkler, G. Gompper, Dynamic regimes of fluids simulated by multi-particle-collision dynamics, *Phys. Rev. E* 72 (2005) 016701.
- [207] W. Briels, Theory of polymer dynamics, lecture notes, Uppsala.
- [208] J.-P. Hansen, I. R. McDonald, Theory of simple liquids: with applications to soft matter, Academic Press, 2013.
- [209] G. Nägele, The physics of colloidal soft matter, Centre of Excellence for Advanced Materials and Structures Warsaw, 2004.
- [210] A. J. Banchio, G. Nägele, Short-time transport properties in dense suspensions: from neutral to charge-stabilized colloidal spheres, *The Journal of chemical physics* 128 (10) (2008) 104903.
- [211] G. Nägele, On the dynamics and structure of charge-stabilized suspensions, *Physics Reports* 272 (5-6) (1996) 215–372.
- [212] J. Riest, G. Nägele, Short-time dynamics in dispersions with competing short-range attraction and long-range repulsion, *Soft Matter* 11 (2015) 9273–9280.
- [213] G. Zerah, J.-P. Hansen, Self-consistent integral equations for fluid pair distribution functions: Another attempt, *The Journal of Chemical Physics* 84 (4) (1986) 2336.
- [214] D. Costa, C. Caccamo, J.-M. Bomont, J.-L. Bretonnet, Theoretical description of cluster formation in two-Yukawa competing fluids, *Molecular Physics* 109 (23-24) (2011) 2845–2853.
- [215] W. E. J. Verwey, J. T. G. Overbeek, Theory of the stability of lyophobic colloids, Dover Publications, Mineola, N.Y., 1999.

## Bibliography

---

- [216] M. Doi, S. F. Edwards, *The Theory of Polymer Dynamics*, Clarendon Press, Oxford, 1986.
- [217] J. M. Kim, R. Castañeda-Priego, Y. Liu, N. J. Wagner, On the importance of thermodynamic self-consistency for calculating clusterlike pair correlations in hard-core double Yukawa fluids, *The Journal of Chemical Physics* 134 (6) (2011) 064904.
- [218] R. B. Jadrich, J. A. Bollinger, K. P. Johnston, T. M. Truskett, Origin and detection of microstructural clustering in fluids with spatial-range competitive interactions, *Physical Review E* 91 (4) (2015) 042312. [arXiv:1504.03943](#).
- [219] F. Sciortino, P. Tartaglia, E. Zaccarelli, One-dimensional cluster growth and branching gels in colloidal systems with short-range depletion attraction and screened electrostatic repulsion, *J. Phys. Chem. B* 109 (2005) 21942.
- [220] D. Y. C. Chan, B. Halle, Dissociation kinetics of secondary-minimum flocculated colloidal particles, *Journal of Colloid And Interface Science* 102 (2) (1984) 400–409.
- [221] S. Kim, S. Karrila, *Microhydrodynamics: Principles and Selected Applications*, Butterworth-Heinemann, Boston, 1991.
- [222] D. J. Jeffrey, Y. Onishi, Calculation of the resistance and mobility functions for two unequal rigid spheres in low-Reynolds-number flow, *Journal of Fluid Mechanics* 139 (1984) 261–290.
- [223] R. Jones, R. Schmitz, Mobility matrix for arbitrary spherical particles in solution, *Physica A: Statistical Mechanics and its Applications* 149 (3) (1988) 373–394.
- [224] G. Foffi, G. Savin, S. Bucciarelli, N. Dorsaz, G. M. Thurston, A. Stradner, P. Schurtenberger, Hard sphere-like glass transition in eye lens  $\alpha$ -crystallin solutions, *Proceedings of the National Academy of Sciences* 111 (47) (2014) 16748–16753.
- [225] P. Schurtenberger, R. A. Chamberlin, G. M. Thurston, J. A. Thomson, G. B. Benedek, Observation of critical phenomena in a protein-water solution, *Physical review letters* 63 (19) (1989) 2064.
- [226] F. Roosen-Runge, M. Hennig, F. Zhang, R. M. Jacobs, M. Sztucki, H. Schober, T. Seydel, F. Schreiber, Protein self-diffusion in crowded solutions, *Proceedings of the National Academy of Sciences* 108 (29) (2011) 11815–11820.
- [227] G. Vliegenthart, H. N. Lekkerkerker, Predicting the gas–liquid critical point from the second virial coefficient, *The Journal of Chemical Physics* 112 (12) (2000) 5364–5369.
- [228] G. Foffi, F. Sciortino, On the possibility of extending the noro- frenkel generalized law of correspondent states to nonisotropic patchy interactions, *The Journal of Physical Chemistry B* 111 (33) (2007) 9702–9705.

- 
- [229] A. Lomakin, N. Asherie, G. B. Benedek, Aeolotopic interactions of globular proteins, *Proceedings of the National Academy of Sciences* 96 (17) (1999) 9465–9468.
- [230] A. Ghosh, N. S. Gov, Dynamics of active semiflexible polymers, *Biophys. J.* 107 (2014) 1065.
- [231] R. G. Winkler, Dynamics of flexible active Brownian dumbbells in the absence and the presence of shear flow, *Soft Matter* 12 (2016) 3737.
- [232] T. Eisenstecken, G. Gompper, R. G. Winkler, Conformational properties of active semiflexible polymers, *Polymers* 8 (2016) 304.
- [233] N. Samanta, R. Chakrabarti, Chain reconfiguration in active noise, *J. Phys. A: Math. Theor.* 49 (2016) 195601.
- [234] G. Szamel, E. Flenner, L. Berthier, Glassy dynamics of athermal self-propelled particles: Computer simulations and a nonequilibrium microscopic theory, *Phys. Rev. E* 91 (2015) 062304.
- [235] For strictly 2d systems, the hydrodynamic diffusion coefficient  $D_T$  diverges in the limit of system size  $L \rightarrow \infty$  ( $D_T \sim \ln(L/\sigma)$ ). However, in simulations and experiments—for the latter, there is no strictly 2d system—typically slit geometries, i.e., quasi 2d, or “semi-infinite” systems with self-propelled particles absorbed at a wall are considered. Our simulations of a colloid show that the rotational diffusion coefficient in a quasi-2d system is approximately equal to the bulk value. However, the translational diffusion coefficient is reduced [275,276]. Hence, a ratio  $\Delta$  can be defined also for such systems, however,  $\Delta$  is smaller than the value  $\Delta = 1/3$  of a 3d system.
- [236] M. Raible, A. Engel, Langevin equation for the rotation of a magnetic particle, *Appl. Organometal. Chem.* 18 (2004) 536.
- [237] A. P. Solon, M. E. Cates, J. Tailleur, Active Brownian particles and run-and-tumble particles: A comparative study, *Eur. Phys. J. Spec. Top.* 224 (2015) 1231.
- [238] P. Hänggi, P. Jung, Colored noise in dynamical systems, *Adv. Chem. Phys.* 89 (1995) 239.
- [239] G. Szamel, Self-propelled particle in an external potential: Existence of an effective temperature, *Phys. Rev. E* 90 (2014) 012111.
- [240] C. Sandford, A. Y. Grosberg, J.-F. Joanny, Pressure and Flow of Exponentially Self-Correlated Active Particles, *ArXiv e-prints*.
- [241] R. Zakine, A. Solon, T. Gingrich, F. van Wijland, Stochastic stirling engine operating in contact with active baths, *Entropy* 19 (2017) 193.

## Bibliography

---

- [242] C. Maggi, M. Paoluzzi, N. Pellicciotta, A. Lepore, L. Angelani, R. Di Leonardo, Generalized energy equipartition in harmonic oscillators driven by active baths, *Phys. Rev. Lett.* 113 (2014) 238303.
- [243] U. M. B. Marconi, N. Gnan, M. Paoluzzi, C. Maggi, R. Di Leonardo, Velocity distribution in active particles systems, *Sci. Rep.* 6 (2016) 23297.
- [244] C. Maggi, U. M. B. Marconi, N. Gnan, R. Di Leonardo, Multidimensional stationary probability distribution for interacting active particles, *Sci. Rep.* 5 (2015) 10742.
- [245] J. Saragosti, P. Silberzan, A. Buguin, Modeling *e. coli* tumbles by rotational diffusion. implications for chemotaxis, *PLoS ONE* 7 (2012) e35412.
- [246] S. Tavaddod, M. A. Charsooghi, F. Abdi, H. R. Khalesifard, R. Golestanian, Probing passive diffusion of flagellated and deflagellated *escherichia coli*, *Eur. Phys. J. E* 34 (2011) 1.
- [247] R. F. Fox, Functional-calculus approach to stochastic differential equations, *Phys. Rev. A* 33 (1986) 467.
- [248] R. Stratonovich, *Topics in the Theory of Random Noise*, Vol. 1, Gordon and Breach, New York, 1963.
- [249] J. Elgeti, G. Gompper, Run-and-tumble dynamics of self-propelled particles in confinement, *EPL* 109 (2015) 58003.
- [250] S. A. Mallory, A. Šarić, C. Valeriani, A. Cacciuto, Anomalous thermomechanical properties of a self-propelled colloidal fluid, *Phys. Rev. E* 89 (2014) 052303.
- [251] T. W. Lion, R. J. Allen, Computing the local pressure in molecular dynamics simulations, *Journal of Physics: Condensed Matter* 24 (28) (2012) 284133.
- [252] J.-A. Schweitz, A classical virial theorem for open systems, *Journal of Physics A: Mathematical and General* 10 (4) (1977) 507.
- [253] R. B. Bird, R. C. Armstrong, O. Hassager, *Dynamics of polymeric liquids. vol. 1: Fluid mechanics.*
- [254] H. Xu, A. Pumir, G. Falkovich, E. Bodenschatz, M. Shats, H. Xia, N. Francois, G. Boffetta, Flight–crash events in turbulence, *Proceedings of the National Academy of Sciences* 111 (21) (2014) 7558–7563.
- [255] J. Dunkel, S. Heidenreich, K. Drescher, H. H. Wensink, M. Bär, R. E. Goldstein, Fluid dynamics of bacterial turbulence, *Physical review letters* 110 (22) (2013) 228102.
- [256] M. Belkin, A. Snezhko, I. Aranson, W.-K. Kwok, Magnetically driven surface mixing, *Physical Review E* 80 (1) (2009) 011310.

- 
- [257] V. Bratanov, F. Jenko, E. Frey, New class of turbulence in active fluids, *Proceedings of the National Academy of Sciences* 112 (49) (2015) 15048–15053.
- [258] M. Theers, E. Westphal, G. Gompper, R. G. Winkler, From local to hydrodynamic friction in brownian motion: A multiparticle collision dynamics simulation study, *Phys. Rev. E* 93 (2016) 032604.
- [259] A. Snezhko, I. S. Aranson, Velocity statistics of dynamic spinners in out-of-equilibrium magnetic suspensions, *Soft matter* 11 (30) (2015) 6055–6061.
- [260] N. H. Nguyen, D. Klotsa, M. Engel, S. C. Glotzer, Emergent collective phenomena in a mixture of hard shapes through active rotation, *Physical review letters* 112 (7) (2014) 075701.
- [261] K. Yeo, E. Lushi, P. M. Vlahovska, Collective dynamics in a binary mixture of hydrodynamically coupled microrotors, *Physical review letters* 114 (18) (2015) 188301.
- [262] G. Kokot, A. Snezhko, I. S. Aranson, Emergent coherent states and flow rectification in active magnetic colloidal monolayers, *Soft Matter* 9 (29) (2013) 6757–6760.
- [263] X.-L. Wu, A. Libchaber, Particle diffusion in a quasi-two-dimensional bacterial bath, *Physical Review Letters* 84 (13) (2000) 3017.
- [264] A. Sokolov, R. E. Goldstein, F. I. Feldchtein, I. S. Aranson, Enhanced mixing and spatial instability in concentrated bacterial suspensions, *Physical Review E* 80 (3) (2009) 031903.
- [265] K. C. Leptos, J. S. Guasto, J. P. Gollub, A. I. Pesci, R. E. Goldstein, Dynamics of enhanced tracer diffusion in suspensions of swimming eukaryotic microorganisms, *Physical Review Letters* 103 (19) (2009) 198103.
- [266] A. E. Patteson, A. Gopinath, P. K. Purohit, P. E. Arratia, Particle diffusion in active fluids is non-monotonic in size, *Soft matter* 12 (8) (2016) 2365–2372.
- [267] T. Kasyap, D. L. Koch, M. Wu, Hydrodynamic tracer diffusion in suspensions of swimming bacteria, *Physics of Fluids* (1994-present) 26 (8) (2014) 081901.
- [268] T. Eisenstecken, G. Gompper, R. G. Winkler, Internal dynamics of semiflexible polymers with active noise, *J. Chem. Phys.* 146 (2017) 154903.
- [269] H. Kellay, W. I. Goldburg, Two-dimensional turbulence: a review of some recent experiments, *Reports on Progress in Physics* 65 (5) (2002) 845.
- [270] A. Esmaeeli, G. Tryggvason, An inverse energy cascade in two-dimensional low reynolds number bubbly flows, *Journal of Fluid Mechanics* 314 (1996) 315–330.
- [271] M. Lance, J. Bataille, Turbulence in the liquid phase of a uniform bubbly air–water flow, *Journal of Fluid Mechanics* 222 (1991) 95–118.

## Bibliography

---

- [272] A. Groisman, V. Steinberg, Elastic turbulence in a polymer solution flow, arXiv preprint nlin/0104052.
- [273] H. Wensink, H. Löwen, Emergent states in dense systems of active rods: from swarming to turbulence, *Journal of Physics: Condensed Matter* 24 (46) (2012) 464130.
- [274] R. Roa, J. Riest, G. Nägele, Ultrafiltration modeling of charge-stabilized colloidal dispersions, in preparation.
- [275] A. Imperio, J. T. Padding, W. Briels, Force calculation on walls and embedded particles in multiparticle-collision-dynamics simulations, *Physical Review E* 83 (2011) 046704.
- [276] J. Blaschke, M. Maurer, K. Menon, A. Zöttl, H. Stark, Phase separation and coexistence of hydrodynamically interacting microswimmers, *Soft Matter* 12 (2016) 9821.

# Erklärung

Ich versichere, daß ich die von mir vorgelegte Dissertation selbständig angefertigt, die benutzten Quellen und Hilfsmittel vollständig angegeben und die Stellen der Arbeit einschließlich Tabellen, Karten und Abbildungen, die anderen Werken im Wortlaut oder dem Sinn nach entnommen sind, in jedem Einzelfall als Entlehnung kenntlich gemacht habe; daß diese Dissertation noch keiner anderen Fakultät oder Universität zur Prüfung vorgelegen hat; daß sie abgesehen von unten angegebenen Teilpublikationen noch nicht veröffentlicht worden ist sowie, daß ich eine solche Veröffentlichung vor Abschluß des Promotionsverfahrens nicht vornehmen werde. Die Bestimmungen dieser Promotionsordnung sind mir bekannt. Die von mir vorgelegte Dissertation ist von Prof. Dr. Gerhard Gompper betreut worden.

Jülich, 20 Nov. 2017

Shibananda Das

## Publikationen

- S. Bucciarelli, J. S. Myung, B. Farago, S. Das, G. A. Vliegenthart, O. Holderer, R. G. Winkler, P. Schurtenberger, G. Gompper, and A. Stradner  
Dramatic influence of patchy attractions on short-time protein diffusion under crowded conditions, *Science Advances* 2 (12) (2016) e1601432.
- G. Kokot, S. Das, R. G. Winkler, G. Gompper, I. S. Aranson, and A. Snezhko  
Active turbulence in a gas of self-assembled spinners, *PNAS* 114 (49) (2017) 12870.
- S. Das, J. Riest, R. G. Winkler, G. Gompper, J. K. G. Dhont, and G. Nägele  
Clustering and Dynamics of Particles in Dispersions with Competing Interactions: Theory and Simulation, *Soft Matter* 14 (1) (2018) 92.
- S. Das, G. Gompper, and R. G. Winkler  
Confined active Brownian particles: Theoretical description of propulsion-induced accumulation, *New Journal of Physics* 20 (1) (2018) 015001.





# Curriculum Vitæ

## Personal Information

**Name** Shibananda Das  
**Date of Birth** 31<sup>st</sup> May 1991  
**Nationality** Indian

## School Education

**2005-2007** Shishu Niketan High School, Agartala  
Percentage - 88%

**2007-2009** Umakanta Academy, Agartala  
Percentage - 78%

## Academic Record

**2009-2014** Master of Science (Integrated BS-MS)- IISER Pune  
CGPA: 8.4/10.0  
Advisor: Dr. Apratim Chatterji

**since 2014** Ph.D. student at Universität zu Köln and Forschungszentrum Jülich  
Advisors: Prof. Dr. Gerhard Gompper, Prof. Dr. Roland G. Winkler